ASL2739

THREE-DIMENSIONAL CURVILINEAR-GRID MODELING OF BAROCLINIC CIRCULATION AND MIXING IN A PARTIALLY-MIXED ESTUARY

By

JEI-KOOK CHOI

A DISSERTATION PRESENTED TO THE GRADUATE SCHOOL
OF THE UNIVERSITY OF FLORIDA IN
PARTIAL FULFILLMENT OF THE REQUIREMENTS
FOR THE DEGREE OF DOCTOR OF PHILOSOPHY

UNIVERSITY OF FLORIDA

1992

ACKNOWLEDGEMENTS

This dissertation could not have been completed without the advice, ideas, and financial support of my committee chairman, Dr. Y. Peter Sheng throughout this study. I would also like to express my thanks to my dissertation committee member, Dr. Robert G. Dean, Dr. Max Sheppard, and Dr. Louis H. Motz, for their patience in reviewing this dissertation. I would also like to thank Dr. Albert Y. Kuo of Virgina Institute of Marine Science, for providing the field data obtained from the James River. Initial funding for this research was provided by the state of Virginia through Virginia Institute of Marine Science.

I would like to dedicate this dissertation to my parents who have been praying for me to be faithful, kind, and honest all the time.

Last but not least, I would like to thank my wife, Mija for her encouragemnet and support, and my son, Jungmin for his sincere prayer.

TABLE OF CONTENTS

ACKNOWLEDGEMENTS ii

LIST OF FIGURES iv

LIST OF TABLES v

ABSTRACT vi

CHAPTERS

1 INTRODUCTION 1

1.1 Background 1

1.2 Review of Previous Works 4

1.3 Modeling Strategy 7

1.4 Scope of This Study 10

1.5 Objective of This Study 13

1.6 James River 13

2 GOVERNING EQUATIONS AND SOLUTION TECHNIQUE 16

2.1 Differential Equations 16

2.2 Governing Equations in Stretched Coordinates 20

2.3 Dimensionless Equations in Stretched Coordinates 24

2.4 Dimensionless Vertically Integrated Equations 29

2.5 Boundary-Fitted Coordinate Generation 30

2.6 Transformation of Governing Equations Into Boundary-Fitted Grids . 32

2.6.1 Transformation Rules 32

2.6.2 Dimensionless Equations in Boundary-Fitted Grids 33

2.7 Boundary Conditions and Initial Conditions 35

2.7.1 Vertically Stretched System 35
2.7.2 Vertically Stretched and Laterally Boundary-Fitted System . . 38
2.8 Solution Technique 40
2.9 Finite Difference Equation 41
2.9.1 External Mode in (x, y, σ) (Two-Time-Level Scheme) 43
2.9.2 Internal Mode in (x, y, σ) (Two-Time-Level Scheme) 46
2.9.3 External Mode in (ξ, η, σ) (Two-Time-Level Scheme) 47
2.9.4 Internal Mode in (ξ, η, σ) (Two-Time-Level Scheme) 51
2.9.5 Salinity Scheme (Two-Time-Level Scheme) 51
2.9.6 Advection Terms 54
2.9.7 Horizontal Diffusion Terms 58
2.9.8 Numerical Stability 59
2.10 Turbulence Model for Mass and Momentum Exchange Coefficients . . 61
3 MODEL ANALYTICAL TEST: COMPARISON BETWEEN MODEL RESULTS AND ANALYTIC SOLUTIONS 73
3.1 Forced Constant Surface Slope 73
3.2 Seiche Test 80
3.3 Tidal Forcing 84
3.4 Wind Forcing 92
3.5 Density-Driven Currents 100
3.6 Summary 103
4 ANALYSIS OF OBSERVED HYDRODYNAMIC DATA FROM JAMES RIVER 105
4.1 Water Level Data 106
4.2 Tidal Currents 109
4.3 Circulation Pattern 109
4.4 Slack-Water Salinity Data 110

4.5 Front Dynamics 110
5 APPLICATION OF THREE-DIMENSIONAL MODEL TO JAMES RIVER 119
5.1 Procedure of Model Simulation 119
5.2 Simulation of Tidal Circulation 125
5.3 Sensitivity Tests 135
5.3.1 Effect of Bottom Friction 136
5.3.2 Effect of Bathymetry 141
5.3.3 Effect of Horizontal Grid 141
5.3.4 Effect of Time Step 142
5.4 Neap-Spring Stratification and Destratification Cycle 142
5.5 Salinity Intrusion 153
5.6 Frontal Dynamics 160
5.7 Model Calibration and Validation 231
5.8 Comparison of σ- and z-baroclinic approaches 236
6 CONCLUSIONS 254
BIBLIOGRAPHY 258
APPENDICES
A HIGHER-ORDER-TERMS (H.O.T.) IN σ-GRID SYSTEM 264
B TRANSFORMATION OF GOVERNING EQUATIONS 265
B.1 Transformation Rules 265
B.2 Dimensionless Tensor Invariant Governing Equations 266
B.3 Transformation of stress components 267
C HORIZONTAL DIFFUSION TERMS IN BOUNDARY-FITTED GRIDS 268
D MORE COMPACT MOMENTUM EQUATIONS 270
E FINITE DIFFERENCE EQUATIONS IN (ξ, η, σ) (THREE-TIME-LEVEL) 272
E.1 External Mode 272
E.2 Internal Mode 275

LIST OF FIGURES

1.1 The James River Estuary from Old Point Comfort, at the mouth, to Jamestown Island (upper left corner). Seed oyster beds are shown as irregularly shaped darkened areas (Byrne *et al.*, 1987). 15

2.1 The right-handed Cartesian coordinate system. 18

2.2 σ_t density field calculated from Eckart formula. 19

2.3 The vertically stretched grid (From Sheng and Butler, 1982). . . 22

2.4 Field transfomation (From Thompson *et al.*, 1977). 31

2.5 Staggered numerical grids in lateral and vertical directions (From Sheng, 1983). 42

2.6 Comparison of stability functions for (a) some epirical formulae versus (b) the simplified second-order closure model (From Sheng, 1983). 69

3.1 A non-uniform rectangular grid system for testing the forced surface slope test. 75

3.2 Simulated steady-state vertically-averaged velocity field in a rectangular basin forced by a constant surface slope. Horizontal grid is shown in Figure 3.1. 76

3.3 Same as Figure 3.2, except that the basin is rotated by 30° in the counterclockwise direction. 77

3.4 An irregular grid system for rectangular basin with irregular grids 78

3.5 Same as Figure 3.2, except that the irregular curvilinear grid as shown in Figure 3.4 is used. 79

3.6 Comparison between simulated surface elevation (diamond symbol) and analytic solution (solid lines) for seiche oscillation in a closed basin (T is seiche period). 81

3.7 Comparison between simulated vertically-averaged velocities (diamond symbol) and analytic solution (solid line) for seiche oscillation in a closed basin (T is seiche period). 82

3.8 Maximum velocities for seiche case. 83

3.9 Comparison between simulated surface elevations and velocities (*'s) and analytic solutions for a tidally forced flat-bottom basin (Elevation and velocity are in phase). 87

3.10 Comparison of simulated maximum surface elevations at the closed end and maximum velocities at the open end with the analytic solution for a tidally forced sloping bottom basin. 88

3.11 Grid system for the annular section 89

3.12 Comparison between simulated surface elevations and velocities (*'s) and analytic solutions for a tidally forced flat-bottom annular section. 90

3.13 Maximum ebb and flood velocities in a tidally forced flat-bottom annular section at the end of tidal 10 cycles run. 91

3.14 Comparison between simulated maximum surface elevation and analytic solution for a sloping bottom basin forced by wind (a_o is the setup in the flat bottom). 95

3.15 Comparison between simulated vertical velocity structure and analytic solution for a constant wind in a closed basin. 96

3.16 Grid system for wind setup test in a bowtie-shaped basin. 97

3.17 Steady state setup in cm for (a) 1 $dyne/cm^2$ eastward wind, and (b) 1 $dyne/cm^2$ northward wind. 98

3.18 Comparison between simulated results and analytic solution for the vertical structure of horizontal velocity induced by density gradient. 102

4.1 Lower James River and Hampton Roads (After Hepworth and Kuo (1989)). 107

4.2 Observed Eulerian residual velocity over transect 'JB' (After Hamrick (1990)). 108

4.3 Surface elevation at the open boundary between June 19 and July 17, 1985. 111

4.4 Observed longitudinal-vertical salinity at slackwater before flood on June 19, 1985. 112

4.5 Observed longitudinal-vertical salinity at slackwater before flood on July 3, 1985. 113

4.6 Observed longitudinal-vertical salinity at slackwater before flood on July 9, 1985. 114

4.7 Observed longitudinal-vertical salinity at slackwater before flood on July 17, 1985. 115

4.8 Configuration of fronts at 1118 hours. From aerial photographs of August 29, 1985. Generalized flow direction shown by arrows. Dotted lines are depth contours in *ft*. (After Byrne, 1987) 116

4.9 Configuration of fronts at 1400 hours. From aerial photographs of August 29, 1985. Generalized flow direction shown by arrows. Dotted lines are depth contours in *ft*. (After Byrne, 1987) 117

5.1 Curvilinear grid for the James River coarse grid system (physical domain). 121

5.2 Curvilinear grid for the James River fine grid system (physical domain). 122

5.3 Curvilinear grid for the James River coarse grid system (computation domain). 123

5.4 Curvilinear grid for the James River fine grid system (computation domain). 124

5.5 Eulerian residual current at surface in the James River between June 19 and July 17, 1985. 126

5.6 Eulerian residual current at mid-depth in the James River between June 19 and July 17, 1985. 127

5.7 Eulerian residual current near bottom in the James River between June 19 and July 17, 1985. 128

5.8 Vertical velocity profile at spring near the James River Bridge. The numbers on top of plot indicate the time evolution in hours. 129

5.9 Vertical velocity profile at neap near the James River Bridge. The numbers on top of plot indicate the time evolution in hours. . . . 130

5.10 Computed near-surface tidal currents near the James River Bridge between June 19 and July 17, 1985. 131

5.11 Contours of 29-day residual longitudinal velocity at a transect near the James River Bridge (along i=65). 132

5.12 Simulated longitudinal-vertical salinity at slackwater before flood on July 3, 1985. 144

5.13 Simulated longitudinal-vertical salinity at slackwater before flood on July 9, 1985. 145

5.14 Computed elevation, and velocity and salinity at surface, mid, and bottom level for 29-day simulation at Station 1. 147

5.15 Computed elevation, and velocity and salinity at surface, mid, and bottom level for 29-day simulation at Station 2. 148

5.16 Computed elevation, and velocity and salinity at surface, mid, and bottom level for 29-day simulation at Station 3. 149

5.17 Model predicted longitudinal surface salinity distribution with 3000 ft^3/sec of river discharge on July 3, 1985. 150

5.18 Model predicted longitudinal surface salinity distribution with 3000 ft^3/sec of river discharge on July 9, 1985. 151

5.19 Model predicted longitudinal surface salinity distribution with 3000 ft^3/sec of river discharge on July 17, 1985. 152

5.20 Model predicted longitudinal surface salinity distribution with 1000 ft^3/sec of river discharge on July 3, 1985. 154

5.21 Model predicted longitudinal surface salinity distribution with 1000 ft^3/sec of river discharge on July 9, 1985. 155

5.22 Model predicted longitudinal surface salinity distribution with 1000 ft^3/sec of river discharge on July 17, 1985. 156

5.23 Model predicted longitudinal surface salinity distribution with 9000 ft^3/sec of river discharge on July 3, 1985. 157

5.24 Model predicted longitudinal surface salinity distribution with 9000 ft^3/sec of river discharge on July 9, 1985. 158

5.25 Model predicted longitudinal surface salinity distribution with 9000 ft^3/sec of river discharge on July 17, 1985. 159

5.26 Instantaneous near-surface horizontal velocity and salinity (*ppt*) distribution in lower James River at 1 a.m. 1 on July 3, 1985. . . 165

5.27 Instantaneous near-surface horizontal velocity and salinity (*ppt*) distribution in lower James River at 2 a.m. on July 3, 1985. . . . 166

5.28 Instantaneous near-surface horizontal velocity and salinity (*ppt*) distribution in lower James River at 3 a.m. on July 3, 1985. . . . 167

5.29 Instantaneous near-surface horizontal velocity and salinity (*ppt*) distribution in lower James River at 4 a.m. on July 3, 1985. . . . 168

5.30 Instantaneous near-surface horizontal velocity and salinity (*ppt*) distribution in lower James River at 5 a.m. on July 3, 1985. . . . 169

5.31 Instantaneous near-surface horizontal velocity and salinity (*ppt*) distribution in lower James River at 6 a.m. on July 3, 1985. . . . 170

5.32 Instantaneous near-surface horizontal velocity and salinity (*ppt*) distribution in lower James River at 7 a.m. on July 3, 1985. . . . 171

5.33 Instantaneous near-surface horizontal velocity and salinity (*ppt*) distribution in lower James River at 8 a.m. on July 3, 1985. . . . 172

5.34 Instantaneous near-surface horizontal velocity and salinity (*ppt*) distribution in lower James River at 9 a.m. on July 3, 1985. . . . 173

5.35 Instantaneous near-surface horizontal velocity and salinity (*ppt*) distribution in lower James River at 10 a.m. on July 3, 1985. . . 174

5.36 Instantaneous near-surface horizontal velocity and salinity (*ppt*) distribution in lower James River at 11 a.m. on July 3, 1985. . . 175

5.37 Instantaneous near-bottom horizontal velocity and salinity (*ppt*) distribution in lower James River at 1 a.m. on July 3, 1985. . . . 176

5.38 Instantaneous near-bottom horizontal velocity and salinity (*ppt*) distribution in lower James River at 2 a.m. on July 3, 1985. . . . 177

5.39 Instantaneous near-bottom horizontal velocity and salinity (*ppt*) distribution in lower James River at 3 a.m. on July 3, 1985. . . . 178

5.40 Instantaneous near-bottom horizontal velocity and salinity (*ppt*) distribution in lower James River at 4 a.m. on July 3, 1985. . . . 179

5.41 Instantaneous near-bottom horizontal velocity and salinity (*ppt*) distribution in lower James River at 5 a.m. on July 3, 1985. . . . 180

5.42 Instantaneous near-bottom horizontal velocity and salinity (*ppt*) distribution in lower James River at 6 a.m. on July 3, 1985. . . . 181

5.43 Instantaneous near-bottom horizontal velocity and salinity (*ppt*) distribution in lower James River at 7 a.m. on July 3, 1985. . . . 182

5.44 Instantaneous near-bottom horizontal velocity and salinity (*ppt*) distribution in lower James River at 8 a.m. on July 3, 1985. . . . 183

5.45 Instantaneous near-bottom horizontal velocity and salinity (*ppt*) distribution in lower James River at 9 a.m. on July 3, 1985. . . . 184

5.46 Instantaneous near-bottom horizontal velocity and salinity (*ppt*) distribution in lower James River at 10 a.m. on July 3, 1985. . . 185

5.47 Instantaneous near-bottom horizontal velocity and salinity (*ppt*) distribution in lower James River at 11 a.m. on July 3, 1985. . . 186

5.48 Instantaneous velocity in (x, z) domain along the channel in lower James River at 1 a.m. on July 3, 1985. 187

5.49 Instantaneous velocity in (x, z) domain along the channel in lower James River at 2 a.m. on July 3, 1985. 188

5.50 Instantaneous velocity in (x, z) domain along the channel in lower James River at 3 a.m. on July 3, 1985. 189

5.51 Instantaneous velocity in (x, z) domain along the channel in lower James River at 4 a.m. on July 3, 1985. 190

5.52 Instantaneous velocity in (x, z) domain along the channel in lower James River at 5 a.m. on July 3, 1985. 191

5.53 Instantaneous velocity in (x, z) domain along the channel in lower James River at 6 a.m. on July 3, 1985. 192

5.54 Instantaneous velocity in (x, z) domain along the channel in lower James River at 7 a.m. on July 3, 1985. 193

5.55 Instantaneous velocity in (x, z) domain along the channel in lower James River at 8 a.m. on July 3, 1985. 194

5.56 Instantaneous velocity in (x, z) domain along the channel in lower James River at 9 a.m. on July 3, 1985. 195

5.57 Instantaneous velocity in (x, z) domain along the channel in lower James River at 10 a.m. on July 3, 1985. 196

5.58 Instantaneous velocity in (x, z) domain along the channel in lower James River at 11 a.m. on July 3, 1985. 197

5.59 Instantaneous velocity in (x, z) domain along the one-grid away from the channel in lower James River at 1 a.m. on July 3, 1985. 198

5.60 Instantaneous velocity in (x, z) domain along the one-grid away from the channel in lower James River at 2 a.m. on July 3, 1985. 199

5.61 Instantaneous velocity in (x, z) domain along the one-grid away from the channel in lower James River at 3 a.m. on July 3, 1985. 200

5.62 Instantaneous velocity in (x, z) domain along the one-grid away from the channel in lower James River at 4 a.m. on July 3, 1985. 201

5.63 Instantaneous velocity in (x, z) domain along the one-grid away from the channel in lower James River at 5 a.m. on July 3, 1985. 202

5.64 Instantaneous velocity in (x, z) domain along the one-grid away from the channel in lower James River at 6 a.m. on July 3, 1985. 203

5.65 Instantaneous velocity in (x, z) domain along the one-grid away from the channel in lower James River at 7 a.m. on July 3, 1985. 204

5.66 Instantaneous velocity in (x, z) domain along the one-grid away from the channel in lower James River at 8 a.m. on July 3, 1985. 205

5.67 Instantaneous velocity in (x, z) domain along the one-grid away from the channel in lower James River at 9 a.m. on July 3, 1985. 206

5.68 Instantaneous velocity in (x, z) domain along the one-grid away from the channel in lower James River at 10 a.m. on July 3, 1985. 207

5.69 Instantaneous velocity in (x, z) domain along the one-grid away from the channel in lower James River at 11 a.m. on July 3, 1985. 208

5.70 u at surface, w at mid-depth, salinity at surface-, mid-, and bottom-depth, and elevation along the one-grid away from the channel in lower James River at 1 a.m. on July 3, 1985. 209

5.71 u at surface, w at mid-depth, salinity at surface-, mid-, and bottom-depth, and elevation along the one-grid away from the channel in lower James River at 2 a.m. on July 3, 1985. 210

5.72 u at surface, w at mid-depth, salinity at surface-, mid-, and bottom-depth, and elevation along the one-grid away from the channel in lower James River at 3 a.m. on July 3, 1985. 211

5.73 u at surface, w at mid-depth, salinity at surface-, mid-, and bottom-depth, and elevation along the one-grid away from the channel in lower James River at 4 a.m. on July 3, 1985. 212

5.74 u at surface, w at mid-depth, salinity at surface-, mid-, and bottom-depth, and elevation along the one-grid away from the channel in lower James River at 5 a.m. on July 3, 1985. 213

5.75 u at surface, w at mid-depth, salinity at surface-, mid-, and bottom-depth, and elevation along the one-grid away from the channel in lower James River at 6 a.m. on July 3, 1985. 214

5.76 u at surface, w at mid-depth, salinity at surface-, mid-, and bottom-depth, and elevation along the one-grid away from the channel in lower James River at 7 a.m. on July 3, 1985. 215

5.77 u at surface, w at mid-depth, salinity at surface-, mid-, and bottom-depth, and elevation along the one-grid away from the channel in lower James River at 8 a.m. on July 3, 1985. 216

5.78 u at surface, w at mid-depth, salinity at surface-, mid-, and bottom-depth, and elevation along the one-grid away from the channel in lower James River at 9 a.m. on July 3, 1985. 217

5.79 u at surface, w at mid-depth, salinity at surface-, mid-, and bottom-depth, and elevation along the one-grid away from the channel in lower James River at 10 a.m. on July 3, 1985. 218

5.80 u at surface, w at mid-depth, salinity at surface-, mid-, and bottom-depth, and elevation along the one-grid away from the channel in lower James River at 11 a.m. on July 3, 1985. 219

5.81 Salinity contours (ppt) in (x, z) domain along the one-grid away from the channel in lower James River at 1 a.m. on July 3, 1985. 220

5.82 Salinity contours (ppt) in (x, z) domain along the one-grid away from the channel in lower James River at 2 a.m. on July 3, 1985. 221

5.83 Salinity contours (*ppt*) in (x, z) domain along the one-grid away from the channel in lower James River at 3 a.m. on July 3, 1985. 222

5.84 Salinity contours (*ppt*) in (x, z) domain along the one-grid away from the channel in lower James River at 4 a.m. on July 3, 1985. 223

5.85 Salinity contours (*ppt*) in (x, z) domain along the one-grid away from the channel in lower James River at 5 a.m. on July 3, 1985. 224

5.86 Salinity contours (*ppt*) in (x, z) domain along the one-grid away from the channel in lower James River at 6 a.m. on July 3, 1985. 225

5.87 Salinity contours (*ppt*) in (x, z) domain along the one-grid away from the channel in lower James River at 7 a.m. on July 3, 1985. 226

5.88 Salinity contours (*ppt*) in (x, z) domain along the one-grid away from the channel in lower James River at 8 a.m. on July 3, 1985. 227

5.89 Salinity contours (*ppt*) in (x, z) domain along the one-grid away from the channel in lower James River at 9 a.m. on July 3, 1985. 228

5.90 Salinity contours (*ppt*) in (x, z) domain along the one-grid away from the channel in lower James River at 10 a.m. on July 3, 1985. 229

5.91 Salinity contours (*ppt*) in (x, z) domain along the one-grid away from the channel in lower James River at 11 a.m. on July 3, 1985. 230

5.92 Time series of u-velocity and salinity in z-baroclinic with diffusion at grid point (65,16). 238

5.93 Time series of u-velocity and salinity in σ-baroclinic with diffusion at grid point (65,16). 239

5.94 Time series of u-velocity and salinity in σ-baroclinic without diffusion at grid point (65,16). 240

5.95 Time series of u-velocity and salinity in z-baroclinic with diffusion at grid point (65,17). 241

5.96 Time series of u-velocity and salinity in σ-baroclinic with diffusion at grid point (65,17). 242

5.97 Time series of u-velocity and salinity in σ-baroclinic without diffusion at grid point (65,17). 243

5.98 Time series of u-velocity and salinity in z-baroclinic with diffusion at grid point (65,18). 244

5.99 Time series of u-velocity and salinity in σ-baroclinic with diffusion at grid point (65,18). 245

5.100 Time series of u-velocity and salinity in σ-baroclinic without diffusion at grid point (65,18). 246

5.101 Time series of u-velocity and salinity in z-baroclinic with diffusion at grid point (65,19). 247

5.102 Time series of u-velocity and salinity in σ-baroclinic with diffusion at grid point (65,19). 248

5.103 Time series of u-velocity and salinity in σ-baroclinic without diffusion at grid point (65,19). 249

5.104 Time series of salinity in z-baroclinic with diffusion, σ-baroclinic with diffusion, and σ-baroclinic without diffusion at grid point (65,16). 250

5.105 Time series of salinity in z-baroclinic with diffusion, σ-baroclinic with diffusion, and σ-baroclinic without diffusion at grid point (65,17). 251

5.106 Time series of salinity in z-baroclinic with diffusion, σ-baroclinic with diffusion, and σ-baroclinic without diffusion at grid point (65,18). 252

5.107 Time series of salinity in z-baroclinic with diffusion, σ-baroclinic with diffusion, and σ-baroclinic without diffusion at grid point (65,19). 253

LIST OF TABLES

2.1 Characteristic Time Scales of Various Physical Processes in Estuaries and Lakes. 27

3.1 Characteristics of model analytical tests. 104

4.1 Tidal amplitude harmonic constants obained from June 19 to July 17, 1985. (period in *hour*, amplitude in *cm*, phase lag in degree) 106

5.1 Comparison of the model predicted harmonic constants of water level with the measured data. 133

5.2 Comparison of the model predicted harmonic constants of velocity with the measured data (St. 4, Depth=8.5 m) 134

5.3 Test cases performed. 137

5.4 Comparison between observed and simulated tidal elevation constituents at Station 1 (amplitude in *cm*, phase lag in degree). . . 138

5.5 Comparison between observed and simulated tidal elevation constituents at Station 2 (amplitude in *cm*, phase lag in degree). . . 139

5.6 Comparison between observed and simulated tidal elevation constituents at Station 3 (amplitude in *cm*, phase lag in degree). . . 140

5.7 Comparison of data and model tidal constituents of surface *u*-velocity at Station 4 (amplitude in *cm*, phase lag in degree, 6/19 - 7/17/85). 142

5.8 Comparison of data and model tidal constituents of surface *v*-velocity at Station 4 (amplitude in *cm*, phase lag in degree, 6/19 - 7/17/85). 143

5.9 Model skill parameters for the sensitivity test to surface elevation at Station 1. 234

5.10 Model skill parameters for the sensitivity test to surface elevation at Station 2. 234

5.11 Model skill parameters for the sensitivity test to *u*-velocity at Station A. 235

5.12 Model skill parameters for the sensitivity test to v-velocity at Station A. 235

Abstract of Dissertation Presented to the Graduate School
of the University of Florida in Partial Fulfillment of the
Requirements for the Degree of Doctor of Philosophy

THREE-DIMENSIONAL CURVILINEAR-GRID MODELING OF BAROCLINIC CIRCULATION AND MIXING IN A PARTIALLY-MIXED ESTUARY

By

JEI-KOOK CHOI

December 1992

Chairman: Dr. Y. Peter Sheng
Major Department: Coastal and Oceanographic Engineering

Three-dimensional curvilinear-grid hydrodynamic models for partially-mixed estuaries developed by Sheng (1989) and Sheng *et al.* (1989) were significantly enhanced, applied to the James River, and tested to determine the sensitivity of model results to numerous model parameters. The model computes the inter-tidal and longterm dynamics of surface elevation and three-dimensional field of velocity, and salinity in partially-mixed estuaries with complex geometry and bathymetry.

The momentum and continuity equations in the curvilinear coordinates are solved on a space-staggered grid system using an implicit finite-difference algorithm for the "external" vertically-integrated flow and vertically implicit procedure for the "internal" flow. Details of the numerical procedures are presented. The numerical accuracy of the model is verified by comparing model results with analytic solutions for a variety of idealized problems describing circulations in simple basins forced by constant surface slope, seiche, tide, wind, and density gradient.

Model application to the James River reproduces the observed density-driven current. Effect of spring-to-neap tidal dynamics on vertical stratification and density-driven currents is simulated by the model. Longitudinal position of the head of

salinity intrusion was found to move up and down the estuary due to change in river discharge and tidal condition. Increasing river discharge caused an increase in relative stratification. Spring tide produced more mixing and enhanced salt intrusion while neap tide produced more stratification. The observed frontal structure near Newport News Point was successfully simulated as a narrow zone of surface flow convergence and strong vertical transport. Simulation of the formation and evaluation of the front show reasonable agreement with available field data. Sensitivity of the model results to such parameters as turbulence model, advection scheme, horizontal grid, vertical grid, and bottom boundary condition was investigated and the results were presented.

CHAPTER 1
INTRODUCTION

1.1 Background

Estuaries are the transition regions where the fresh water from the land mixes with the saline water from the sea. Cameron and Pritchard (1963) have defined an estuary as "a semi-enclosed coastal body of water which has a free connection with the open sea and within which sea water is measurably diluted with fresh water derived from land drainage" (p. 306). This definition implies two important dynamics in an estuary: a horizontal density gradient between the fresh water and the sea water, and a generation of kinetic energy caused by tidal currents. These dynamics control the circulation pattern, the mixing processes, and the salinity and temperature distributions that are the major physical problems that need to be understood in an estuary. Ecologically, most estuaries are controlled by physical factors (Kinne, 1967) such as tide, river discharge, wind, salinity, and morphology of the estuarine area.

Vertical mixing caused by the bottom and/or surface friction, tidal currents, and the river discharge produces vertical and longitudinal gradients of salinity in the mixing zone. Large river discharge and small mixing energy form sharp vertical gradients in an estuary, which is referred to as "stratified". Salt-wedge is the limiting case of the stratified estuary. If the river discharge is small and the tidal mixing energy large, slight vertical gradients of salinity will be developed. In the limiting case, a "well-mixed" estuary is formed.

Partially-mixed estuaries are intermediate between salt-wedge and well-mixed estuaries. James River is a partially-mixed, coastal plain type estuary like the majority of estuaries along the east coast of the United States. These estuaries are charac-

terized dynamically by vertical salinity variations of 1-10 $^{\circ}/_{\circ\circ}$ (Bowden, 1967) and a net circulation pattern which moves seaward in the upper layers and landward in the lower layers due to the pressure gradient caused by the density difference of the salt and fresh waters. Rattray and Hansen (1962) showed that residual currents were directly proportional to the longitudinal density gradient and inversely proportional to the vertical eddy viscosity. Stratification exists in partially-mixed estuaries, and this changes in various ways according to the relative amount of river discharge and available tidal mixing energy. If the mixing energy is cyclical, like a spring-neap tidal variation, alternate stratification and destratification may be evident (Haas, 1977; Cerco, 1982). Current-induced turbulent mixing plays an important role in affecting the stratification and destratification in a partially-mixed estuary. Vertical salt flux occurs through vertical advection and entrainment of salinity across the interface between fresh water and salt water. Tidal motion enhances the vertical turbulent exchange of momentum and salt. A two-layered flow exists in a partially-mixed estuary with the surface of no net motion near the maximum salinity gradient (halocline). In addition to the longitudinal and vertical salinity gradients, a lateral salinity gradient also occurs because of the Coriolis force and complex shorelines. Thus, motions in partially-mixed estuaries are basically three-dimensional and time-dependent because of irregular shape of the basin, density-induced baroclinicity and the Coriolis force.

Salinity and temperature influence the density of estuarine waters, but salinity is more effective than temperature because the range of salinity variation is much larger than that of temperature variation. Salinity ranges from freshwater to saltwater in the estuary. Wind also influences the vertical salinity and velocity structures while interacting with internal friction and bottom friction. Surface currents are generally in the same direction as the local wind stress even though they are affected by the Coriolis force. Thus downestuary winds increase stratification while upestuary winds decrease it. Nonlocal wind effects can affect stratification through change of sea level

at the mouth of the estuary (Wang and Elliott, 1978).

River or open sea boundary conditions vary with time, and the location of salinity intrusion changes accordingly. If the head of salt intrusion is defined as the point where freshwater meets saltwater, the head of salt intrusion is dependent on the amount of river discharge, the salinity at the open sea boundary, tidal currents, wind stresses, and the geometry of the basin. They are all time-dependent except the geometry of the basin. Accurate specification of the boundary conditions is essential to accurate prediction of circulation and salinity distribution.

Turbulence models have been developed to simulate the mean and turbulent motions in most stratified flow situations. A turbulence model is defined as a system of equations which calculate Reynolds stress terms in the mean-flow equations and similar terms in temperature and salinity equations. They parameterize the effect of turbulence on the mean flow. Through the Reynolds decomposition of the governing equations and Reynolds averaging, Reynolds stress equations are developed. However, the system of equations is not closed since every equation contains terms consisting of higher order correlations which are unknown. The system can only be closed by using a semi-empirical (e.g. various levels of second-order closure model) or ad-hoc empirical models (e.g. simple eddy-viscosity models). An equilibrium closure model (Sheng *et al.*, 1989) is included in the three-dimensional model used for this study. To reduce computational effort, the system of equations can be simplified with such assumptions as local equilibrium of turbulence. Although Reynolds stress models can provide rather accurate results (e.g. Sheng, 1984; Sheng and Villaret, 1989), Reynolds stress models are quite complicated, and require substantial computer resources.

At present, hydrodynamic models of circulation are important tools used by both engineers and scientists attempting to quantify and understand complex physical, chemical and biological processes in estuaries and coastal areas. Historically, engineers and scientists preferred physical modeling to mathematical modeling for studying cir-

culation and transport in most of the complicated environmental systems because of difficulties in finding mathematical solutions. However, physical modeling has inherent scaling problems and is very costly. As computers become faster and more accurate, mathematical models have replaced physical modeling as the major tool for studying circulation and transport. Some differences exist between numerical results and analytical solutions of mathematical problems because of the digital nature of the computations. To reduce these differences and enhance efficiency of the computations, numerous numerical schemes and solution techniques have been developed. The numerical models developed must be checked against analytical solutions before applying them. Agreement between numerical results and analytical solutions suggests accurate and consistent numerics of the numerical model. To test the model's ability to simulate such physical processes as turbulent mixing and bottom friction, it is necessary to calibrate and verify the numerical model with laboratory and/or field data on circulation and transport.

1.2 Review of Previous Works

Modeling of circulation and salinity transport dynamics in the James River has been active over the last decade. Circulation modeling has included the flow induced by tide, wind, and density gradients, with the primary emphasis on the tidally driven circulation. Cerco (1982) applied a two-dimensional laterally averaged model to the James River to predict intertidal variation of surface level, velocity, and salinity. This model could simulate the destratification-stratification cycle coincident with the spring-neap tidal cycle in the James River Estuary. Heltzel and Granat (1988) applied a two-dimensional vertically-averaged model to the lower James River to study the impact of artificial islands for dredge spoil disposal, channel deepening, and port expansion. This model could simulate the convergence phenomena in the tidal flow, but could not show the complex vertical structure of the flow field.

Most of the early work on the numerical modeling of estuaries used vertically-

integrated equations (Hansen, 1956; Leendertse, 1967; Blumberg, 1975; Wang, 1975; Johnson, 1980). This approach was found to be useful for studying tidal dynamics and storm surges although it cannot simulate the internal features of the estuarine circulation. In other cases, laterally averaged equations were used to study the vertical structure of currents and species (Spaulding, 1974; Blumberg, 1976; Cerco, 1982), although no lateral flow structure could be provided. The development of three-dimensional numerical models started in the late 1960's, but have progressed significantly during the past decade because of the availability of high speed computers. Details of a few three-dimensional numerical estuarine models can be found in Caponi (1976), Sheng (1983,1987), Lynch (1983), Blumberg and Mellor (1983), and Oey *et al.* (1985).

The early three-dimensional models were developed by dividing the vertical water-column into layers and solving each layer with a vertically averaged two-dimensional model (e.g., Laevastu, 1974). Laevastu (1974) introduced a two-layer model consisting of a stack of two vertically averaged models and a staggered finite difference grid system. Wang and Connor (1975) also used the layer concept using a finite element method. This layered approach has the disadvantage that a layer thickness can disappear in simulations with strong vertical velocities such as downwelling and upwelling. To alleviate this weakness, many researchers have used the leveled approach. In a leveled model, the level interfaces are fixed, and free exchanges of water mass, momentum, salt and heat are allowed across the interfaces. The leveled approach is used by Leendertse and Liu (1975), Caponi (1976), and Sheng (1983, 1987).

Sheng (1986c, 1986d, 1987) developed a three-dimensional hydrodynamic model which can be used in non-orthogonal boundary-fitted grid as well as orthogonal or Cartesian grid. As in the earlier Cartesian grid model (Sheng, 1983), the curvilinear-grid model uses similar model-splitting technique, vertical turbulence closure scheme, modified alternating direction implicit (ADI) scheme for the external mode, and

vertically-implicit numerical schemes. The governing equations in the curvilinear grid system were derived by tensor transformation in terms of the contravariant velocity components.

Swanson (1987) developed a three-dimensional boundary-fitted hydrodynamic model in terms of Cartesian velocity components. He developed a Helmholtz equation for surface elevations, which is derived by eliminating the velocities from the continuity equation and the momentum equations, and solved it with the Gaussian elimination or successive over relaxation (SOR) method. This method has an advantage in handling boundary conditions since velocity components are known simultaneously at the new time step compared with an ADI method. However, the advantage of an ADI scheme is far greater in terms of its efficiency. The tridiagonal matrix associated with the ADI method is very efficient to solve on any computer, while SOR needs more computing time because of the repeated iterations required. Swanson used constant vertical eddy coefficients, which is incorrect (turbulence is time-dependent and spatially-varying) and is difficult to adjust in each new model.

The development of turbulence closure models has been of major significance because of the need to accurately simulate the vertical fluxes of salt and momentum and their dependence on stratification. A number of turbulence models have been developed. For example, Donaldson (1973) and his colleagues at Aeronautical Research Associates of Princeton developed a hierachy of turbulence models. Sheng (1982, 1984) modified the Reynolds stress model and Sheng and Chiu (1986) and Sheng and Villaret (1989) modified the equilibrium closure and turbulent kinetic energy (TKE) closure models for marine and freshwater applications. Mellor and Yamada (1982) described a similar turbulence model which was applied by Blumberg and Mellor (1983) and Oey *et al.* (1985). They classified the turbulence model as level 4 (Reynolds stress), level 3 (TKE closure), level 2 (equilibrium closure), and level 2.5 models according to the complexity of the turbulence equations. The turbulence

closure models have been applied to simulate complex mixing processes (Sheng, 1982, 1985; Blumberg and Mellor, 1983; Oey *et al.*, 1985). In addition to the Reynolds stress equations of turbulent motion, equations for turbulent kinetic energy and turbulent macroscale had to be added to the system of equations to complete the turbulence model. Although various levels of turbulence closure models have been used by various modelers, little has been done to compare the results obtained with various levels of closure models versus realistic data from estuaries.

Conventional finite-difference models use only Cartesian-grid and have shortcomings for applications where physical boundaries are very complex and thus may require excessively fine grid in order to resolve the boundary in the model. To allow a more flexible arrangement and spatial variation of the grids, one can use curvilinear-grid finite-difference models which were discussed above or finite-element models (Wang, 1975; Wang and White, 1976). The finite-element models allow flexibility in the discretization of the spatial domain. However, because the matrix of the discretized system is irregular, direct inversion method which requires very extensive computational effort, is usually used. In the finite-difference models, however, tridiagonal matrix system generally exists and can be efficiently solved. The curvilinear-grid finite-difference models (e.g. Spaulding, 1984; Sheng, 1986c, 1986d, 1987). This allow extensive user flexibility in spacing of the horizontal grid structure while still maintaining a rather simple matrix system and allowing efficient solutions. However, there are some disadvantages of this approach such as more computational efforts due to the extra terms in the transformed equations and potential numerical dissipation/dispersion problems caused by skewness and rapid change in grids.

1.3 Modeling Strategy

The examination and analysis of available data, such as river flow, water elevations, wind, current, and salinity, should be performed to classify the dynamics of the water body along with its range of variability. Models that do not adequately

resolve the depths of navigation channels of an estuarine system may have difficulty in predicting the correct degree of stratification and the strength of tidally averaged, near-bottom upstream flow. The Hansen and Rattray theory (1965) indicates the importance of tidal dispersion in maintaining the salt balance in an estuary.

The tide in an estuary may have the characteristics of a progressive, standing, or mixed wave. Flood and ebb tide are not only unequal in velocity at a fixed point in most estuaries, but also do not always flow opposite to each other. Ludwick (1975) attributed this inequality in tidal flow to three factors: (1) mixing between river water and sea water produced by turbulent exchange and vertical entrainment across a density interface, (2) the Coriolis force which deflects the ebb and flood dominant flows along different perimeters of the estuary, and (3) evasion of ebb- and flood-tidal pathway. Although all three factors may occur concurrently, the effect of the Coriolis force is usually overshadowed by the other two factors.

Exchange of various forms of energy produces the mixing in a vertically stratified system. For example, turbulent kinetic energy extracted from the mean flow in a frictional boundary layer produces mixing when exchanged with potential energy. Various parameters have been introduced to classify the degree of stratification. Ippen (1966) introduced the stratification parameter defined as the ratio of rate of turbulent energy dissipation divided by rate of gain of potential energy. Hansen and Rattray (1965) developed the dimensionless parameter by which the degree of stratification can be related to buoyancy and mixing energy.

Festa and Hansen (1976) discussed the effects of depth and river discharge on estuarine circulation and salinity in their two-dimensional model based on vorticity and salt-balance equations. They found that decreasing the discharge allowed the head of salt intrusion to move upstream. As the discharge is decreased, estuarine circulation is also weakened, although it occurs over the larger area. Greater depths enhanced circulation and moved the head of salt intrusion upstream.

Geyer and Farmer (1989) measured the time variation of salt intrusion in an estuary during a variety of tidal and run-off conditions using high-resolution instruments and sampling methods. The salt wedge was found to vary considerably in position and vertical structure throughout the tidal cycle due to interaction of tidal flow and density-induced motion. During the flood cycle, salt wedge progresses up the estuary as a gravity current, while during the ebb the salinity structure was eroded by shear instability, in which vertical shears become so large that the pycnocline becomes unstable and causes the salt wedge to break down. Here the most important dynamic variable is the gradient Richardson number (Ri), which reflects the stability of the shear layer and thus determines whether momentum and salt can be exchanged across the pycnocline.

Tides in estuaries are modulated by river-forced estuarine plumes. A numerical study of this phenomena was done by Chao (1990). In a typical midlatitude estuary-shelf environment, the river-forced circulation can be divided into three regions: a seaward surface flow and a landward undercurrent inside the estuary, a strong anticyclonic surface gyre overlying a weak cyclon off the estuary mouth, and a coastal jet flowing in the direction of Kelvin wave propagation farther down-stream. The tidal residual eddies enhance the plume growth but tend to trap the plume.

Frontal systems in estuaries are also very important in estuarine circulation and transport. Limited observations by Byrne *et al.* (1987) suggested that oyster larvae remain in the water column for a period of two to three weeks and are carried by water movement associated with tidal front and tidal residual circulation. A mathematical model that describes the formation and dilution of a frontally bounded river plume is presented by O'Donnell (1990). The behavior of plumes in time-dependent flows like tidal current were examined in his numerical test. The interaction of the plume front and the ambient flow was found to have major influence on the spreading and mixing of the buoyant water. River plumes may only mix significantly with the underlying

ambient fluid at particular phase of the tide, but the mixing generally occurs over a large area. Thus the boundary conditions applied in estuarine circulation models may need to be carefully reconsidered.

In any case, the density distribution determines the stratification. Therefore, a synoptic density-field survey should be made. To remove tidal effects as much as possible, it is desirable to sample at slack. During slack water, stratification may be stronger than during the other stages, making water column sampling easier in low currents. The usual way to sample at slack is that the boat is following slack water.

1.4 Scope of This Study

Modeling of a partially mixed estuary is one of the most challenging areas in computational coastal hydrodynamics. Partial stratification takes place in many coastal plain estuaries like the James River (Figure 1.1), where freshwater inflows and tidal mixing interact significantly. Partial stratification requires that vertical variation of flow variables be adequately resolved such that the model can simulate the density-driven currents. Thus, in contrast to traditional barotropic tidal hydrodynamics, the simulation of baroclinic circulation requires the accurate representation of vertical velocity and density structures, and the use of three-dimensional models (Sheng, 1983; Oey *et al.*). Sheng *et al.* (1989a) simulated the tidal, wind-driven, and baroclinic circulation in Chesapeake Bay, while Sheng *et al.* (1989b) simulated the tidal circulation and baroclinic circulation in the James River using a very coarse grid. This study provide more detailed simulations of tidal and baroclinic circulation in the James River.

Traditionally, Cartesian grids have been used for the estuarine hydrodynamic model. For most estuaries, the geometry and bathymetry are quite complex and irregular so that the generation of an orthogonal grid is very difficult. Models developed by Blumberg and Mellor (1987) require an orthogonal grid and cannot accept a non-orthogonal grid, and hence cannot accurately resolve the complex shorelines. On the

other hand, boundary-fitted grid hydrodynamic models appear to be an excellent tool to allow the user to accurately resolve complex geometries for estuarine and coastal applications. Few studies focused on model development and validation against analytic solutions. For example, Sheng and Hirsh (1984) developed a two-dimensional curvilinear-grid model for coastal ocean circulation. Spaulding (1984) applied a two-dimensional model to simulate tides in the North Sea. Practical applications generally require a fully three-dimensional model analysis because of stratification, complex geometry, and topography. Although the three-dimensional boundary-fitted grid hydrodynamic model developed by Sheng has been tested against some analytic solutions (Sheng and Hirsh, 1984; Sheng, 1987), this study provides more detailed analytical tests of the three-dimensional model.

Despite the complexity of the Reynolds stress models, such models do contain more physics and hence the model constants remain unchanged for all model applications (Sheng, 1982). A Reynolds stress model was used to produce successful simulations of the wave boundary layer (Sheng, 1982; Sheng, 1984; Sheng, 1986a; Sheng and Villaret, 1989), wave-current boundary layer (Sheng, 1984), and vegetation boundary layer (Sheng, 1982). However, three-dimensional models generally do not use Reynolds stress models to represent the turbulent mixing, because of the complexity. Instead, simplified second-order closure models have been developed and used with three-dimensional models. These include the turbulent kinetic energy closure model (Sheng and Villaret, 1989) and the equilibrium closure model (Sheng and Chiu, 1986; Sheng *et al.*, 1989a). Both of these models contain the assumption that the turbulence time scale is much less than the mean flow time scale. The equilibrium closure model contains the additional assumption that turbulence does not change significantly over the turbulent macroscale. The TKE closure model resolves the turbulent dynamics by including the differential transport equation for q^2, while the other second-order correlation equations are simplified to algebraic equations. The

TKE closure model is similar to the Level-3 model of Mellor and Yamada (1982) and the $k-\varepsilon$ model of Rodi (1980), but uses an equation for the macroscale (Λ) instead of the equation for turbulence dissipation (ε) used by the other two models. The equilibrium closure model is slightly more simplified than the TKE closure model, since only algebraic equations are used to resolve the second-order correlations. The equilibrium closure model is similar to Mellor and Yamada's Level-2 model. Instead of solving the differential transport equations for Λ which consists completely of modeled terms, simplified second-order closure models often solve a set of integral constraints for Λ (Sheng and Chiu, 1986).

Results of the simplified second-order closure models have been quite successful. Sheng and Villaret (1989) used the TKE closure model to simulate a wave boundary layer, a thermally stratified boundary layer and a sediment-laden boundary layer. On the other hand, the equilibrium closure model has also been found to be very successful for simulating the vertical mixing in estuaries (Sheng *et al.*, 1989b, 1989c; Johnson *et al.*, 1991), despite the further simplification. There exists no unequivocal evidence to suggest that the TKE closure model is superior to the equilibrium closure model. This subject will be investigated in this study by comparing results of TKE closure model and equilibrium closure model versus field data from the James River.

Recent field studies in the James River have obtained quantitative or qualitative information on the temporal and spatial variations of salinity stratification, frontal structure, and gyre formation (Bryne, 1987; Hepworth and Kuo, 1989). These field data provide a good opportunity for detailed calibration and validation of the three-dimensional curvilinear grid hydrodynamic model developed by Sheng (1989). Model calibration and validation will be conducted in terms of detailed intertidal dynamics, water level vertical flow and salinity structures, spring-to-neap and residual long-term circulation and salinity transport, and formation and evolution of tidal fronts in the Hampton Roads area. Sheng *et al.* (1989c) reported that the use of σ-grid may lead

to numerically-induced salinity transport from the navigation channel to the shallow shoal, unless special care is taken to improve the evaluation of baroclinic terms and the advection terms. This subject will also be further investigated in this study.

1.5 Objective of This Study

The objectives of this study are (1) to further enhance the three-dimensional hydrodynamic curvilinear-grid model developed by Sheng (1989) and Sheng *et al.* (1989) for simulating circulation and transport patterns in coastal areas and estuarine systems, (2) to apply the model to the James River to simulate the observed short-term and long-term circulation features, (3) to determine the model sensitivity to various model features including horizontal grid resolution, bottom friction, turbulence closure scheme, and vertical grid.

1.6 James River

The Chesapeake Bay estuarine system was formed by the drowning of a cascading series of river valleys, the most seaward of which was the James. Estuaries formed in this way are called coastal plain estuaries. In this type of estuary, the primary forcing functions for salinity and current distribution are tidal mixing which depends on the tidal range and basin configuration, gravitational circulation due to freshwater discharge, and Coriolis force due to the earth rotation. An estuary where gravitational circulation is dominant is called a salt wedge estuary. But the tidal oscillation increases mixing between the salt and freshwater and reduces the effectiveness of the gravitational circulation. James River is called a partially mixed estuary because both the gravitational circulation and the tidal mixing play an important role in the estuarine dynamics.

The James River (Figure 1.1) originates in the Appalachian mountains of Virginia at the confluence of the Jackson and Cowpasture Rivers. The river runs approximately 530 *km* into Chesapeake Bay southeastward. About one third of it, the 160 *km* (from the mouth at Sewell's Point to the fall-line at Richmond) is a tidal zone, and about

one third of this tidal zone is the estuary proper. The central half of the estuarine portion of the James River contains some of the most productive seed oyster beds in the world. These beds cover an area of 25,000 acres, of which 16,150 acres have been determined to be higher or moderately productive (Haven and Whitcomb, 1983).

The average tidal range varies from 76 *cm* at Sewell's Point to 58 *cm* near the Chickahominy River mouth to 98 *cm* at Richmond. Mean annual freshwater discharge at Richmond is 215 m^3/sec and in the summer months flow is more typically in the range of 35 to 75 m^3/sec. (Cerco, 1982). Salt generally intrudes upstream to the Jamestown Island, but the intrusion may approach Hopewell or be forced downstream as far as Newport News due to low flow and heavy rainfall. The lower James River near Hampton Roads generally shows an extremely complex three-dimensional and time-varying density field due to complicated geometry, highly irregular bottom topography, tidal flow, wind effect, and variable river discharge.

As shown in Figure 1.1, the James River is channelized as far upstream as Richmond with a minimum depth at mid-channel of approximately 8 *m*. Maximum depth in the estuary is 10 - 15 *m* and average depth is about 6 *m*. Cross-sectional area ranges from approximately 27,000 m^2 near the James River Bridge to 1,000 m^2 at Richmond. In general, the basin is on the order of 7 *km* wide from the mouth at Old Point Comfort to a constricted region at Mulberry Point, just upstream of the broader (10 *km* wide) region of Burwell Bay. The remaining portion of the estuary, from Mulberry Point to Jamestown Island is from 4 to 6 *km* wide.

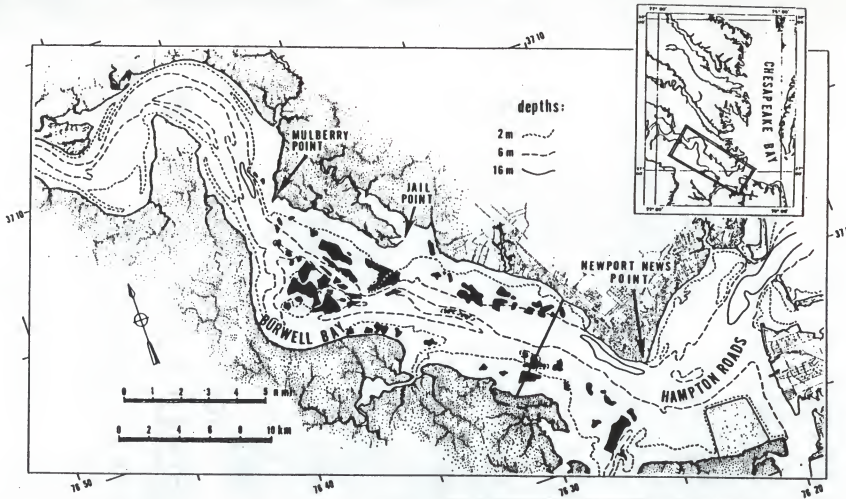

Figure 1.1: The James River Estuary from Old Point Comfort, at the mouth, to Jamestown Island (upper left corner). Seed oyster beds are shown as irregularly shaped darkened areas (Byrne *et al.*, 1987).

CHAPTER 2
GOVERNING EQUATIONS AND SOLUTION TECHNIQUE

In this chapter, the basic mathematical model for estuarine circulation is described. First of all, assumptions and differential equations for estuarine circulation models are described in terms of a Cartesian (x, y, z) coordinate system. The equations are then transformed into a vertically-stretched (x, y, σ) coordinate system. Following that, equations in dimensionless form are presented. Anticipating model applications to estuaries with complex geometry, a method for generating boundary-fitted grid is briefly discussed. Equations in the boundary-fitted (ξ, η, σ) coordinate system are then presented. Following a presentation of boundary conditions, initial conditions, solution technique, and finite-difference equations are presented.

2.1 Differential Equations

The four basic assumptions used here for deriving the governing equations are: (1) The flow is incompressible so that the flow is nondivergent. (2) The vertical accelerations are negligible compared to gravity, thus, the vertical pressure distribution satisfies hydrostatic approximation. (3) Density is approximated by its mean value except when multiplied by gravity, *i.e.*, the Boussinesq approximation is valid. (4) The concept of turbulent (or eddy) viscosity and diffusivity is introduced. The smallest scales of motion in real fluids, *i.e.*, the dissipative scales, are always several orders of magnitude larger than the molecular scales (Tennekes and Lumley, 1972). In contrast to their molecular parts, turbulent viscosity and diffusivity are not fluid characteristics but depend strongly on the state of turbulence. They are properties of the flow instead of the fluid and hence are temporally and spatially dependent. Using a right-handed Cartesian coordinate system (x, y, z) with the origin at the water

surface and z measured upward as shown in Figure 2.1, the equations may be written as follows (Sheng, 1989)

$$\frac{\partial u}{\partial x}+\frac{\partial v}{\partial y}+\frac{\partial w}{\partial z}=0 \tag{2.1}$$

$$\begin{aligned}\frac{\partial u}{\partial t}+\frac{\partial u^2}{\partial x}+\frac{\partial uv}{\partial y}+\frac{\partial uw}{\partial z} &= fv-\frac{1}{\rho_o}\frac{\partial p}{\partial x}+\frac{\partial}{\partial x}\left(A_H\frac{\partial u}{\partial x}\right) \\ &+ \frac{\partial}{\partial y}\left(A_H\frac{\partial u}{\partial y}\right)+\frac{\partial}{\partial z}\left(A_v\frac{\partial u}{\partial z}\right)\end{aligned} \tag{2.2}$$

$$\begin{aligned}\frac{\partial v}{\partial t}+\frac{\partial uv}{\partial x}+\frac{\partial v^2}{\partial y}+\frac{\partial vw}{\partial z} &= -fu-\frac{1}{\rho_o}\frac{\partial p}{\partial y}+\frac{\partial}{\partial x}\left(A_H\frac{\partial v}{\partial x}\right) \\ &+ \frac{\partial}{\partial y}\left(A_H\frac{\partial v}{\partial y}\right)+\frac{\partial}{\partial z}\left(A_v\frac{\partial v}{\partial z}\right)\end{aligned} \tag{2.3}$$

$$\frac{\partial p}{\partial z}=-\rho g \tag{2.4}$$

$$\begin{aligned}\frac{\partial T}{\partial t}+\frac{\partial uT}{\partial x}+\frac{\partial vT}{\partial y}+\frac{\partial wT}{\partial z} &= \frac{\partial}{\partial x}\left(K_H\frac{\partial T}{\partial x}\right)+\frac{\partial}{\partial y}\left(K_H\frac{\partial T}{\partial y}\right) \\ &+ \frac{\partial}{\partial z}\left(K_v\frac{\partial T}{\partial z}\right)\end{aligned} \tag{2.5}$$

$$\begin{aligned}\frac{\partial S}{\partial t}+\frac{\partial uS}{\partial x}+\frac{\partial vS}{\partial y}+\frac{\partial wS}{\partial z} &= \frac{\partial}{\partial x}\left(D_H\frac{\partial S}{\partial x}\right)+\frac{\partial}{\partial y}\left(D_H\frac{\partial S}{\partial y}\right) \\ &+ \frac{\partial}{\partial z}\left(D_v\frac{\partial S}{\partial z}\right)\end{aligned} \tag{2.6}$$

$$\rho=\rho(T,S) \tag{2.7}$$

where (u,v,w) are mean fluid velocities in the (x,y,z) directions, f is the Coriolis parameter defined as $2\Omega\sin\phi$ where Ω is the rotational speed of the earth and ϕ is the latitude, $g=9.81ms^{-2}$ is the Earth's gravitational acceleration, ρ is density, p is pressure, T is temperature, S is salinity, (A_H,K_H,D_H) are horizontal turbulent eddy coefficients, and (A_v,K_v,D_v) are vertical turbulent eddy coefficients. Variable eddy

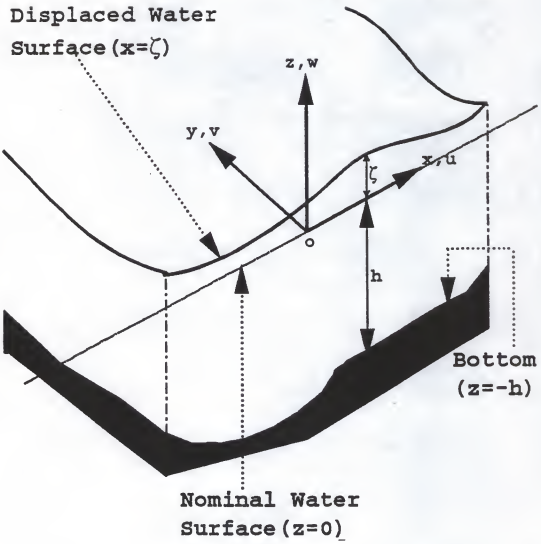

Figure 2.1: The right-handed Cartesian coordinate system.

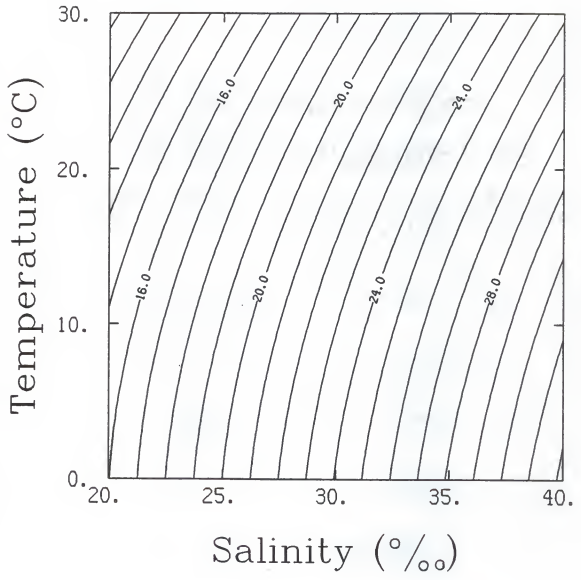

Figure 2.2: σ_t density field calculated from Eckart formula.

coefficients are allowed in the present model. In addition to the above equations, the program code contains an equation for dissolved species concentration similar to Eq. (2.6).

Equation (2.1) represents the continuity equation as conservation of water mass. Equations (2.2) and (2.3) are conservation of momentum in the x and y directions. Eq. (2.4) expresses the hydrostatic balance. Equations (2.5) and (2.6) represent a conservation of energy and conservation of salt, respectively. An equation of state for seawater, Eq. (2.7), relating salinity and temperature to density closes the system. In the present model, the equations given by Eckart (1958) are used

$$\begin{aligned} \rho &= (P+1)/(\alpha + 0.698P) \\ P &= 5890 + 38T - 0.375T^2 + 3S \\ \alpha &= 1779.5 + 11.25T - 0.0745T^2 - (3.8 + 0.01T)S \end{aligned} \tag{2.8}$$

where T is in °C, S is in ‰, and ρ is in g cm^{-3}. Figure 2.2 shows σ_t density field calcualted from Eckart formula.

2.2 Governing Equations in Stretched Coordinates

To simulate circulation and transport in water bodies with gradual bathymetric variation, it is common to use σ-transformation such that both the free surface and the bottom become the coordinate surfaces with an equal number of coordinate surfaces in between. This transformation, *i.e.*, the so called σ-stretching, leads to a smooth representation of the topography with the same order of vertical resolution for the shallow and deeper parts of the water body (Figure 2.3). The σ-stretching introduces extra terms to the original Cartesian equations of motion. However, most of these extra terms appear in the horizontal diffusion terms, which are generally not very important compared to the other terms. The σ-grid model is suitable for simulating flow and salinity transport in regions of gradual bathymetric variation and gives a more accurate estimation of bottom stress than the z-grid model, which resolves the depth

with "stair-step" grids. Recent studies by Sheng *et al.* (1989c) and Haney (1990) found that, when there are sufficient grid points across regions of sharp bathymetric change, the σ-grid model can yield good results. In case of insufficient grid points, special care must be exercised. Sheng *et al.* (1989c) suggested direct evaluation of the horizontal density gradient terms along the constant z-plane and avoiding the use of higher-order advective schemes along the sharp bathymetric variation to reduce numerical error. This issue will be further discussed later.

The transformation from the Cartesian grid (x, y, z, t) to the vertically-stretched grid (x', y', σ, t') is defined as

$$x' = x,\ y' = y,\ \sigma(x, y, z, t) = \frac{z - \zeta(x, y, t)}{h(x, y) + \zeta(x, y, t)},\ t' = t \tag{2.9}$$

where h is the water depth relative to mean sea level, and ζ is the free surface elevation relative to mean sea level, and σ is the transformed vertical coordinate such that $\sigma = 0$ at the free surface and $\sigma = 1$ at the bottom. Using the chain rule, the following partial differential expression can be derived

$$\frac{\partial F}{\partial x} = \frac{\partial F}{\partial x'}\frac{\partial x'}{\partial x} + \frac{\partial F}{\partial y'}\frac{\partial y'}{\partial x} + \frac{\partial F}{\partial \sigma}\frac{\partial \sigma}{\partial x} + \frac{\partial F}{\partial t'}\frac{\partial t'}{\partial x} \tag{2.10}$$

where $F(x, y, z, t) = F(x', y', \sigma, t')$. The first-order differential operators in the (x, y, z, t) coordinate system are related to those in the (x', y', σ, t) coordinate system as

$$\begin{aligned}
\frac{\partial}{\partial x} &= \frac{\partial}{\partial x'} - \gamma_x \frac{\partial}{\partial \sigma} \\
\frac{\partial}{\partial y} &= \frac{\partial}{\partial y'} - \gamma_y \frac{\partial}{\partial \sigma} \\
\frac{\partial}{\partial z} &= \frac{1}{H}\frac{\partial}{\partial \sigma} \\
\frac{\partial}{\partial t} &= \frac{\partial}{\partial t'} - \frac{1}{H}[(1+\sigma)\frac{\partial \zeta}{\partial t'}]\frac{\partial}{\partial \sigma}
\end{aligned} \tag{2.11}$$

where

$$\gamma_x = \frac{1}{H}[(1+\sigma)\frac{\partial \zeta}{\partial x'} + \sigma\frac{\partial h}{\partial x'}]$$

$$\sigma = \frac{z - \zeta}{\zeta + h}$$

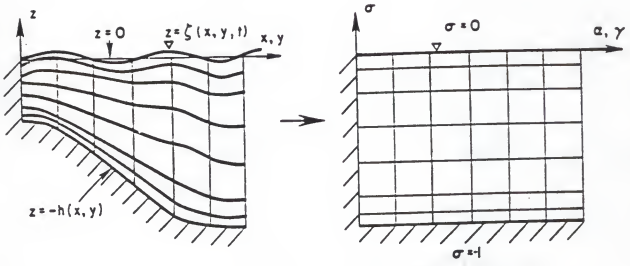

Figure 2.3: The vertically stretched grid (From Sheng and Butler, 1982).

$$\gamma_y = \frac{1}{H}[(1+\sigma)\frac{\partial \zeta}{\partial y'} + \sigma\frac{\partial h}{\partial y'}] \tag{2.12}$$
$$H = h + \zeta$$

The hydrostatic equation in the transformed coordinate system is

$$\partial p = -\rho g \partial z = -\rho g H \partial \sigma \tag{2.13}$$

Integrating from the surface ($\sigma = 0$) to some depth σ,

$$p(\sigma) = p_a - g\int_0^\sigma \rho H \, d\sigma \tag{2.14}$$

where p_a is atmospheric pressure. Taking the x-derivative while applying the coordinate transformation results in

$$\frac{\partial p}{\partial x} = \frac{\partial p_a}{\partial x'} - g\int_0^\sigma [\frac{\partial \rho}{\partial x'} - \frac{1}{H}(\frac{\partial \zeta}{\partial x'} + \sigma\frac{\partial H}{\partial x'})\frac{\partial \rho}{\partial \sigma}]H \, d\sigma + g\rho_0\frac{\partial \zeta}{\partial x'} \tag{2.15}$$

where ρ_0 is the mean density. After some algebraic manipulation, Eq. (2.15) can be written as

$$\frac{\partial p}{\partial x} = \frac{\partial p_a}{\partial x'} - g\int_0^\sigma \frac{\partial \rho H}{\partial x'} d\sigma + g\frac{\partial H}{\partial x'}\sigma\rho + g\frac{\partial \zeta}{\partial x'} \tag{2.16}$$

Now we will drop all the primes(′) for convenience. Using the flux conservative form for the nonlinear advective terms and neglecting the atmospheric pressure gradients, complete equations of motion can be written as follows (higher- order-terms (H.O.T.) are shown in Appendix A)

Conservation of momentum in x direction

$$\frac{\partial Hu}{\partial t} + \frac{\partial Hu^2}{\partial x} + \frac{\partial Huv}{\partial y} + \frac{\partial Hu\omega}{\partial \sigma} = fvH + g\frac{H}{\rho_0}(\int_0^\sigma \frac{\partial \rho H}{\partial x} d\sigma - \rho\sigma\frac{\partial H}{\partial x}) \tag{2.17}$$
$$- gH\frac{\partial \zeta}{\partial x} + H[\frac{\partial}{\partial x}\left(A_H\frac{\partial u}{\partial x}\right) + \frac{\partial}{\partial y}\left(A_H\frac{\partial u}{\partial y}\right) + \frac{1}{H^2}\frac{\partial}{\partial \sigma}\left(A_v\frac{\partial u}{\partial \sigma}\right)] + H.O.T.$$

Conservation of momentum in y direction

$$\frac{\partial Hv}{\partial t} + \frac{\partial Huv}{\partial x} + \frac{\partial Hv^2}{\partial y} + \frac{\partial Hv\omega}{\partial \sigma} = -fuH + g\frac{H}{\rho_0}\left(\int_0^\sigma \frac{\partial \rho H}{\partial y}\, d\sigma - \rho\sigma\frac{\partial H}{\partial y}\right) \quad (2.18)$$
$$- gH\frac{\partial \zeta}{\partial y} + H\left[\frac{\partial}{\partial x}\left(A_H\frac{\partial v}{\partial x}\right) + \frac{\partial}{\partial y}\left(A_H\frac{\partial v}{\partial y}\right) + \frac{1}{H^2}\frac{\partial}{\partial \sigma}\left(A_v\frac{\partial v}{\partial \sigma}\right)\right] + H.O.T.$$

Conservation of water mass

$$\frac{\partial \zeta}{\partial t} + \frac{\partial Hu}{\partial x} + \frac{\partial Hv}{\partial y} + \frac{\partial H\omega}{\partial \sigma} = 0 \quad (2.19)$$

Conservation of heat

$$\frac{\partial HT}{\partial t} + \frac{\partial HuT}{\partial x} + \frac{\partial HvT}{\partial y} + \frac{\partial H\omega T}{\partial \sigma} = H\frac{\partial}{\partial x}\left(K_H\frac{\partial T}{\partial x}\right) \quad (2.20)$$
$$+ H\frac{\partial}{\partial y}\left(K_H\frac{\partial T}{\partial y}\right) + \frac{1}{H}\frac{\partial}{\partial \sigma}\left(K_v\frac{\partial T}{\partial \sigma}\right)$$

Conservation of salt

$$\frac{\partial HS}{\partial t} + \frac{\partial HuS}{\partial x} + \frac{\partial HvS}{\partial y} + \frac{\partial H\omega S}{\partial \sigma} = H\frac{\partial}{\partial x}\left(D_H\frac{\partial S}{\partial x}\right) \quad (2.21)$$
$$+ H\frac{\partial}{\partial y}\left(D_H\frac{\partial S}{\partial y}\right) + \frac{1}{H}\frac{\partial}{\partial \sigma}\left(D_v\frac{\partial S}{\partial \sigma}\right)$$

where the vertical velocity, ω, is

$$\omega = \frac{d\sigma}{dt} = \frac{w}{H} - \frac{1}{H}(1+\sigma)\frac{\partial \zeta}{\partial t} - \gamma_x u - \gamma_y v \quad (2.22)$$

which is a result of the σ coordinate transformation.

2.3 Dimensionless Equations in Stretched Coordinates

The dimensionless equations make it easy to compare the relative importance of various terms in the equations. In a properly non-dimensionalized equation to be

shown later, the part of each term contained within a parenthesis or bracket should be of order unity, while the part of that term containing the dimensionless number(s) should indicate the order of the term. This should allow one to compare the relative importance of all the terms and to simplify the model equations under certain circumstances. The following non-dimensionalization procedure follows that used by Sheng (1986b) and Sheng *et al.* (1991). The added insight justifies the slightly more complicated form of the dimensionless equations.

Dimensionless Variables

$$
\begin{aligned}
(u^*, v^*, w^*) &= (u, v, wX_r/Z_r)\ /U_r \\
(x^*, y^*, z^*) &= (x, y, zX_r/Z_r)\ /X_r \\
(\tau_x^*, \tau_y^*) &= (\tau_x^w, \tau_y^w)/(\rho_o f Z_r U_r) = (\tau_x^w, \tau_y^w)/\tau_r \\
t^* &= tf \\
q_s^* &= T_o/(T_r - T_o) * q/(\rho_o c_p f Z_r T_o) \\
\zeta^* &= g\zeta/(fU_r X_r) = \zeta/S_r \\
\rho^* &= (\rho - \rho_o)/(\rho_r - \rho_o) \\
T^* &= (T - T_o)/(T_r - T_o) \\
A_H^* &= A_H/A_{Hr} \\
A_v^* &= A_v/A_{vr} \\
K_H^* &= K_H/K_{Hr} \\
K_v^* &= K_v/K_{vr} \\
D_H^* &= D_H/D_{Hr} \\
D_v^* &= D_v/D_{vr} \\
\omega^* &= \omega X_r/U_r
\end{aligned}
\tag{2.23}
$$

Dimensionless Parameters

$$
\begin{aligned}
\text{Vertical Ekman Number:} \quad & E_V = A_{vr}/(fZ_r^2) = t_i/t_{vdm} \\
\text{Lateral Ekman Number:} \quad & E_H = A_{Hr}/(fX_r^2) = t_i/t_{\ell dm} \\
\text{Vertical Prandtl Number:} \quad & Pr_v = A_{vr}/K_{vr} = t_{vdh}/t_{vdm} \\
\text{Lateral Prandtl Number:} \quad & Pr_H = A_{Hr}/K_{Hr} = t_{\ell dh}/t_{\ell dm} \\
\text{Vertical Schmidt Number:} \quad & Sc_v = A_{vr}/D_{vr} = t_{vds}/t_{vdm} \\
\text{Lateral Schmidt Number:} \quad & Sc_H = A_{Hr}/D_{Hr} = t_{\ell ds}/t_{\ell dm} \\
\text{Froude Number:} \quad & Fr = U_r/(gZ_r)^{1/2} = t_{ge}/t_c \\
\text{Rossby Number:} \quad & Ro = U_r/(fX_r) = t_i/t_c \\
& \beta = gZ_r/(f^2X_r^2) \equiv (Ro/Fr)^2 = (t_i/t_{ge})^2 \\
& S_z = S_r/Z_r \\
& \varepsilon = (\rho_r - \rho_o)/\rho_o \\
\text{Densimetric Froude Number:} \quad & Fr_D = Fr/\sqrt{\varepsilon} = t_{gi}/t_c
\end{aligned}
\tag{2.24}
$$

where the various t's appearing in the above expressions represent the characteristic time scales associated with various physical processes in lakes and estuaries (Table 2.1).

Utilizing the dimensionless variables and parameters defined above and suppressing the asterisks for clarity, one can derive the following dimensionless equations

$$
\frac{\partial \zeta}{\partial t} + \beta \frac{\partial Hu}{\partial x} + \beta \frac{\partial Hv}{\partial y} + \beta H \frac{\partial \omega}{\partial \sigma} = 0 \tag{2.25}
$$

$$
\begin{aligned}
\frac{1}{H}\frac{\partial Hu}{\partial t} = & - \frac{\partial \zeta}{\partial x} + \frac{E_v}{H^2}\frac{\partial}{\partial \sigma}\left(A_v \frac{\partial u}{\partial \sigma}\right) + v \\
& - \frac{Ro}{H}\left(\frac{\partial Huu}{\partial x} + \frac{\partial Huv}{\partial y} + \frac{\partial Hu\omega}{\partial \sigma}\right)
\end{aligned}
\tag{2.26}
$$

Table 2.1: Characteristic Time Scales of Various Physical Processes in Estuaries and Lakes.

Physical Process	Time Scale	Order of Magnitude
Periodic Forcing	t_f	$1/\omega$
Convection	t_c	X_r/U_r
Inertia Oscillation	t_i	$1/f$
Vertical Turbulent Diffusion	$t_{vdm}, t_{vdh}, t_{vds}$	$Z_r^2/A_{vr}, Z_r^2/K_{vr}, Z_r^2/D_{vr}$
Lateral Turbulent Diffusion	$t_{tdm}, t_{tdh}, t_{tds}$	$X_r^2/A_{Hr}, X_r^2/K_{Hr}, X_r^2/D_{Hr}$
Gravity Wave	t_{ge}	$X_r/\sqrt{gZ_r}$
Internal Gravity Wave	t_{gi}	$X_r/\sqrt{gZ_r\Delta\rho/\rho_o}$

$$
\begin{aligned}
&+ \quad E_H\left[\frac{\partial}{\partial x}\left(A_H\frac{\partial u}{\partial x}\right)+\frac{\partial}{\partial y}\left(A_H\frac{\partial u}{\partial y}\right)+H.O.T.\right]\\
&- \quad \frac{Ro}{Fr_D^2}\left[H\int_\sigma^0\frac{\partial \rho}{\partial x}d\sigma+\frac{\partial H}{\partial x}\left(\int_\sigma^0\rho d\sigma+\sigma\rho\right)\right]\\
\equiv\ &- \quad \frac{\partial \zeta}{\partial x}+\frac{E_v}{H^2}\frac{\partial}{\partial \sigma}\left(A_v\frac{\partial u}{\partial \sigma}\right)+B_x
\end{aligned}
$$

$$
\begin{aligned}
\frac{1}{H}\frac{\partial Hv}{\partial t} =\ &- \quad \frac{\partial \zeta}{\partial y}+\frac{E_v}{H^2}\frac{\partial}{\partial \sigma}\left(A_v\frac{\partial v}{\partial \sigma}\right)-u \qquad (2.27)\\
&- \quad \frac{Ro}{H}\left(\frac{\partial Huv}{\partial x}+\frac{\partial Hvv}{\partial y}+\frac{\partial Hv\omega}{\partial \sigma}\right)\\
&+ \quad E_H\left[\frac{\partial}{\partial x}\left(A_H\frac{\partial v}{\partial x}\right)+\frac{\partial}{\partial y}\left(A_H\frac{\partial v}{\partial y}\right)+H.O.T.\right]\\
&- \quad \frac{Ro}{Fr_D^2}\left[H\int_\sigma^0\frac{\partial \rho}{\partial y}d\sigma+\frac{\partial H}{\partial y}\left(\int_\sigma^0\rho d\sigma+\sigma\rho\right)\right]\\
\equiv\ &- \quad \frac{\partial \zeta}{\partial y}+\frac{E_V}{H^2}\frac{\partial}{\partial \sigma}A_v\left(\frac{\partial v}{\partial \sigma}\right)+B_y
\end{aligned}
$$

$$
\begin{aligned}
\frac{1}{H}\frac{\partial HT}{\partial t} &= \frac{E_v}{Pr_v}\frac{\partial}{H^2\partial \sigma}\left(K_v\frac{\partial T}{\partial \sigma}\right) \qquad (2.28)\\
&- \frac{Ro}{H}\left(\frac{\partial HuT}{\partial x}+\frac{\partial HvT}{\partial y}+\frac{\partial H\omega T}{\partial \sigma}\right)\\
&- \frac{E_H}{Pr_H}\left[\frac{\partial}{\partial x}\left(K_H\frac{\partial T}{\partial x}\right)+\frac{\partial}{\partial y}\left(K_H\frac{\partial T}{\partial y}\right)+H.O.T.\right]
\end{aligned}
$$

$$
\begin{aligned}
\frac{1}{H}\frac{\partial HS}{\partial t} &= \frac{E_v}{Sc_v}\frac{\partial}{H^2\partial \sigma}\left(D_v\frac{\partial S}{\partial \sigma}\right) \qquad (2.29)\\
&- \frac{Ro}{H}\left(\frac{\partial HuS}{\partial x}+\frac{\partial HvS}{\partial y}+\frac{\partial H\omega S}{\partial \sigma}\right)\\
&+ \frac{E_H}{Sc_H}\left[\frac{\partial}{\partial x}\left(D_H\frac{\partial S}{\partial x}\right)+\frac{\partial}{\partial y}\left(D_H\frac{\partial S}{\partial y}\right)+H.O.T.\right]
\end{aligned}
$$

$$
\rho=\rho(T,S) \qquad (2.30)
$$

where $H=h(x,y)+\zeta(x,y,t)$ is the total depth. The H.O.T.s are omitted here for simplicity.

2.4 Dimensionless Vertically Integrated Equations

The external mode consists of the surface elevation and the vertically-integrated velocities. The vertically integrated equations represent the "external mode" of the 3-D model. The dimensionless vertically integrated equations are

$$\frac{\partial \zeta}{\partial t} + \beta \left(\frac{\partial U}{\partial x} + \frac{\partial V}{\partial y} \right) = 0 \tag{2.31}$$

$$\begin{aligned} \frac{\partial U}{\partial t} = & - H \frac{\partial \zeta}{\partial x} + \tau_{sx} - \tau_{bx} + V \\ & - Ro \left[\frac{\partial}{\partial x} \left(\frac{UU}{H} \right) + \frac{\partial}{\partial y} \left(\frac{UV}{H} \right) \right] \\ & + E_H \left[\frac{\partial}{\partial x} \left(A_H \frac{\partial U}{\partial x} \right) + \frac{\partial}{\partial y} \left(A_H \frac{\partial U}{\partial y} \right) \right] \\ & - \frac{Ro}{{Fr_D}^2} \frac{H^2}{2} \frac{\partial \rho}{\partial x} \\ \equiv & - H \frac{\partial \zeta}{\partial x} + D_x \end{aligned} \tag{2.32}$$

$$\begin{aligned} \frac{\partial V}{\partial t} = & - H \frac{\partial \zeta}{\partial y} + \tau_{sy} - \tau_{by} - U \\ & - Ro \left[\frac{\partial}{\partial x} \left(\frac{UV}{H} \right) + \frac{\partial}{\partial y} \left(\frac{VV}{H} \right) \right] \\ & + E_H \left[\frac{\partial}{\partial x} \left(A_H \frac{\partial V}{\partial x} \right) + \frac{\partial}{\partial y} \left(A_H \frac{\partial V}{\partial y} \right) \right] \\ & - \frac{Ro}{{Fr_D}^2} \frac{H^2}{2} \frac{\partial \rho}{\partial y} \\ \equiv & - H \frac{\partial \zeta}{\partial y} + D_y \end{aligned} \tag{2.33}$$

where $(U, V) = \int_{-1}^{0} H(u, v) d\sigma$ are the vertically integrated velocities. The nonlinear inertia, lateral diffusion, and baroclinic pressure gradient terms in Equations (2.32) and (2.33) are obtained by vertically integrating the corresponding terms in Equations (2.26) and (2.27), respectively. However, these terms contain idealized assumptions

about the vertical profiles of horizontal velocities and density, *i.e.*, the horizontal velocities and density are assumed to be uniform in the vertical direction, and hence are not exact.

2.5 Boundary-Fitted Coordinate Generation

The basic idea of the boundary-fitted coordinate system approach is to make computations on curvilinear grids so that one of the curvilinear coordinates always follows a boundary. According to the work of Thompson *et al.* (1974), the natural coordinates ξ and η are taken as solutions of an elliptic boundary value problem with one of the coordinates being constant on the boundaries. The same methodology was used to generate the curvilinear grids for the present study. Detail discussions are given Thompson *et al.* (1974, 1976, 1977a, b), Thames (1975), and Thames *et al.* (1977).

The curvilinear coordinates are determined by solving an elliptic system

$$\xi_{xx} + \xi_{yy} = P(\xi, \eta) \tag{2.34}$$

$$\eta_{xx} + \eta_{yy} = Q(\xi, \eta) \tag{2.35}$$

with Dirichlet boundary conditions,*i.e.*, the values of ξ and η are specified as constants on the boundaries. (x, y) is coordinate system in the physical domain, and (ξ, η) is coordinate system in the transformed domain. Subscripts indicate differentiation. To obtain the grid locations in the (x, y) plane corresponding to known uniform rectangular grid in the (ξ, η) plane, the dependent and independent variables in Eq. (2.34) and Eq. (2.35) are interchanged. This results in a coupled system of quasi-linear elliptic equations for determining $x(\xi, \eta)$ and $y(\xi, \eta)$ in the transformed plane. Figure 2.4 shows the relation between physical domain and transformed domain.

$$\alpha x_{\xi\xi} - 2\beta x_{\xi\eta} + \gamma x_{\eta\eta} + \alpha x_{\xi}\overline{P} + \gamma x_{\eta}\overline{Q} = 0 \tag{2.36}$$

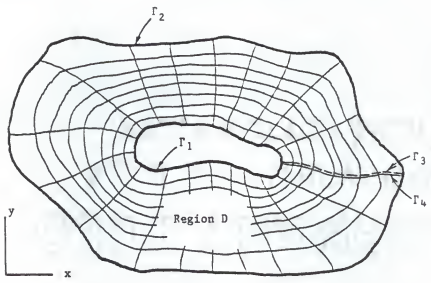

Physical Plane

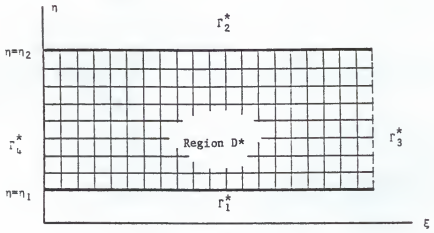

Transformed Plane

Figure 2.4: Field transfomation (From Thompson *et al.*, 1977).

$$\alpha y_{\xi\xi} - 2\beta y_{\xi\eta} + \gamma y_{\eta\eta} + \alpha y_{\xi}\overline{P} + \gamma y_{\eta}\overline{Q} = 0 \tag{2.37}$$

where the coefficients are

$$\begin{aligned} \alpha &= x_{\eta}^2 + y_{\eta}^2 \\ \beta &= x_{\xi}x_{\eta} + y_{\xi}y_{\eta} \\ \gamma &= x_{\xi}^2 + y_{\xi}^2 \\ P(\xi,\eta) &= \frac{1}{J^2}\alpha\overline{P} \\ Q(\xi,\eta) &= \frac{1}{J^2}\gamma\overline{Q} \\ J &= x_{\xi}y_{\eta} - x_{\eta}y_{\xi} \end{aligned} \tag{2.38}$$

Here $\overline{P}$ and $\overline{Q}$ are the control functions that serve to concentrate the grid lines. With a weight function w, $\overline{P} = w_{\xi}/w, \overline{Q} = w_{\eta}/w$.

2.6 Transformation of Governing Equations Into Boundary-Fitted Grids

2.6.1 Transformation Rules

Generation of a boundary-fitted grid is an essential step in the development of a boundary-fitted hydrodynamic model. It is, however, only the first step. A more important step is the transformation of governing equations into the boundary-fitted coordinates. A straightforward method is to only transform the dependent variables, i.e., the coordinates, while retaining the Cartesian components of velocities. Johnson (1982) developed such a two-dimensional vertically-integrated model of estuarine hydrodynamics. The advantage of such method is its simplicity in generating the transformed equations via the chain rule. The dimensional forms of the continuity equation and the vertically- integrated momentum equations are shown by Equations (2.17), (2.18) and (2.19). The resulting equations, however, are rather complex. Even when an orthogonal or a conformal grid is used, the equations do not become any simpler. Additional disadvantages are: (1) the boundary conditions are quite complicated because the Cartesian velocity components are generally not aligned with the

grid lines, (2) the staggered grid cannot be readily used, and (3) numerical instability may develop unless additional variables (e.g., surface elevation or pressure) are solved at additional grid points (Sheng, 1989).

To alleviate the problems mentioned in the previous paragraph, we have chosen to transform the dependent variables as well as the independent variables. Equations in the transformed coordinates (ξ, η) can be obtained in terms of the contravariant, or covariant, or physical velocity components via tensor transformation (Sokolnikoff, 1960). Rules of transformation and dimensionless tensor invariant governing equations are described in Appendix B.

2.6.2 Dimensionless Equations in Boundary-Fitted Grids

It is clear that if a proper transformation is given by Equations (2.36), (2.37), (2.38) and (2.39), one can compute the metric tensor and Christoffel symbols accordingly, and then expand Equations (2.48) and (2.49) in terms of the two contravariant velocity components and sum up all the terms over the range of indices. This process is rather tedious and highly prone to human error. To alleviate these problems, we used a symbolic manipulator to expand the tensor-invariant equations. After rearranging the resulting terms of expansion, we obtain

$$\zeta_t + \frac{\beta}{\sqrt{g_o}}\left[\frac{\partial}{\partial\xi}(\sqrt{g_o}Hu) + \frac{\partial}{\partial\eta}(\sqrt{g_o}Hv)\right] + \beta\frac{\partial H\omega}{\partial\sigma} = 0 \tag{2.39}$$

$$\begin{aligned}
\frac{1}{H}\frac{\partial Hu}{\partial t} = & - \left(g^{11}\frac{\partial\zeta}{\partial\xi} + g^{12}\frac{\partial\zeta}{\partial\eta}\right) + \frac{g_{12}}{\sqrt{g_0}}u + \frac{g_{22}}{\sqrt{g_0}}v \\
& - \frac{Ro}{H}\left[\frac{\partial}{\partial\xi}(Huu) + \frac{\partial}{\partial\eta}(Huv) + (2D^1_{11} + D^2_{12})Huu\right. \\
& + \left.(3D^1_{12} + D^2_{22})Huv + D^1_{22}Hvv + \frac{\partial Hu\omega}{\partial\sigma}\right] \\
& + \frac{E_v}{H^2}\frac{\partial}{\partial\sigma}\left(A_v\frac{\partial u}{\partial\sigma}\right) \\
& - \frac{Ro}{Fr^2}\left[H\int_\sigma^\circ\left(g^{11}\frac{\partial\rho}{\partial\xi} + g^{12}\frac{\partial\rho}{\partial\eta}\right)d\sigma\right. \\
& + \left.\left(g^{11}\frac{\partial H}{\partial\xi} + g^{12}\frac{\partial H}{\partial\eta}\right)\left(\int_\sigma^\circ\rho d\sigma + \sigma\rho\right)\right]
\end{aligned} \tag{2.40}$$

$$+ \quad E_H A_H(\text{Horizontal Diffusion})$$

$$\begin{aligned}
\frac{1}{H}\frac{\partial Hv}{\partial t} = & - \left(g^{21}\frac{\partial \zeta}{\partial \xi} + g^{22}\frac{\partial \zeta}{\partial \eta}\right) - \left(\frac{g_{11}}{\sqrt{g_o}}u + \frac{g_{21}}{\sqrt{g_o}}v\right) \\
& - \frac{Ro}{H}\left[\frac{\partial}{\partial \xi}(Huv) + \frac{\partial}{\partial \eta}(Hvv) + D_{11}^{1}Huu\right. \\
& + \left.(D_{11}^{1} + 3D_{12}^{2})Huv + (D_{12}^{1} + 2D_{22}^{2})Hvv\right] \\
& + \frac{E_v}{H^2}\frac{\partial}{\partial \sigma}\left(A_v\frac{\partial v}{\partial \sigma}\right) \qquad (2.41) \\
& - \frac{Ro}{Fr^2}\left[H\int_{\sigma}^{o}\left(g^{21}\frac{\partial \rho}{\partial \xi} + g^{22}\frac{\partial \rho}{\partial \eta}\right)d\sigma\right. \\
& + \left.\left(g^{21}\frac{\partial H}{\partial \xi} + g^{22}\frac{\partial H}{\partial \eta}\right)\left(\int_{\sigma}^{o}\rho d\sigma + \sigma\rho\right)\right] \\
& + E_H A_H(\text{Horizontal Diffusion})
\end{aligned}$$

where the horizontal diffusion terms are listed in Appendix C. The temperature and salinity equations can be obtained according to the same procedure as

$$\begin{aligned}
\frac{1}{H}\frac{\partial HT}{\partial t} = & \frac{E_v}{Pr_v}\frac{\partial}{H^2\partial \sigma}\left(K_v\frac{\partial T}{\partial \sigma}\right) \\
& - \frac{Ro}{H}\frac{1}{\sqrt{g_o}}\left[\frac{\partial}{\partial \xi}(\sqrt{g_o}HuT) + \frac{\partial}{\partial \eta}(\sqrt{g_o}HvT)\right] - \frac{Ro}{H}\frac{\partial H\omega T}{\partial \sigma} \\
& + \frac{E_H}{Pr_H}\left[g^{11}T_{,1,1} + g^{12}T_{,1,2}\right. \\
& + \left. g^{21}T_{,2,1} + g^{22}T_{,2,2}\right] \qquad (2.42)
\end{aligned}$$

$$\begin{aligned}
\frac{1}{H}\frac{\partial HS}{\partial t} = & \frac{E_v}{Sc_v}\frac{\partial}{H^2\partial \sigma}\left(D_v\frac{\partial S}{\partial \sigma}\right) \\
& - \frac{Ro}{H}\frac{1}{\sqrt{g_o}}\left[\frac{\partial}{\partial \xi}(\sqrt{g_o}HuS) + \frac{\partial}{\partial \eta}(\sqrt{g_o}HvS)\right] \\
& - \frac{Ro}{H}\frac{\partial H\omega S}{\partial \sigma} + \frac{E_H}{Sc_H}\left[g^{11}S_{,1,1} + g^{12}S_{,1,2}\right. \\
& + \left. g^{21}S_{,2,1} + g^{22}S_{,2,2}\right] \qquad (2.43)
\end{aligned}$$

Recently, the nonlinear terms in the momentum equations have been replaced by a more compact formulation (Sheng, 1989). The u-equation and v-equation are shown

in Appendix D. The more compact equations do yield better numerical stability than the earlier equations shown in Equations (2.40) and (2.41).

2.7 Boundary Conditions and Initial Conditions

Boundary conditions are required for computing the six dependent variables on or near the boundary. If the closed boundary is fixed in space, the component of fluid velocity normal to it must be zero ($\vec{V} \cdot \vec{n} = 0$, where $\vec{n}$ is the unit normal vector to the boundary). If the fluid is viscous, an additional condition, *i.e.*, the no-slip condition ($\vec{V} \cdot \vec{s} = 0$, where $\vec{s}$ is the unit tangential vector to the boundary) is applied. Application of the above closed and no-slip conditions is made here which result in the fluid at the boundary having zero velocity with respect to the boundary itself. At the closed boundary, no normal flux of momentum, salt, or energy is allowed since the velocity is zero. All the variables shown below are dimensionless based on the nondimensionalization in section 2.3 except for S.

2.7.1 Vertically Stretched System

The boundary conditions at the free surface ($\sigma = 0$) are

$$A_v \left(\frac{\partial u}{\partial \sigma}, \frac{\partial v}{\partial \sigma} \right) = \frac{H}{E_v} (\tau_{sx}, \tau_{sy})$$

$$\frac{\partial T}{\partial \sigma} = \frac{H Pr_v}{E_v} q_s \tag{2.44}$$

$$\frac{\partial S}{\partial \sigma} = 0$$

The boundary conditions at the bottom ($\sigma = -1$) are

$$\begin{aligned} A_v \left(\frac{\partial u}{\partial \sigma}, \frac{\partial v}{\partial \sigma} \right) &= \frac{H}{E_v} (\tau_{bx}, \tau_{by}) \\ &= \frac{U_r}{A_{vr}} H_r Z_r C_d (u_1^2 + v_1^2)^{1/2} (u_1, v_1) \end{aligned} \tag{2.45}$$

$$\frac{\partial T}{\partial \sigma} = 0 \tag{2.46}$$

$$\frac{\partial S}{\partial \sigma} = 0 \tag{2.47}$$

where u_1 and v_1 represent the velocity components at the first grid point above the bottom.

Along the shoreline where river inflow or outflow may occur, the conditions are generally

$$\begin{aligned} u &= u(x, y, \sigma, t) \\ v &= v(x, y, \sigma, t) \\ \omega &= 0 \\ T &= T(x, y, \sigma, t) \\ S &= S(x, y, \sigma, t) \end{aligned} \tag{2.48}$$

The kinematic boundary condition is also imposed at the surface.

$$\omega = \frac{\partial \zeta}{\partial t} + u\frac{\partial \zeta}{\partial x} + v\frac{\partial \zeta}{\partial y} \tag{2.49}$$

The boundary condition required for the pressure is $P = 0$ at $\sigma = 0$ which expresses the assumption that either the contribution of the atmospheric pressure to the pressure of the fluid column is negligible, or that the atmospheric pressure gradients are unimportant.

The open boundary condition is much more complicated, since momentum and mass transport occur through the boundary. Salinity and temperature need to be specified with ζ or velocity at the open boundary. For the elevation ζ, there are currently several options

$$\zeta = \zeta(x, y, t) = \sum_{n=1}^{n_{max}} A_n \cos\left(\frac{2\pi t}{T_n} + \phi_n\right) \tag{2.50}$$

$$\frac{\partial \zeta}{\partial x} = 0 \qquad \text{or} \qquad \frac{\partial \zeta}{\partial y} = 0 \tag{2.51}$$

where A_n, T_n and ϕ_n are the amplitude, period and phase angle of the tabular tidal constituents. When open boundary conditions are given in terms of ζ, the normal velocity component is assumed to be of zero slope while the tangential velocity component may be either (1) zero, or (2) zero slope, or (3) computed from the momentum equations. But in reality the velocity gradients are impossible to obtain from field observation. In the present study, it is assumed that the velocity gradients are zero at the open boundary.

The salinity along an open boundary or river entrance is generally prescribed throughout the tidal cycle. The present model allows the salinity at the open boundary to be computed from a 1-D advection equation during the outflow. For example, along an open boundary on the left or right (Sheng, 1986)

$$\frac{\partial HS}{\partial t} + Ro\frac{\partial HuS}{\partial x} = 0 \tag{2.52}$$

where the spatial salinity flux is evaluated from the salinity values at the boundary and the interior grid point via a one-sided differencing scheme. During the inflow, however, the salinity value at the open boundary can either take on a prescribed value or be determined from the 1-D advection equation while using the boundary salinity value and the prescribed salinity value to evaluate the spatial flux term.

To initiate a run, the initial spatial distributions of ζ, u, v, ω, T and S need to be specified. When initial data are unknown, one could start with zero initial fields. When initial data are known at a limited number of locations, an initial field can be generated by some interpolation scheme. It is desirable if the interpolated field satisfies the conservation law governing that field variable.

For practical simulations, the present model usually assumes zero initial flow if little initial data are known. In case of salinity simulation, the spin-up time is longer and an interpolation routine is provided to produce a reasonable initial field from limited data points.

2.7.2 Vertically Stretched and Laterally Boundary-Fitted System

The boundary conditions at the free surface ($\sigma = 0$) are

$$\begin{aligned} A_v\left(\frac{\partial u}{\partial \sigma}, \frac{\partial u}{\partial \sigma}\right) &= \frac{H}{E_v}(\tau_{s\xi}, \tau_{s\eta}) \\ \frac{\partial T}{\partial \sigma} &= \frac{HPr_v}{E_v} q_s \\ \frac{\partial S}{\partial \sigma} &= 0 \end{aligned} \tag{2.53}$$

The boundary conditions at the bottom ($\sigma = -1$) are

$$\begin{aligned} A_v\left(\frac{\partial u}{\partial \sigma}, \frac{\partial v}{\partial \sigma}\right) &= \frac{H}{E_v}(\tau_{b\xi}, \tau_{b\eta}) \\ &= \frac{U_\tau}{A_{v\tau}} H_\tau Z_\tau C_d \left[g_{11}u_1^2 + 2g_{12}u_1v_1 + g_{22}v_1^2\right](u_1, v_1) \\ \frac{\partial T}{\partial \sigma} &= 0 \\ \frac{\partial S}{\partial \sigma} &= 0 \end{aligned} \tag{2.54}$$

where u_1 and v_1 are the contravariant velocity components at the first grid point above the bottom.

Due to the use of contravariant velocity components, the lateral boundary conditions in the (ξ, η, σ) grid are similar to those in the (x, y, σ) system. Along the solid boundary, the no-slip condition dictates that the tangential velocity is zero while the slip condition requires that the normal velocity is zero. When flow is specified at the open boundary or river boundary, the normal velocity component is prescribed.

Initial conditions on vectors, if given in the Cartesian or prototype system, such as the velocity and the surface stress, must be first transformed before being used in the transformed equations. Thus, the surface stress in the transformed coordinate system is given by

$$\bar{\tau}^1 = \frac{\partial \xi}{\partial x}\tau^1 + \frac{\partial \xi}{\partial y}\tau^2 \tag{2.55}$$

$$\bar{\tau}^2 = \frac{\partial \eta}{\partial x}\tau^1 + \frac{\partial \eta}{\partial y}\tau^2 \tag{2.56}$$

where $\overline{\tau}^1$, $\overline{\tau}^2$ are the contravariant components of the stress in the transformed system and τ^1, τ^2 are the contravariant components in the Cartesian system. Note that in the Cartesian system, the contravariant, covariant and physical components of a vector are identical. The contravariant components of the initial velocity vectors can be transformed in the same manner to obtain the proper initial conditions for the transformed momentum equations.

2.8 Solution Technique

The solution of the difference equations may differ from the solution of the differential equations because of a variety of errors (truncation error, dispersion error, and round-off error) even if the scheme is stable. For explicit methods, the stability condition is that the CFL (Courant-Friedrichs-Lewy) criteria based on the shallow water wave speed (Roach, 1976) should be satisfied. The basic numerical technique to enhance the model efficiency is the mode-splitting technique (Sheng *et al.*, 1978; Sheng, 1985; Madala and Piascek, 1977), which basically solves the equations of motion by splitting them into an "external" or vertically-averaged mode and an "internal" or vertical structure mode. The external mode is solved implicitly, and the internal mode is solved explicitly except for the vertical diffusion terms. Semi-implicit methods (Sheng, 1983; Sheng and Choi, 1989) can be introduced to take advantage of the merits of both the explicit method and the implicit method. This approach solves implicitly those terms in the governing equations which possess rather stringent stability criteria if explicit schemes were used. These terms include those that govern the propagation of surface gravity waves: local acceleration, and surface slope terms in the momentum equations and all terms in the continuity equation. Furthermore, vertical diffusion terms in the momentum and transport equations are solved implicitly. All other terms in the equations are solved explicitly.

The governing equations are solved by a finite difference scheme along with proper boundary conditions. A space-staggered grid system shown in Figure 2.5, is used to

discretize the differential equation (Sheng, 1983). In the staggered grid, elevation, vertical velocity, temperature, salinity, and density are defined at the center of a cell, and u-velocity at the left and right sides of a cell, and v-velocity at the top and bottom sides of a cell. A staggered grid system has an accuracy of $O(\Delta x^2)$ with the same mesh system compared with an accuracy of $O(\Delta x)$ in a non-staggered grid system. For the time marching, forward time difference (two-time-level) or leapfrog technique (three-time- level) can be used. The present study uses a two-time-level scheme. Both the leapfrog technique and spatial difference are centered differences, and the accuracy in space and time is second-order. The separation of solutions caused by the leapfrog method is corrected by using a periodic time smoothing. The diffusion terms are evaluated at the previous time level to avoid numerical instabilities.

In the computational procedure, first the spatial derivatives $x_\xi, x_\eta, y_\xi, y_\eta$, and Jacobian J at each grid point are computed using the transformation equations (Eq. (2.34) - Eq. (2.38)). These derivatives are used as input to the circulation and transport model. The "external mode" equations are solved using an alternating-direction implicit (ADI) method. This solution technique consists of a two-step calculation which advances the solution first from time level n to * (an intermediate step) and then from * to $n+1$. In the first step, ζ and U are advanced from n to * by an implicit calculation along each row in the ξ direction, while treating V and η-derivative terms explicitly. In the second step, ζ and V are advanced from * to $n+1$ by an implicit calculation along every column in the η direction, while treating U and ξ-derivatives explicitly. Then deviations of the velocities from the vertically averaged velocities are calculated, while treating implicitly the vertical diffusion terms in the equations for the deficit velocities. The deficit velocities are then added to the vertically-averaged velocities to produce the three-dimensional velocity field. Conservation equations for salinity and heat are then solved explicitly, except for the vertical diffusion term. The implicit schemes used in the external mode and the internal mode require the

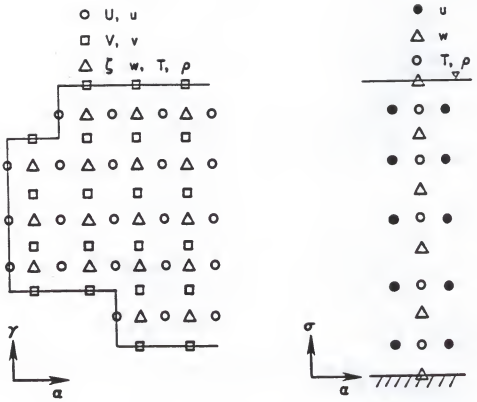

Figure 2.5: Staggered numerical grids in lateral and vertical directions (From Sheng, 1983).

inversion of only tridiagonal matrix systems.

2.9 Finite Difference Equation

In the following, a set of two-time-level difference equations in (x, y, σ) system are presented. A set of three-time-level difference equations in (ξ, η, σ) system are presented in Appendix E. The results presented in this study are obtained with the two-time-level equations. The finite difference representation of a dependent variable can be written

$$\phi_{ijk}^{n} = \phi(x, y, \sigma, t) = \phi(i\Delta x, j\Delta y, k\Delta\sigma, n\Delta t)$$

$$\delta_x \phi \;=\; (\phi_{i+1/2} - \phi_{i-1/2})/\Delta x$$

Finite-difference equations for the external mode and the internal mode are listed in the following. The basic two-time-level schemes are similar to those presented in Sheng (1983) and Sheng (1987). For three-time-level schemes, refer to Appendix E.

2.9.1 External Mode in (x, y, σ) (Two-Time-Level Scheme)

The external mode consists of the surface displacement ζ and the vertically-integrated velocities U and V and is described by Equations (2.31) through (2.33). The finite-difference schemes treat all of the terms in the continuity equation implicitly. The time derivatives and surface slopes in the momentum equations are generally treated implicitly, while the bottom stresses are computed explicitly from the latest vertical profiles of horizontal velocities assuming the presence of a turbulent bottom boundary layer. In that case, one can either specify a drag coefficient or a roughness height, instead of the conventional Chezy-Manning coefficients which are used in many two- dimensional models. When used in two-dimensional mode, however, the model computes implicitly the bottom stresses in the u and v equations with with Chezy-Manning formulation. The dimensionless finite-difference equations in the following are

$$AF^{n+1} = F^{n} + \Delta t D^{n} \tag{2.57}$$

where superscripts $n+1$ and n denote the present and previous time-step of integration, Δt is the time-step, and

$$A = \begin{bmatrix} 1 & \alpha_x \delta_x & \alpha_y \delta_y \\ \gamma_x \delta_x & 1 & 0 \\ \gamma_y \delta_y & 0 & 1 \end{bmatrix}$$

$$F = \begin{pmatrix} \zeta \\ U \\ V \end{pmatrix}$$

$$D = \begin{pmatrix} 0 \\ D_x \\ D_y \end{pmatrix}$$

with D_x and D_y as defined by Equations (2.32) and (2.33), and

$$\alpha_x = \frac{\beta \Delta t}{\Delta x} \tag{2.58}$$

$$\alpha_y = \frac{\beta \Delta t}{\Delta y} \tag{2.59}$$

$$\gamma_x = \frac{H \Delta t}{\Delta x} \tag{2.60}$$

$$\gamma_y = \frac{H \Delta t}{\Delta y} \tag{2.61}$$

where Δx and Δy are grid spacings in the x and y directions, respectively.

For increased efficiency of computation as previously discussed, the ADI method factors the matrix A into the sum of three matrices: the identity matrix I, a matrix A_x, and a matrix A_y:

$$A_x = \begin{bmatrix} 0 & \alpha_x \delta_x & 0 \\ \gamma_x \delta_x & 0 & 0 \\ 0 & 0 & 0 \end{bmatrix} \tag{2.62}$$

$$A_y = \begin{bmatrix} 0 & 0 & \alpha_y\delta_y \\ 0 & 0 & 0 \\ \gamma_y\delta_y & 0 & 0 \end{bmatrix} \tag{2.63}$$

To solve the factored version of Equation (2.57), the ADI method proceeds by first computing in the x-directions (the "x-sweep"), and then computing in the y-direction (the "y-sweep"). Carrying out the factorization of Equation (2.57), and neglecting terms of order Δt^2 yields

x-sweep:

$$[I + A_x]F^* = [I - A_y]F^n + \Delta t D^n \tag{2.64}$$

y-sweep:

$$[I + A_y]F^{n+1} = F^* + A_y F^n \tag{2.65}$$

where F^* represents the intermediate solution

$$F^* = \begin{pmatrix} \zeta^* \\ U^* \\ V^* \end{pmatrix} \tag{2.66}$$

The more detailed equations for the x-sweep and y-sweep are

x-sweep:

$$\zeta^* + \alpha_x\delta_x U^* = \zeta^n - \alpha_y\delta_y V^n \tag{2.67}$$

$$U^* + \gamma_x\delta_x\zeta^* = U^n + \Delta t D_x^n \tag{2.68}$$

$$V^* = V^n - \gamma_y\delta_y\zeta^n + \Delta t D_x^n \tag{2.69}$$

The ζ^* and U^* are two unknowns in the x-direction. The above equation can be readily solved by simple inversion of tridiagonal matrices along all the grid rows.

y-sweep:

$$\zeta^{n+1} + \alpha_y \delta_y V^{n+1} = \zeta^* + \alpha_y \delta_y V^n \tag{2.70}$$

$$V^{n+1} + \gamma_y \delta_y \zeta^{n+1} = V^* + \gamma_y \delta_y \zeta^n \tag{2.71}$$

$$U^{n+1} = U^* \tag{2.72}$$

The ζ^{n+1} and V^{n+1} are two unknowns in the y- direction. Again, inversion of tridiagonal matrices along all the grid columns are performed to solve the above equation by substituting the equation for V^* from the x-sweep into the equation in the y-sweep.

2.9.2 Internal Mode in (x, y, σ) (Two-Time-Level Scheme)

Defining deficit velocities as $\tilde{u} \equiv u - \overline{u}$ and $\tilde{v} \equiv v - \overline{v}$, we obtain the differential equations for the internal mode by subtracting the vertically-averaged momentum equations from the three-dimensional momentum equations multiplied by H (Sheng, 1986)

$$\frac{1}{H}\frac{\partial H\tilde{u}}{\partial t} = B_x - \frac{D_x}{H} + \frac{E_v}{H^2}\frac{\partial}{\partial \sigma}\left(A_v \frac{\partial}{\partial \sigma}(\overline{u} + \tilde{u})\right) \tag{2.73}$$

$$\frac{1}{H}\frac{\partial H\tilde{v}}{\partial t} = B_y - \frac{D_y}{H} + \frac{E_v}{H^2}\frac{\partial}{\partial \sigma}\left(A_v \frac{\partial}{\partial \sigma}(\overline{v} + \tilde{v})\right) \tag{2.74}$$

The finite difference equations are

$$\begin{aligned}(H\tilde{u})^{n+1} &= (H\tilde{u})^n + \Delta t(HB_x - D_x)^n \\ &+ \frac{E_v}{H^n}\Delta t \frac{\partial}{\partial \sigma} A_v \frac{\partial}{\partial \sigma}\left((\overline{u} + \tilde{u})^{n+1}\right)\end{aligned} \tag{2.75}$$

$$\begin{aligned}(H\tilde{v})^{n+1} &= (H\tilde{v})^n + \Delta t(HB_y - D_y)^n \\ &+ \frac{E_v}{H^n}\Delta t \frac{\partial}{\partial \sigma} A_v \frac{\partial}{\partial \sigma}\left((\overline{v} + \tilde{v})^{n+1}\right)\end{aligned} \tag{2.76}$$

The vertical diffusion terms in the momentum equations are treated implicitly to ensure numerical stability in shallow waters. It is also important to ensure that the

vertically-integrated perturbation velocities are always equal to zero

$$\sum_{k=1}^{k_{max}} \tilde{u}_{i,j,k} = 0 \tag{2.77}$$

$$\sum_{k=1}^{k_{max}} \tilde{v}_{i,j,k} = 0 \tag{2.78}$$

In order to ensure that Equations (2.77) and (2.78) are satisfied, the nonlinear inertia and turbulent diffusion terms in the vertically-integrated Equations (2.32) and (33) must be evaluated by summing the corresponding terms in the three-dimensional equations at all vertical levels.

Once $\tilde{u}^{n+1}$ and $\tilde{v}^{n+1}$ are obtained, u and v can be obtained from

$$u^{n+1} = \tilde{u}^{n+1} + U^{n+1}/H^{n+1} \tag{2.79}$$

$$v^{n+1} = \tilde{v}^{n+1} + V^{n+1}/H^{n+1} \tag{2.80}$$

Following these, the vertical velocities ω^{n+1} and w^{n+1} can be computed from

$$\omega_k^{n+1} = \omega_{k-1}^{n+1} - \frac{\Delta\sigma}{\beta H}\frac{\partial\zeta^{n+1}}{\partial t} - \frac{\Delta\sigma}{H}\left[\left(\frac{\partial Hu}{\partial x}\right)_k^{n+1} + \left(\frac{\partial Hv}{\partial y}\right)_k^{n+1}\right] \tag{2.81}$$

$$w_k^{n+1} = H^{n+1}\omega_k^{n+1} + \frac{1+\sigma}{\beta}\frac{d\zeta^{n+1}}{dt} + \sigma\left(u\frac{\partial h}{\partial x} + v\frac{\partial h}{\partial y}\right)_k^{n+1} \tag{2.82}$$

The vertical velocity ω should be nearly zero at the free surface.

2.9.3 External Mode in (ξ, η, σ) (Two-Time-Level Scheme)

The present study generally uses the following two-time-level scheme instead of the two-time-level scheme described earlier. Vertically-integrated differential equations are written as follows (Sheng, 1986)

$$\zeta_t + \frac{\beta}{\sqrt{g_o}}\left[\frac{\partial}{\partial\xi}(\sqrt{g_o}U) + \frac{\partial}{\partial\eta}(\sqrt{g_o}V)\right] = 0 \tag{2.83}$$

$$U_t + Hg^{11}\zeta_\xi + Hg^{12}\zeta_\eta = \frac{g_{12}}{\sqrt{g_o}}U - C_{\tau\xi}U + D'_x \tag{2.84}$$

$$V_t + Hg^{12}\zeta_\xi + Hg^{22}\zeta_\eta = -\frac{g_{11}}{\sqrt{g_o}}U - \frac{g_{12}}{\sqrt{g_o}}V + D'_y \tag{2.85}$$

where $C_{\tau\xi}$ is drag coefficient in ξ-direction, and D'_x and D'_y are all the terms in the x-direction and y-direction which are not shown in the momentum equations. The above equations are written in finite difference forms as follows

$$\begin{aligned}\zeta^{n+1} - \zeta^n &+ \frac{\beta\Delta T}{\Delta\xi \cdot \sqrt{g_o}}[T_1\delta_\xi(\sqrt{g_o}U)^{n+1} + (1-T_1)\delta_\xi(\sqrt{g_o}U^n)] \\ &+ \frac{\beta\Delta T}{\Delta\eta \cdot \sqrt{g_o}}[T_1\delta_\eta(\sqrt{g_o}V^{n+1}) + (1-T_1)\delta_\eta(\sqrt{g_o}V^n)] = 0\end{aligned} \tag{2.86}$$

$$\begin{aligned}U^{n+1} - U^n &+ \Delta T\left\{\frac{Hg^{11}}{\Delta\xi}\left[T_1\delta_\xi(\zeta^{n+1}) + (1-T_1)\delta_\xi(\zeta^n)\right]\right. \\ &+ \left.\frac{Hg^{12}}{\Delta\eta}\left[T_1\delta_\eta(\zeta^{n+1}) + (1-T_1)\delta_\eta(\zeta^n)\right]\right\} \\ &= -\Delta T\left[T_2 C_{\tau\xi}U^{n+1} + (1-T_2)C_{\tau\xi}U^n - T_3\frac{g_{12}}{\sqrt{g_o}}U^{n+1}\right. \\ &- \left.(1-T_3)\frac{g_{12}}{\sqrt{g_o}}U^n\right] + D'^n_x\end{aligned} \tag{2.87}$$

$$\begin{aligned}V^{n+1} - V^n &+ \Delta T\left\{\frac{Hg^{12}}{\Delta\xi}\left[T_1\delta_\xi(\zeta^{n+1}) + (1-T_1)\delta_\xi(\zeta^n)\right]\right. \\ &+ \left.\frac{Hg^{22}}{\Delta_\eta}\left[T_1\delta_\eta(\zeta^{n+1}) + (1-T_1)\delta_\eta(\zeta^n)\right]\right\} \\ &= -\Delta T\left[T_2 C_{\tau\eta}V^{n+1} + (1-T_2)C_{\tau\eta}V^n + T_3\frac{g_{12}}{\sqrt{g_o}}V^{n+1}\right. \\ &+ \left.(1-T_3)\frac{g_{12}}{\sqrt{g_o}}V^n\right] + D'^n_y\end{aligned} \tag{2.88}$$

Instead of solving the above equations directly, however, they can be written in ADI scheme as follows

ξ-sweep:

$$\begin{aligned}\zeta^* + T_1\alpha_\xi\delta_\xi(\sqrt{g_o}U^*) &= \zeta^n - \alpha_\xi(1-T_1)\delta_\xi(\sqrt{g_o}U^n) \\ &- \alpha_\eta\delta_\eta(\sqrt{g_o}V^n)\end{aligned} \tag{2.89}$$

$$
\begin{aligned}
& T_1\sqrt{g_o}\gamma^{11}\delta_\xi(\zeta^*) + \left[1 + \Delta t\left(T_2 C_{\tau\xi} - T_3\frac{g_{12}}{\sqrt{g_o}}\right)\right](\sqrt{g_o}U^*) \\
= \; - \; & T_1\sqrt{g_o}\gamma^{12}\delta_\eta(\zeta^n) + (\sqrt{g_o}U^n) \\
- \; & (1-T_1)\sqrt{g_o}\gamma^{11}\delta_\xi(\zeta^n) - (1-T_1)\sqrt{g_o}\gamma^{12}\delta_\eta(\zeta^n) \\
- \; & (\sqrt{g_o}U^n)\left[\Delta T(1-T_2)C_{\tau\xi} - \Delta t(1-T_3)\frac{g_{12}}{\sqrt{g_o}}\right] + D_x'^n
\end{aligned}
\tag{2.90}
$$

η-sweep:

$$
\zeta^{n+1} + T_1\alpha_\eta\delta_\eta(\sqrt{g_o}V^{n+1}) = \zeta^* + T_1\alpha_\eta\delta_\eta(\sqrt{g_o}V^n) \tag{2.91}
$$

$$
\begin{aligned}
& T_1\sqrt{g_o}\gamma^{22}\delta_\eta(\zeta^{n+1}) + \left[1 + \Delta t\left(T_2 C_{\tau\eta} + T_3\frac{g_{12}}{\sqrt{g_o}}\right)\right][\sqrt{g_o}V^{n+1}] \\
= \; - \; & T_1\sqrt{g_o}\gamma^{12}\delta_\xi(\zeta^*) - (1-T_1)\sqrt{g_o}\gamma^{12}\delta_\xi(\zeta^n) - (1-T_1)\sqrt{g_o}\gamma^{22}\delta_\eta(\zeta^n) \\
+ \; & (\sqrt{g_o}V^n) - (\sqrt{g_o}V^n)\left[\Delta t(1-T_2)C_{\tau\eta} + \Delta t(1-T_3)\frac{g_{12}}{\sqrt{g_o}}\right] + D_y'^n
\end{aligned}
\tag{2.92}
$$

$$
T_1\sqrt{g_o}\gamma^{12}\delta_\eta(\zeta^{n+1}) + (\sqrt{g_o}U^{n+1}) = (\sqrt{g_o}U^*) + T_1\sqrt{g_o}\gamma^{12}\delta_\eta(\zeta^{n-1}) \tag{2.93}
$$

where T_1, T_2 and T_3 are all constants between 0 and 1. For example, the wave propagation terms are treated explicitly if $T_1 = 0$, but implicitly if $T_1 = 1$. m can be $n-1$ or n. Additional parameters appearing in the equations are

$$
\begin{aligned}
\alpha_\xi &\equiv \frac{\beta\Delta t}{g_0\Delta\xi} \\
\alpha_\eta &\equiv \frac{\beta\Delta t}{g_0\Delta\eta} \\
\gamma^{11} &\equiv \frac{H\Delta t g^{11}}{\Delta\xi} \\
\gamma^{12} &\equiv \frac{H\Delta t g^{12}}{\Delta\xi} \\
\gamma^{22} &\equiv \frac{H\Delta t g^{22}}{\Delta\eta} \\
\gamma^{21} &\equiv \frac{H\Delta t g^{12}}{\Delta\eta}
\end{aligned}
\tag{2.94}
$$

The system of equations can be rewritten in the following matrix form

$$[A]F^{n+1} = AF^{n-1} + \bar{D} \tag{2.95}$$

$$[I + A_\xi]F^* = [B - A_\eta]F^{n-1} + \bar{D} \tag{2.96}$$

$$[I + A_\eta]F^{n+1} = F^* + A_\eta F^{n-1} \tag{2.97}$$

where

$$[A] = \begin{bmatrix} 1 & \alpha_x T_1 \delta_\xi & \alpha_y T_1 \delta_\eta \\ \sqrt{g_0}\gamma^{11} T_1 \delta_\xi & 1 + \Delta T \left(C_{\tau\xi} T_2 - \frac{g_{12}}{\sqrt{g_0}} T_3 \right) & 0 \\ \sqrt{g_0}\gamma^{22} T_1 \delta_\eta & 0 & 1 + \Delta T \left(C_{\tau\eta} T_2 + \frac{g_{12}}{\sqrt{g_0}} T_3 \right) \end{bmatrix} \tag{2.98}$$

$$[A_\xi] = \begin{bmatrix} 0 & \alpha_x T_1 \delta_\xi & 0 \\ \sqrt{g_0}\gamma^{11} T_1 \delta_\xi & \Delta T \left(C_{\tau\xi} T_2 - \frac{g_{12}}{\sqrt{g_0}} T_3 \right) & 0 \\ 0 & 0 & 0 \end{bmatrix} \tag{2.99}$$

$$[A_\eta] = \begin{bmatrix} 0 & 0 & \alpha_y T_1 \delta_\eta \\ 0 & 0 & 0 \\ \sqrt{g_0}\gamma^{22} T_1 \delta_\eta & 0 & \Delta T \left(C_{\tau\eta} T_2 + \frac{g_{12}}{\sqrt{g_0}} T_3 \right) \end{bmatrix} \tag{2.100}$$

$$[B] = \begin{bmatrix} 1 & 0 & 0 \\ 0 & 1 & 0 \\ 0 & 0 & 1 \end{bmatrix} \tag{2.101}$$

$$F = \begin{bmatrix} \zeta \\ \sqrt{g_0}U \\ \sqrt{g_0}V \end{bmatrix} \tag{2.102}$$

$$\bar{D} = \begin{bmatrix} -\alpha_x(1-T_1\delta_\xi(\sqrt{g_0}U^n)) - \alpha_y(1-T_1)\delta_\eta(\sqrt{g_0}V^n) \\ \sqrt{g_0}U^n\Delta T\left(-(1-T_2)C_{\tau\xi} + (1-T_3)\frac{g_{12}}{\sqrt{g_0}}\right) - \sqrt{g_0}\gamma^{11}(1-T_1)\delta_\xi\zeta^n \\ -\sqrt{g_0}\gamma^{21}\delta_\eta\zeta^n + \Delta T D'_x\sqrt{g_0} \\ \sqrt{g_0}V^n\Delta T\left(-(1-T_2)C_{\tau\eta} - (1-T_3)\frac{g_{12}}{\sqrt{g_0}}\right) - \sqrt{g_0}\gamma^{12}\delta_\xi\zeta^n \\ -\sqrt{g_0}\gamma^{22}(1-T_1)\delta_\eta\zeta^n + \Delta T D'_y\sqrt{g_0} \end{bmatrix} \tag{2.103}$$

2.9.4 Internal Mode in (ξ,η,σ) (Two-Time-Level Scheme)

$$\begin{aligned} \frac{\partial}{\partial t}H\tilde{u} &= \frac{g^{12}}{\sqrt{g_o}}H\tilde{u} + \frac{g^{22}}{\sqrt{g_o}}H\tilde{v} + F_3 \\ &+ \frac{E_v}{H^2}\frac{\partial}{\partial\sigma}\left(A_v\frac{\partial H\tilde{u}}{\partial\sigma}\right) - (\tau_{s\xi} - \tau_{b\xi}) - F_2 \end{aligned} \tag{2.104}$$

$$\begin{aligned} \frac{\partial}{\partial t}H\tilde{v} &= -\frac{g^{11}}{\sqrt{g_o}}H\tilde{u} - \frac{g^{21}}{\sqrt{g_o}}H\tilde{v} + G_3 \\ &+ \frac{E_v}{H^2}\frac{\partial}{\partial\sigma}\left(A_v\frac{\partial H\tilde{v}}{\partial\sigma}\right) - (\tau_{s\eta} - \tau_{b\eta}) - G_2 \end{aligned} \tag{2.105}$$

and F_2 and G_2 indicate all the explicit terms in U and V equations, respectively, and F_3 and G_3 indicate all the explicit terms in the u and v equations, respectively.

$$\begin{aligned} (H\tilde{u})^{n+1} &= (H\tilde{u})^n + 2\Delta t\frac{g^{12}}{\sqrt{g_o}}H^{n+1}\tilde{u}^{n+1} \\ &+ 2\Delta t\frac{g^{22}}{\sqrt{g_o}}H^n\tilde{u}^n + 2\Delta t(F_3 - F_2)^n \\ &+ 2\Delta t\frac{E_v}{(H^n)^2}\frac{\partial}{\partial\sigma}\left[A_v\frac{\partial}{\partial\sigma}(H^{n+1}\tilde{u}^{n+1})\right] \\ &- (\tau_{s\xi} - \tau_{b\xi})^{n+1} \end{aligned} \tag{2.106}$$

$$\begin{aligned} (H\tilde{v})^{n+1} &= (H\tilde{v})^n - 2\Delta t\frac{g^{11}}{\sqrt{g_o}}H^n\tilde{v}^{n+1} \\ &- 2\Delta t\frac{g^{21}}{\sqrt{g_o}}H^{n+1}\tilde{v}^{n+1} + 2\Delta t(G_3 - G_2)^n \\ &+ 2\Delta t\frac{E_v}{(H^n)^2}\frac{\partial}{\partial\sigma}\left[A_v\frac{\partial}{\partial\sigma}(H^{n+1}\tilde{v}^{n+1})\right] \\ &- (\tau_{s\eta} - \tau_{b\eta})^{n+1} \end{aligned} \tag{2.107}$$

2.9.5 Salinity Scheme (Two-Time-Level Scheme)

The finite difference equation for salinity are similar to the internal mode solution. The vertical diffusion terms are treated implicitly, while the horizontal diffusion and advection terms are treated explicitly. The salinity equation in the (ξ, η, σ) coordinate system is shown in the following (Sheng, 1986)

$$\frac{\partial HS}{\partial t} = \frac{E_v}{HS_{c_v}} \frac{\partial}{\partial \sigma} \left(D_v \frac{\partial S}{\partial \sigma} \right) + G \tag{2.108}$$

where G is advection plus horizontal diffusion terms, and

$$\begin{aligned}
S_{c_v} &= \frac{A_{v_R}}{D_{v_R}} \\
S_{c_H} &= \frac{A_{H_R}}{D_{H_R}} \\
G &= -\frac{Ro}{\sqrt{g_o}} \left[\frac{\partial}{\partial \xi}(HuS\sqrt{g_o}) + \frac{\partial}{\partial \eta}(HvS\sqrt{g_o}) + \sqrt{g_o}\frac{\partial}{\partial \sigma}(H\omega S) \right] \\
&+ \frac{HE_H}{S_{c_H}} \left(g^{11}\frac{\partial^2 S}{\partial \xi^2} + 2g^{12}\frac{\partial^2 S}{\partial \xi \partial \eta} + g^{22}\frac{\partial^2 S}{\partial \eta^2} \right)
\end{aligned}$$

Using i, j, and k as grid indices in the ξ-, η-, and σ-directions, respectively, the finite difference equation for salinity can be written as (Sheng and Choi, 1989)

$$\begin{aligned}
H^{n+1}S^{n+1}_{i,j,k} - H^n S^n_{i,j,k} &= -\frac{\Delta t \cdot R_o}{\sqrt{g_o}} \left[\frac{\partial}{\partial \xi}(HuS\sqrt{g_o})^n \right. \\
&\left. + \frac{\partial}{\partial \eta}(HvS\sqrt{g_o})^n + \sqrt{g_o}\frac{\partial}{\partial \sigma}(H\omega S)^n \right] \\
&+ \frac{E_v(\Delta t)}{H^{n+1}S_{c_v}} \frac{1}{\Delta \sigma_k} \left[\frac{D_{v+}}{\Delta \sigma_+} \left(S^{n+1}_{k+1} - S^{n+1}_k \right) \right. \\
&\left. - \frac{D_{v-}}{\Delta \sigma_-} \left(S^{n+1}_k - S^{n+1}_{k-1} \right) \right] \\
&+ \frac{HE_H \cdot \Delta t}{S_{c_H}} \left(g^{11}\frac{\partial^2 S}{\partial \xi^2} + 2g^{12}\frac{\partial^2 S}{\partial \xi \partial \eta} + g^{22}\frac{\partial^2 S}{\partial \eta^2} \right)^n
\end{aligned} \tag{2.109}$$

Dividing by H^{n+1} gives

$$- \frac{E_v \cdot \Delta t}{(H^{n+1})^2 S_{c_v} \cdot \Delta \sigma_k} \left(\frac{D_{v-}}{\Delta \sigma_-} S^{n+1}_{i,j,k-1} + \frac{D_{v+}}{\Delta \sigma_+} S^{n+1}_{i,j,k+1} \right) \tag{2.110}$$

$$+ \quad \left[1 + \frac{E_v \cdot \Delta t}{(H^{n+1})^2 S_{c_v} \Delta\sigma_k}\left(\frac{D_{v+}}{\Delta\sigma_+} + \frac{D_{v-}}{\Delta\sigma_-}\right)\right] S^{n+1}_{i,j,k}$$

$$= \quad \frac{H^n}{H^{n+1}} S^n_{i,j,k} - \frac{\Delta t}{H^{n+1}} \frac{R_o}{\sqrt{g_o}} \left[\frac{\partial}{\partial\xi}(HuS\sqrt{g_o})^n + \frac{\partial}{\partial\eta}(HvS\sqrt{g_o})^n + \sqrt{g_o}\frac{\partial}{\partial\sigma}(H\omega S)^n\right]$$

$$+ \quad \frac{H^n}{H^{n+1}} \frac{E_H \cdot \Delta t}{S_{c_H}} \left(g^{11}\frac{\partial^2 S}{\partial\xi^2} + 2g^{12}\frac{\partial^2 S}{\partial\xi\partial\eta} + g^{22}\frac{\partial^2 S}{\partial\eta^2}\right)^n$$

Rearranging Eq. (2.110) gives

$$-\gamma_k \alpha_{k-\frac{1}{2}} S^{n+1}_{i,j,k-1} \quad + \quad \left[1 + \gamma_k(\alpha_{k-\frac{1}{2}} + \alpha_{k+\frac{1}{2}})\right] S^{n+1}_{i,j,k} - \gamma_k \alpha_{k+\frac{1}{2}} S^{n+1}_{i,j,k+1} \qquad (2.111)$$

$$= \quad \frac{H^n}{H^{n+1}} S^n_{i,j,k} + G^n_k$$

This is applied for $1 < k < km$: where

$$\gamma_k \quad = \quad \frac{E_v \Delta t}{\left(H^{n+1}_{i,j}\right)^2 S c_v \Delta\sigma_k} \qquad (2.112)$$

$$\alpha_{k+1/2} \quad = \quad \frac{D_{v+}}{\Delta\sigma_+} \qquad (2.113)$$

$$\alpha_{k-1/2} \quad = \quad \frac{D_{v-}}{\Delta\sigma-} \qquad (2.114)$$

$$G_k \quad = \quad \text{advection + diffusion} \qquad (2.115)$$

For $k = 1$, i.e., the lowest σ-level:

$$\left[1 + \gamma_1 \alpha_{3/2}\right] S^{n+1}_{i,j,1} \quad - \quad \gamma_1 \alpha_{3/2} S^{n+1}_{i,j,2} \qquad (2.116)$$

$$= \quad \frac{H^n}{H^{n+1}} S^n_{i,j,1} + G^n_1$$

For $k = km$, i.e., the upper-most σ-level:

$$-\gamma_{km}\alpha_{km-\frac{1}{2}}S^{n+1}_{i,j,km-1} + \left[1 + \gamma_{km-\frac{1}{2}}\alpha_{km-\frac{1}{2}}\right]S^{n+1}_{i,j,km} \tag{2.117}$$

$$= \frac{H^n}{H^{n+1}}S^n_{i,j,km} + G^n_{km}$$

Equations (2.111), (2.116), (2.117), can be written as the following tridiagonal system of algebraic equations

$$A1(K) * S(K-1) + A2(K) * S(K) + A3(K) * S(K+1) = A4(K) \tag{2.118}$$

where $A1, A2, A3$, and $A4$ are defined as

$$\begin{aligned}
A1(K) &= \begin{cases} 0 & K = 1 \\ -\gamma_k\alpha_{k-1/2} & 1 < K \leq KM \end{cases} \\
A2(K) &= \begin{cases} 1 + \gamma_1\alpha_{3/2} & K = 1 \\ 1 + \gamma_k(\alpha_{km-1/2} + \alpha_{k+1/2}) & 1 < K < KM \\ 1 + \gamma_{km-1/2}\alpha_{km-1/2} & K = KM \end{cases} \\
A3(K) &= \begin{cases} -\gamma_k\alpha_{k+1/2} & 1 \leq K < KM \\ 0 & K = KM \end{cases} \\
A4(K) &= \frac{H^n}{H^{n+1}}S^n_{i,j,k} + G^n_k \quad 1 \leq K \leq KM
\end{aligned} \tag{2.119}$$

The above tridiagonal system of equations given by Equation (2.118) is efficiently solved by a tridiagonal solver first developed by Thomas (1954), which is often called "The Thomas Algorithm".

2.9.6 Advection Terms

1. Central Difference Scheme

The central difference option has the advantage of second-order accuracy, but a disadvantage of numerical dispersion. When a large concentration gradient exists in

the model domain with insufficient grid points across the gradient, negative concentrations may sometimes develop in the simulation. The finite-difference form is

$$\begin{aligned}\frac{\partial}{\partial\xi}(HuS\sqrt{g_o}) &= \frac{(HS\sqrt{g_o}u)_+ - (HS\sqrt{g_o}u)_-}{\Delta\xi} \\ &= \frac{1}{\Delta\xi}\left[\frac{(HS\sqrt{g_o})_{i,j,k} + (HS\sqrt{g_o})_{i+1,j,k}}{2}\cdot u_{i+1,j,k}\right. \\ &\quad \left. - \frac{(HS\sqrt{g_o})_{i,j,k} + (HS\sqrt{g_o})_{i-1,j,k}}{2}\cdot u_{i,j,k}\right]\end{aligned} \tag{2.120}$$

$$\begin{aligned}\frac{\partial}{\partial\eta}(HvS\sqrt{g_o}) &= \frac{(HS\sqrt{g_o}v)_+ - (HS\sqrt{g_o}v)_-}{\Delta\eta} \\ &= \frac{1}{\Delta\eta}\left[\frac{(HS\sqrt{g_o})_{i,j,k} + (HS\sqrt{g_o})_{i,j+1,k}}{2}\cdot v_{i,j+1,k}\right. \\ &\quad \left. - \frac{(HS\sqrt{g_o})_{i,j,k} + (HS\sqrt{g_o})_{i,j-1,k}}{2}\cdot v_{i,j,k}\right]\end{aligned} \tag{2.121}$$

$$\frac{\partial}{\partial\sigma}(H\omega S) = \frac{H}{\Delta\sigma}\left[\omega_k\cdot\frac{1}{2}(S_{i,j,k}+S_{i,j,k+1}) - \omega_{k-1}\cdot\frac{1}{2}(S_{i,j,k}+S_{i,j,k-1})\right] \tag{2.122}$$

2. Upwind Difference Scheme

The upwind difference option has the advantage of increased stability versus the central difference option, but at a cost of increased numerical diffusion. The upwind difference option guarantees positive salinity concentrations. The finite-difference form is

$$\frac{\partial}{\partial\xi}(HuS\sqrt{g_o}) = (S_+u^T_{i+1,j,k} - S_-u^T_{i,j,k})/\Delta\xi \tag{2.123}$$

where $u^T \equiv Hu\sqrt{g_o}$.

if $u^T_{i+1,j,k} \geq 0$

$$S_+ = S_{i,j,k} \tag{2.124}$$

if $u^T_{i+1,j,k} < 0$

$$S_+ = S_{i+1,j,k} \tag{2.125}$$

Thus

$$S_+ u^T_{i+1,j,k} = \frac{1}{2}\left(u^T_{i+1,j,k} + |u^T i+1,j,k|\right) S_{i,j,k} + \frac{1}{2}\left(u^T_{i+1,j,k} - |u^T_{i+1,j,k}|\right) S_{i+1,j,k} \quad (2.126)$$

Likewise,

$$S_- u^T_{i,j,k} = \frac{1}{2}\left(u^T_{i,j,k} + |u^T_{i,j,k}|\right) S_{i-1,j,k} + \frac{1}{2}\left(u^T_{i,j,k} - |u^T_{i,j,k}|\right) S_{i,j,k} \quad (2.127)$$

3. Combined Central-Upwind Difference Option

The combined central and upwind option gives the advantages of central and upwind options together, but minimizes the disadvantages. The combined option is, however, more computationally demanding. The finite-difference form is

$$\frac{\partial}{\partial \xi}(Hu S\sqrt{g_o}) = (S_+ u^T_{i+1,j,k} - S_- u^T_{i,j,k})/\Delta\xi \quad (2.128)$$

where $u^T \equiv Hu\sqrt{g_o}$.

$$\text{if } u^T_{i,j,k} > 0 \text{ and } S_{i,j,k} > S_{i+1,j,k} \quad : \quad S_+ = \frac{c_{i,j,k} + c_{i+1,j,k}}{2} \quad (2.129)$$

$$\text{if } u^T_{i,j,k} > 0 \text{ and } S_{i,j,k} < S_{i+1,j,k} \quad : \quad S_+ = S_{i,j,k} \quad (2.130)$$

$$\text{if } u^T_{i,j,k} < 0 \text{ and } S_{i,j,k} > S_{i+1,j,k} \quad : \quad S_+ = S_{i+1,j,k} \quad (2.131)$$

$$\text{if } u^T_{i,j,k} < 0 \text{ and } S_{i,j,k} < S_{i+1,j,k} \quad : \quad S_+ = \frac{S_{i,j,k} + S_{i+1,j,k}}{2} \quad (2.132)$$

4. Higher Order Advective Schemes

To improve the accuracy of advective terms in the numerical model, it is possible to use higher order advective schemes which have formal truncation errors that are third order or fourth order in Δx. For example, Sheng (1983) applied the Flux-Corrected-Transport (FCT) scheme (Zalesak, 1979) to simulate the advection and diffusion of salinity and suspended sediments by wind-driven currents, and compared

the performance of the FCT scheme versus the three advective schemes discussed above. The performance of the combined central upwind option was found to be quite comparable to that of the FCT scheme. More recently, Johnson *et al.* (1989) applied the QUICKEST scheme developed by Leonard (1979) to the curvilinear grid, and obtained improved results when the z-grid version of CH3D was used. Sheng *et al.* (1989) found that, when a σ-grid model is used, higher-order advective schemes should be avoided in regions of sharp bathymetric gradient when insufficient grid points exist to resolve the sharp gradient.

The higher-order schemes have been primarily applied to solve the advection and diffusion equations but not to solve the Navier-Stokes equations. Several other higher-order schemes can be used to improve the accuracy of advective terms. The application of higher-order advective schemes requires additional programming and computational effort, due to the fact that a differencing formula involving four or five points is needed to represent the first-order derivative term.

The QUICKEST scheme used for this study has third order accuracy. This method uses cubic upstream-weighted interpolation with five points of $i-2, i-1, i, i+1$,and $i+2$. Because this is a five-point interpolation the fluxes near boundaries must be calculated using lower order schemes.

The finite difference equations for advection terms using the QUICKEST scheme are in ξ-direction,

$$
\begin{aligned}
\frac{\partial}{\partial \xi}\left(HuS\sqrt{g_o}\right) &= \left(u_{i+1,j,k} - |u_{i+1,j,k}|\right)\frac{1}{2}\left(S_{i,j,k} + S_{i+1,j,k}\right) \\
&- \frac{1}{6}\left(1 - \left(u_{i+1,j,k}\Delta t\right)^2\right)\left(S_{i+2,j,k} - 2S_{i+1,j,k} + S_{i,j,k}\right) \\
&- \frac{1}{2}u_{i+1,j,k}\Delta t\left(S_{i+1,j,k} - S_{i,j,k}\right) \\
&+ \left(u_{i+1,j,k} + |u_{i+1,j,k}|\right)\frac{1}{2}\left(S_{i,j,k} + S_{i+1,j,k}\right) \\
&- \frac{1}{6}\left(1 - \left(u_{i+1,j,k}\Delta t\right)^2\right)\left(S_{i+1,j,k} - 2S_{i,j,k} + S_{i-1,j,k}\right) \\
&- \frac{1}{2}u_{i+1,j,k}\Delta t\left(S_{i+1,j,k} - S_{i,j,k}\right)\frac{1}{2}\sqrt{g_{o_{i+1,j,U}}}H_{i+1,j,U}
\end{aligned}
$$

$$
\begin{aligned}
&- \ (u_{i,j,k} - |u_{i,j,k}|)\,\frac{1}{2}\,(S_{i-1,j,k} + S_{i,j,k}) \\
&- \ \frac{1}{6}\left(1 - (u_{i,j,k}\Delta t)^2\right)(S_{i+1,j,k} - 2S_{i,j,k} + S_{i-1,j,k}) \\
&- \ \frac{1}{2}u_{i,j,k}\Delta t\,(S_{i,j,k} - S_{i-1,j,k}) \\
&+ \ (u_{i,j,k} + |u_{i,j,k}|)\,\frac{1}{2}\,(S_{i-1,j,k} + S_{i,j,k}) \\
&- \ \frac{1}{6}\left(1 - (u_{i,j,k}\Delta t)^2\right)(S_{i,j,k} - 2S_{i-1,j,k} + S_{i-2,j,k}) \\
&- \ \frac{1}{2}u_{i,j,k}\Delta t\,(S_{i,j,k} - S_{i-1,j,k})\,\frac{1}{2}\sqrt{g_{o_{i,j,U}}}H_{i,j,U}\frac{1}{\sqrt{g_{o_{i,j,\zeta}}}H_{i,j,\zeta}}
\end{aligned}
\tag{2.133}
$$

and in the η-direction,

$$
\begin{aligned}
\frac{\partial}{\partial\xi}\left(Hv\sqrt{g_o}\right) \ = \ &(v_{i+1,j,k} - |v_{i+1,j,k}|)\,\frac{1}{2}\,(S_{i,j,k} + S_{i+1,j,k}) \\
&- \ \frac{1}{6}\left(1 - (v_{i+1,j,k}\Delta t)^2\right)(S_{i+2,j,k} - 2S_{i+1,j,k} + S_{i,j,k}) \\
&- \ \frac{1}{2}v_{i+1,j,k}\Delta t\,(S_{i+1,j,k} - S_{i,j,k}) \\
&+ \ (v_{i+1,j,k} + |v_{i+1,j,k}|)\,\frac{1}{2}\,(S_{i,j,k} + S_{i+1,j,k}) \\
&- \ \frac{1}{6}\left(1 - (v_{i+1,j,k}\Delta t)^2\right)(S_{i+1,j,k} - 2S_{i,j,k} + S_{i-1,j,k}) \\
&- \ \frac{1}{2}v_{i+1,j,k}\Delta t\,(S_{i+1,j,k} - S_{i,j,k})\,\frac{1}{2}\sqrt{g_{o_{i+1,j,V}}}H_{i+1,j,V} \\
&- \ (v_{i,j,k} - |v_{i,j,k}|)\,\frac{1}{2}\,(S_{i-1,j,k} + S_{i,j,k}) \\
&- \ \frac{1}{6}\left(1 - (v_{i,j,k}\Delta t)^2\right)(S_{i+1,j,k} - 2S_{i,j,k} + S_{i-1,j,k}) \\
&- \ \frac{1}{2}v_{i,j,k}\Delta t\,(S_{i,j,k} - S_{i-1,j,k}) \\
&+ \ (v_{i,j,k} + |v_{i,j,k}|)\,\frac{1}{2}\,(S_{i-1,j,k} + S_{i,j,k}) \\
&- \ \frac{1}{6}\left(1 - (v_{i,j,k}\Delta t)^2\right)(S_{i,j,k} - 2S_{i-1,j,k} + S_{i-2,j,k}) \\
&- \ \frac{1}{2}v_{i,j,k}\Delta t\,(S_{i,j,k} - S_{i-1,j,k})\,\frac{1}{2}\sqrt{g_{o_{i,j,V}}}H_{i,j,V}\frac{1}{\sqrt{g_{o_{i,j,\zeta}}}H_{i,j,\zeta}}
\end{aligned}
\tag{2.134}
$$

2.9.7 Horizontal Diffusion Terms

The finite-difference form of the horizontal gradient in the horizontal diffusion terms is the standard second-order divided difference. There is no need to treat the horizontal diffusion terms implicitly because the time step constraint associated with

them are usually much larger than that allowed by the advection terms.

$$g^{11}\frac{\partial^2 S}{\partial \xi^2} = g^{11} \cdot \frac{S_{i+1,j,k} - 2S_{i,j,k} + S_{i-1,j,k}}{(\Delta\xi)^2} \tag{2.135}$$

(2.136)

$$\begin{aligned} g^{12}\frac{\partial^2 S}{\partial \xi \partial \eta} &= g^{12}\left[(S_{i+1/2,j+1/2,k} - S_{i+1/2,j-1/2,k}) \right. \\ &- \left. (S_{i-1/2,j+1/2,k}) - S_{i-1/2,j-1/2,k} - S_{i-1/2,j-1/2,k})\right] / \Delta\xi\Delta\eta \end{aligned} \tag{2.137}$$

$$g^{22}\frac{\partial^2 S}{\partial \eta^2} = g^{22} \cdot \frac{S_{i,j+1,k} - 2S_{i,j,k} + S_{i,j-1,k}}{(\Delta\eta)^2} \tag{2.138}$$

2.9.8 Numerical Stability

Since the numerical scheme used here is not fully implicit, the time step of numerical computation cannot exceed the limits associated with the advection terms, the Coriolis terms, the baroclinic pressure gradient terms, and the horizontal diffusion terms

$$\begin{aligned} (\Delta t)_{\text{advection}} &\leq \frac{1}{(\frac{|u|}{\Delta x}) + \frac{|v|}{\Delta y} + \frac{|w|}{\Delta z})} \\ (\Delta t)_{\text{Coriolis}} &\leq 1/f \\ (\Delta t)_{\text{baroclinic}} &\leq \frac{1}{\sqrt{\frac{\Delta\rho}{\rho} g H_{max}(\frac{1}{\Delta x} + \frac{1}{\Delta y})_{max}}} \\ (\Delta t)_{\text{diffusion}} &\leq \frac{1}{2A_H\left[\frac{1}{(\Delta x)^2} + \frac{1}{(\Delta y)^2}\right]_{max}} \end{aligned} \tag{2.139}$$

If the allowable internal time step according to the above equations is much (10 to 100 times) larger than the Δt allowed by the surface gravity wave as shown in Equation (2.139), then it is feasible to use a small time step for the internal mode (Δt_i). If the difference between the allowable internal time step is only a few times larger than the external step, then it is better to simply use the same Δt_e and Δt_i. The selection of time step is still very much an "art" because all the time step limits

are based on stability analysis which is strictly valid only in a linear system without considering the effects of nonlinearity and boundary conditions.

2.10 Turbulence Model for Mass and Momentum Exchange Coefficients

Various models are available to parameterize the vertical turbulent mixing of momentum, heat, and salinity in the water column. For reviews of turbulence models, the readers are referred to Lewellen (1977), Rodi (1980), Mellor and Yamada(1982), and Sheng (1986). The starting point of a turbulence model is to derive the mean flow equations from the conservation equations for mass, momentum, energy, and species. For incompressible flows, conservation equations can be written in tensor notation as

$$\frac{\partial u_i}{\partial x_i} = 0 \tag{2.140}$$

$$\frac{\partial u_i}{\partial t} + u_j \frac{\partial u_i}{\partial x_j} = -\frac{1}{\rho_0}\frac{\partial p}{\partial x_i} + g_i \frac{(\rho - \rho_o)}{\rho_o} - 2\varepsilon_{ijk}\Omega_j u_k + \frac{\partial}{\partial x_j}\left(\nu \frac{\partial u_i}{\partial x_j}\right) \tag{2.141}$$

$$\frac{\partial \phi}{\partial t} + u_j \frac{\partial \phi}{\partial x_j} = +\frac{\partial}{\partial x_j}\left(k \frac{\partial \phi}{\partial x_j}\right) \tag{2.142}$$

where ϕ is either density or temperature or salinity, ρ is density, ρ_0 is reference density, ε_{ijk} is the permutation tensor, Ω_j is the rotational speed of earth, and ν and k are the molecular viscosity and diffusivity.

When the variables are separated into mean and fluctuating quantities, the mean flow equations can be written as

$$\frac{\partial \overline{u_i}}{\partial x_i} = 0 \tag{2.143}$$

$$\begin{aligned} \frac{\partial \overline{u_i}}{\partial t} + \overline{u_j}\frac{\partial \overline{u_i}}{\partial x_j} &= -\frac{\partial \overline{u_i' u_j'}}{\partial x_j} - \frac{1}{\rho_0}\frac{\partial \overline{p}}{\partial x_i} + g_i \frac{(\rho - \rho_o)}{\rho_o} \\ &- 2\varepsilon_{ijk}\Omega_j \overline{u_k} + \frac{\partial}{\partial x_j}\left(\nu \frac{\partial \overline{u_i}}{\partial x_j}\right) \end{aligned} \tag{2.144}$$

$$\frac{\partial \overline{\phi}}{\partial t} + \overline{u_j}\frac{\partial \overline{\phi}}{\partial x_j} = -\frac{\partial \overline{u_j' \phi'}}{\partial x_j} + \frac{\partial}{\partial x_j}\left(k \frac{\partial \overline{\phi}}{\partial x_j}\right) \tag{2.145}$$

where $\overline{u_i}$, $\overline{u_j}$, and $\overline{u_k}$ are the mean velocity components, u_i' and u_j' are the fluctuating velocity components, $\overline{\phi}$ and ϕ' are the mean and fluctuating temperature or salinity, and $\overline{p}$ is the mean pressure. This system of equations is not closed because of the Reynolds stress terms.

Basically, turbulence models can be classified as eddy viscosity models and second-order closure models. The eddy viscosity models assume the turbulent Reynolds stresses to be the products of mean velocity gradients and "eddy viscosities," and the turbulent heat and mass fluxes to be the products of mean temperature and concentration gradients and "eddy diffusitivities"

$$-\overline{u_i'u_j'} = A_t\left(\frac{\partial\overline{u_i}}{\partial x_j} + \frac{\partial\overline{u_j}}{\partial x_i}\right) - \frac{q^2}{3}\delta_{ij} \tag{2.146}$$

$$-\overline{u_i'\phi'} = K_t\frac{\partial\overline{\phi}}{\partial x_i} \tag{2.147}$$

where $q^2 = \overline{u_i'u_i'}$, and A_t and K_t are turbulent eddy viscosity and diffusivity, respectively.

The eddy coefficients are assumed to be certain known functions of, for example, mean flow parameters (Munk and Anderson, 1948), depths and wind speeds. These functions, however, are difficult to determine and are often *ad-hoc* in nature, and hence may have to be adjusted for application to a new site or a new flow situation. Obviously, this limits the "predictability" of the hydrodynamics model.

The second-order closure models, on the other hand, resolve the dynamics of turbulence by including the differential transport equations for the turbulence variables; i.e., the second-order correlations ($-\overline{u_i'u_j'}$, $-\overline{u_i'\phi'}$ and $\overline{\phi'\phi'}$). In the most complicated case, i.e., the Reynolds stress model, differential transport equations are solved (Lewellen, 1977; Sheng,1982; Sheng and Villaret, 1989). The time averaged momentum equations are subtracted from the instantaneous Navier-Stokes equations to produce the primed-variable equations. The resulting equation for the i-component is multiplied by u_j', and j- component equation by u_i'. Adding two equations and

averaging by time, gives the $\overline{u_i' u_j'}$–equation.

$$\begin{aligned}\frac{\partial \overline{u_i' u_j'}}{\partial t} &+ \overline{u_k}\frac{\partial \overline{u_i' u_j'}}{\partial x_k} = -\overline{u_i' u_k'}\frac{\partial \overline{u_j}}{\partial x_k} - \overline{u_j' u_k'}\frac{\partial \overline{u_i}}{\partial x_k} + g_i\frac{\overline{u_j'\phi'}}{\overline{\phi}} + g_j\frac{\overline{u_i'\phi'}}{\overline{\phi}} \\ &- 2\varepsilon_{ikl}\Omega_k\overline{u_l' u_j'} - 2\varepsilon_{jlk}\Omega_l\overline{u_k' u_i'} - \frac{\partial}{\partial x_k}(\overline{u_k' u_i' u_j'}) \\ &- \frac{\overline{u_i'}}{\rho_0}\frac{\partial \overline{p'}}{\partial x_j} - \frac{\overline{u_j'}}{\rho_0}\frac{\partial \overline{p'}}{\partial x_i} + \nu\frac{\partial^2 \overline{u_i' u_j'}}{\partial x_k^2} - 2\nu\overline{\frac{\partial u_i'}{\partial x_k}\frac{\partial u_j'}{\partial x_k}} \end{aligned} \tag{2.148}$$

$$\begin{aligned}\frac{\partial \overline{u_i'\phi'}}{\partial t} + \overline{u_j}\frac{\partial \overline{u_i\phi'}}{\partial x_j} &= -\overline{u_i' u_j'}\frac{\partial \overline{\phi}}{\partial x_j} - \overline{u_j'\phi'}\frac{\partial \overline{u_i}}{\partial x_j} + g_i\frac{\overline{\phi'\phi'}}{\overline{\phi}} - 2\varepsilon_{ijk}\Omega_j\overline{u_k'\phi'} \\ &- \frac{\partial \overline{u_i' u_j'\phi'}}{\partial x_j} - \frac{\overline{\phi'}}{\rho_0}\frac{\partial \overline{p'}}{\partial x_i} - \nu\phi'\frac{\partial^2 \overline{u_i'}}{\partial x_j^2} - k u_i'\frac{\partial^2 \overline{\phi'}}{\partial x_j^2} \end{aligned} \tag{2.149}$$

$$\begin{aligned}\frac{\partial \overline{\phi'\phi'}}{\partial t} + \overline{u_j}\frac{\partial \overline{\phi'\phi'}}{\partial x_j} = -2\overline{u_j'\phi'}\frac{\partial \overline{\phi}}{\partial x_j} &- \frac{\partial}{\partial x_k}(\overline{u_j'\phi'\phi'}) \\ &+ k\frac{\partial^2 \overline{\phi'\phi'}}{\partial x_j^2} - 2k\overline{\frac{\partial \phi'}{\partial x_j}\frac{\partial \phi'}{\partial x_j}} \end{aligned} \tag{2.150}$$

where x_i are coordinate axes, t is time, $(\overline{u_i}, \overline{u_j}, \overline{u_k})$ are the mean velocity components, (u_i', u_j', u_k') are the fluctuating velocity components, $\overline{\phi}$ and ϕ' are the mean and fluctuating values of density or temperature or salinity, ε_{ijk} is the alternating tensor, and Ω is earth rotation.

The above system of equations is not closed since each equation contains unknown terms. Following the second-order closure model described in Lewellen (1977) and

Sheng (1982), the above equations are replaced by the following equations.

$$
\begin{aligned}
\frac{\partial \overline{u_i' u_j'}}{\partial t} + \overline{u_k}\frac{\partial \overline{u_i' u_j'}}{\partial x_k} &= && \text{(Evolution)} \\
&- && \overline{u_i' u_k'}\frac{\partial \overline{u_j}}{\partial x_k} - \overline{u_j' u_k'}\frac{\partial \overline{u_i}}{\partial x_k} && \text{(Production)} \\
&+ && g_i \frac{\overline{u_j' \phi'}}{\phi} + g_j \frac{\overline{u_i' \phi'}}{\phi} && \text{(Buoyancy)} \\
&- && 2\varepsilon_{ikl}\Omega_k \overline{u_j' u_l'} - 2\varepsilon_{jlk}\Omega_l \overline{u_k' u_i'} && \text{(Rotation)} \\
&+ && v_c \frac{\partial}{\partial x_k}\left(q\Lambda \frac{\partial \overline{u_i' u_j'}}{\partial x_k}\right) && \text{(Diffusion)} \\
&- && \frac{q}{\Lambda}\left(\overline{u_i' u_j'} - \delta_{ij}\frac{q^2}{3}\right) && \text{(Tendency)} \\
&- && \delta_{ij}\frac{2bq^3}{12\Lambda} - \frac{2a\nu \overline{u_i' u_j'}}{\Lambda^2} && \text{(Dissipation)}
\end{aligned}
\tag{2.151}
$$

$$
\begin{aligned}
\frac{\partial \overline{u_i' \phi'}}{\partial t} + \overline{u_j}\frac{\partial \overline{u_i' \phi'}}{\partial x_j} &= && \text{(Evolution)} \\
&- && \overline{u_i' u_j'}\frac{\partial \Phi}{\partial x_i} - \overline{\phi' u_j'}\frac{\partial u_i}{\partial x_j} && \text{(Production)} \\
&+ && g_i \frac{\overline{\phi' \phi'}}{\phi} && \text{(Buoyancy)} \\
&- && 2\varepsilon_{ijk}\Omega_j \overline{u_k' \phi'} && \text{(Rotation)} \\
&+ && v_c \frac{\partial}{\partial x_j}\left(q\Lambda \frac{\partial \overline{u_i' \phi'}}{\partial x_j}\right) && \text{(Diffusion)} \\
&- && \frac{A_q}{\Lambda}\overline{u_i' \phi'} - \frac{2a\nu}{\Lambda^2}\overline{u_i' \phi'} && \text{(Dissipation)}
\end{aligned}
\tag{2.152}
$$

$$
\begin{aligned}
\frac{\partial \overline{\phi' \phi'}}{\partial t} + \overline{u_j}\frac{\partial \overline{\phi' \phi'}}{\partial x_j} &= && \text{(Evolution)} \\
&- && 2\overline{u_j' \phi'}\frac{\partial \overline{\phi}}{\partial x_j} && \text{(Production)} \\
&+ && v_c \frac{\partial}{\partial x_j}\left(q\Lambda \frac{\partial \overline{\phi' \phi'}}{\partial x_j}\right) && \text{(Diffusion)} \\
&- && \frac{2bsq}{\Lambda}\overline{\phi' \phi'} - \frac{2a s\nu}{\Lambda}\overline{\phi' \phi'} && \text{(Dissipation)}
\end{aligned}
\tag{2.153}
$$

where δ_{ij} is the Kronecker delta, $q = (\overline{u_i' u_i'})^{1/2}$ is the total rms fluctuating velocity, and Λ is the turbulence macroscale which is a measure of the average turbulent eddy size. A total of five model coefficients: a, A, b, v_c, and s are contained in the above equations. By matching model results to data from critical laboratory experiments

where only one or two of the turbulent transport processes are important, these model constants were found to be (Lewellen, 1977) $a = 2.5, A = 0.75, b = 0.125, v_c = 0.3$ and $s = 1.8$. An additional equation for Λ is needed to close the system.

The present study tested several methods for calculating the vertical turbulent eddy coefficients: (1) constant eddy coefficients, (2) Munk-Anderson type eddy coefficients, (3) a simplified second-order closure model of turbulent transport, i.e., the equilibrium closure model, and (4) another simplified second-order closure model, i.e., the turbulent kinetic energy (TKE) closure model. These methods are discussed in the following.

- Constant Eddy Coefficients

Constant eddy coefficients are generally used in preliminary model runs. The rule of thumb is that the vertical eddy coefficients should increase with increasing wind stress and/or tidal amplitude. Coefficients can be adjusted until a reasonable fit exists between model results and data. In the absence of data, however, it is difficult to adjust the constant eddy coefficients to give good results.

- Munk-Anderson Type Eddy Coefficients

In non-stratified flow situations, a variable eddy coefficient of the following form is used

$$A_{v_o} = \frac{Z_r U_r \Lambda_o^2}{H} \left[\left(\frac{\partial u}{\partial \sigma} \right)^2 + \left(\frac{\partial v}{\partial \sigma} \right)^2 \right]^{1/2} \tag{2.154}$$

where u and v are dimensionless horizontal velocities, the turbulence macroscale Λ_o is assumed to be a linear function of σ, increasing with distance above the bottom or below the free surface, and with its peak value at mid-depth not exceeding a certain fraction of the local depth. In the presence of strong waves, turbulent mixing in

the upper layers may be significantly enhanced. In such a case, the length scale Λ_o throughout the upper layers may be assumed to be equal to the maximum value at mid-depth.

In stratified flow situations, the effect of buoyancy on eddy coefficients can be parameterized in terms of several Richardson number-dependent stability functions

$$A_v = A_{vo}\phi_1(Ri); \quad K_v = K_{vo}\phi_2(Ri); \quad D_v = D_{vo}\phi_2(Ri) \tag{2.155}$$

where

$$Ri = \frac{-gHZ_r\varepsilon}{U_r^2(1+\varepsilon\rho)}\frac{\partial\rho}{\partial\sigma}\left[\left(\frac{\partial u}{\partial\sigma}\right)^2 + \left(\frac{\partial v}{\partial\sigma}\right)^2\right]^{-1} \tag{2.156}$$

where A_{vo}, K_{vo}, and D_{vo} are eddy coefficients in the absence of any density stratification, and ϕ_1 and ϕ_2 are stability functions traditionally assumed to be of the following forms

$$\phi_1 = (1+\alpha_1\, Ri)^{\beta_1}; \quad \phi_2 = (1+\alpha_2\, Ri)^{\beta_2} \tag{2.157}$$

As discussed by Sheng (1983), there exist great discrepancies among the many existing empirical forms of the stability functions. To determine the coefficients in these stability functions, one needs sufficient data to achieve the "best fit" between modeled and measured results. As such, the specific formulae and coefficients will vary with the problem, the environment, and the available data. Munk and Anderson (1948) used the following formula in a study of the marine thermocline

$$\phi_1 = (1+10Ri)^{-1/2}; \quad \phi_2 = (1+3.33Ri)^{-3/2} \tag{2.158}$$

Others (Kent and Pritchard, 1959; Blumberg, 1975; Bowden and Hamilton, 1975) used ϕ_1 and ϕ_2 in the form of Equation (2.157) but with coefficients different from those in Equation (2.158). Not only the form of the stability function may vary with the problem, but different Richardson numbers may also be used for different types of problems. For example, the formation and deepening of the thermocline in

a relatively shallow basin depends strongly on the relative importance of wind stress and heat flux at the free surface. In such a case, the following Richardson number could be used

$$Ri = \frac{\kappa^2 g H Z_r \sigma^2 \varepsilon}{U_r^2 u_*^2 (1+\varepsilon\rho)} \frac{\partial \rho}{\partial \sigma} \tag{2.159}$$

where κ is the von-Karman constant, and u_* is the dimensionless friction velocity at the free surface.

- A Simplified Second-Order Closure Model: The Equilibrium Closure Model

An equilibrium closure model (Sheng, 1985; Sheng and Chiu, 1986; Sheng *et al.*, 1989) has been used to compute the vertical turbulence. As discussed before, the local equilibrium condition is valid when the time scale of mean flow is much larger than that for turbulence and when turbulence varies little over the turbulence macroscale. In this case, the evolution terms and the diffusion terms in Equations (2.151)-(2.153) become negligible with respect to other terms. The equilibrium closure model is significantly simpler than the complete second-order closure model (Reynolds stress model) and has been found to give very good results in mean flow, salinity and temperature with little or no tuning of model coefficients.

In addition to the mean flow equations, a set of algebraic equations are solved for the second-order correlation quantities to obtain the stability functions ϕ_1 and ϕ_2 in terms of the mean flow variables. These equations, when written in dimensional and tensor forms, are

$$\begin{aligned} 0 &= -\overline{u_i' u_k'} \frac{\partial \overline{u_j}}{\partial x_k} - \overline{u_j' u_k'} \frac{\partial \overline{u_i}}{\partial x_k} + g_i \frac{\overline{u_j' \rho'}}{\rho_o} + g_j \frac{\overline{u_i' \rho}}{\rho_o} \\ &- 2\varepsilon_{ikt}\Omega_k \overline{u_\ell' u_j'} - 2\varepsilon_{jkt}\Omega_\ell \overline{u_k' u_i'} \\ &- \frac{q}{\Lambda}\left(\overline{u_i' u_j'} - \delta_{ij}\frac{q^2}{3}\right) - \delta_{ij}\frac{q^3}{12\Lambda} \end{aligned} \tag{2.160}$$

$$0 = - \overline{u_i' u_j'} \frac{\partial \overline{\rho}}{\partial x_j} - \overline{u_j' \rho'} \frac{\partial \overline{u_i}}{\partial x_j} - \frac{g_i \overline{\rho' \rho'}}{\rho_o} - 2\varepsilon_{ijk}\Omega_j \overline{u_k' \rho'} - 0.75 q \frac{\overline{u_i' \rho'}}{\Lambda} \tag{2.161}$$

$$0 = 2\overline{u_j' \rho'} \frac{\partial \overline{\rho}}{\partial x_j} + \frac{0.45 q \overline{\rho' \rho'}}{\Lambda} \tag{2.162}$$

where the subscripts i, j, k can take on the values of 1, 2, or 3. Hence Equation (2.160) represents six equations and Equation (2.161) represents three equations in general. A total of five model coefficients are contained in the above equations. These coefficients were determined from comparing model results with data from critical laboratory experiments where only one or two of the turbulent transport processes are dominant. These coefficients remained "invariant" in application of the equilibrium closure model, the kinetic energy closure model (Sheng and Villaret, 1989) and the Reynolds stress model (Sheng, 1982; Sheng, 1984; Sheng and Villaret, 1989). A graphical comparison of this formulation versus some empirical formulae is shown in Figure 2.10.

As shown in Sheng *et al.* (1989), q^2 can be determined from the following dimensional equations when mean flow variables are known

$$3A^2 b^2 s Q^4 + A[(bs + 3b + 7b^2 s)\, Ri - Abs(1 - 2b)]Q^2 + b(s + 3 + 4bs)\, Ri^2 + (bs - A)(1 - 2b)\, Ri = 0 \tag{2.163}$$

where A, b, and s are model constants, Ri is the Richardson number and

$$q = Q\Lambda \sqrt{\left(\frac{\partial u}{\partial z}\right)^2 + \left(\frac{\partial v}{\partial z}\right)^2} \tag{2.164}$$

Once q^2 are computed, the vertical eddy coefficients can be computed from

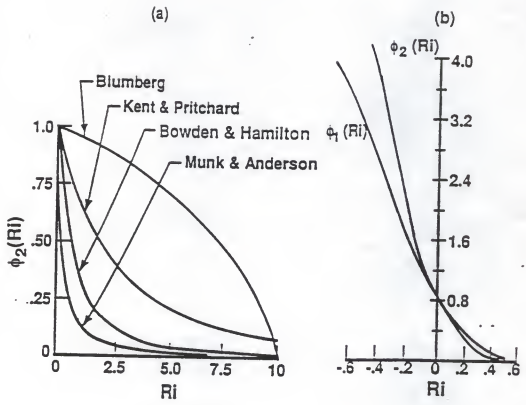

Figure 2.6: Comparison of stability functions for (a) some epirical formulae versus (b) the simplified second-order closure model (From Sheng, 1983).

$$A_v = \frac{A + \bar{w}\overline{w'w'}}{A - wq_2}\Lambda q \tag{2.165}$$

$$K_v = \frac{bs}{(bs - w)A}\frac{\overline{w'w'}}{q^2}\Lambda q \tag{2.166}$$

where

$$w = Ri/(AQ^2) \tag{2.167}$$

$$\bar{w} = w/(1 - w/bs) \tag{2.168}$$

$$\overline{w'w'} = \frac{1 - 2b}{3(1 - 2\bar{w})}q^2 \tag{2.169}$$

In the complete second-order closure model, a differential transport equation for the turbulent macroscale Λ is derived. The equation is

$$\begin{aligned}\frac{\partial \Lambda}{\partial t} + u_j\frac{\partial \Lambda}{\partial x_j} &= 0.35\frac{\Lambda}{q^2}\overline{u_i'u_j'}\frac{\partial u_i}{\partial x_j} + 0.75q + 0.3\frac{\partial}{\partial x_i}(\frac{\partial \Lambda}{\partial x_i}) \\ &- \frac{0.375}{q}(\frac{\partial q\Lambda}{\partial x_i})^2 + \frac{0.8\Lambda}{q^2}g_i\frac{\overline{u_i'\phi'}}{\Phi}\end{aligned} \tag{2.170}$$

However, the Λ equation contains four model coefficients that must be calibrated with experimental data. For ease of application but without loss of generality, the turbulent macroscale Λ is assumed to satisfy a number of integral constraints. First of all, Λ is assumed to be a linear function of vertical distance immediately above the bottom or below the free surface. In addition, the turbulent macroscale Λ must satisfy the following relationships (Sheng and Chiu, 1986; Sheng *et al.*, 1989)

$$\left|\frac{d\Lambda}{dz}\right| \leq 0.65 \tag{2.171}$$

$$\Lambda \leq C_1 \cdot H \tag{2.172}$$

$$\Lambda \leq C_1 \cdot H_p \tag{2.173}$$

$$\Lambda \leq C_2 \cdot \delta_{q^2} \tag{2.174}$$

$$\Lambda \leq \frac{q}{N} \tag{2.175}$$

where C_1 is a number usually within the range of 0.1 to 0.25; H is the total depth; H_p is the depth of the pycnocline; C_2, which is between 0.1 and 0.25, is the fractional cut-off limitation of turbulent macroscale based on δ_{q^2}, the spread of turbulence determined from the turbulent kinetic energy (q^2) profile; and N is the Brunt-Väisäla frequency defined as

$$N = \left(-\frac{g}{\rho} \frac{\partial \rho}{\partial z} \right)^{1/2} \tag{2.176}$$

Although the simplified second-order closure model presented above is strictly valid when the turbulence time scale (Λ/q) is much less than the mean flow time scale and when turbulence does not change rapidly over Λ, it has been found to be quite successful in simulating vertical flow structures in estuarine and coastal waters. Recent simulations of wind-induced mixing of salinity in Chesapeake Bay (Sheng *et al.*, 1989a; Johnson *et al.*, 1989) and wind-driven circulation and sediment transport in Lake Okeechobee (Sheng *et al.*, 1989b) gave good results with little or no tuning of model coefficients.

- Turbulent Kinetic Energy (TKE) Closure Model

A simplified TKE closure model (Sheng and Villaret, 1989) has been used to compute the vertical turbulence. When the time scale of the mean flow evolution is much greater than the time scale of turbulence (Λ/q), the evolution terms and the diffusion

terms in the second-order closure model become negligible with respect to other terms. Instead of calculating q^2 by algebraic equations, q^2 is obtained in a dynamic equation

$$\begin{aligned}\frac{\partial q^2}{\partial t}+\overline{u_k}\frac{\partial q^2}{\partial x_k} &= -2\overline{u_i'u_k'}\frac{\partial \overline{u_i}}{\partial x_k}+2g_i\frac{\overline{u_i'\phi'}}{\overline{\phi}} \\ &+ 0.3\frac{\partial}{\partial x_k}(q\Lambda\frac{\partial q^2}{\partial x_k})-\frac{q^3}{4\Lambda} \end{aligned} \tag{2.177}$$

In the one-dimensional vertical case of the σ-grid, the equation is

$$\begin{aligned}\frac{\partial q^2}{\partial t}+\frac{1}{H}\frac{\partial Huq^2}{\partial x} &+ \frac{\partial \omega q^2}{H\partial\sigma}=\frac{1}{H^2}\frac{\partial}{\partial\sigma}(0.3q\Lambda\frac{\partial q^2}{\partial\sigma}) \\ &+ 2\frac{A_v}{H^2}(\frac{\partial u}{\partial\sigma})^2+\frac{2gK_v}{\overline{\phi}H}\frac{\partial\rho}{\partial\sigma}-\frac{q^3}{4\Lambda} \end{aligned} \tag{2.178}$$

Applying the rules in section 2.3, nondimensionalization of the above equation gives (all the variables are now nondimensional)

$$\begin{aligned}\frac{\partial q^2}{\partial t}+\frac{Ro}{H}\frac{\partial Huq^2}{\partial x} &+ \frac{Ro_v\partial\omega q^2}{H\partial\sigma}=\frac{1}{H^2}\frac{\partial}{\partial\sigma}(0.3q\Lambda\frac{\partial q^2}{\partial\sigma}) \\ &+ 2\frac{E_vA_v}{H^2}(\frac{\partial u}{\partial\sigma})^2+\frac{2E_vK_v}{Fr_b^2H}\frac{\partial\rho}{\partial\sigma}-Ro_v\frac{q^3}{4\Lambda} \end{aligned} \tag{2.179}$$

where A_v and K_v are nondimensionalized with A_{vr}, $Ro_v=U_r/fZ_r$ is a vertical type Rossby number, and $E_v=A_{vr}/fZ_r^2$.

Again, integral constraints for Λ are used as the equilibrium closure model.

CHAPTER 3
MODEL ANALYTICAL TEST: COMPARISON BETWEEN MODEL RESULTS AND ANALYTIC SOLUTIONS

When numerical models are used to simulate circulation and transport in realistic estuarine environments, it is common to find discrepancies between numerical results and data. The discrepancies often result from a variety of errors: errors associated with measurement, errors associated with the formulation of the physical problem (e.g., dimensionality, turbulence closure scheme, moving boundary scheme, etc.), errors associated with the formulation of the numerical problem (e.g., finite-difference schemes or finite-element schemes for various terms of the governing equations), and errors associated with the computer and programming (e.g., computer round-off error and programming error). Before the model is applied to a realistic estuary, it is necessary to test and improve the numerical accuracy of the various numerical schemes used in the model. This chapter presents a study on the numerical accuracy of the three-dimensional hydrodynamic model by comparing model results with a number of analytic solutions describing the circulation in idealized basins forced by a constant surface slope, seiche, tide, wind, and density gradients.

3.1 Forced Constant Surface Slope

The first test considers the steady-state response of a water body in a rectangular basin forced by constant surface slope with uniform density. At steady state, the surface slope balances the bottom stress. Assuming one-dimensional flow with the quadratic bottom friction, the governing equation is given as

$$-gh\frac{\partial \zeta}{\partial x} = C_d \mid u \mid u \tag{3.1}$$

with boundary conditions $\zeta = a$ at $x = 0$, and $\zeta = -a$ at $x = l$ (Figure 3.1), where u is the vertically-averaged velocity, ζ is surface elevation above mean sea level, h is water depth, g is gravitational acceleration ($= 981\ cm/s^2$), l is the basin length, and C_d is the bottom friction factor. A non-uniform rectangular grid as shown in Figure 3.1 was used. The basin is open at the left and right ends. Model simulation was started with zero elevation and velocity initially. Model tests were performed for the cases of linear bottom friction and quadratic bottom friction. The following parameter values were used

$$\begin{aligned} a &= 25\ cm \\ l = \text{basin length} &= 62\ km \\ \text{basin width} &= 14\ km \\ h &= 10\ m \\ C_d &= \begin{cases} 0.003 \text{ for quadratic bottom friction} \\ 0.3 \text{ for linear bottom friction} \end{cases} \end{aligned} \tag{3.2}$$

According to Equation (3.1), the steady state velocity was found to be $u = 52.17\ cm/sec$ for the quadratic bottom friction case, and $u = 27.2\ cm/sec$ for the linear bottom friction case.

Using a time step of 360 seconds, model results reached steady state in about 300 time steps. The steady-state vertically-averaged velocities in the x-y plane as shown in Figure 3.2 agree well with the analytical results. Figure 3.3 shows the velocity distribution in a basin which is rotated in the x-y plane by 30° in the counterclockwise direction. The results appear to be the same. The model was then tested using an irregular curvilinear grid shown in Figure 3.4. The same steady velocity is reproduced (Figure 3.5).

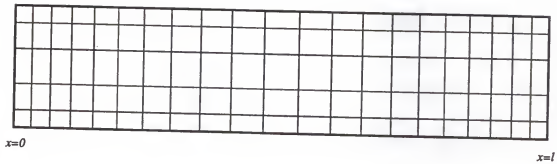

Figure 3.1: A non-uniform rectangular grid system for testing the forced surface slope test.

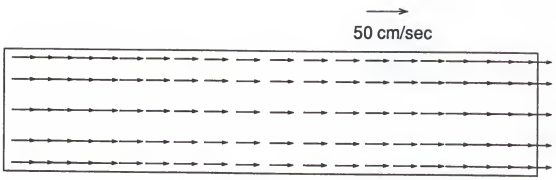

Figure 3.2: Simulated steady-state vertically-averaged velocity field in a rectangular basin forced by a constant surface slope. Horizontal grid is shown in Figure 3.1.

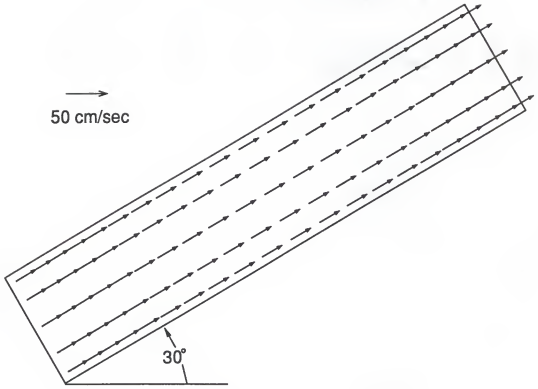

Figure 3.3: Same as Figure 3.2, except that the basin is rotated by 30° in the counterclockwise direction.

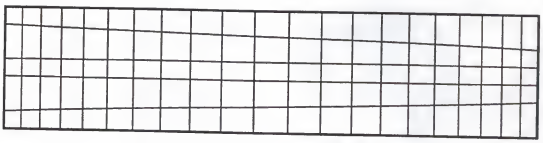

Figure 3.4: An irregular grid system for rectangular basin with irregular grids

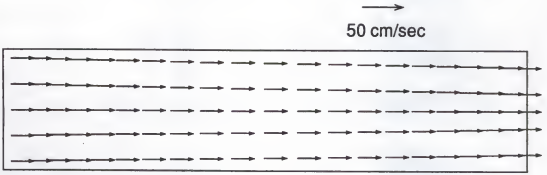

Figure 3.5: Same as Figure 3.2, except that the irregular curvilinear grid as shown in Figure 3.4 is used.

3.2 Seiche Test

The second test was designed to test the model's ability to simulate a seiche (standing wave) in a closed basin. The local acceleration term balances the pressure term. Neglecting vertical and horizontal diffusion, bottom and side-wall friction, convective acceleration, and Coriolis acceleration, the equations of motion reduce to the following one-dimensional equations

$$\frac{\partial u}{\partial t} = -g\frac{\partial \zeta}{\partial x} \tag{3.3}$$

$$h\frac{\partial u}{\partial x} = -\frac{\partial \zeta}{\partial t} \tag{3.4}$$

with boundary conditions $u = 0$ at $x = 0, l$, where u is velocity, ζ is surface elevation, h is water depth, g is gravitational acceleration ($= 981\ cm/s^2$), and l is the basin length. The analytical solutions of the lowest mode for the above two equations are

$$\zeta = a\cos\omega t\cos kx \tag{3.5}$$

$$u = \frac{gak}{\omega}\sin\omega t\sin kx \tag{3.6}$$

where a is the wave amplitude, ω is the circular frequency, and k is the wave number. The grid system used here is the same as that shown Figure 3.1. The following values were used for this test case

$$\begin{aligned} a &= 15\ cm \\ l = \text{basin length} &= 62\ km = \lambda/2 \\ \text{basin width} &= 14\ km \\ h &= 5\ m \end{aligned} \tag{3.7}$$

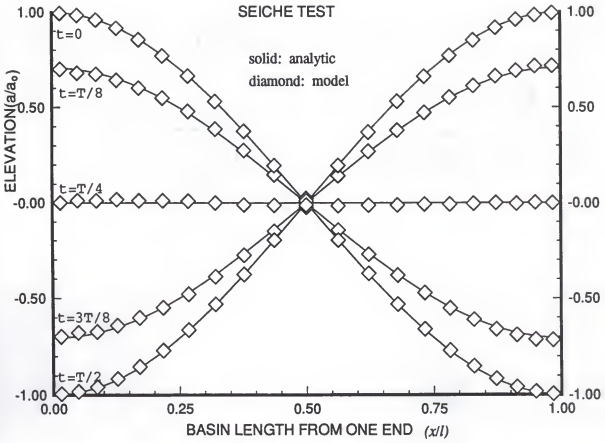

Figure 3.6: Comparison between simulated surface elevation (diamond symbol) and analytic solution (solid lines) for seiche oscillation in a closed basin (T is seiche period).

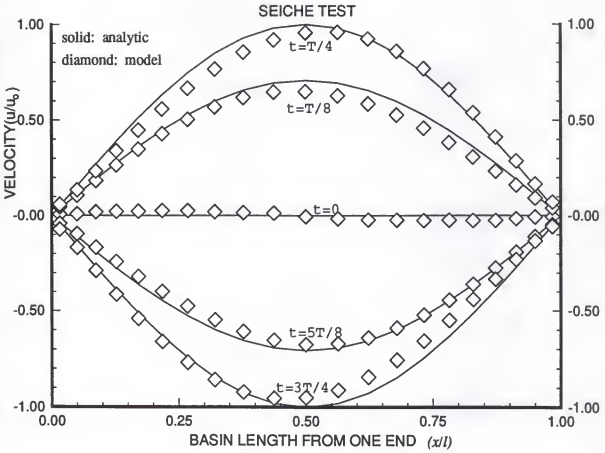

Figure 3.7: Comparison between simulated vertically-averaged velocities (diamond symbol) and analytic solution (solid line) for seiche oscillation in a closed basin (T is seiche period).

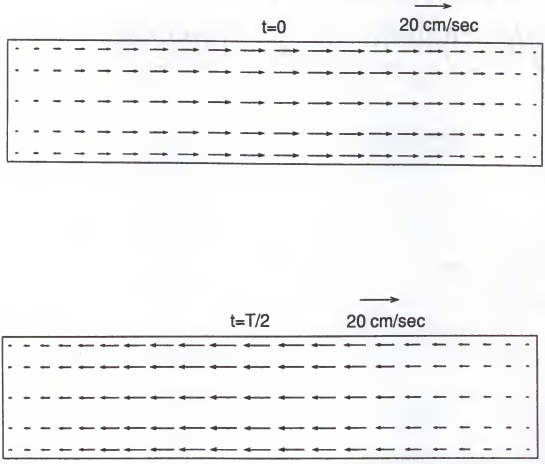

Figure 3.8: Maximum velocities for seiche case.

The wave characteristics are calculated as

$$\begin{aligned} k &= 2\pi/\lambda = 5.0671 \cdot 10^{-7}/cm \\ T &= \lambda/\sqrt{gh} = 4.92\ hours \\ \omega &= 2\pi/T = 3.5488 \cdot 10^{-4}/s \end{aligned} \tag{3.8}$$

The above values and a time step of 300 seconds were used in the numerical simulation, using the vertically-integrated version of the three-dimensional model. Figures 3.6 and 3.7 show the comparison between model results and analytic solution after the model has been run for ten tidal cycles. Figure 3.6 shows the surface elevations distribution along the channel at increments of one eighth tidal period. Figure 3.7 shows the velocity distribution at corresonding times. The model predictions match the analytic solution very well with a maximum error of 3 % in amplitude of both the elevation and the velocity. Figure 3.8 shows the instantaneous velocity fields at two instants of time when the velocity is maximum. The maximum velocity occurs at the center and zero velocity occurs at both closed ends.

3.3 Tidal Forcing

One of the most common applications of an estuarine hydrodynamic model is tidal simulation. Therefore, before applying the model to a real field, the model result should be compared with the analytic solution describing the response of a rectangular estuary to forced oscillation at the open boundary. Lynch and Gray (1978) derived the analytic solutions for a tidally forced estuary with a flat bottom and a sloping bottom. Neglecting nonlinear, Coriolis, horizontal diffusion, and y-direction terms and assuming linear bottom friction, one obtains the following vertically-averaged equations

$$\frac{\partial \zeta}{\partial t} + \frac{\partial hu}{\partial x} = 0 \tag{3.9}$$

$$\frac{\partial u}{\partial t} + g\frac{\partial \zeta}{\partial x} + \frac{ku}{h} = 0 \tag{3.10}$$

with the following boundary conditions: at the closed end, x_l, $\partial\zeta/\partial x = 0$; and at the open end, x_0, $\zeta = a\cos\omega t$, where u is the velocity, ζ is surface elevation, g is gravitational acceleration, k is the linear bottom friction coefficient, a is the tidal amplitude, ω is the tidal frequency, and h is the depth. Generally h is defined as $h(x) = H_o x^n$, while h with a linear slope is given as

$$h = \frac{H_0 - H_l}{l}x = sx \tag{3.11}$$

where H_0 is the depth at the open end ($x = 0$), H_l is the depth at the closed end ($x = l$), l is the basin length, and s is the bottom slope. Flat bottom and linear bottom slope cases are considered for model tests.

The solution for a flat bottom ($n = 0$) is (Lynch and Gray, 1978)

$$\zeta(x,t) = \mathrm{Re}[ae^{i\omega t}\frac{\cos(\beta(x - x_l))}{\cos(\beta l)}] \tag{3.12}$$

$$u(x,t) = \mathrm{Re}[\frac{-i\omega a}{\beta H_0}e^{i\omega t}\frac{\sin(\beta(x - x_l))}{\cos(\beta l)}] \tag{3.13}$$

where a is the tidal amplitude at the open end, and

$$\beta = (\frac{\omega^2 - i\omega k/h}{gH_o})^{0.5} \tag{3.14}$$

The solution for a linear sloping bottom is (Lynch and Gray, 1978)

$$\zeta(x,t) = \mathrm{Re}[(AJ_0(2\beta\sqrt{x}) + BY_0(2\beta\sqrt{x}))e^{i\omega t}] \tag{3.15}$$

$$u(x,t) = \mathrm{Re}[\frac{1}{\sqrt{x}}[(-AJ_1(2\beta\sqrt{x}) - BY_1(2\beta\sqrt{x}))]\frac{i\omega}{\beta s}e^{i\omega t}] \tag{3.16}$$

where J_0, J_1, Y_0, and Y_1 are Bessel functions, β is redefined with s instead of H_o, and

$$A = \frac{aY_1(2\beta\sqrt{x_l})}{[J_0(2\beta\sqrt{x_0})Y_1(2\beta\sqrt{x_l}) - Y_0(2\beta\sqrt{x_0})J_1(2\beta\sqrt{x_l})]} \tag{3.17}$$

$$B = \frac{-aJ_1(2\beta\sqrt{x_l})}{[J_0(2\beta\sqrt{x_0})Y_1(2\beta\sqrt{x_l}) - Y_0(2\beta\sqrt{x_0})J_1(2\beta\sqrt{x_l})]} \tag{3.18}$$

The following parameter values were used in the test run

$$\begin{aligned} a &= 100\ cm \\ T &= 600\ sec \\ k &= 1\ cm/s \\ l &= 6200\ m \\ (H_0 + H_1)/2 &= 350\ m \\ \Delta t &= 5\ s \end{aligned} \tag{3.19}$$

For a flat bottom, Figure 3.9 shows comparison between model results and the analytic solution for elevation and velocity along the basin length. Maximum error is less than 2% for elevation, and 3% for velocity. For a sloping bottom, Figure 3.10 shows simulated and analytical results as a function of bottom slope for maximum surface elevation at the closed end and for velocity at the open end. Simulated velocity and elevation both agree well with the analytic solution.

Another tidal forcing test was done with the annular section configuration shown in Figure 3.11. Here h is defined as $h(x) = H_o r^n$, and β is defined as $\beta^2 = (\omega^2 - i\omega k/h)/gH_o$. Flow is required to be tangent to the solid boundaries at $r = r_1$. A tidal forcing function is specified at $r = r_2$. The analytic solution for a flat bottom ($n = 0$) is (Lynch and Gray, 1978)

$$\zeta(r,t) = \mathrm{Re}[(AJ_0(\beta r) + BY_0(\beta r))e^{i\omega t}] \tag{3.20}$$

$$u(r,t) = \mathrm{Re}[(-AJ_1(\beta r) - BY_1(\beta r))\frac{i\omega}{\beta H_o}e^{i\omega t}] \tag{3.21}$$

where J_0, J_1, Y_0, and Y_1 are Bessel functions, and

$$A = \frac{aY_1(\beta r_1)}{[J_0(\beta r_2)Y_1(\beta r_1) - Y_0(\beta r_2)J_1(\beta r_1)]} \tag{3.22}$$

$$B = \frac{-aJ_1(\beta r_1)}{[J_0(\beta r_2)Y_1(\beta r_1) - Y_0(\beta r_2)J_1(\beta r_1)]} \tag{3.23}$$

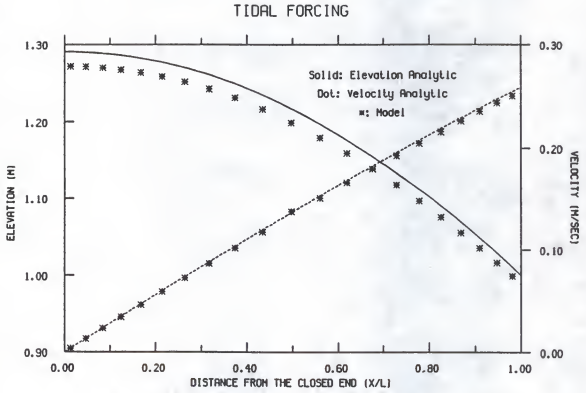

Figure 3.9: Comparison between simulated surface elevations and velocities (*'s) and analytic solutions for a tidally forced flat-bottom basin (Elevation and velocity are in phase).

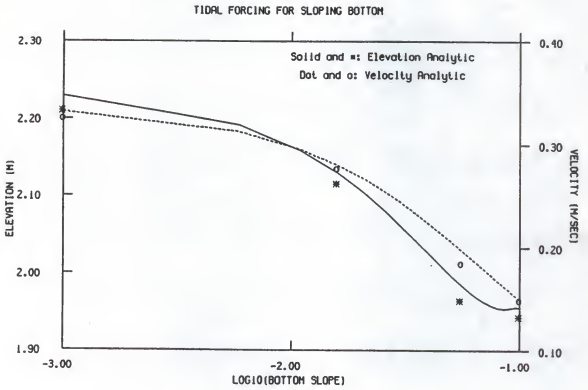

Figure 3.10: Comparison of simulated maximum surface elevations at the closed end and maximum velocities at the open end with the analytic solution for a tidally forced sloping bottom basin.

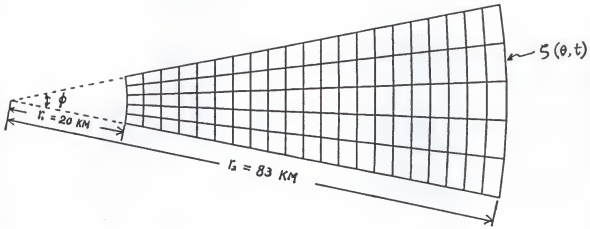

Figure 3.11: Grid system for the annular section

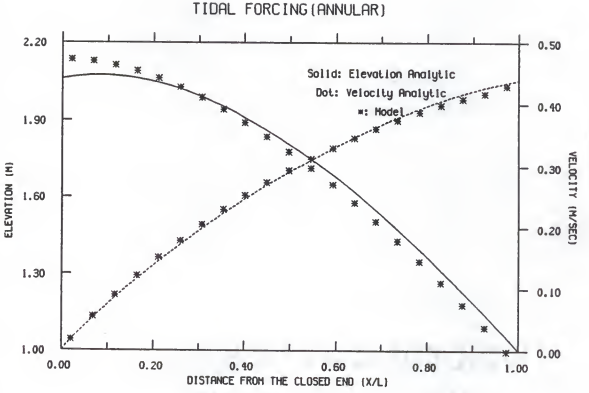

Figure 3.12: Comparison between simulated surface elevations and velocities (*'s) and analytic solutions for a tidally forced flat-bottom annular section.

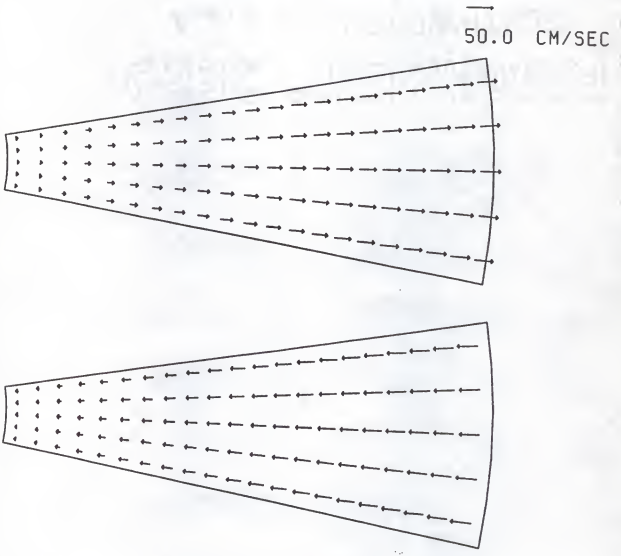

Figure 3.13: Maximum ebb and flood velocities in a tidally forced flat-bottom annular section at the end of tidal 10 cycles run.

A sinusoidal tidal forcing was prescribed along the outer radius for the model simulation. The following values were used in the test run

$$\begin{aligned} a &= 100\ cm \\ T &= 2.5\ hours \\ k &= 1\ cm/s \\ l &= 63\ km \\ h &= 100\ m \\ \Delta t &= 100\ s \end{aligned} \tag{3.24}$$

The model was run up to 10 cycles, at which steady state conditions were obtained. Figure 3.12 shows the resulting surface elevation and velocity at maximum conditions. Model results appear to agree well with the analytic solution. Maximum ebb and flood velocities are plotted in Figure 3.13. The radial symmetry is also precisely reproduced in the model results.

3.4 Wind Forcing

Three simulations of wind forcing have been done. The first test was conducted to examine the effect of bottom slope on surface setup in a rectangular basin with one open end. The second test was to examine the vertical profile of horizontal velocity in a closed basin. The third test was to examine the surface setup in bowtie-shaped estuary.

The analytic solution for the first test was solved by Lynch and Gray (1978) by neglecting the convective acceleration, horizontal friction, Coriolis, and y-direction terms, while assuming small amplitude surface oscillation and using a linearized bottom friction. Thus the vertically-averaged, linearized shallow water equations are given as

$$\frac{\partial \zeta}{\partial t} + \frac{\partial hu}{\partial x} = 0 \tag{3.25}$$

$$\frac{\partial u}{\partial t} + g\frac{\partial \zeta}{\partial x} + \frac{ku}{h} - \frac{\tau_w}{\rho h} = 0 \tag{3.26}$$

with the boundary condition at the closed end, x_l, as

$$\frac{\partial \zeta}{\partial x} = \frac{\tau_w}{\rho g h} \tag{3.27}$$

and at the open end, x_0, as

$$\zeta = 0 \tag{3.28}$$

where u is the velocity, ζ is surface elevation, g is gravitational acceleration, k is the linear bottom friction coefficient, τ_w is the wind stress, ρ is the water density, and h is the depth. Generally h is defined as $h(x) = H_o x^n$ while h with a linear slope is given as

$$h = \frac{H_0 - H_l}{l} x = sx \tag{3.29}$$

where H_0 is the depth at the open end, H_l is the depth at the closed end, l is the basin length, and s is the bottom slope.

The analytic solution for the steady wind setup is

$$\zeta = \frac{\tau_w}{\rho g H_o}(x - x_o) \quad \text{for } n = 0 \tag{3.30}$$

$$\zeta = \frac{\tau_w}{\rho g s}(\log x - \log x_o) \quad \text{for } n = 1 \tag{3.31}$$

where x_o is the coordinate at the open end, while x_l is the coordinate at the closed end ($0 < x_l < x < x_o$).

For the second test, the analytic solution for the vertical velocity profile driven by a constant wind stress in a closed basin can be readily obtained. Considering only pressure and vertical diffusion terms, the governing equations are given as

$$g\frac{\partial \zeta}{\partial x} = A\frac{\partial^2 u}{\partial z^2} \tag{3.32}$$

$$\int_{-h}^{0} u\, dz = 0 \tag{3.33}$$

with the boundary condition at the surface ($z = \zeta$) being

$$A\frac{\partial u}{\partial z} = \frac{\tau_w}{\rho} \tag{3.34}$$

and that at the bottom ($z = -h$) being

$$A\frac{\partial u}{\partial z} = ku_b \tag{3.35}$$

where u is velocity, ζ is surface elevation, A is the vertical eddy viscosity, τ_w is wind stress, ρ is water density, k is the linearized bottom friction coefficient, and u_b is the bottom velocity.

Integrating Eq. (3.32) twice and applying the boundary conditions, the solution is given as follow with a constant vertical eddy viscosity (Neumann and Pierson, 1969)

$$u = g\frac{\partial \zeta}{\partial x}[\frac{(z^2 - h^2)}{2A} - \frac{h}{k}] + \frac{\tau_w}{\rho A}[z + h + \frac{A}{k}] \tag{3.36}$$

where $\partial\zeta/\partial x$ is calculated from Equations (3.32) and (3.36) as

$$\frac{\partial \zeta}{\partial x} = \frac{3}{2}\frac{\tau_w}{\rho g h}\frac{(hk + 2A)}{(hk + 3A)} \tag{3.37}$$

The following values were used in the model simulation for the steady state wind setup

$$\begin{aligned} \tau_w &= 1000\ dyne/cm^2 \\ \rho &= 1\ gm/cm^3 \\ k &= 1\ cm/s \\ l &= 62\ km \\ (H_o + H_l)/2 &= 4000\ m \\ 0 \le s &\le 0.1 \\ \Delta t &= 100\ s \end{aligned} \tag{3.38}$$

Comparison between model results and the analytic solution for the setup as a

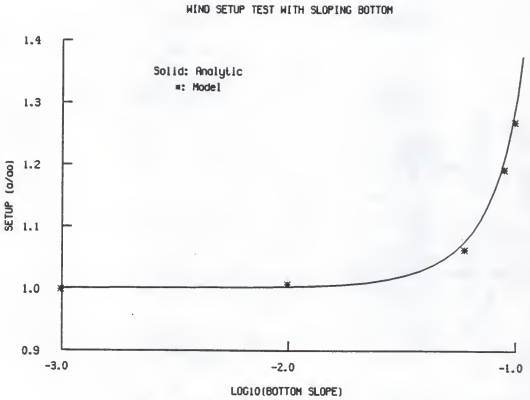

Figure 3.14: Comparison between simulated maximum surface elevation and analytic solution for a sloping bottom basin forced by wind (a_o is the setup in the flat bottom).

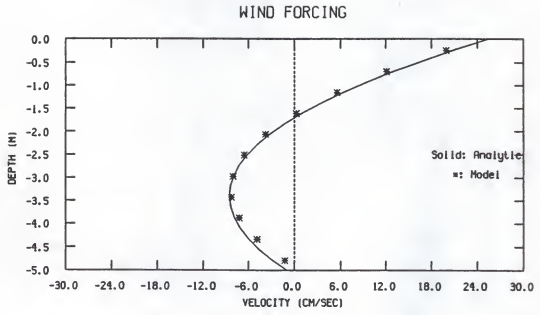

Figure 3.15: Comparison between simulated vertical velocity structure and analytic solution for a constant wind in a closed basin.

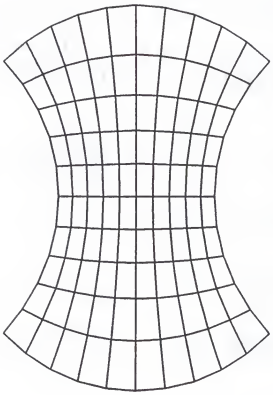

Figure 3.16: Grid system for wind setup test in a bowtie-shaped basin.

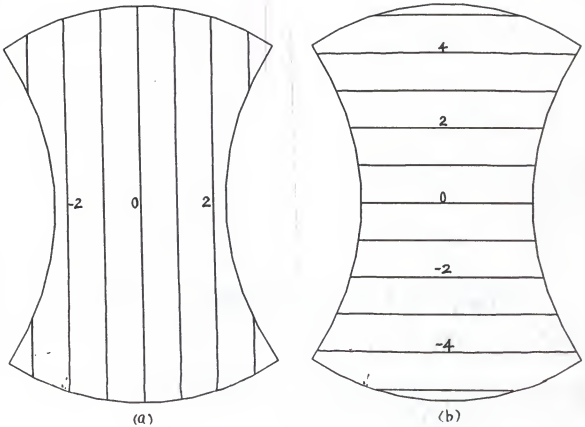

Figure 3.17: Steady state setup in *cm* for (a) 1 $dyne/cm^2$ eastward wind, and (b) 1 $dyne/cm^2$ northward wind.

function of bottom slope is shown in Figure 3.14. The model estimates the setup at all slopes with less than 3% error.

The following values were used in the model simulation for the vertical structure of horizontal velocity

$$\begin{aligned} \tau_w &= 1\ dyne/cm^2 \\ \rho &= 1\ gm/cm^3 \\ k &= 0.5\ cm/s \\ l &= 62\ km \\ (H_o + H_l)/2 &= 5\ m \\ A &= 5\ cm^2/s \\ \Delta t &= 300\ s \end{aligned} \tag{3.39}$$

Comparison between model results and analytic solution of the vertical structure of horizontal velocity is shown in Figure 3.15. Eleven vertical levels were used in this test. The error is less than 2 %. When the number of vertical levels was increased, the model approached the analytic solution, particularly near the bottom. With fewer vertical levels, the error was found to increase especially near the bottom although the model results still compare well with the analytic vertical structure of velocity.

The third test for the steady-state response to wind forcing in a bowtie-shaped estuary was performed. Figure 3.16 shows the test grid system in the bowtie-shaped basin. The basin has a longest distance of 60 km in the y-direction, and a shortest distance of 25 km in the x-direction. A constant wind stress of 1 $dyne/cm^2$ to the north and east was used for the simulation. The bottom friction coefficient was set to zero. As shown in Figure 3.17, the simulated setup is in excellent agreement with the analytic solution in both directions.

3.5 Density-Driven Currents

Fresh water runoff and intrusion of salt water from ocean combine to produce density-driven currents. For testing baroclinic flow simulation, analytic solutions developed by Hansen and Rattray (1965) were used. A typical estuarine flow shows a two-layer system: seaward flow at the surface and up-estuary flow at the bottom. Neglecting nonlinear terms, Coriolis, horizontal diffusion, and y-direction terms, one can obtain the following continuity, momentum, and salinity equations (Hansen and Rattray, 1965)

$$\frac{\partial u}{\partial x} + \frac{\partial w}{\partial z} = 0 \tag{3.40}$$

$$g\frac{\partial \zeta}{\partial x} + g\alpha z\frac{\partial S}{\partial x} = A_v\frac{\partial^2 u}{\partial z^2} \tag{3.41}$$

$$u\frac{\partial S}{\partial x} + w\frac{\partial S}{\partial z} = \frac{\partial}{\partial x}(K_h\frac{\partial S}{\partial x}) + \frac{\partial}{\partial z}(K_v\frac{\partial S}{\partial z}) \tag{3.42}$$

with an equation of state for estuarine water

$$\rho = \rho_0(1 + \alpha S) \tag{3.43}$$

where ζ is surface elevation, S is salinity, A_v is vertical eddy viscosity, u is horizontal velocity, w is vertical velocity, K_h is horizontal eddy diffusivity, K_v is vertical eddy diffusivity, α is a constant, ρ_0 is density of freshwater, and g is gravitational acceleration. Eq. (3.41) means that the surface elevation gradient plus the density gradient balance the vertical diffusion of momentum.

Boundary conditons are no-slip at the bottom, net horizontal transport equals river flow, and zero normal salt flux at the boundaries. In the central regime of the estuary, Hansen and Rattray (1965) assumed that both the vertical salinity stratification and velocity structure are independent of longitudinal positions. The salinity

solutions are

$$u = -u_f \frac{d\phi}{d\eta} \tag{3.44}$$

$$\begin{aligned} \frac{S}{S_0} &= 1 + \nu\xi + \frac{\nu}{M}[(\eta - \frac{1}{2}) - \frac{1}{2}(\eta^2 - \frac{1}{3}) \\ &- \int_0^\eta \phi\, d\eta + \int_0^1 \int_0^\eta \phi\, d\eta'\, d\eta] \end{aligned} \tag{3.45}$$

where

$$\phi = \frac{1}{2}(2 - 3\eta + \eta^3) - \frac{\nu R_a}{48}(\eta - 3\eta^3 + 2\eta^4) \tag{3.46}$$

where $\eta = z/D$ and $\xi = Rx/BDK_{h0}$ are dimensionless vertical and horizontal co-ordinates, respectively, and zero subscripts indicate values at $x = 0$. D is channel depth, B channel width, ν is a constant, ϕ stream function, $R_a = g\alpha S_0 D^3/A_v K_{h0}$ estuarine Rayleigh number, $M = K_v K_{h0} B^2/R^2$ a ratio of tidal mixing to the river flow, and R river discharge rate. ν is the positive root of

$$1680M(1 - \nu) = 32\nu + 76\frac{R_a}{48}\nu^2 + \frac{152}{3}(\frac{R_a}{48})^2\nu^3 \tag{3.47}$$

The horizontal exchange coefficient, K_h, must increase seaward at a rate equal to the integral mean velocity or fresh water discharge velocity

$$\frac{d}{dx}K_h = \frac{R}{BD} = u_f \tag{3.48}$$

For this test, the computer model code was modified to incorporate the above non-uniform horizontal eddy diffusivity, while also using the following parameters

$$\begin{aligned} K_v &= 5\ cm^2/s \\ K_{h0} &= 10^5\ cm^2/s \\ A_v &= 5\ cm^2/s \end{aligned}$$

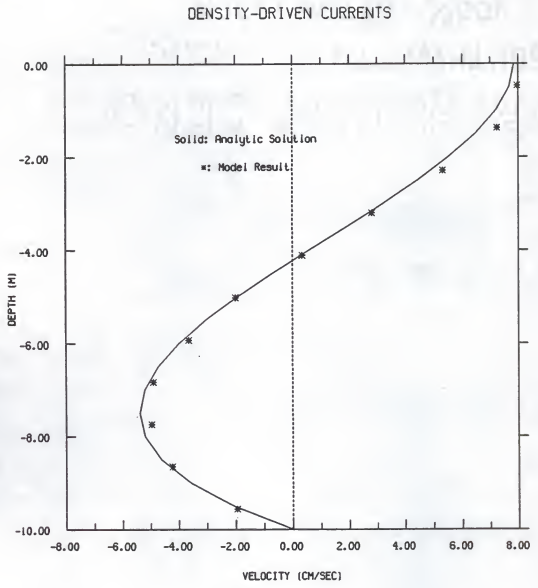

Figure 3.18: Comparison between simulated results and analytic solution for the vertical structure of horizontal velocity induced by density gradient.

$$\begin{aligned} \alpha &= 6 \cdot 10^{-4} \\ S_0 &= 30\ ppt \\ B &= 4\ km \\ D &= 10\ m \\ R &= 2 \cdot 10^7\ cm^3/s \\ \rho_0 &= 1.0\ g/cm^3 \end{aligned} \tag{3.49}$$

From the above information, ν has a value of 0.2122. The simulation was started with an initial salinity distribution which has a horizontal gradient of 0.318 ppt/km and the river inflow given above. As shown in Figure 3.18, simulation velocity structure obtained with 11 vertical levels agree well with the analytic solution with less than 2%.

3.6 Summary

Tests performed in this chapter indicate the basic soundness of the numerical schemes used for many terms in the three-dimensional model. Moreover, the effect of a curvilinear grid on accuracy of the model was also tested. Table 3.1 summarizes all the test runs made here. However, good agreement between model results and analytic solutions of idealized linearized problems only ensures the numerical accuracy of the model and does not ensure the correctness of the parameterization of physical processes (*e.g.*, turbulent mixing, bottom friction, and nonlinear acceleration, *etc.*). To test the soundness of the turbulence model and bottom friction formulation, it is necessary to compare model results with laboratory and field data.

Table 3.1: Characteristics of model analytical tests.

Model Features	Forced Constant Surface Slope	Seiche	Tidal Forcing	Wind Forcing	Density-Driven
Basin Geometry	uniform and non-uniform rectangular	uniform rectangular	uniform rectangular, annular	uniform rectangular, bowtie	uniform rectangular
Basin Bottom	flat	flat	flat, sloping	flat, sloping	flat
Dimensionality	2-D	2-D	2-D	2-D,3-D	3-D
Surface Slope	yes	yes	yes	yes	yes
Local Acceleration	no	yes	yes	yes	yes
Bottom Stress	yes	no	yes	yes	no
Vertical Diffusion	no	no	no	yes	yes

CHAPTER 4
ANALYSIS OF OBSERVED HYDRODYNAMIC DATA FROM JAMES RIVER

Before the hydrodynamic model is applied to James River, it is necessary to learn about the circulation of James River from observed hydrodynamic data. A comprehensive set of hydrodynamic data has been collected from the James River estuary by the Virginia Institute of Marine Science (VIMS). Byrne *et al.* (1987) and Hepworth and Kuo (1989) presented a detailed description of data collection techniques and analyses of data. The major elements of the data collection program included a network of tide guages, a series of current meters and CTD mooring deployments (Figure 4.1), and a series of slack water measurements of vertical-longitudinal salinity profiles. Time series of measured surface elevations and currents were analyzed using a least-squares method to obtain the harmonic constants. These results will be used for model calibration and verification by comparing them with model results. A series of slack water vertical-longitudinal salinity profiles along the axis of the river will be used to calibrate the vertical mixing parameterization in the salinity equation. The Eulerian residual current distribution over the transect 'JB' shown in Figure 4.2 will be used to evaluate the ability of the model to reproduce the general features of the residual current structure over this section.

In the next chapter, the three-dimensional hydrodynamic model will be applied to James River and model results will be compared with field data described in this chapter with various sensitivity tests to quantify the parameter-varying sensitivity. And stratification-destratification phenomena of vertical salinity structure will be simulated according to the spring-neap tidal cycle. Next salinity intrusion problem and frontal system will be analyzed. And model calibration and validation process

Table 4.1: Tidal amplitude harmonic constants obained from June 19 to July 17, 1985. (period in *hour*, amplitude in *cm*, phase lag in degree)

Station No.				1	2	3	4
NOS No.	Const.	Period					
1	M2	12.42	Amp.	33.4	36.4	36.7	37.0
			Phase lag	327.6	313.9	286.9	278.9
2	S2	12.00	Amp.	4.4	4.5	5.0	5.0
			Phase lag	338.3	318.1	278.2	267.8
3	N2	12.66	Amp.	5.9	6.3	6.7	6.6
			Phase lag	193.0	185.2	152.0	143.9
4	K1	23.93	Amp.	4.4	4.3	4.4	4.5
			Phase lag	327.0	310.9	296.3	291.4
5	M4	6.21	Amp.	1.0	0.8	0.5	0.5
			Phase lag	183.2	162.4	83.2	310.0
6	O1	25.82	Amp.	4.6	4.5	4.9	4.9
			Phase lag	22.5	5.9	347.1	341.7
7	M6	4.14	Amp.	1.0	0.2	0.4	0.5
			Phase lag	18.1	359.5	0.3	304.2

wil be discussed. Finally we will discuss the σ- and z-baroclinic effects.

4.1 Water Level Data

According to the field data analysis, the sea surface elevation records showed that tidal forcing accounts for about 85 to 95 % of the surface fluctuations in the James River. Clearly, tide is the dominant hydrodynamic factor. The semi-diurnal M2 constituent was the strongest component with the form ratio, $F = (K1+O1)/(M2+S2) = 0.2$, which is classified as a semi-diurnal dominant tidal type. The other constituents contribute only variations such as the spring-neap cycle. Shallow water components of M4 and M6, caused from M2, were negligible with less than 1 *cm* in most areas. The tidal harmonic analysis for a 29-day period starting from June 19, 1985 is shown in Table 4.1. The M2 constituent at the open boundary of Station 4 has an amplitude of 37.0 *cm*, and is modulated by the S2 (5.0 *cm*) and N2 (6.6 *cm*) constituents at periods of 14.8 and 27.6 days, respectively. The interaction of the

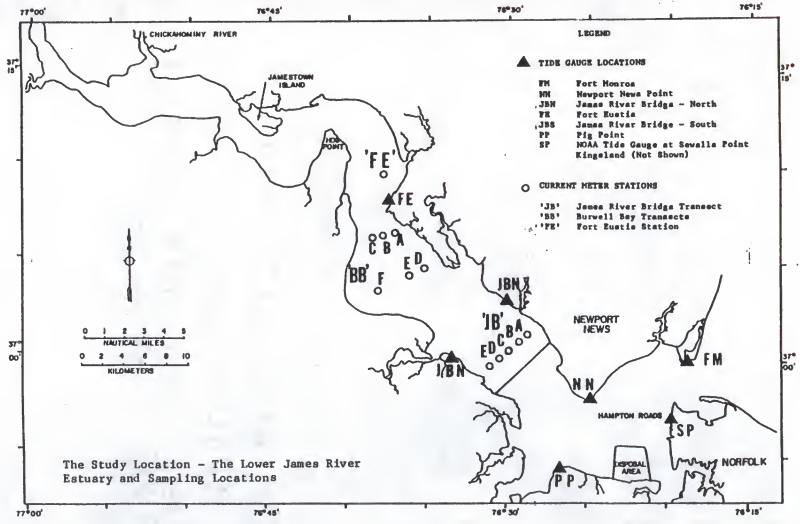

Figure 4.1: Lower James River and Hampton Roads (After Hepworth and Kuo (1989)).

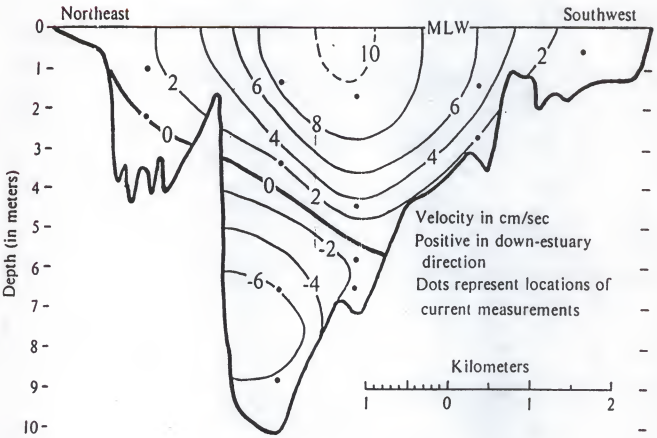

Figure 4.2: Observed Eulerian residual velocity over transect 'JB' (After Hamrick *et al.* ,1989).

three constituents causes the semi-diurnal tidal amplitude to vary between 25.4 *cm* at neap condition to 48.6 *cm* at spring condition.

The amplitudes of the two significant diurnal constituents O1 (4.9*cm*) and K1 (4.5 *cm*) are about 25 % of the M2 constituent. Their only significant contribution to the tidal character of the area is to create a diurnal inequality, which is shown in Figure 4.3.

4.2 Tidal Currents

Tidal currents in the James River are again dominated by the M2 constituent, which have a surface amplitude of 50.5 cm/s in u- direction and 38.8 cm/s in v-direction at Station A of 'JB' in Figure 4.1. The near bottom currents are half as high as the surface currents. The S2 and N2 constituents have approximately one sixth the magnitude of the M2 and interact with it to create the spring-neap variation in the semidiurnal band. The magnitude of the diurnal constituents (K1, O1) are quite significant on the order of 7 - 12 cm/s, while the M4 and M6 are quite small, on the order of 1 - 2 cm/s.

4.3 Circulation Pattern

Circulation patterns in the James River estuary were reported based on hydraulic model experiments (Byrne *et al.*, 1987). They showed that the lower James River was a "leaky closed system" wherein surface circulation is expanded as an elongated counterclockwise gyre with slight losses of material upstream past Mulberry Point and substantial losses downstream past Sewells Point. Bottom circulation has a net upstream progression with some indication of counterclockwise tendency in the upper reaches of Burwell Bay. Nontidal circulation pattern was substantiated by results of a current measurement experiment conducted near the James River Bridge in the summer of 1985 (Byrne *et al.*, 1987). The longitudinal component of residual currents shows a circulation at this location as a typical two layer system (Figure 4.2). The level of no net motion in Figure 4.2 is higher on the left when looking downstream.

Circulation in Hampton Roads based on hydraulic model experiments indicates the cyclonic nature of circulation.

4.4 Slack-Water Salinity Data

A series of slack water vertical-longitudinal salinity profiles along the axis of the river is shown in Figure 4.4 - 4.7. These will be used to calibrate the vertical mixing parameterization in the salinity equation.

4.5 Front Dynamics

Fronts are regions where flow convergence and strong exchange between different water masses occurs, and are hence important in estuarine dynamics. Estuarine fronts have significant biological consequences, since they are areas of high productivity for all elements of the food chain from phytoplankton to fish. The location of estuarine frontal zones should be considered in the design of waste water discharge outfalls to avoid excessive concentration and contamination. Frontal circulation affects the dispersion of oil spills and ocean dumped wastes. Thus, the study of estuarine fronts must be incorporated into environmental monitoring programs to determine how pollutants are transported and concentrated into biologically active areas.

Frontogenesis in estuaries is often a transient and local phenomenon which is related to particular geometric features and occurring during a particular portion of a tidal cycle. In coastal areas where tidal currents are strong enough, outflow plumes may be swept back into the estuary by the flood current. Simpson and Nunes (1981) called it a tidal intrusion front. According to them, the frontal boundary, marking the surface convergence where the incoming water flows under the less dense surface layer, propagates upriver in a characteristic V-shaped configuration with strong point convergence at the apex of the V.

Observations revealed that the front in the lower James/Hampton Roads is V-shaped and persistent in terms of its occurrence (Byrne, 1987). The front occurs in a small area off Newport News Point at flood tide during every tidal cycle, although its

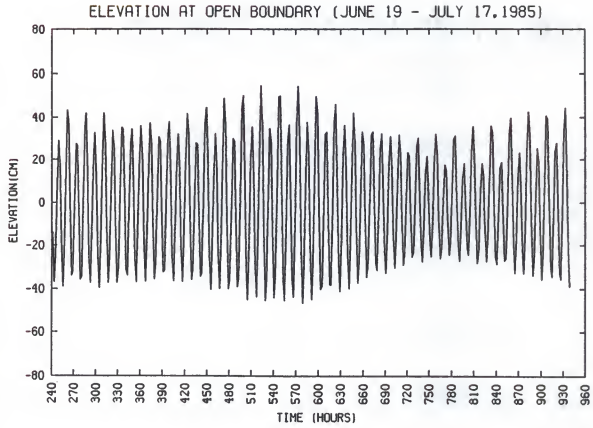

Figure 4.3: Surface elevation at the open boundary between June 19 and July 17, 1985.

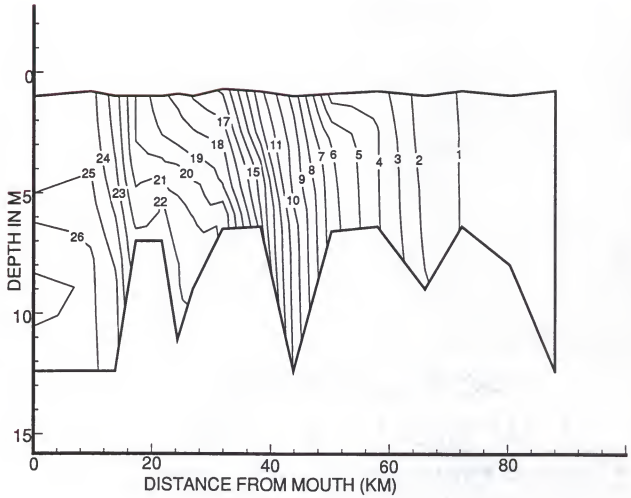

Figure 4.4: Observed longitudinal-vertical salinity at slackwater before flood on June 19, 1985.

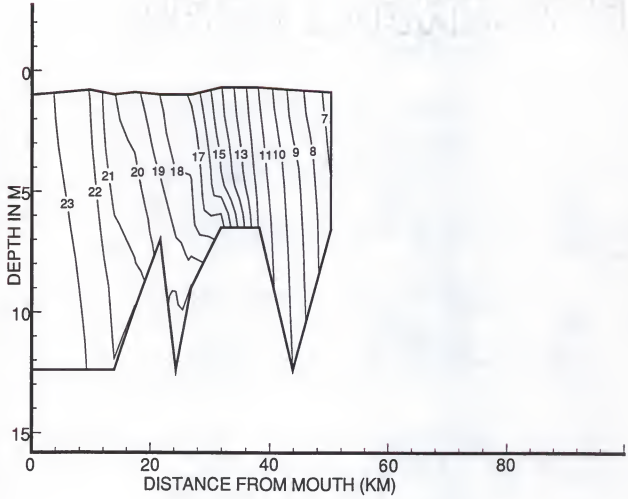

Figure 4.5: Observed longitudinal-vertical salinity at slackwater before flood on July 3, 1985.

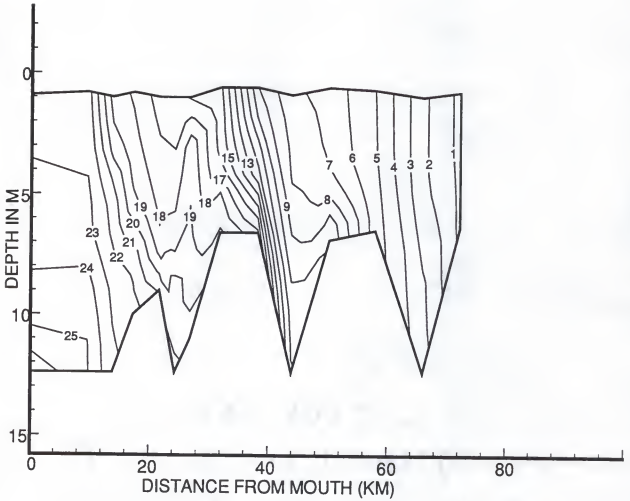

Figure 4.6: Observed longitudinal-vertical salinity at slackwater before flood on July 9, 1985.

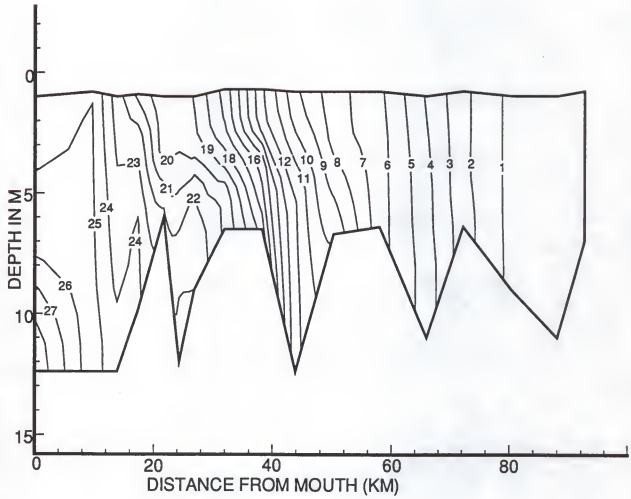

Figure 4.7: Observed longitudinal-vertical salinity at slackwater before flood on July 17, 1985.

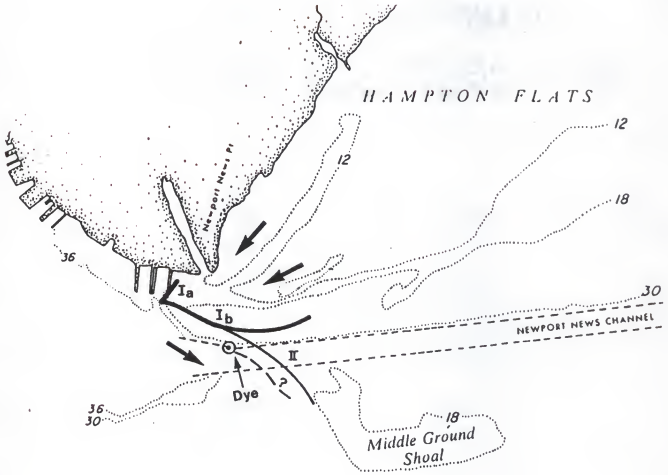

Figure 4.8: Configuration of fronts at 1118 hours. From aerial photographs of August 29, 1985. Generalized flow direction shown by arrows. Dotted lines are depth contours in *ft*. (After Byrne, 1987)

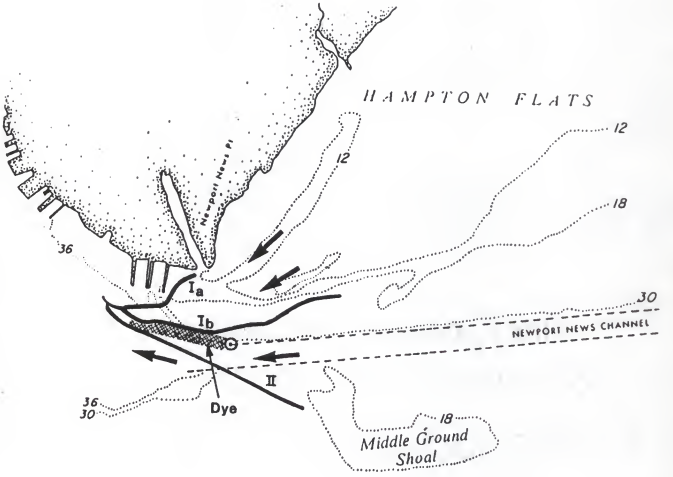

Figure 4.9: Configuration of fronts at 1400 hours. From aerial photographs of August 29, 1985. Generalized flow direction shown by arrows. Dotted lines are depth contours in ft. (After Byrne, 1987)

evolution with time is somewhat variable with respect to tide condition. During its life span the front is revealed as a narrow zone of surface flow convergence and strong vertical transport. The vertical transport across the frontal system was examined by the dye release experiment (Byrne, 1987). The dye was released at the surface near the downriver side. When the upriver water column was stratified, the peak dye concentration tended to locate at depth where the vertical gradient was greatest. This shows that the material in the upper portion of the water column are transported into lower horizons where the net estuarine transport is upriver. This also tells that there is a strong vertical flow.

According to Byrne (1987), field observations suggest that the frontal system and its general evolution may be described in terms of three segments as shown in Figure 4.8. The initial phase in frontal development is associated with flow exiting Hampton Flats near Newport News Point, designated as branch Ia of the frontal system. During the early phase of flood tide, there is also a distinct boundary parabathytic with the southern flank of Hampton Flats. This boundary designated as branch Ib, apparently represents flow contributions from flow coursing between Hampton Flats and the navigation channel. These two segments usually join together at the western edge of Newport News Bar to form a V shape front. The front position generally rests near the 9 m depth contour. The third segment, branch II, of the frontal system is that associated with the advancing flood current along the Newport News Channel. So as the flood tide currents progress up the channel section, the more saline waters entering Hampton Roads encounter the estuarine salinity gradient. Another boundary segment is formed which progresses upriver with the flood tide, and frequently joins an apex formed by the three boundaries on the slope leading to the deep water of the lower James (Figure 4.9).

CHAPTER 5
APPLICATION OF THREE-DIMENSIONAL MODEL TO JAMES RIVER

5.1 Procedure of Model Simulation

In this chapter, model application to James River is described. First of all, the model simulation procedure is described. Simulation of tidal circulation is then presented, followed by simulation of the stratification-destratification process cycle associated with the spring-to-neap cycle. Following that, simulation of salt intrusion is presented before a detailed presentation on the simulation of formation and evaulation of a tidal intrusion front.

First of all, using the grid generation program, two sets of non-orthogonal grid systems in the horizontal plane were generated for the James River: a coarse grid system with 76x38 grid points (Figure 5.1) and a fine grid system with 121x45 (Figure 5.2). Figure 5.3 and Figure 5.4 show the same grid systems when plotted in (ξ, η) coordinates, respectively. A space-staggered grid system as discussed before was used. Next, the depth at each grid point was interpolated from bathymetric data on the NOAA/NOS navigation chart. In the vertical direction, a total of 11 vertical levels is used with a uniformly spaced σ grid.

The simulations performed here use a two-time-level scheme for time stepping, and generally central difference schemes for spatial gradients. The external mode is solved implicitly, and the internal mode is solved explicitly except that the vertical diffusion term is treated implicitly. The vertical eddy coefficients for momentum and salinity are determined by the simplified second-order closure schemes of Sheng (1983) and Sheng and Villaret (1989).

The model was applied to simulate the circulation and salinity transport in the

James River during a 29-day period starting June 19, 1985. Based on a series of four synoptic scale slack-water (slack-before-flood (SBF)) salinity surveys made in the James River between June 19 and July 17, 1985, it is apparent that the estuary goes through a periodic cycle of stratification and destratification according to the neap-spring tidal variation. Salinity was measured at slack-before-flood, from the mouth of the river to the head of the salt intrusion with 5 to 10 km distance between two neighboring stations. Longitudinal and vertical salinity distributions for each survey are shown in chapter 4.

To simulate the process of stratification and destratification, it is necessary to define river discharge, tidal forcing at the open boundary, and initial conditions of salinity and flow field. The river discharge at Richmond averaged 81 m^3/sec during the sampling period, and this value was used for the fresh water flow in the model simulation. For tidal forcing at the open boundary (*i.e.*, entrance to Chesapeake Bay), 7 tidal harmonic constituents (NOS number : 1 to 7) were used and computed by the method of least squares (Boon and Kiley, 1978). A time series of surface level at the open boundary is shown in Figure 4.3. For salinity boundary conditions, a constant, vertically-uniform salinity of 26 *ppt* was used during the simulation.

For the initial conditions of salinity and flow field, the model is first spun up by a M2 tide with an amplitude of 38 *cm* at the open boundary which corresponds to the tidal condition on June 19, 1985. The model is spun up from the condition of no flow and homogeneous temperature for 5 days without considering salinity. The model simulation is then continued for 5 more days with an initial salinity field interpolated from the slackwater data on June 19, 1985. During this 5-day simulation, the salinity field is held fixed while the velocity field is allowed to adjust to the baroclinic field. After the 5-day baroclinic adjustment, the model is allowed to start the dynamic simulation from June 19 to July 17, 1985, wherein both the velocity and salinity field can change with time.

Figure 5.1: Curvilinear grid for the James River coarse grid system (physical domain).

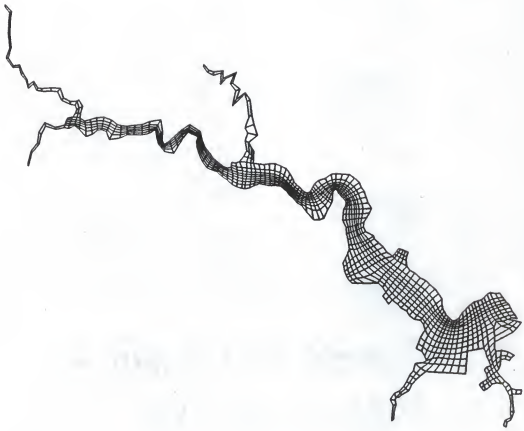

Figure 5.2: Curvilinear grid for the James River fine grid system (physical domain).

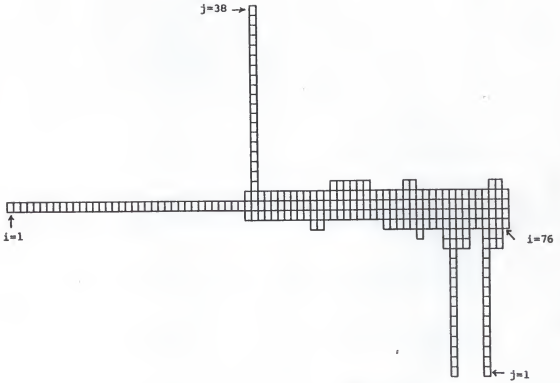

Figure 5.3: Curvilinear grid for the James River coarse grid system (computation domain).

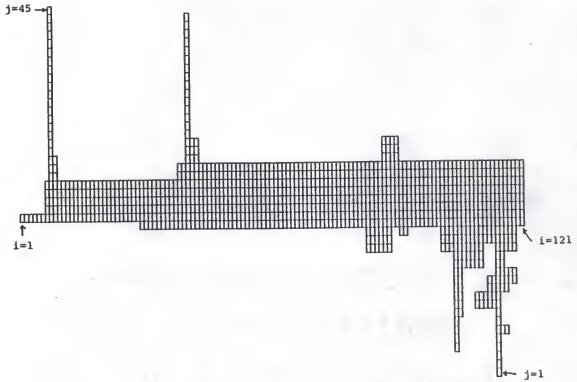

Figure 5.4: Curvilinear grid for the James River fine grid system (computation domain).

5.2 Simulation of Tidal Circulation

Comparison between simulated (coarse grid) and tidal elevation and tidal currents was made by means of harmonic analysis of the computed and observed data. The computed and observed water levels at the 3 stations shown in Figure 5.1 were analyzed using the harmonic analysis program and the results were compared with data. Table 5.1 lists the amplitudes and phase angles for 5 tidal constituents at Stations 1, 2, and 3. It is apparent that the computed amplitude and phase angle agree well with observations with a maximum error of 9 % in surface elevation amplitude at Station 3 and with a maximum error of 6 minutes of phase lag at Station 2 (M2 case).

The harmonic constants of computed tidal currents were also compared with the observed ones. Table 5.2 lists the amplitude and phase angle of computed tidal currents at four different levels at Station 4. The model generally predicts the amplitude of near-surface currents quite well within 2 % error (M2 case), but appears to overpredict the amplitude of near-bottom currents. The error may be due to the use of a relatively poorly resolved bottom topography associated with the coarse grid and due to an inaccurate density-driven circulation.

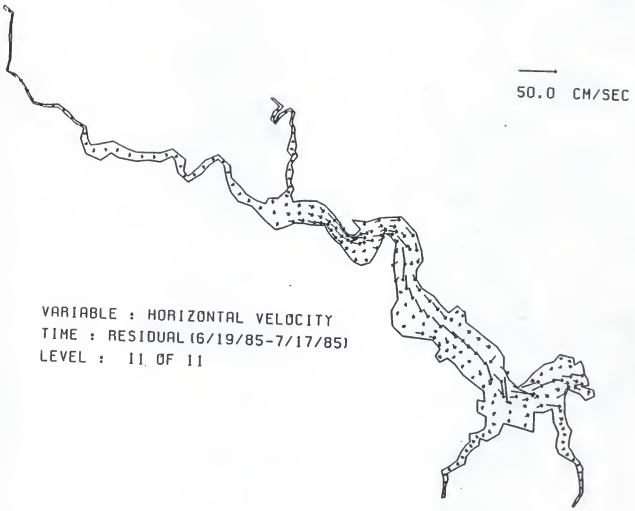

Figure 5.5: Eulerian residual current at surface in the James River between June 19 and July 17, 1985.

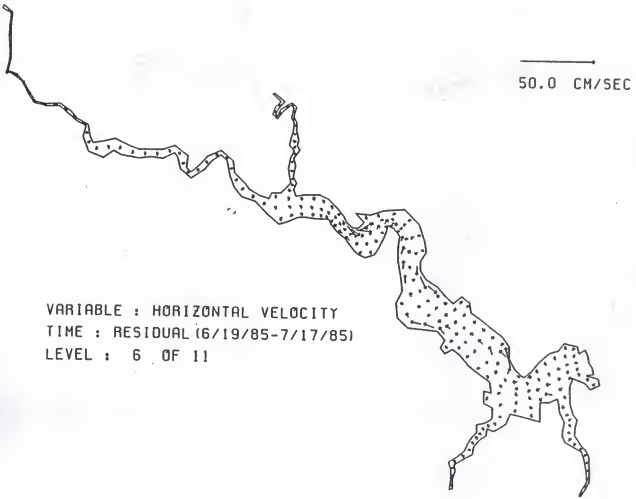

Figure 5.6: Eulerian residual current at mid-depth in the James River between June 19 and July 17, 1985.

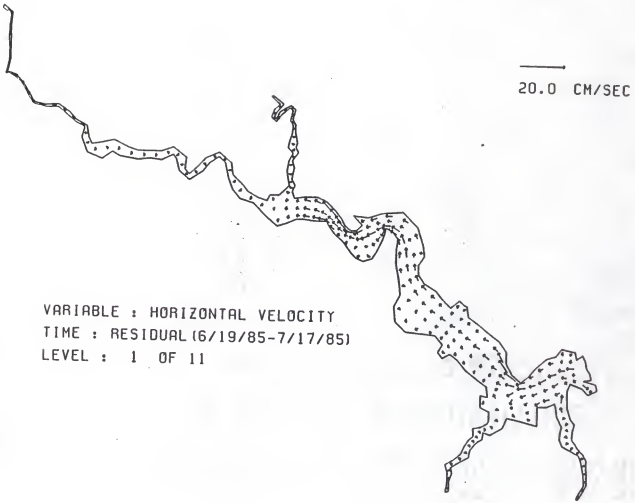

Figure 5.7: Eulerian residual current near bottom in the James River between June 19 and July 17, 1985.

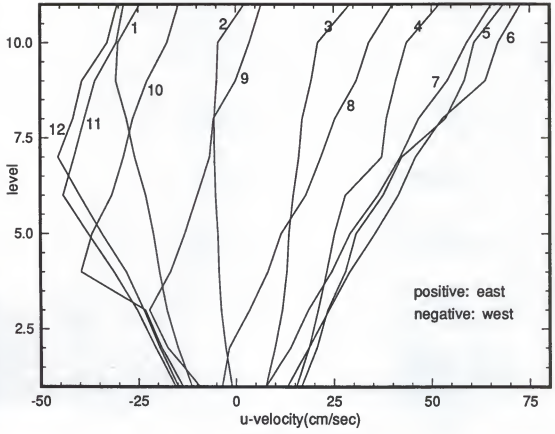

Figure 5.8: Vertical velocity profile at spring near the James River Bridge. The numbers on top of plot indicate the time evolution in hours.

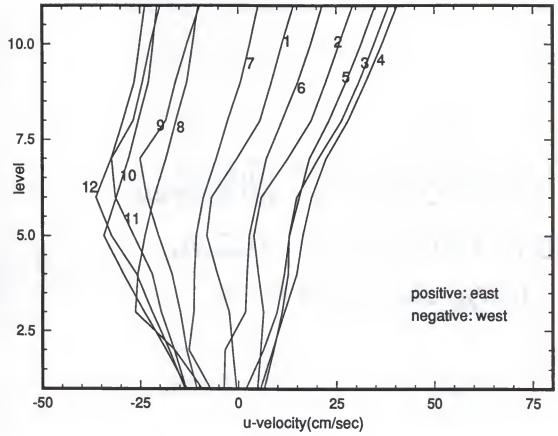

Figure 5.9: Vertical velocity profile at neap near the James River Bridge. The numbers on top of plot indicate the time evolution in hours.

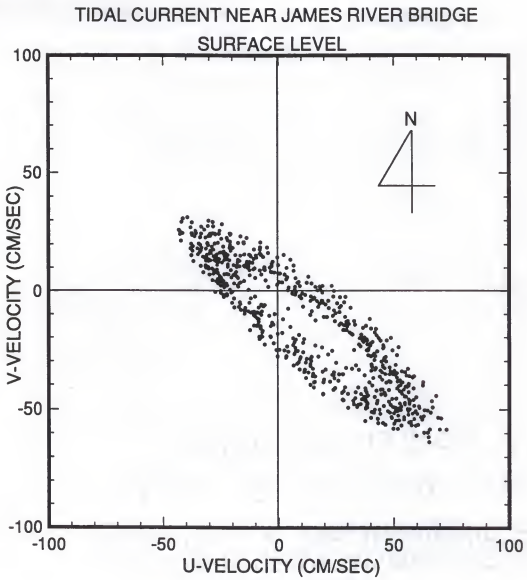

Figure 5.10: Computed near-surface tidal currents near the James River Bridge between June 19 and July 17, 1985.

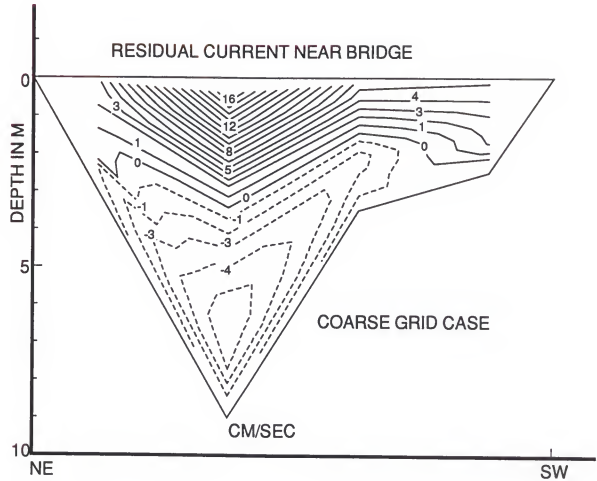

Figure 5.11: Contours of 29-day residual longitudinal velocity at a transect near the James River Bridge (along i=65).

Table 5.1: Comparison of the model predicted harmonic constants of water level with the measured data.

		Constituent	M2	S2	N2	K1	O1
St.1	Amplitude	Data	33.4	4.4	5.9	4.4	4.6
(i=57,	(cm)	Model	36.4	5.6	6.2	2.9	4.5
j=19)	Phase lag	Data	327.6	338.3	193.0	327.0	22.5
	(degree)	Model	327.0	315.5	190.1	316.5	7.8
St.2	Amplitude	Data	36.4	4.5	6.3	4.3	4.5
(i=64,	(cm)	Model	37.5	6.0	6.5	2.9	4.6
j=16)	Phase lag	Data	310.4	299.4	174.6	308.4	359.0
	(degree)	Model	313.4	303.9	179.0	311.4	2.9
St.3	Amplitude	Data	36.7	5.0	6.7	4.4	4.9
(i=74,	(cm)	Model	36.5	5.9	6.4	2.8	4.5
j=17)	Phase lag	Data	286.9	278.2	152.0	296.3	347.1
	(degree)	Model	286.1	265.5	150.3	294.2	347.4

The simulated Eulerian residual currents over the entire James River at surface-level, mid-depth, and bottom-level during the 29-day simulation are shown in Figures 5.5, 5.6, and 5.7, respectively. The results exhibit a typical estuarine circulation pattern, showing a down-estuary flow in the upper portion of the water column and an up-estuary flow in the lower portion of the water column. Generally the velocity differences through the water column associated with an estuarine circulation will be an order of magnitude greater than the velocity differences associated with a riverine shear flow in which there is no longitudinal density gradient force (Officer, 1978). The shear in the vertical velocity profile is due to a combination of bottom friction and internal friction effects. In the middle of lower reaches of most estuaries, however, the vertical velocity profile is due to a combination of the longitudinal surface slope (barotropic) term and the longitudinal density gradient (baroclinic) term which acts in the opposite direction and increases as a function of depth. Figure 5.8 and Figure 5.9 show the computed vertical structure of the horizontal velocities near the James River Bridge (Station 4) at spring and neap tides, respectively. Two-layer estuarine flows are clearly seen in these plots with more positive u-velocities in the

Table 5.2: Comparison of the model predicted harmonic constants of velocity with the measured data (St. 4, Depth=8.5 m)

depth			Const.	M2	S2	N2	K1	O1
1.2 m	Amplitude (cm/sec)	u	Data	50.5	7.2	9.8	10.1	6.0
			Model	49.5	7.2	8.0	4.5	5.7
		v	Data	38.8	4.2	5.7	8.4	4.3
			Model	40.9	5.4	5.8	5.0	5.9
	Phase lag (degree)	u	Data	128.4	147.3	196.5	106.7	167.7
			Model	120.2	117.8	188.0	77.4	144.8
		v	Data	308.0	327.0	18.1	282.2	343.6
			Model	323.2	314.9	22.0	293.6	353.2
3.1 m	Amplitude (cm/sec)	u	Data	48.8	7.0	7.3	8.5	5.9
			Model	48.1	6.7	7.6	4.5	1.9
		v	Data	28.6	4.7	4.1	4.4	2.4
			Model	36.7	4.8	5.5	4.0	3.7
	Phase lag (degree)	u	Data	123.5	143.3	168.8	106.7	168.2
			Model	125.8	120.4	188.7	75.9	140.7
		v	Data	294.9	319.2	355.2	263.4	324.8
			Model	316.3	303.7	10.7	256.7	321.7
6.3 m	Amplitude (cm/sec)	u	Data	38.6	4.4	6.1	5.8	4.5
			Model	34.2	4.5	4.9	2.5	2.9
		v	Data	10.2	1.3	2.2	1.7	1.7
			Model	24.9	2.9	2.9	1.0	1.5
	Phase lag (degree)	u	Data	112.4	137.5	182.2	94.4	149.3
			Model	113.3	94.6	162.6	62.7	131.6
		v	Data	283.2	329.8	340.5	275.9	353.3
			Model	261.8	295.5	329.7	223.6	284.6
8.5 m	Amplitude (cm/sec)	u	Data	30.3	3.2	5.2	4.1	3.1
			Model	24.3	3.6	3.8	2.1	2.1
		v	Data	6.5	1.0	1.8	1.2	1.1
			Model	16.2	2.3	2.3	0.7	0.9
	Phase lag (degree)	u	Data	105.8	136.5	179.6	95.5	151.1
			Model	111.91	95.8	164.3	63.8	135.3
		v	Data	285.1	326.6	357.3	289.9	310.4
			Model	256.9	258.6	327.7	230.9	293.5

upper layer and more negative u-velocities in the lower layer. During spring tide, velocity profiles show a larger range of fluctuation due to the high tidal range.

Instantaneous tidal currents at station 4 near the James River Bridge during the 29-day period are shown in Figure 5.10, which agree quite well with the data shown in Hamrick et al. (1990).

An isotach contour plot of simulated residual current across the James River Bridge transect are shown in Figure 5.11. The isotach lines compared quite well with the measured data, considering the fact that there are only four grid points across the James River in this section. The residual isotach lines are very sensitive to the bathymetry and horizontal boundary conditions of flow and salinity.

According to Pritchard (1956) and Hamrick (1989), the net non-tidal velocity showed a down-estuary movement in the upper half of the water column and an up-estuary movement in the lower half of the water column. Figure 4.2 shows the two-layer circulation pattern near the James River Bridge, where the mean vertical salinity variation was about 4 *ppt* in 9 *m* depth. The net circulation in James River is primarily due to the freshwater discharge and the gravitational convection caused by the density difference between freshwater and seawater. The gravitational convection is a result of dynamic interactions between the salinity and current distributions, and tends to increase stratification.

5.3 Sensitivity Tests

The purpose of sensitivity tests is to determine the sensitivity of the results of the present curvilinear hydrodynamic modeling system to changes in model parameters, and thereby to gain insight into the relevance of the model parameters to the physical processes governing salinity transport.

A total of 12 test cases were run with various combinations of model parameters shown in Table 5.3. The sensitivity of model results to changes in the various model parameters was investigated by comparing results of the test cases (Table 5.3) with

measured data or the baseline run (case2) which was presented in the last section. Table 5.5, Table 5.6, and Table 5.7 list the tidal elevation constituents at stations 1, 2, and 3, respectively. Table 5.8 lists the tidal constituents of near-surface u-velocity (east-west direction) at station 4. Table 5.9 lists the tidal constituents of near-surface v-velocity at station 4.

5.3.1 Effect of Bottom Friction

Bottom friction is frequently the most important non-linear term in shallow water and generates overtides on its own account (Doodson and Proudman, 1923). Bottom friction influences both the tidal range and the phase lag. It is possible to adjust the bottom friction coefficient to achieve better agreement between predicted and measured surface elevations. The zone where the flow is appreciably retarded by friction against the surface and/or bottom is known as the boundary layer. The most obvious constraint is that the viscosity of the fluid enforces the no-slip condition. Bottom stress can be expressed as a linear or quadratic function of the velocity. Normally in tidal dynamics a quadratic law is assumed. Bottom stress is obtained by matching the measured velocity profile to the logarithmic law of the wall in shallow water. The logarithmic velocity profile in the inertial sublayer is one of the major results in turbulent theory. From the law of the wall, the drag coefficient C_d is determined by

$$C_d = \kappa^2[\ln(H + z_b)/z_0]^{-2} \tag{5.1}$$

where z_b is the grid point nearest the bottom, z_0 is the roughness height, and κ is the von Karman constant set to 0.40 here.

Bursinger et al. (1971) also defined a vertically-varying Monin-Oboukhov length as

$$L = \frac{u_*^3}{\kappa g \overline{w'\rho'}/\rho_0} = \frac{-\mid \tau_b \mid^{3/2}}{\kappa g K_v(\partial\rho/\partial z)/\rho_0} \tag{5.2}$$

where u_* is the frictional velocity defined as $(\tau_b/\rho)^{1/2}$, where τ_b is the bottom shear stress,ρ is the density, and K_v is the vertical eddy diffusivity. They calculated a

Table 5.3: Test cases performed.

	Grid system	Bottom friction	Bottom roughness height	Monin-Obukhov	Law of the wall	Constant bottom friction
case1	coarse	explicit	0.4	yes	yes	no
case2	coarse	implicit	0.4	yes	yes	no
case3	coarse	implicit	0.4	no	yes	no
case4	coarse	implicit	0.1	yes	yes	no
case5	coarse	implicit	0.04	yes	yes	no
case6	coarse	implicit	no	no	no	0.002
case7	coarse	implicit	no	no	no	0.003
case8	coarse	implicit	no	no	no	0.004
case9	fine	implicit	0.4	yes	yes	no
case10	fine	implicit	0.04	yes	yes	no
case11	fine	implicit	no	no	no	0.003
case12	fine	implicit	0.4	no	yes	no

stability function $\phi(z/L)$ based on data in a stably stratified atmospheric surface layer:

$$\phi(\frac{z}{L}) = \frac{\kappa z}{u_*}\frac{\partial u}{\partial z} = 1 + 4.7\frac{z}{L} \tag{5.3}$$

Monin-Oboukhov have successfully used z/L as the basic independent variable for the description of the surface layer, both in stable and unstable conditions. In this stably stratified case, C_d is given by

$$C_d = \kappa^2(\ln\frac{H + z_b}{z_0} + \frac{4.7z}{L})^{-2} \tag{5.4}$$

Table 5.4: Comparison between observed and simulated tidal elevation constituents at Station 1 (amplitude in *cm*, phase lag in degree).

	constituent	M2	S2	N2	K1	O1
data	amplitude	33.4	4.4	5.9	4.4	4.6
	phase lag	327.6	338.3	193.0	327.0	22.5
case1	amplitude	39.1	6.1	6.6	3.2	4.9
	phase lag	328.1	313.9	188.9	310.8	2.9
case2	amplitude	33.6	4.9	5.4	2.5	4.1
	phase lag	331.1	323.3	197.0	322.5	13.9
case3	amplitude	38.3	5.7	6.1	2.9	4.6
	phase lag	329.4	317.4	191.0	314.6	6.7
case4	amplitude	35.6	5.4	5.9	2.7	4.4
	phase lag	328.1	318.2	192.1	318.3	10.0
case5	amplitude	36.4	5.6	6.2	2.9	4.5
	phase lag	327.0	315.5	190.1	316.5	7.8
case6	amplitude	39.1	6.4	7.0	3.4	5.1
	phase lag	329.3	313.1	188.7	308.3	359.5
case7	amplitude	39.1	6.3	6.8	3.2	5.0
	phase lag	328.3	313.7	188.6	309.9	1.7
case8	amplitude	38.9	6.1	6.5	3.1	4.9
	phase lag	328.1	313.9	188.4	311.7	3.7
case9	amplitude	29.3	3.9	4.5	2.1	3.4
	phase lag	342.4	341.3	212.9	336.0	28.4
case10	amplitude	32.2	4.7	5.3	2.5	4.0
	phase lag	332.7	328.8	200.2	332.5	23.6
case11	amplitude	32.5	4.9	5.5	2.6	4.2
	phase lag	329.9	324.6	196.5	330.5	21.6

Table 5.5: Comparison between observed and simulated tidal elevation constituents at Station 2 (amplitude in *cm*, phase lag in degree).

	constituent	M2	S2	N2	K1	O1
data	amplitude	36.4	4.5	6.3	4.3	4.5
	phase lag	313.9	318.1	185.2	310.9	5.9
case1	amplitude	38.2	6.3	6.8	3.1	4.8
	phase lag	310.5	298.2	172.8	305.7	356.2
case2	amplitude	35.6	5.4	5.8	2.6	4.2
	phase lag	314.3	305.4	180.1	312.3	3.2
case3	amplitude	37.7	6.0	6.5	2.9	4.6
	phase lag	312.6	301.4	175.0	308.8	359.9
case4	amplitude	37.0	5.8	6.2	2.8	4.5
	phase lag	311.6	301.4	176.5	309.8	0.5
case5	amplitude	37.5	6.0	6.5	2.9	4.6
	phase lag	310.4	299.4	174.6	308.4	359.0
case6	amplitude	37.8	6.4	6.9	3.2	4.9
	phase lag	309.9	296.7	171.8	303.6	354.2
case7	amplitude	38.0	6.4	6.8	3.1	4.8
	phase lag	310.1	297.6	172.4	304.9	355.8
case8	amplitude	37.9	6.3	6.7	3.0	4.8
	phase lag	310.6	298.2	172.8	306.0	356.8
case9	amplitude	33.9	4.8	5.5	2.4	3.9
	phase lag	321.3	315.1	190.2	317.7	9.0
case10	amplitude	36.6	5.6	6.2	2.6	4.2
	phase lag	313.5	307.0	180.9	315.7	6.1
case11	amplitude	36.7	5.7	6.2	2.7	4.3
	phase lag	311.1	304.3	177.8	315.0	5.2

Table 5.6: Comparison between observed and simulated tidal elevation constituents at Station 3 (amplitude in *cm*, phase lag in degree).

	constituent	M2	S2	N2	K1	O1
data	amplitude	36.7	5.0	6.7	4.4	4.9
	phase lag	286.9	278.2	152.0	296.3	347.1
case1	amplitude	36.7	5.9	6.5	2.9	4.5
	phase lag	285.5	264.7	149.4	293.2	346.8
case2	amplitude	35.6	5.6	6.2	2.7	4.4
	phase lag	287.7	267.0	151.7	295.2	348.5
case3	amplitude	36.3	5.8	6.4	2.8	4.5
	phase lag	286.6	266.2	150.7	295.0	347.6
case4	amplitude	36.3	5.8	6.3	2.8	4.4
	phase lag	286.6	266.1	150.9	294.6	347.7
case5	amplitude	36.5	5.9	6.4	2.8	4.5
	phase lag	286.1	265.5	150.3	294.2	347.4
case6	amplitude	36.9	6.0	6.5	2.9	4.5
	phase lag	284.9	264.1	148.4	293.3	346.0
case7	amplitude	36.8	6.0	6.5	2.9	4.5
	phase lag	285.2	264.5	149.1	293.5	346.5
case8	amplitude	36.6	5.9	6.5	2.8	4.5
	phase lag	285.6	264.9	149.4	293.7	346.8
case9	amplitude	38.2	6.2	6.7	2.8	4.5
	phase lag	289.7	276.9	153.7	296.2	347.7
case10	amplitude	38.9	6.3	6.8	2.9	4.5
	phase lag	287.8	267.7	151.7	295.3	347.1
case11	amplitude	38.8	6.2	6.8	2.9	4.5
	phase lag	287.3	267.3	151.3	295.3	347.1

Sensitivity tests with constant bottom friction coefficients of 0.002, 0.003, and 0.004 showed that the differences in the tidal elevation and the phase lag were hardly noticeable (case 6, case 7, case 8 in Table 5.5, Table 5.6, Table 5.7). Phase lag increased slightly with the increased bottom friction coefficient. When the law of the wall was used (case 3), the tidal elevation and phase lag were improved with respect to the observation data when compared to results from those obtained with constant bottom friction coefficients. However, the tidal elevation at Station 1 was overestimated both with the constant bottom friction coefficients and with the law of

the wall. When the Monin-Oboukhov length was used with the law of the wall, the result was improved substantially (case 2). Sensitivity to bottom roughness height was performed with 0.4, 0.1, and 0.04 in case 2, case 4, and case 5, respectively. With the smaller roughness height, the tidal elevation increased and the phase lag decreased. In the fine grid system, case 9 and case 10 showed the same trend for the tidal elevation as in coarse grid system for the test of roughness height. For u-velocity, v-velocity, both amplitude and phase lag increased with a small roughness height (case 9 and case 10 in Table 5.8 and Table 5.9).

5.3.2 Effect of Bathymetry

Sensitivity of model prediction to the bathymetry was examined with several different sets of bathymetry used in the simulations. Naturally bathymetry is one of the most important simulation parameters responsible for accurate model results. The bathymetry change is directly related to the bottom friction. Depth data were corrected many times to best represent the depth near each grid point. Correction of depth data in a certain grid system must be performed in the model calibration process in order to use the model as prediction tool. Also experience shows that a model that does not accurately resolve the deeper channel of an estuary system cannot predict the correct degree of stratification and two-layer estuarine residual flow.

5.3.3 Effect of Horizontal Grid

The discretization of the governing equations leads unavoidably to approximation errors. Two grid systems: one coarse grid (Figure 5.1) and one fine grid (Figure 5.2) were used in this study. Compared to the coarse grid system, the grid number in the transverse direction is doubled in fine grid system: coarse grid system has only 4 to 5 grid lines in η direction, while fine grid system has 8 to 10 grid lines. Case 2 and case 10 show the deviations in elevations and velocities between two grid systems. As shown in Tables 5.5, 5.6, and 5.7, it is difficult to discern the differences between the coarse-grid and fine-grid results at stations 2, 3, and 4. However in the fine grid

Table 5.7: Comparison of data and model tidal constituents of surface u-velocity at Station 4 (amplitude in cm, phase lag in degree, 6/19 - 7/17/85).

	constituent	M2	S2	N2	K1	O1
data	amplitude	51.5	8.8	10.0	7.1	5.5
	phase lag	122.72	137.76	355.16	110.50	146.66
case9	amplitude	52.4	7.7	8.3	3.3	4.0
	phase lag	102.94	81.50	321.81	63.29	130.20
case10	amplitude	53.5	8.7	9.1	4.6	5.2
	phase lag	107.48	84.76	328.88	66.85	131.18
case11	amplitude	52.1	8.8	9.2	4.7	5.7
	phase lag	109.77	88.73	333.35	69.54	127.95
case12	amplitude	52.2	7.5	8.3	3.6	4.1
	phase lag	102.88	80.24	322.65	64.81	126.44

system, the circulation gyre near the Hampton Roads (Figure 5.26 and Figure 5.27) is much clearer. The two grid systems represent very similar physical processes.

5.3.4 Effect of Time Step

Various time steps of 120, 180 and 360 seconds were used with a bottom friction factor 0.003 in the coarse grid system. The deviations of the elevations and the velocities for each selected time step at the selected stations were negligible. The results show that time step interval is not a restriction for stability because this model was run with implicit method.

5.4 Neap-Spring Stratification and Destratification Cycle

In a partially-mixed estuary like James River, the degree of stratification and the circulation pattern are controlled by the volume of water flowing up the estuary during the flood tide and the volume of fresh water flowing down the estuary. A primary source of mixing energy is tidal forcing. The effect associated with neap-to-spring tide in James River is seen in Figure 5.12 and Figure 5.13 near the James River bridge. During the spring tide with high tide range (July 3), well mixed condition

Table 5.8: Comparison of data and model tidal constituents of surface v-velocity at Station 4 (amplitude in cm, phase lag in degree, 6/19 - 7/17/85).

	constituent	M2	S2	N2	K1	O1
data	amplitude	39.5	2.7	5.8	5.5	3.8
	phase lag	302.34	324.92	176.36	296.27	321.37
case9	amplitude	36.6	4.5	4.4	1.9	2.8
	phase lag	298.04	275.47	152.24	274.85	326.79
case10	amplitude	38.3	5.3	5.4	2.6	3.8
	phase lag	299.29	277.20	158.76	275.72	323.91
case11	amplitude	37.7	5.4	5.6	2.6	4.0
	phase lag	299.98	280.69	160.17	272.97	320.12
case12	amplitude	36.4	4.6	4.5	2.0	2.8
	phase lag	297.84	272.06	151.59	275.04	325.32

was developed, while during the ebb tide with lower tide range (July 9), stratification became more apparent.

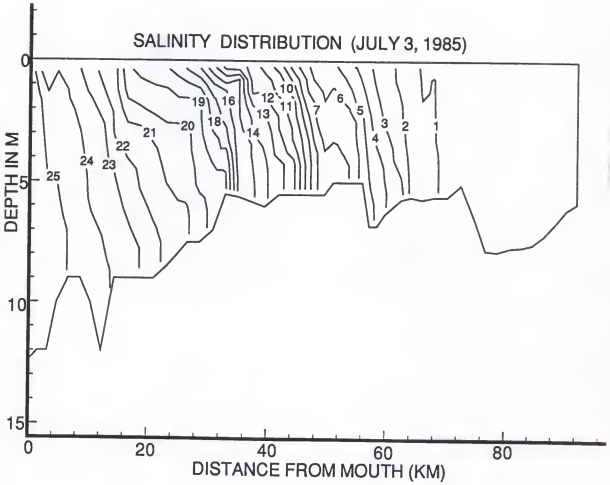

Figure 5.12: Simulated longitudinal-vertical salinity at slackwater before flood on July 3, 1985.

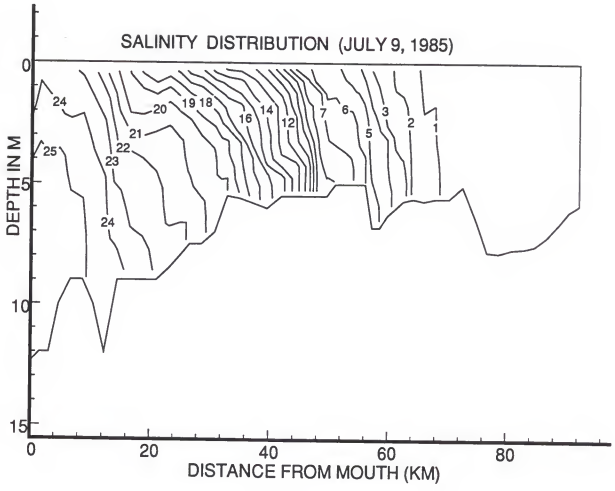

Figure 5.13: Simulated longitudinal-vertical salinity at slackwater before flood on July 9, 1985.

The degree of stratification can be related to buoyancy and mixing energy through the non-dimensional parameter M (Hansen and Rattray, 1965) which was defined in section 3.5. As M increases, stratification decreases until it becomes well-mixed. However, it is difficult to evaluate the mixing parameters and relate them to tidal action. Cerco (1982) used an alternative dimensionless quantity which expresses the ratio of buoyancy to mixing action with u_f/u_t, i.e., the ratio of freshwater velocity to tidal velocity. He divided two regions delineated by $\Delta s/s = 0.1$ and $u_f/u_t = 0.008$. For values of $u_f/u_t > 0.008$, observed stratification is generally greater than 10%. For values of $u_f/u_t < 0.008$, stratification is generally less than 10%. Spring tides produce stronger tidal currents, and hence more intense mixing than neap tides. According to his analysis in the James River data, the cyclical nature of stratification in the estuary and the relationship of the stratification-destratification cycle to the spring-neap tidal cycle are clear.

Model response to variation in tidal range was examined through the 29-day simulation of the baseline run (case 2). Figures 5.14, 5.15, and 5.16 show the salinity and velocity time-series during the 29-day period at three levels (surface, mid, and bottom level) at Station 1, Station 2, and Station 3, respectively. The effect of the spring-neap tidal cycle was apparent in the time series of salinity and velocity. An increase in tidal range during the spring tide results in an increase in velocity and a decrease in stratification while a decrease in tidal range results in an increase in stratification.

The near-surface longitudinal salinity distributions on July 3 (spring tide), on July 9 (neap tide), and July 17 (spring tide) during the 29-day simulation are shown in Figures 5.17, 5.18, and 5.19, respectively. The measured profile is generally within the range of the simulated salinity profiles. The range of variation in time changes according to the spring-neap tidal variation. It is clear that the vertical salinity profiles go through cycles of stratification and destratification in direct response to

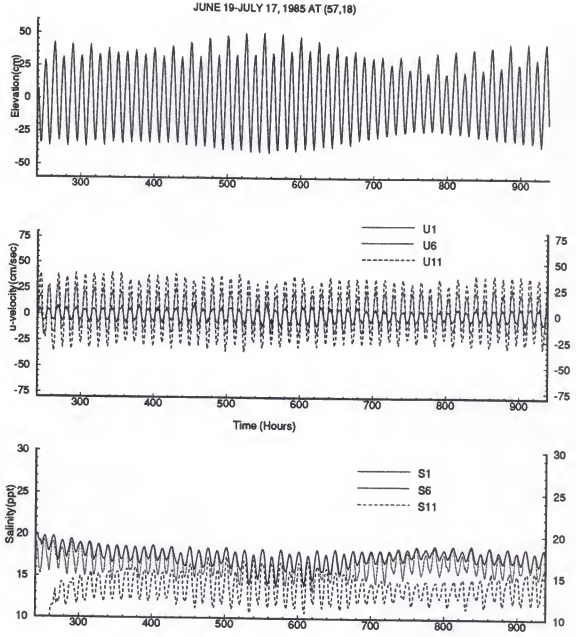

Figure 5.14: Computed elevation, and velocity and salinity at surface, mid, and bottom level for 29-day simulation at Station 1.

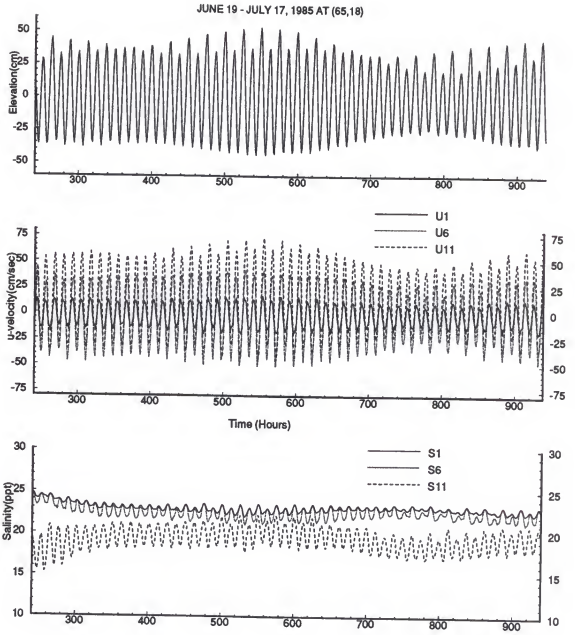

Figure 5.15: Computed elevation, and velocity and salinity at surface, mid, and bottom level for 29-day simulation at Station 2.

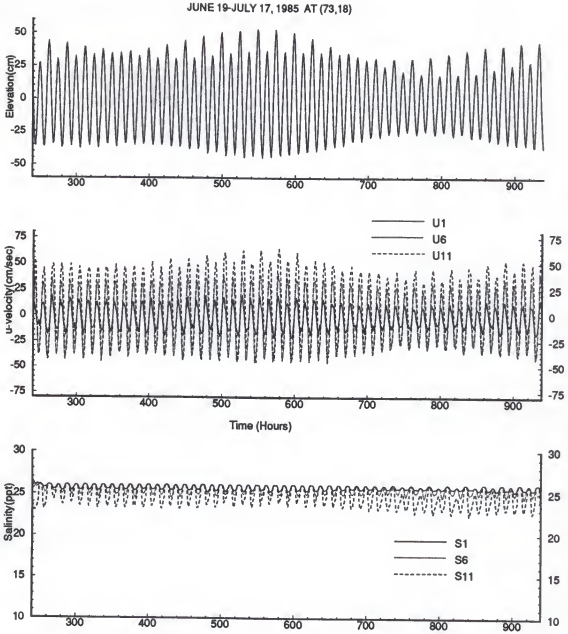

Figure 5.16: Computed elevation, and velocity and salinity at surface, mid, and bottom level for 29-day simulation at Station 3.

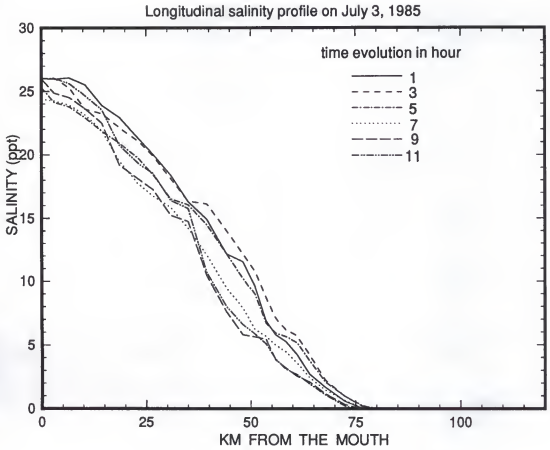

Figure 5.17: Model predicted longitudinal surface salinity distribution with 3000 ft^3/sec of river discharge on July 3, 1985.

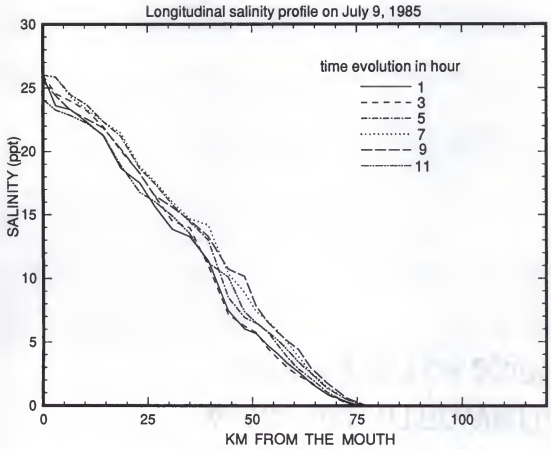

Figure 5.18: Model predicted longitudinal surface salinity distribution with 3000 ft^3/sec of river discharge on July 9, 1985.

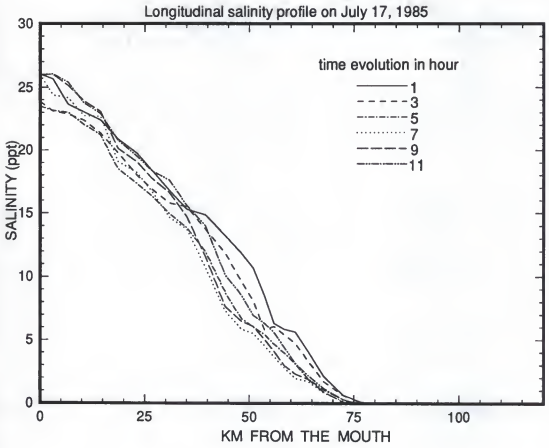

Figure 5.19: Model predicted longitudinal surface salinity distribution with 3000 ft^3/sec of river discharge on July 17, 1985.

the varying tidal conditions and vertical mixing in the water column.

Model results corresponding to the slackwater salinity distributions on July 3 and July 9, 1985 are presented in Figures 5.12 and 5.13. These model results exhibit a significant spring-to-neap variation in salinity distribution as was found in the measured data.

5.5 Salinity Intrusion

The salinity intrusion in an estuary is subjected to longitudinal displacement and changes in vertical structure as a result of variations in freshwater runoff and tidal motion. The location of the upstream limit of the salinity intrusion is determined primarily by the force balance between the downstream hydrostatic head of the freshwater flow and the upstream pressure gradient due to the longitudinal salinity gradient. The intrusion moves downstream with increasing freshwater runoff and upstream with decreasing runoff. In the James River, during summer and fall, low-flow conditions prevail and the intrusion gradually moves upstream until the high runoff during winter and spring recurs (Cerco, 1982). In this study, because of the lack of field data, model validation using time-varying river discharge was not made. Instead, a series of sensitivity tests with constant river discharge was performed to investigate the simulated response of the estuary to river flow. Figures 5.17-5.25 show the longitudinal salinity distribution at the surface level (K=11) along the channel (K=18) on July 3 (spring), on July 9 (neap), and on July 17 (spring), with a constant river flow rate of 3000 ft^3/s. Each figure contains 6 salinity distribution lines plotted with two hour increaments. The shapes of the curves are approximately described by the the hyperbolic tangent function which is common for many coastal-plain estuaries.

Hansen and Rattray (1965) developed a pair of steady-state stream-function equations describing circulation and salt balance in an estuary. They solved the equations by defining three salinity regimes: outer regime, central regime, and inner regime. In the central regime, the vertical salinity stratification is nearly independent of longi-

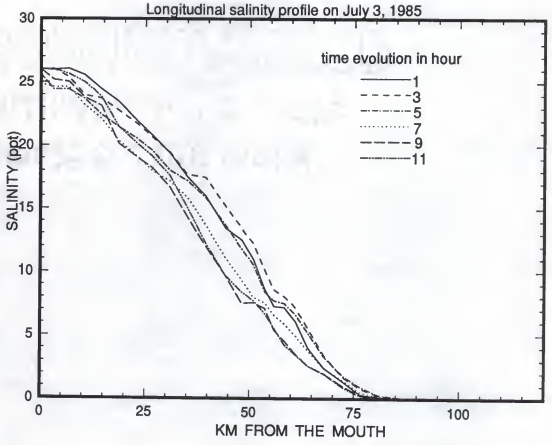

Figure 5.20: Model predicted longitudinal surface salinity distribution with 1000 ft^3/sec of river discharge on July 3, 1985.

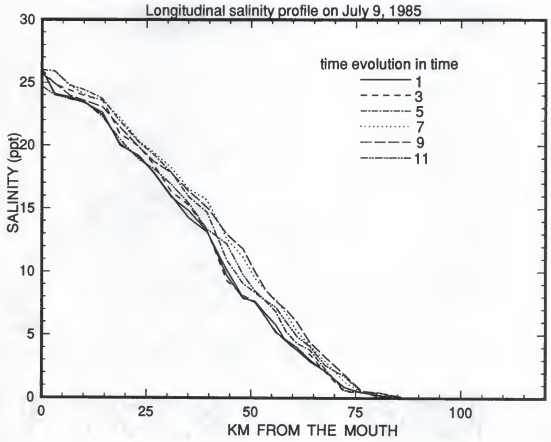

Figure 5.21: Model predicted longitudinal surface salinity distribution with 1000 ft^3/sec of river discharge on July 9, 1985.

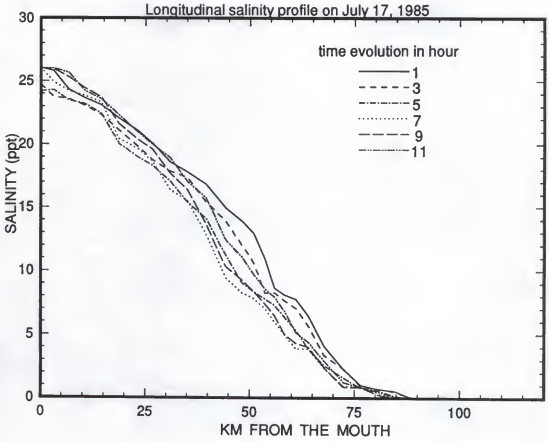

Figure 5.22: Model predicted longitudinal surface salinity distribution with 1000 ft^3/sec of river discharge on July 17, 1985.

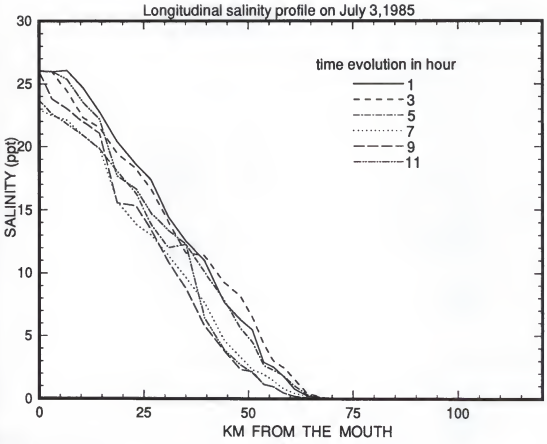

Figure 5.23: Model predicted longitudinal surface salinity distribution with 9000 ft^3/sec of river discharge on July 3, 1985.

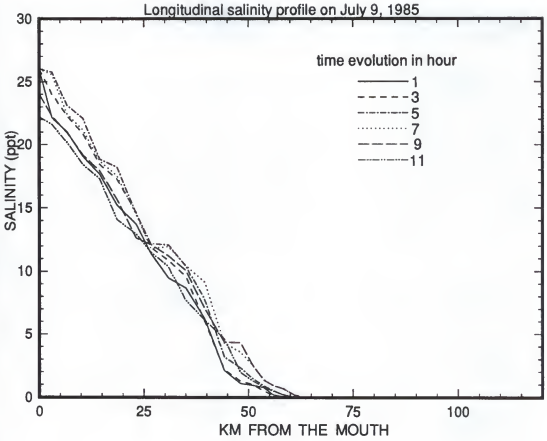

Figure 5.24: Model predicted longitudinal surface salinity distribution with 9000 ft^3/sec of river discharge on July 9, 1985.

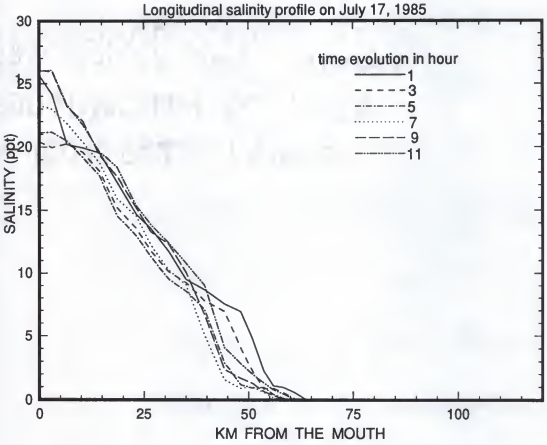

Figure 5.25: Model predicted longitudinal surface salinity distribution with 9000 ft^3/sec of river discharge on July 17, 1985.

tudinal position. In the inner and outer regimes, the degree of stratification becomes smaller in proportion to the distance from the central regime. However the shape of the longitudinal salinity profile constantly moves up and down the estuary in response to changes in river discharge. Figures 5.17-5.25 also show that the vertical range of salinity variation changes in accordance with the spring-neap variation. As expected, during spring tide the variation of salinity distribution is large, and the thickness, hence, is large.

Three additional river discharges were tested: 1000 ft^3/sec (Figures 5.20-5.22) which corresponds to low flow conditions, 3000 ft^3/sec (Figures 5.17-5.19) which corresponds to the average flow condition during the 29-day simulation starting June 19, 1985, and 9000 ft^3/sec (Figures 5.23-5.25) which is a usual mean annual value. With the largest river discharge of 9000 ft^3/sec, the head of salinity intrusion was found near 70 km from the mouth. With the smallest value of river discharge of 1000 ft^3/sec, the head of salinity intrusion was found near 90 km upstream. With 3000 ft^3/sec of river discharge, the head of salt intrusion was located around 80 km from the river mouth.

In the model simulation, concurrent with the high flow rate, the intrusion is pushed to its most downstream location. With low flow rate, the intrusion moves upstream. The salinity variation with time is larger at spring tide than at neap tide. Higher runoff also causes a larger salinity variation with time.

5.6 Frontal Dynamics

To examine this frontal structure in the model simulation, the model was run for 29 days starting from June 19, 1985 in the fine grid system (case 10). In the coarse grid system, it was hard to see a gyre or a convergence area because only 4 or 5 grid cells were constructed in the transverse direction and it was impossible to resolve the real depth configuration. In the fine grid system, the number of cells in the transverse direction was 8 or 9. With these grid cells, we could see a gyre because the

deep channel was resolved. The model results on July 3, 1985 were taken and plotted for one tidal cycle. Time step used here was 360 seconds. Hourly-plottings were made for instantaneous velocity field and salinity contour at the surface (Figures 5.26-5.36), and for instantaneous velocity flield and salinity contour at bottom (Figures 5.37-5.47). Velocity structures in u and w direction are also plotted along the channel (Figures 5.48-5.58) near Newport News and along the one-grid away from the channel (Figures 5.59-5.69), and time evolution of combined u, w, salinity, and elevation along the one-grid away from the channel (Figures 5.70-5.80), where u is at surface, w is at mid-depth, and salinity is at surface, mid, and bottom.

Two factors are essential to the formation of the front. They are the convergence of surface currents and the density contrast between the convergent flows. As the heavier water pushes against the lighter water at the convergence, it dives beneath the lighter water as a result of gravitational force. On the flood phase of tide, the incoming water in Hampton Roads meets the ebbing water of the lower James off Newport News Point (Figures 5.26-5.28). Especially a gyre was formed at hour 1 (Figures 5.26). Bottom currents also show a gyre circulation (Figures 5.37). This convergence zone near Newport News Point was maintained about 3 hours after the flood tide started at the mouth. The density difference between the two water masses is large enough to make the more saline Hampton Roads water dive beneath the fresh water of the lower James. When the salinity contour plots are compared with velocity fields (Figures 5.26-5.36 and Figures 5.37-5.47), the salinity contour lines move up and down according to velocity field. Therefore, the advection of the salinity plays an apparently important role for the salinity distribution. As the heavier water, either from Hampton Flats/Newport News Bar or flowing along Newport News Channel, meets the lighter water off Newport News Point, it also encounters an abrupt change of bottom topography. This steep topographic gradient not only enhances the diving of heavier water but also tends to stabilize the location of the front. Figures 5.59-5.62

show a clear picture of the topographical effects. We can see a plume type of current movement near the abrupt change of bottom topography. Also we can see a strong vertical transport. For the period of frontal zone formation, a gyre of vertical eddy motion appeared because of bottom topography and strong convergence of ebb and flood (Figures 5.50 and Figures 5.61). Figures 5.70-5.80 show the variation of salinity structure and vertical velocity during the front formation. The maximum downward vertical velocity was seen at hour 3 (Figure 5.72).

In the model simulation, strong vertical velocities are shown near the SBF through the front moving upestuary with time (Figures 5.59-5.62).

Results of current measurements indicate that flood tide currents on Hampton Flats lead the current along the Newport News Channel section. This is shown in the model simulation. Figure 5.26 shows a recirculation eddy on the east end of Hampton Flats while the current in the channel is still ebbing. This phenomenon was simulated in the hydraulic model test by Byrne (1987). When the currents within the channel section are slack, the flood current over the shallow Hampton Flats converges at Newport News Point (Figure 5.26). There it encounters ebbing water of less density than the lower and dives beneath the less dense water. As the front moves over the topographic gradient at the western end of the dredged channel, the increase in water depth slows down the upriver movement of the front and also increases the diving action of the surface water (Figure 5.27). The substantial lead of flood current on Hampton Flats over those in deep waters in the channel may be attributed to several mechanisms. The geometry near Newport News Point develops a topographic eddy, where the channel makes a 90° bend. As the ebb flow from the lower James tries to bend, a topographic eddy begins to evolve on the shallow flanks. Toward the late stage of ebb tide, the eddy is fully developed into a counterclockwise circulation over Hampton Flats. The circulation advances the flood phase of tide and enhances the strength of flood currents in its early stage. One dimensional

analysis of tidal dynamics indicates that the friction tends to advance the phase of tidal current relative to that of tidal stage (Ippen, 1966, p.509). Boundary layer theory also indicates that the oscillating current near the boundary will lead that of the interior flow (Lamb, 1962, p.620). Therefore it is expected that flood current on Hampton Flats would lead those in the channel. The friction due to both the shallow depth and lateral boundary, plays a role in the phase variation of tidal current around Newport News Point. Another mechanism in phase sequence is a damped co-oscillating tide. Newport News Point is about one-half tidal wave length from the head of tide. Therefore anti-node of a damped co-oscillating tide is located at this location. Tide table data show a local maximum of tidal range at this location, and a local minimum at an upriver location about one-quarter wave length from the head of tide. A damped co- oscillating tide would possess the same features. The flood current on the downriver side starts much earlier than that on the upriver side, resulting in convergent flow at the anti-node during the early stage of flood tide.

The density field exhibits the usual trends of a coastal plain estuary, with moderate density increases with depth and decreases with distance from the mouth. Observations have revealed that these trends are persistent features with highly localized, sharp horizontal gradients (fronts) in the near-surface density, occurring systematically at particular locations and during a particular phase of the tidal cycle. Early in the flood, a region of relatively strong vertical salinity gradient developed in the upriver side front. Also a region of strong horizontal gradient is found near the front. With time evolution, the front has moved upriver. These density field variations in the model simulation agree with the observed data by Byrne (1987) (Figures 5.26-5.36). In the longitudinal sections, in addition to the horizontal transition of the surface front, there is also an apparent deepening and steepening of the frontal zone as the flood tide progresses (Figures 5.81-5.91). However, this is not a straightforward change of position and shape of a well-defined interface. Rather, higher salinity water

has been incorporated into the downriver side of the high-gradient region, but the depth at which each isohaline approaches the horizontal on the upriver side remains nearly constant throughout the tidal cycle.

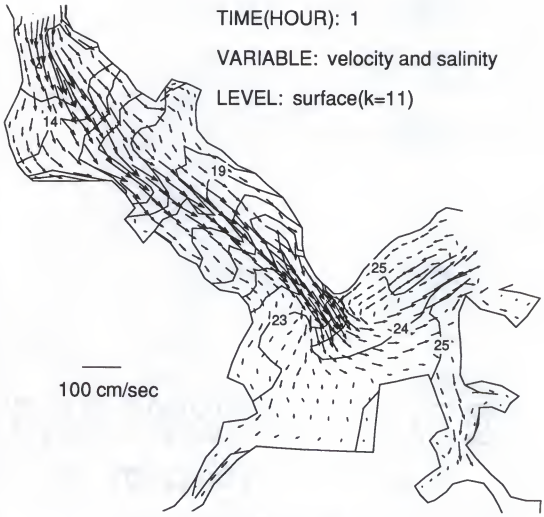

Figure 5.26: Instantaneous near-surface horizontal velocity and salinity (*ppt*) distribution in lower James River at 1 a.m. 1 on July 3, 1985.

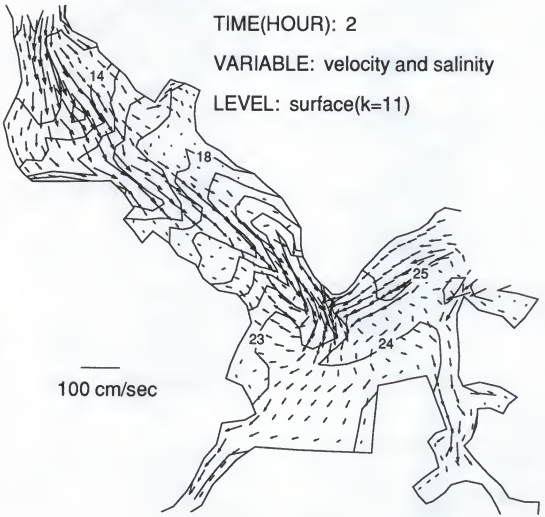

Figure 5.27: Instantaneous near-surface horizontal velocity and salinity (*ppt*) distribution in lower James River at 2 a.m. on July 3, 1985.

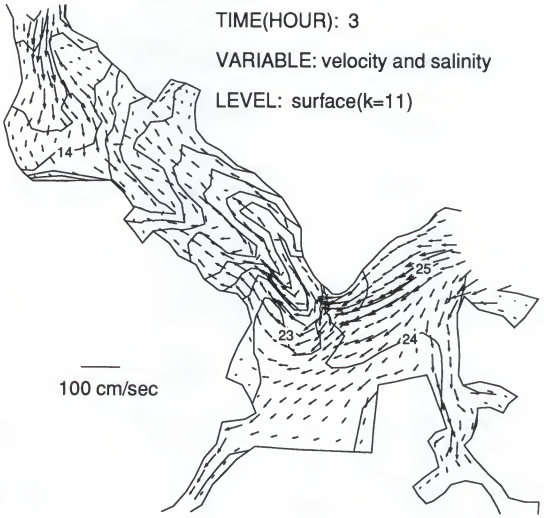

Figure 5.28: Instantaneous near-surface horizontal velocity and salinity (*ppt*) distribution in lower James River at 3 a.m. on July 3, 1985.

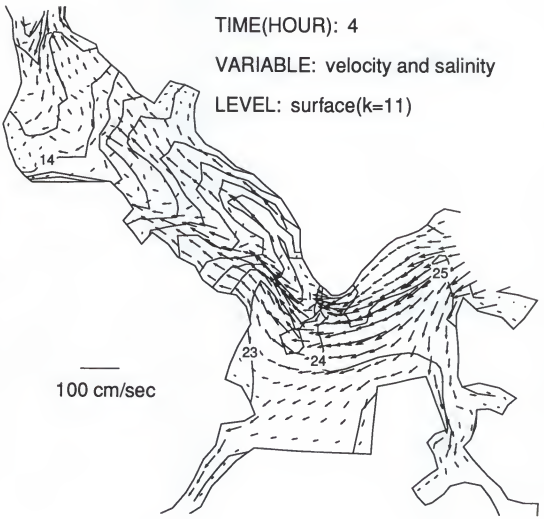

Figure 5.29: Instantaneous near-surface horizontal velocity and salinity (*ppt*) distribution in lower James River at 4 a.m. on July 3, 1985.

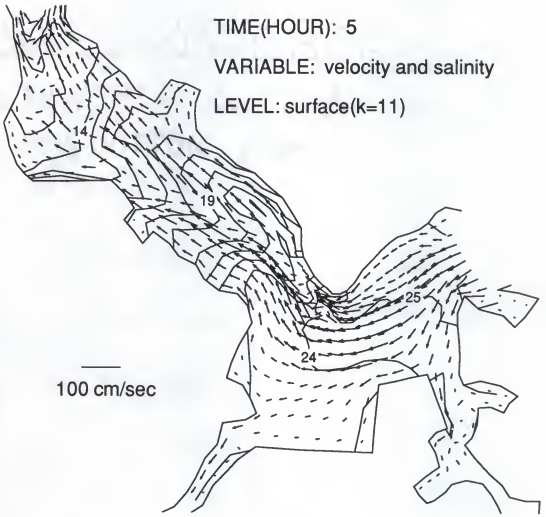

Figure 5.30: Instantaneous near-surface horizontal velocity and salinity (*ppt*) distribution in lower James River at 5 a.m. on July 3, 1985.

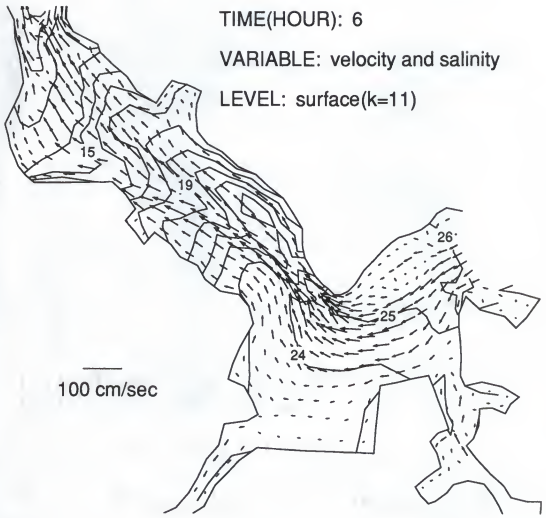

Figure 5.31: Instantaneous near-surface horizontal velocity and salinity (*ppt*) distribution in lower James River at 6 a.m. on July 3, 1985.

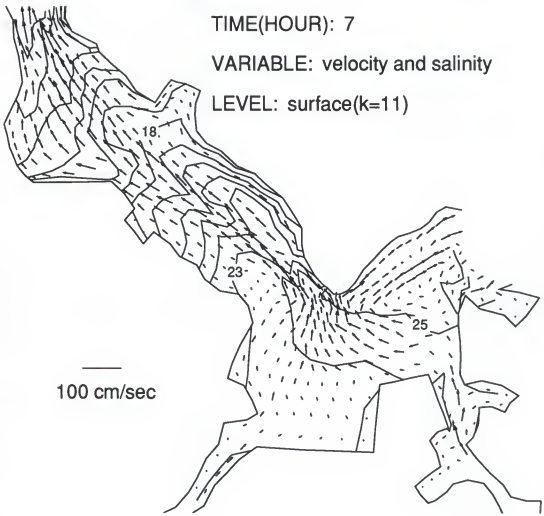

Figure 5.32: Instantaneous near-surface horizontal velocity and salinity (*ppt*) distribution in lower James River at 7 a.m. on July 3, 1985.

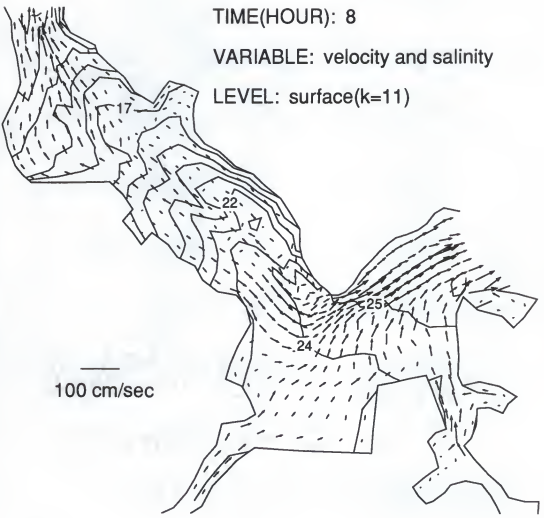

Figure 5.33: Instantaneous near-surface horizontal velocity and salinity (*ppt*) distribution in lower James River at 8 a.m. on July 3, 1985.

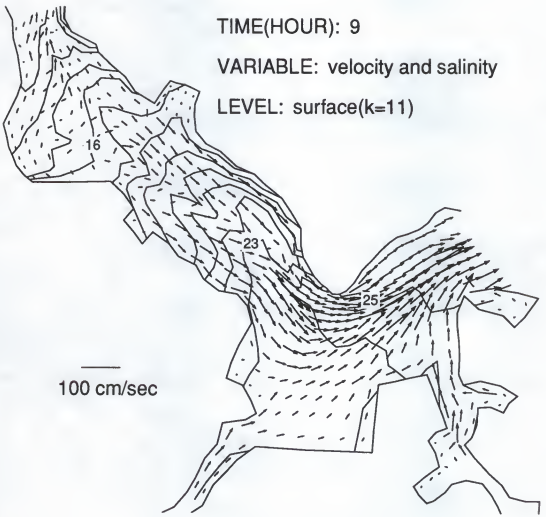

Figure 5.34: Instantaneous near-surface horizontal velocity and salinity (*ppt*) distribution in lower James River at 9 a.m. on July 3, 1985.

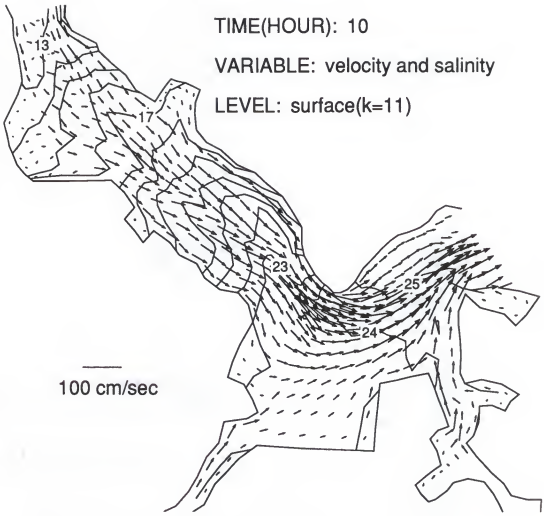

Figure 5.35: Instantaneous near-surface horizontal velocity and salinity (*ppt*) distribution in lower James River at 10 a.m. on July 3, 1985.

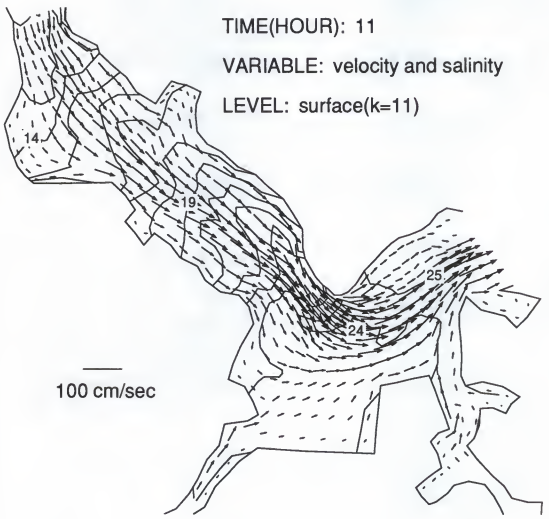

Figure 5.36: Instantaneous near-surface horizontal velocity and salinity (*ppt*) distribution in lower James River at 11 a.m. on July 3, 1985.

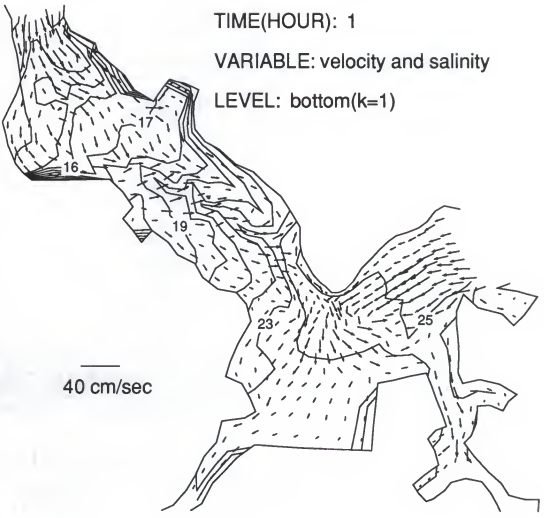

Figure 5.37: Instantaneous near-bottom horizontal velocity and salinity (*ppt*) distribution in lower James River at 1 a.m. on July 3, 1985.

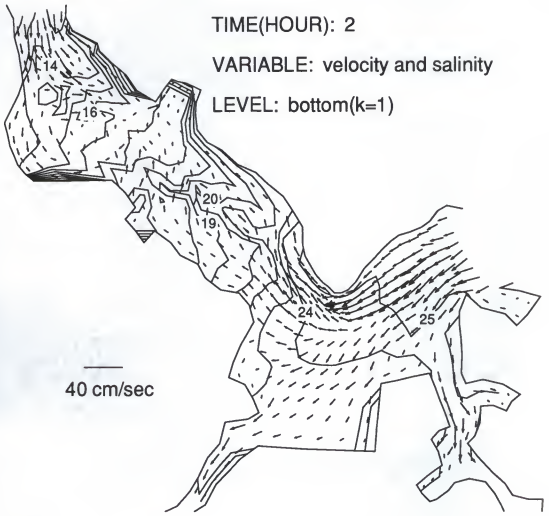

Figure 5.38: Instantaneous near-bottom horizontal velocity and salinity (*ppt*) distribution in lower James River at 2 a.m. on July 3, 1985.

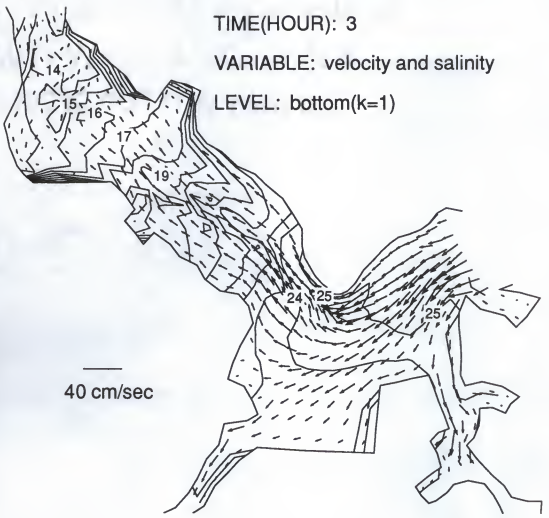

Figure 5.39: Instantaneous near-bottom horizontal velocity and salinity (*ppt*) distribution in lower James River at 3 a.m. on July 3, 1985.

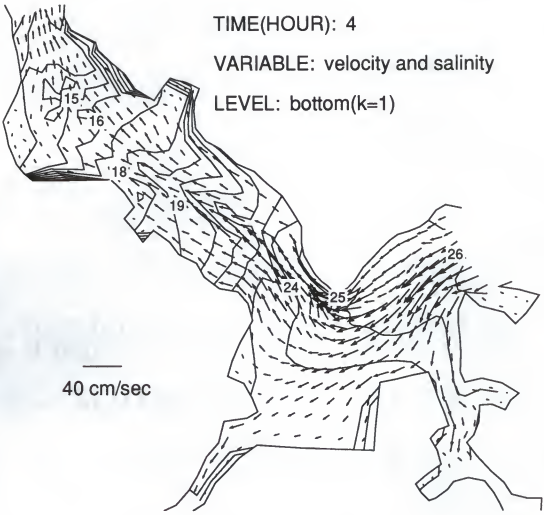

Figure 5.40: Instantaneous near-bottom horizontal velocity and salinity (*ppt*) distribution in lower James River at 4 a.m. on July 3, 1985.

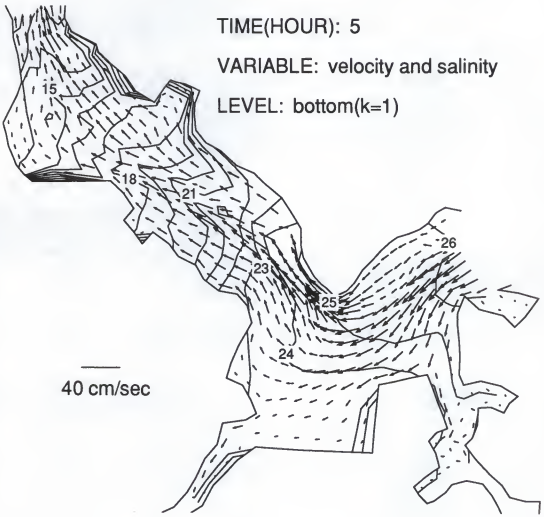

Figure 5.41: Instantaneous near-bottom horizontal velocity and salinity (*ppt*) distribution in lower James River at 5 a.m. on July 3, 1985.

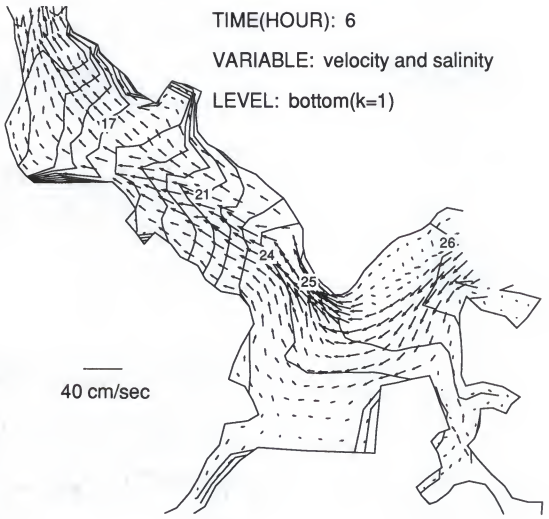

Figure 5.42: Instantaneous near-bottom horizontal velocity and salinity (*ppt*) distribution in lower James River at 6 a.m. on July 3, 1985.

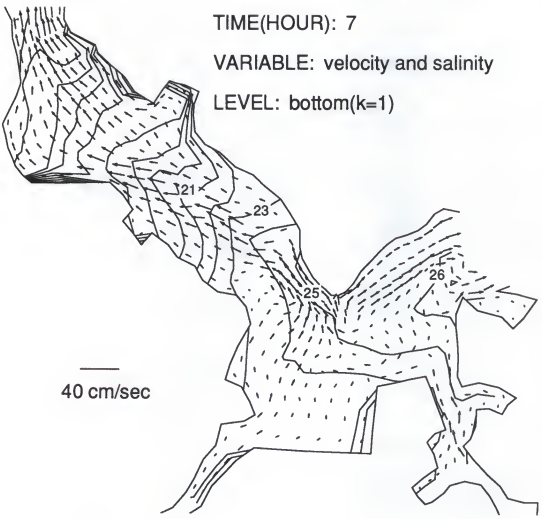

Figure 5.43: Instantaneous near-bottom horizontal velocity and salinity (*ppt*) distribution in lower James River at 7 a.m. on July 3, 1985.

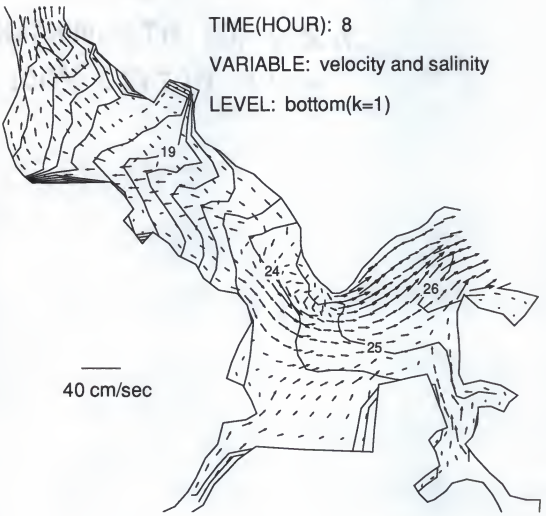

Figure 5.44: Instantaneous near-bottom horizontal velocity and salinity (*ppt*) distribution in lower James River at 8 a.m. on July 3, 1985.

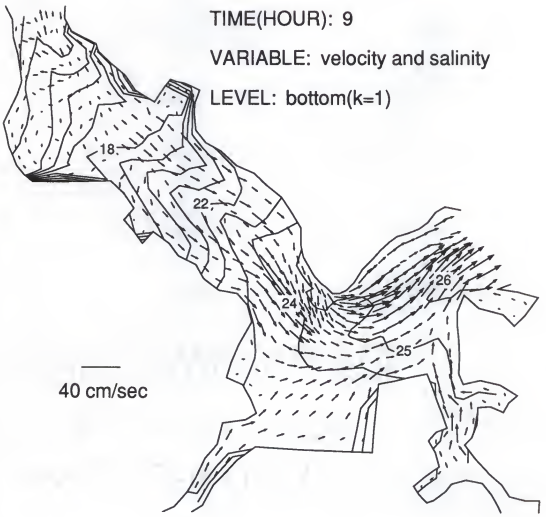

Figure 5.45: Instantaneous near-bottom horizontal velocity and salinity (*ppt*) distribution in lower James River at 9 a.m. on July 3, 1985.

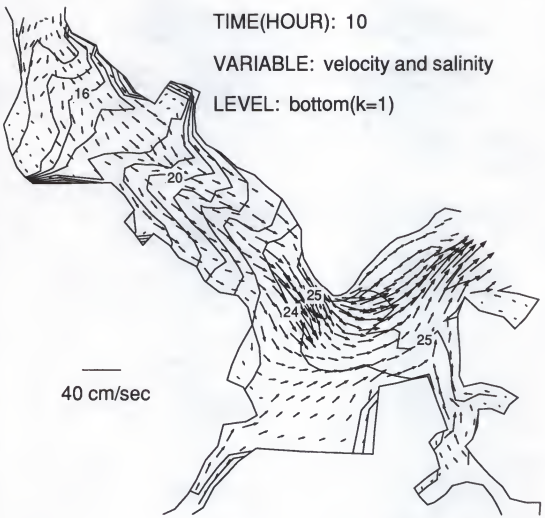

Figure 5.46: Instantaneous near-bottom horizontal velocity and salinity (*ppt*) distribution in lower James River at 10 a.m. on July 3, 1985.

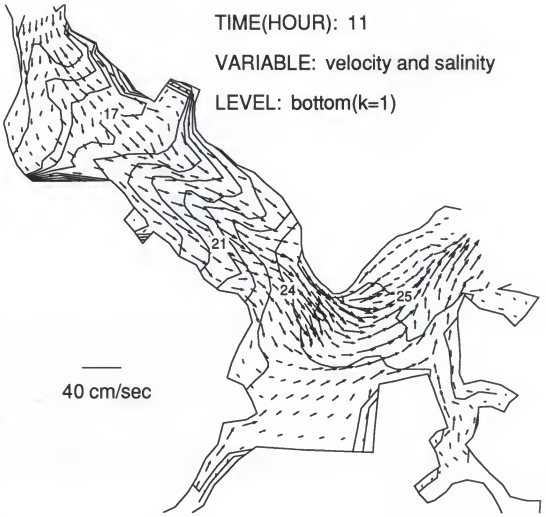

Figure 5.47: Instantaneous near-bottom horizontal velocity and salinity (*ppt*) distribution in lower James River at 11 a.m. on July 3, 1985.

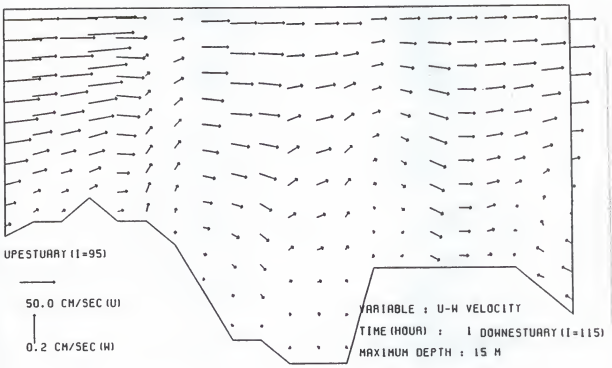

Figure 5.48: Instantaneous velocity in (x, z) domain along the channel in lower James River at 1 a.m. on July 3, 1985.

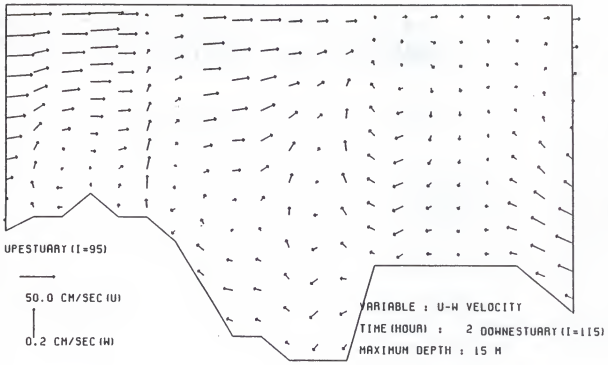

Figure 5.49: Instantaneous velocity in (x, z) domain along the channel in lower James River at 2 a.m. on July 3, 1985.

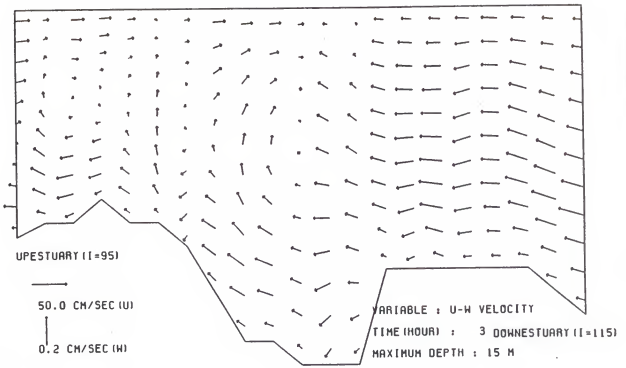

Figure 5.50: Instantaneous velocity in (x, z) domain along the channel in lower James River at 3 a.m. on July 3, 1985.

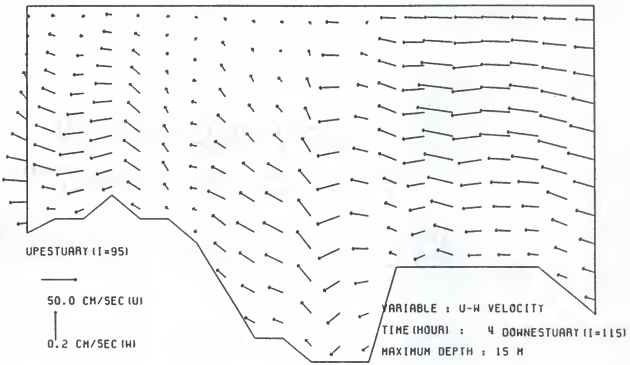

Figure 5.51: Instantaneous velocity in (x, z) domain along the channel in lower James River at 4 a.m. on July 3, 1985.

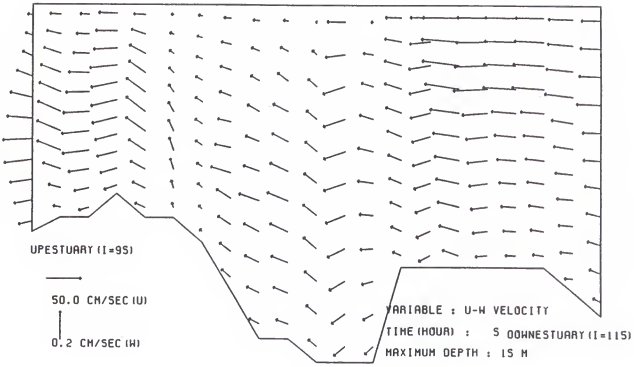

Figure 5.52: Instantaneous velocity in (x, z) domain along the channel in lower James River at 5 a.m. on July 3, 1985.

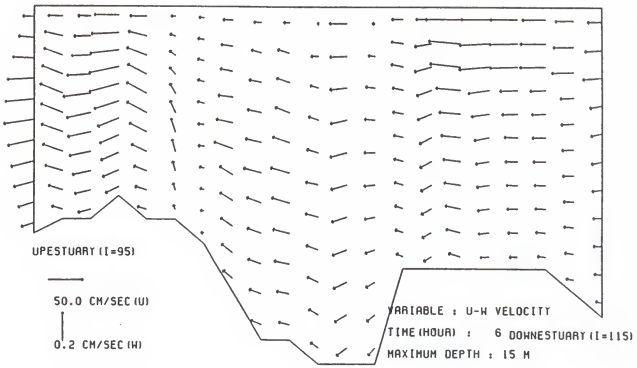

Figure 5.53: Instantaneous velocity in (x, z) domain along the channel in lower James River at 6 a.m. on July 3, 1985.

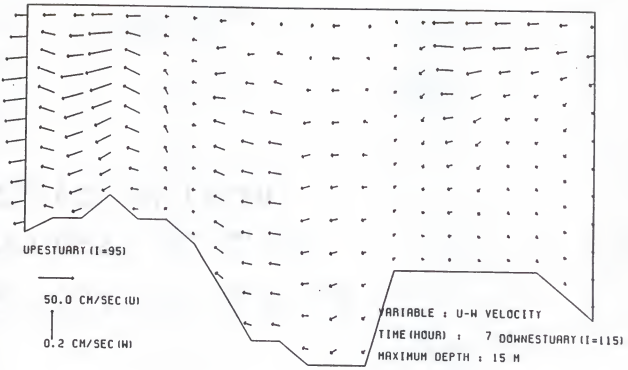

Figure 5.54: Instantaneous velocity in (x, z) domain along the channel in lower James River at 7 a.m. on July 3, 1985.

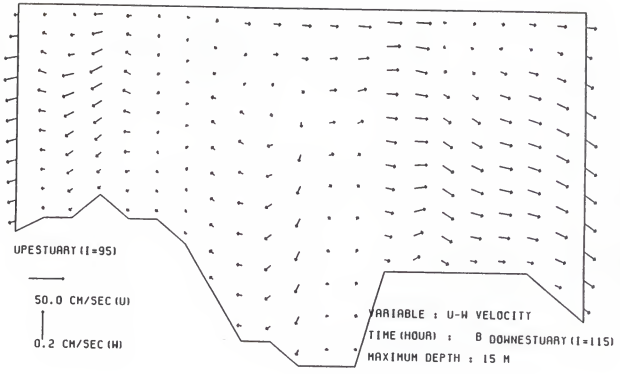

Figure 5.55: Instantaneous velocity in (x, z) domain along the channel in lower James River at 8 a.m. on July 3, 1985.

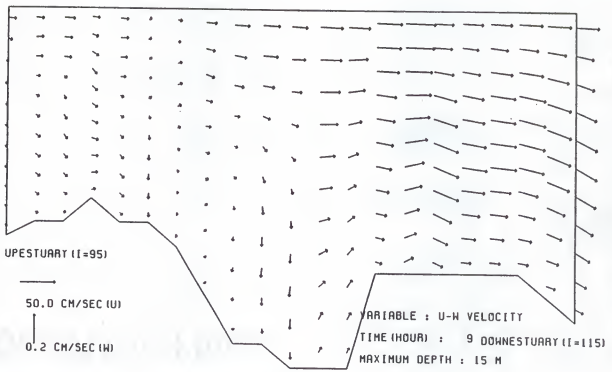

Figure 5.56: Instantaneous velocity in (x, z) domain along the channel in lower James River at 9 a.m. on July 3, 1985.

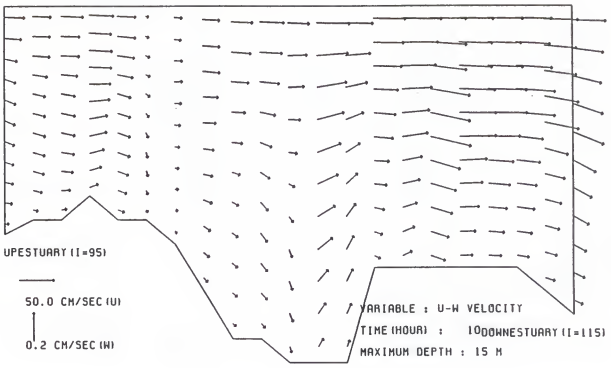

Figure 5.57: Instantaneous velocity in (x, z) domain along the channel in lower James River at 10 a.m. on July 3, 1985.

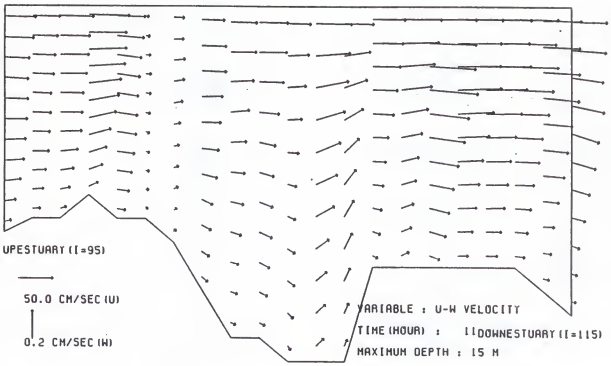

Figure 5.58: Instantaneous velocity in (x, z) domain along the channel in lower James River at 11 a.m. on July 3, 1985.

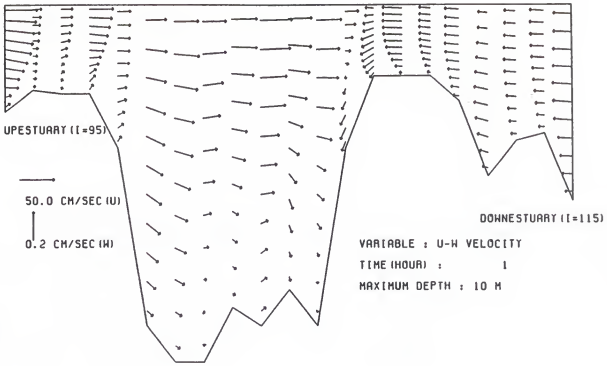

Figure 5.59: Instantaneous velocity in (x, z) domain along the one-grid away from the channel in lower James River at 1 a.m. on July 3, 1985.

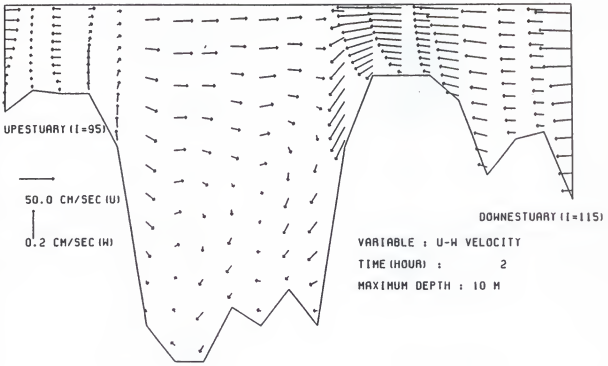

Figure 5.60: Instantaneous velocity in (x, z) domain along the one-grid away from the channel in lower James River at 2 a.m. on July 3, 1985.

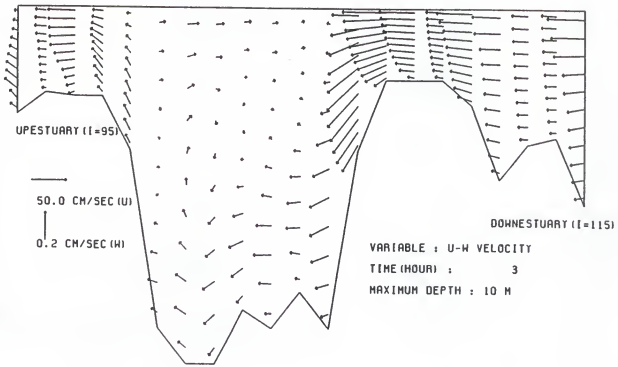

Figure 5.61: Instantaneous velocity in (x, z) domain along the one-grid away from the channel in lower James River at 3 a.m. on July 3, 1985.

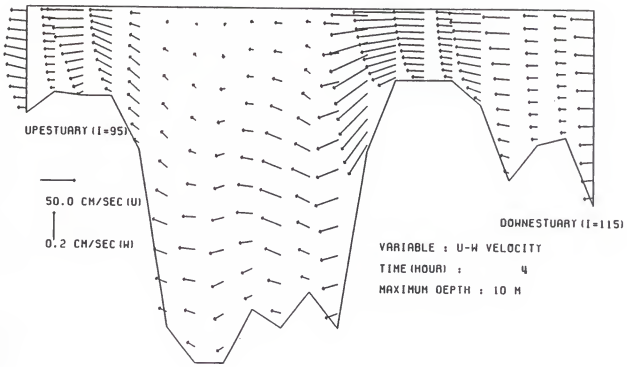

Figure 5.62: Instantaneous velocity in (x, z) domain along the one-grid away from the channel in lower James River at 4 a.m. on July 3, 1985.

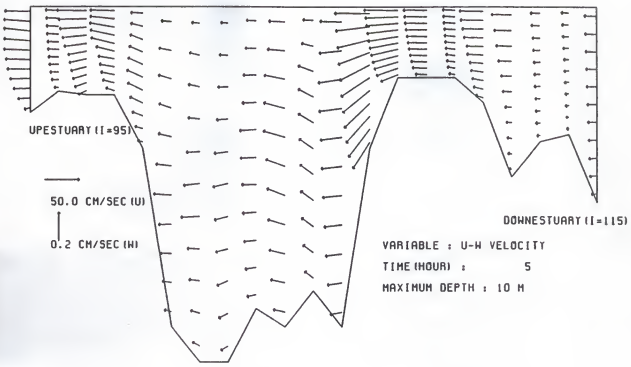

Figure 5.63: Instantaneous velocity in (x, z) domain along the one-grid away from the channel in lower James River at 5 a.m. on July 3, 1985.

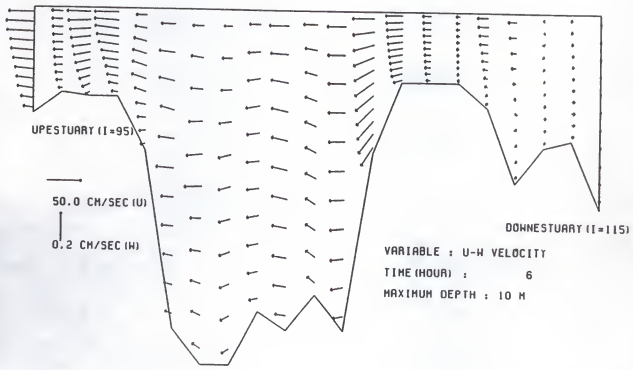

Figure 5.64: Instantaneous velocity in (x, z) domain along the one-grid away from the channel in lower James River at 6 a.m. on July 3, 1985.

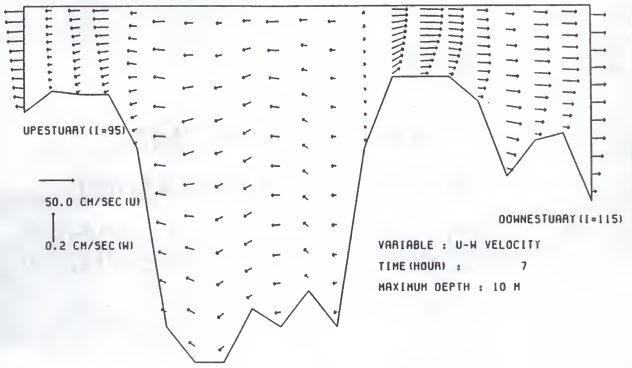

Figure 5.65: Instantaneous velocity in (x, z) domain along the one-grid away from the channel in lower James River at 7 a.m. on July 3, 1985.

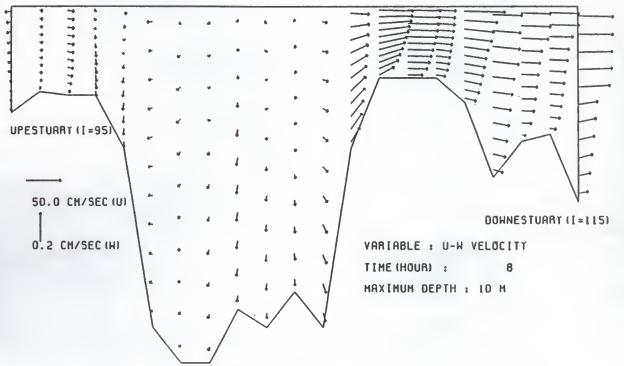

Figure 5.66: Instantaneous velocity in (x, z) domain along the one-grid away from the channel in lower James River at 8 a.m. on July 3, 1985.

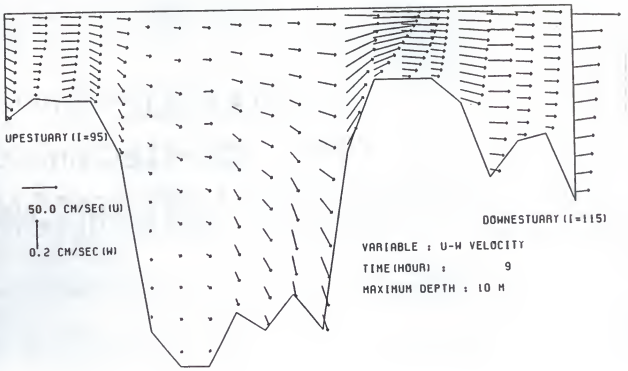

Figure 5.67: Instantaneous velocity in (x, z) domain along the one-grid away from the channel in lower James River at 9 a.m. on July 3, 1985.

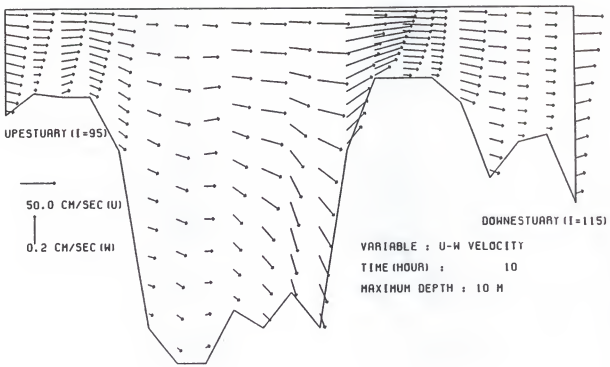

Figure 5.68: Instantaneous velocity in (x, z) domain along the one-grid away from the channel in lower James River at 10 a.m. on July 3, 1985.

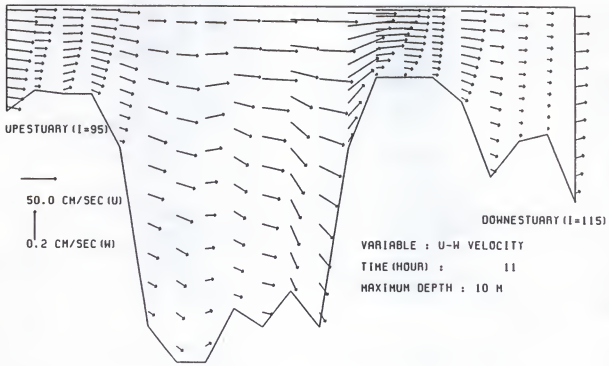

Figure 5.69: Instantaneous velocity in (x, z) domain along the one-grid away from the channel in lower James River at 11 a.m. on July 3, 1985.

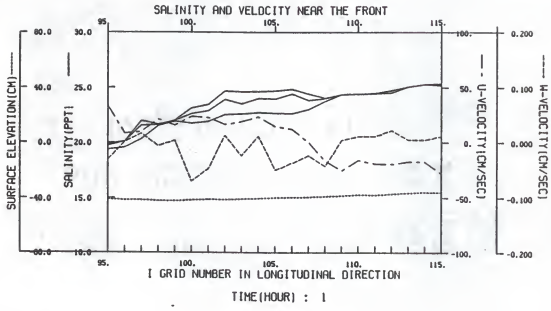

Figure 5.70: u at surface, w at mid-depth, salinity at surface-, mid-, and bottom-depth, and elevation along the one-grid away from the channel in lower James River at 1 a.m. on July 3, 1985.

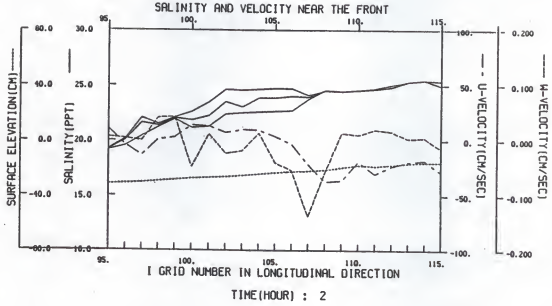

Figure 5.71: u at surface, w at mid-depth, salinity at surface-, mid-, and bottom-depth, and elevation along the one-grid away from the channel in lower James River at 2 a.m. on July 3, 1985.

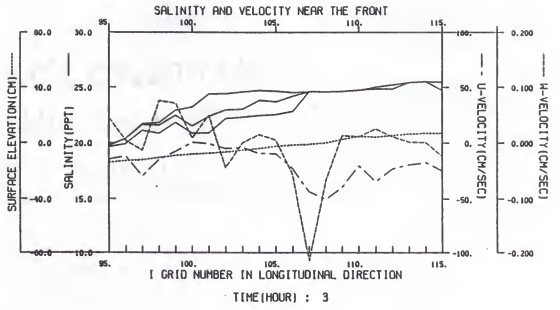

Figure 5.72: u at surface, w at mid-depth, salinity at surface-, mid-, and bottom-depth, and elevation along the one-grid away from the channel in lower James River at 3 a.m. on July 3, 1985.

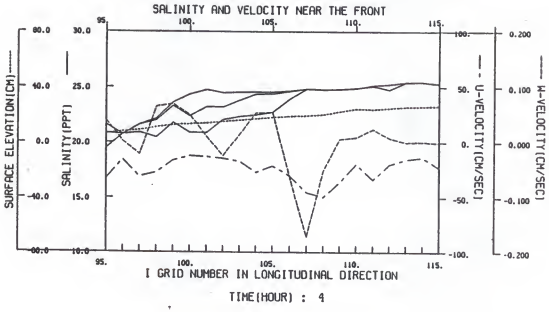

Figure 5.73: u at surface, w at mid-depth, salinity at surface-, mid-, and bottom-depth, and elevation along the one-grid away from the channel in lower James River at 4 a.m. on July 3, 1985.

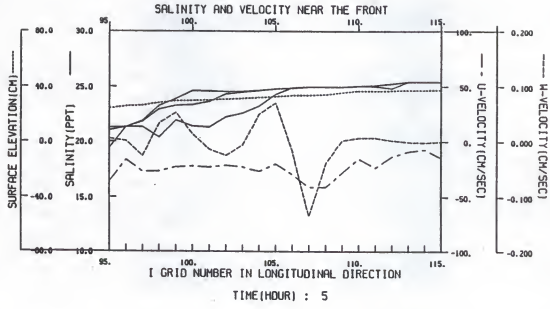

Figure 5.74: u at surface, w at mid-depth, salinity at surface-, mid-, and bottom-depth, and elevation along the one-grid away from the channel in lower James River at 5 a.m. on July 3, 1985.

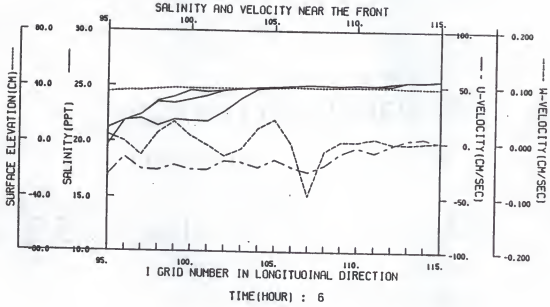

Figure 5.75: u at surface, w at mid-depth, salinity at surface-, mid-, and bottom-depth, and elevation along the one-grid away from the channel in lower James River at 6 a.m. on July 3, 1985.

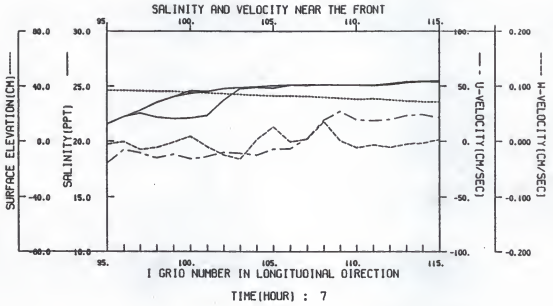

Figure 5.76: u at surface, w at mid-depth, salinity at surface-, mid-, and bottom-depth, and elevation along the one-grid away from the channel in lower James River at 7 a.m. on July 3, 1985.

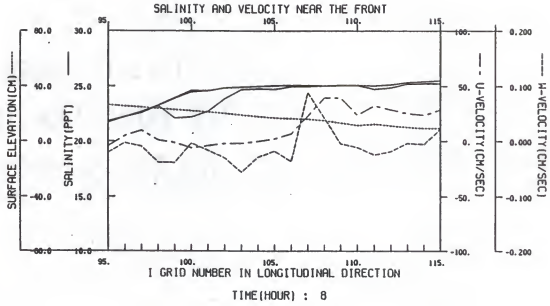

Figure 5.77: u at surface, w at mid-depth, salinity at surface-, mid-, and bottom-depth, and elevation along the one-grid away from the channel in lower James River at 8 a.m. on July 3, 1985.

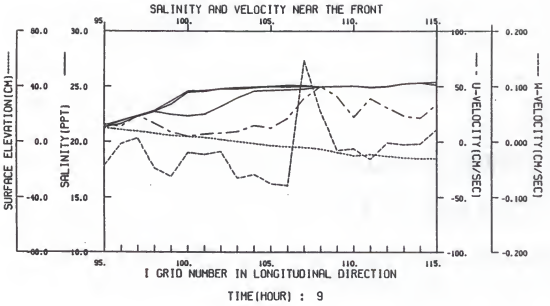

Figure 5.78: u at surface, w at mid-depth, salinity at surface-, mid-, and bottom-depth, and elevation along the one-grid away from the channel in lower James River at 9 a.m. on July 3, 1985.

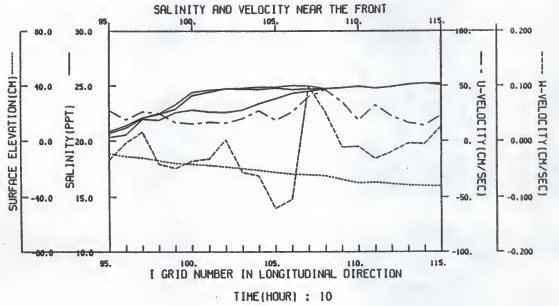

Figure 5.79: u at surface, w at mid-depth, salinity at surface-, mid-, and bottom-depth, and elevation along the one-grid away from the channel in lower James River at 10 a.m. on July 3, 1985.

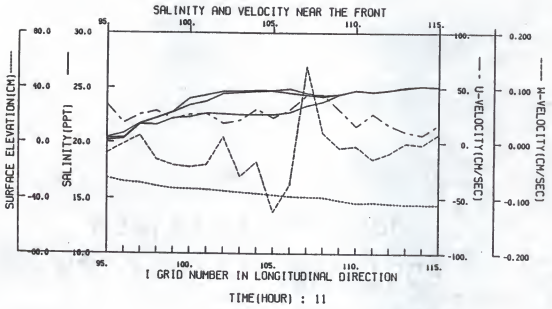

Figure 5.80: u at surface, w at mid-depth, salinity at surface-, mid-, and bottom-depth, and elevation along the one-grid away from the channel in lower James River at 11 a.m. on July 3, 1985.

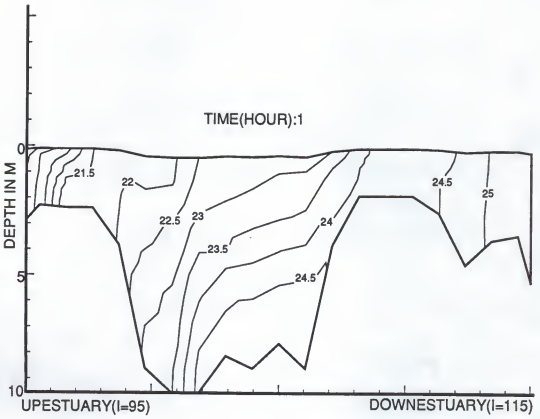

Figure 5.81: Salinity contours (ppt) in (x, z) domain along the one-grid away from the channel in lower James River at 1 a.m. on July 3, 1985.

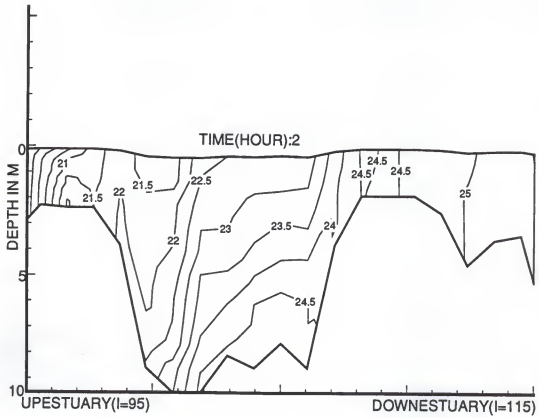

Figure 5.82: Salinity contours (ppt) in (x, z) domain along the one-grid away from the channel in lower James River at 2 a.m. on July 3, 1985.

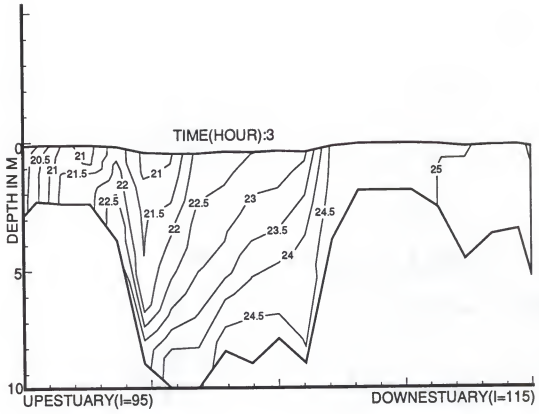

Figure 5.83: Salinity contours (ppt) in (x, z) domain along the one-grid away from the channel in lower James River at 3 a.m. on July 3, 1985.

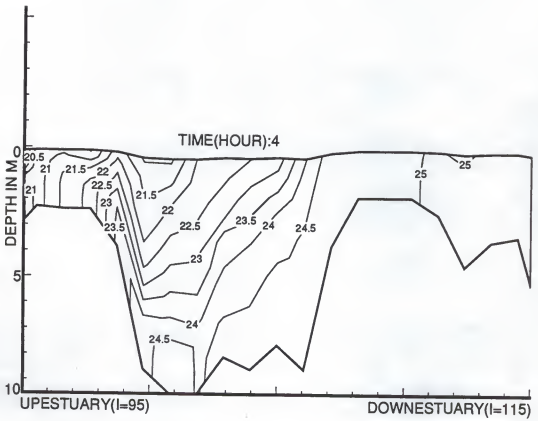

Figure 5.84: Salinity contours (ppt) in (x, z) domain along the one-grid away from the channel in lower James River at 4 a.m. on July 3, 1985.

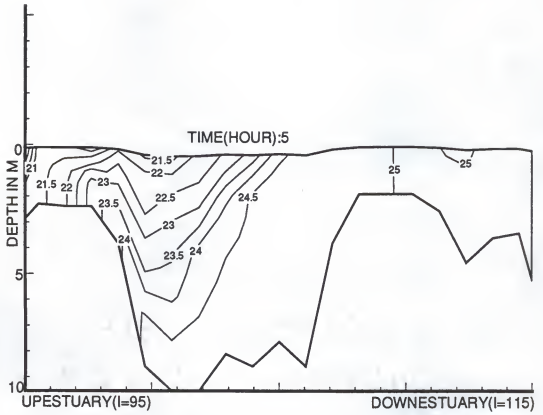

Figure 5.85: Salinity contours (ppt) in (x, z) domain along the one-grid away from the channel in lower James River at 5 a.m. on July 3, 1985.

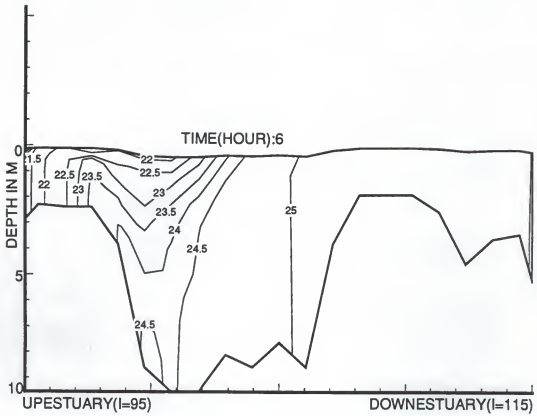

Figure 5.86: Salinity contours (ppt) in (x, z) domain along the one-grid away from the channel in lower James River at 6 a.m. on July 3, 1985.

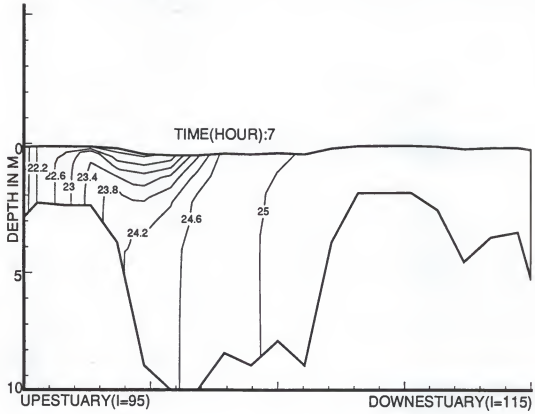

Figure 5.87: Salinity contours (ppt) in (x, z) domain along the one-grid away from the channel in lower James River at 7 a.m. on July 3, 1985.

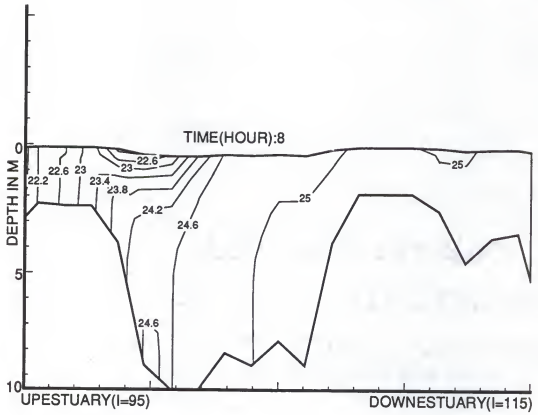

Figure 5.88: Salinity contours (ppt) in (x, z) domain along the one-grid away from the channel in lower James River at 8 a.m. on July 3, 1985.

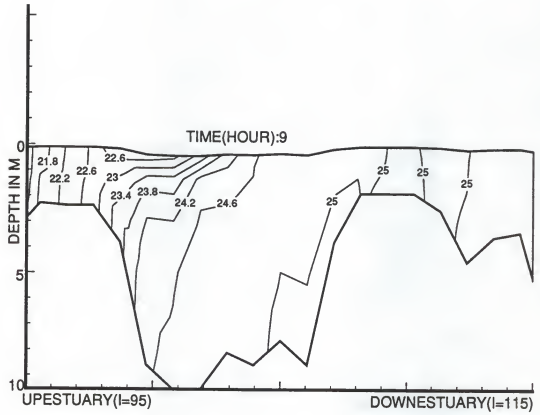

Figure 5.89: Salinity contours (*ppt*) in (x, z) domain along the one-grid away from the channel in lower James River at 9 a.m. on July 3, 1985.

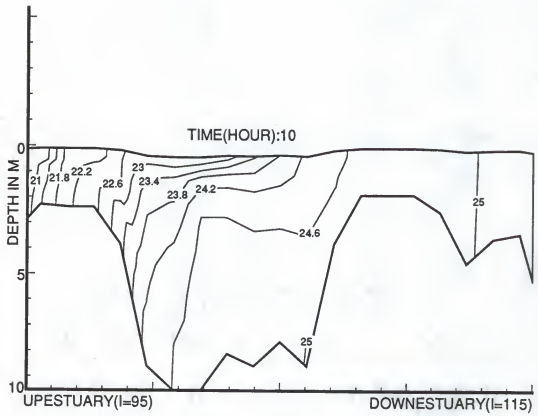

Figure 5.90: Salinity contours (*ppt*) in (x, z) domain along the one-grid away from the channel in lower James River at 10 a.m. on July 3, 1985.

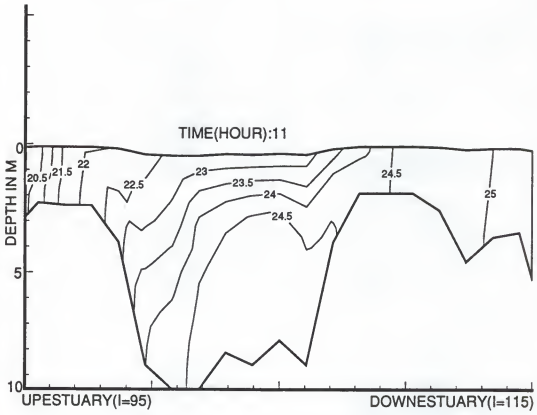

Figure 5.91: Salinity contours (*ppt*) in (x, z) domain along the one-grid away from the channel in lower James River at 11 a.m. on July 3, 1985.

5.7 Model Calibration and Validation

Usually model performance has been assessed based on the subjective inspection of plotting results. The objective analysis of model performance is important because it tells model skill quantitatively and makes it possible to compare one model to others. NOS recently proposed the standards for tides and currents as an assessment of model accuracy. To quantify differences between model output and observed data, Hess (1991) performed statistical analysis of model values and observed values, including rms differences, gain, mean time lag, and rms time lag. Sheng and Peene (1992) used similar statistical analysis to compare their model results with observed water level and current in Tampa Bay and Sarasota Bay.

First consider a series of demeaned observed values, y_i (for $i = 1, \cdots, n$), and a series of demeaned model output values, $\hat{y}_i$, with the same starting time, the same number of values, and uniform time intervals. The difference between values in the modeled and observed time series is

$$d_i = \hat{y}_i - y_i \tag{5.5}$$

and the rms difference is

$$D_{rms} = [\sum_{i=1}^{n} (d_i)^2 / n]^{1/2} \tag{5.6}$$

Since tidal forcing is important in most estuaries, statistics for tidal extrema (highs and lows, floods and ebbs) are used for the statistical analysis. The observed extrema Y_j at times T_j, for $j = 1, 2, \cdots, N$ and the model extrema $\hat{Y}_j$ at times $\hat{T}_j$, for $j = 1, 2, \cdots, \hat{N}$ are found. The mean tidal range, R is

$$R = (\frac{2}{N}) \sum_{j=1}^{N} |Y_j| \tag{5.7}$$

Range is defined as difference from maximum to minimum. Since observed tide ranges can vary widely from station to station, a more meaningful statistic is the ratio of the

rms difference to the mean range (R),

$$D' = D_{rms}/R \tag{5.8}$$

The observed and modeled extrema are then compared by selecting for each individual observed extremum and the closest modeled extremum. There will be ν pairs. A gain (G), ratio of modeled to observed extrema amplitude, is defined as

$$G = \sum_{j=1}^{\nu} (\hat{Y}_{j'}/Y_j)/\nu \tag{5.9}$$

When the observed tide range is non-uniform and small, a weighted gain (G_w) is used with the weight being equal to the individual modeled range divided by R.

$$G_w = (\frac{2}{R}) \sum_{j=1}^{\hat{N}} |\hat{Y}_j|/\hat{N} \tag{5.10}$$

The weighted gain describes characteristics of the whole series. The rms differences for extrema (E_{rms}) gives the information on individual differences, which can be expressed,

$$E_{rms} = [\sum_{j=1}^{\nu} (\hat{Y}_{j'} - Y_j)^2/\nu]^{1/2} \tag{5.11}$$

For phase differences, a mean time lag (L_m) for the extrema is defined as

$$L_m = \sum_{j=1}^{\nu} (\hat{T}_{j'} - T_j)/\nu \tag{5.12}$$

The rms lag (L_{rms}) is defined as

$$L_{rms} = [\sum_{j=1}^{\nu} (\hat{T}_{j'} - T_j)^2/\nu]^{1/2} \tag{5.13}$$

The L_m can show the modeled wave speed errors as a lag (or lead) at all stations. But the L_{rms} is valuable when L_m is small. When the results from stations are compared, these multistation summary statistics are referred to as global quantities,

$$F = (\sum_{i=1}^{s} h\nu_i F_i)/(\sum_{i=1}^{s} h\nu_i) \tag{5.14}$$

where ν is the number of data pairs, h is the sampling interval for each station, and s is the number of stations.

Now the ratio of the E_{rms} difference to the mean range (R) and the ratio of L_{rms} to 6.21 hours (one fourth of M2 tidal period) are used to calculate the model skill parameters ($E' = E_{rms}/R$ and $L' = L_{rms}/6.21$). L' approximates the maximum time between extrema. Three skill parameters are obtained, which are $S_D = 1 - D'$, $S_E = 1 - E'$, and $S_L = 1 - L'$. These skill parameters can be used to judge model accuracy.

During the sensitivity analysis, model inputs are varied to assess changes in the solution for the parameters of interest. The results of a 29-day run for water levels and currents are shown in Table 5.9, Table 5.10, Table 5.11, and Table 5.12. Case 2 was chosen as a calibrated result, which used the law of the wall with the Monin-Oboukhov length with bottom roughness height 0.4 *cm*. Hourly rms amplitude differences (D_{rms}=0.03) are small, model gain ($G_w = 1.01$) is nearly unity, and rms time differences ($L_{rms} = 30 minutes$) are relatively high. Mean lag ($L_m = -4 minutes$) is small and suggests no bias in propagation speed errors. Model skill parameters are all greater than 95 %.

Statistics for water currents from the same run of case 2 are shown in Table 5.11. Model gain for currents ($G_w = 0.87$) showed that the currents were underestimated. The rms time differences ($L_{rms} = 36$ *minutes*) was large, and mean lag ($L_m = 22$ *minutes*) was worse compared to that in the water elevation. Model skill parameters are about 90 % ($S_D = 88\%$, $S_E = 90\%$, $S_L = 90\%$). The model can be improved by the increase of the model grid resolution and the more accurate bottom topography.

The results from the calibration runs show that all the individual model skill parameters for the surface elevations are greater than 90 %, so small changes in the roughness height and bottom friction coefficient are not so significant.

Table 5.9: Model skill parameters for the sensitivity test to surface elevation at Station 1.

	R	D_{rms}	D_{rms}/R	ν	G_w	E_{rms}	L_m	L_{rms}
case1	65.85	4.78	0.07	111	1.18	6.59	-0.03	0.37
case2	65.85	2.46	0.04	111	1.04	2.27	-0.09	0.36
case3	65.85	4.19	0.06	111	1.17	5.59	-0.03	0.37
case4	65.85	2.64	0.04	111	1.09	3.63	-0.01	0.37
case5	65.85	3.09	0.05	111	1.11	4.23	0.02	0.36
case6	65.85	5.00	0.08	111	1.18	6.59	-0.07	0.42
case7	65.85	4.87	0.07	111	1.18	6.61	0.00	0.40
case8	65.85	4.66	0.07	111	1.18	6.42	0.02	0.38

Table 5.10: Model skill parameters for the sensitivity test to surface elevation at Station 2.

	R	D_{rms}	D_{rms}/R	ν	G_w	E_{rms}	L_m	L_{rms}
case1	72.12	3.11	0.04	111	1.04	2.62	0.09	0.40
case2	72.12	1.89	0.03	111	0.99	1.84	-0.05	0.28
case3	72.12	2.35	0.03	111	1.04	2.38	-0.01	0.28
case4	72.12	2.25	0.03	111	1.02	1.98	0.01	0.28
case5	72.12	2.77	0.04	111	1.03	2.25	0.08	0.39
case6	72.12	3.30	0.05	111	1.03	2.44	0.11	0.42
case7	72.12	3.23	0.04	111	1.04	2.55	0.10	0.41
case8	72.12	3.03	0.04	111	1.04	2.54	0.07	0.38

Table 5.11: Model skill parameters for the sensitivity test to u-velocity at Station A.

	R	D_{rms}	D_{rms}/R	ν	G_w	E_{rms}	L_m	L_{rms}
case1	102.2	12.58	0.12	111	0.84	10.18	0.35	0.59
case2	102.2	12.12	0.12	111	0.87	8.95	0.36	0.60
case3	102.2	7.92	0.08	111	0.97	5.82	0.14	0.42
case4	102.2	7.83	0.08	111	0.96	5.92	0.14	0.42

Table 5.12: Model skill parameters for the sensitivity test to v-velocity at Station A.

	R	D_{rms}	D_{rms}/R	ν	G_w	E_{rms}	L_m	L_{rms}
case1	76.81	6.79	0.09	111	0.90	5.30	-0.49	0.70
case2	76.81	7.37	0.10	111	0.94	6.14	-0.30	0.55
case3	76.81	8.52	0.11	111	1.06	4.42	-0.53	0.73
case4	76.81	8.71	0.11	111	1.08	4.68	-0.54	0.74

5.8 Comparison of σ- and z-baroclinic approaches

Recently, some problems on the σ grid model have been raised. One problem is from the horizontal density gradient along the constant σ-surface, which causes a hydrostatic inconsistency due to the bottom topography effect. The hydrostatic assumption in the governing equations makes this problem more important. Another problem is from the advection terms in the transport equation, which enable some communication between the denser bottom water in deep areas and the lighter bottom water in adjacent shallow areas.

The error caused by the pressure gradient force term near steep topography in the σ-coordinate system commonly has been mentioned. The pressure gradient force term is divided into two terms in the σ-coordinate system, the gradient of pressure along a constant σ surface and the gradient of bottom topography. For example, the horizontal pressure gradient in the x-direction is written in the σ-coordinate system as

$$\left.\frac{\partial p}{\partial x}\right|_z = \left.\frac{\partial p}{\partial x}\right|_\sigma - \frac{\sigma}{H}\frac{\partial p}{\partial \sigma}\frac{\partial H}{\partial x} \tag{5.15}$$

where p is the pressure, subscript z indicates the constant z-coordinate surface, H is the total depth, $\sigma = (z+\zeta)/H$, and ζ is the water elevation.

A sufficient condition for a finite difference scheme to be hydrostatically consistent in the σ-coordinate system, is given by Haney (1990), as

$$\left|\frac{\sigma}{H}\frac{\partial H}{\partial x}\right| \delta x < \delta\sigma \tag{5.16}$$

This condition, which requires a sufficiently small grid size for a given vertical grid increment, guarantees that the σ-surface immediately below a given σ-surface remains below a given σ-surface within a horizontal distance of one grid interval. If the above condition is not satisfied, the finite difference scheme is hydrostatically inconsistent and nonconvergent.

To see the problem associated with σ grid model, I tested the effect of an abrupt change of depth. Here a new terminology is defined : σ-baroclinic for the baroclinic term calculated along the constant σ-surface and z-baroclinic for the baroclinic term calculated along the constant z-surface. To change σ-baroclinic to z-baroclinic, the term associated with depth was ignored, which is shown in Equation (5.15). Now density difference is taken in the same z-level. Density at the adjacent point is calculated through the interpolation of σ-level. In doing so, the horizontal density gradient is hydrostatically consistent.

Comparison of σ-baroclinic and z-baroclinic was made with the case2 input. The harmonic constants of elevations at Station 1, 2, and 3 show that there is no significant difference between σ-baroclinic and z-baroclinic. The harmonic constant of velocity at Station 4 also does not show significant difference.

Time series of velocity and salinity fields over transect 'JB' were plotted in Figures 5.92-5.103 for three events of σ-baroclinic with diffusion, z-baroclinic with diffusion, and σ-baroclinic without diffusion. Diffusion coefficient used here was 10000 cm^2/sec. Generally velocity in z-baroclinic was larger than that in σ-baroclinic. The difference was large in shallow depth. The degree of salinity stratification was greater in σ-baroclinic. This is due to the advection terms in transport equation. In the σ-grid system, this is an evidence of communication between deep area and shallow area. The diffusion effect was not significant in the test with diffusion and without diffusion in the σ-grid system . Figure 5.104-5.107 show salinity time series over transect 'JB' at surface and bottom, comparing σ-baroclinic with diffusion, z-baroclinic with diffusion, and σ-baroclinic without diffusion. To reduce the differences between σ- and z-surface, the condition of Equation (5.16) should be satisfied.

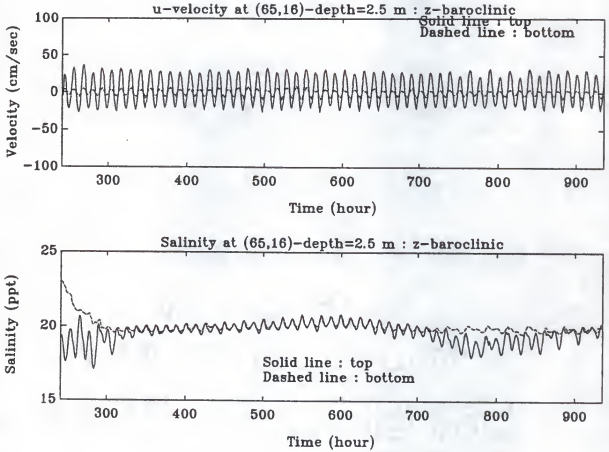

Figure 5.92: Time series of u-velocity and salinity in z-baroclinic with diffusion at grid point (65,16).

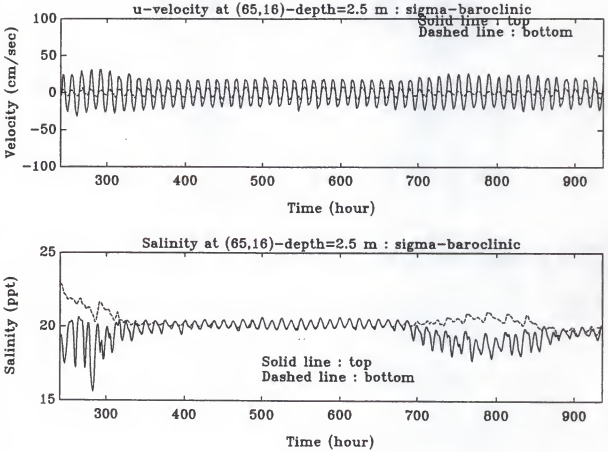

Figure 5.93: Time series of u-velocity and salinity in σ-baroclinic with diffusion at grid point (65,16).

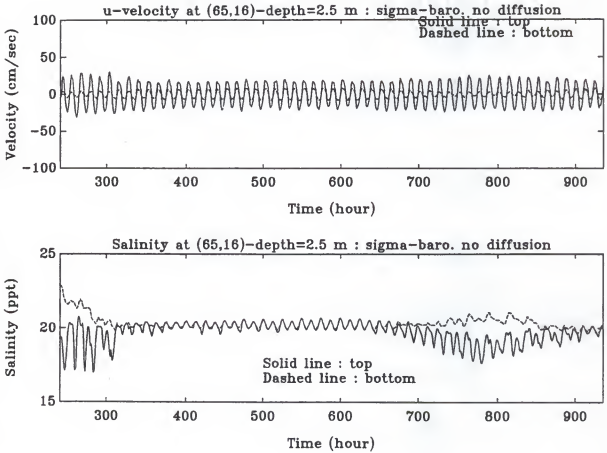

Figure 5.94: Time series of u-velocity and salinity in σ-baroclinic without diffusion at grid point (65,16).

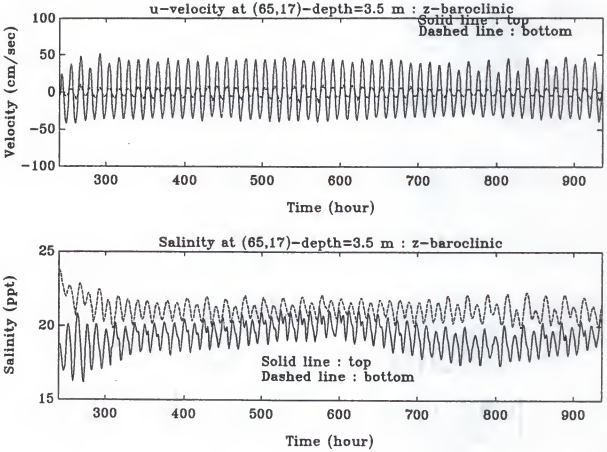

Figure 5.95: Time series of u-velocity and salinity in z-baroclinic with diffusion at grid point (65,17).

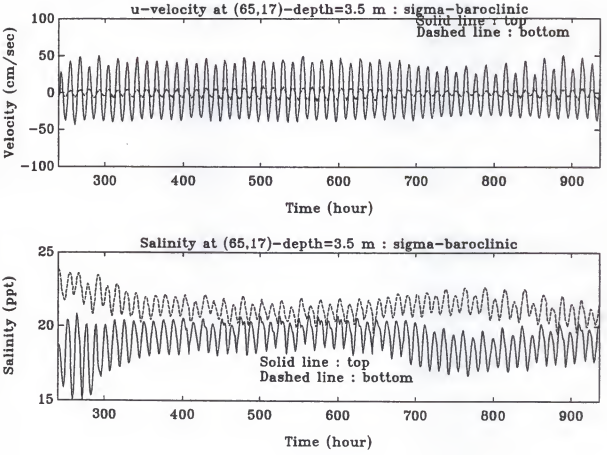

Figure 5.96: Time series of u-velocity and salinity in σ-baroclinic with diffusion at grid point (65,17).

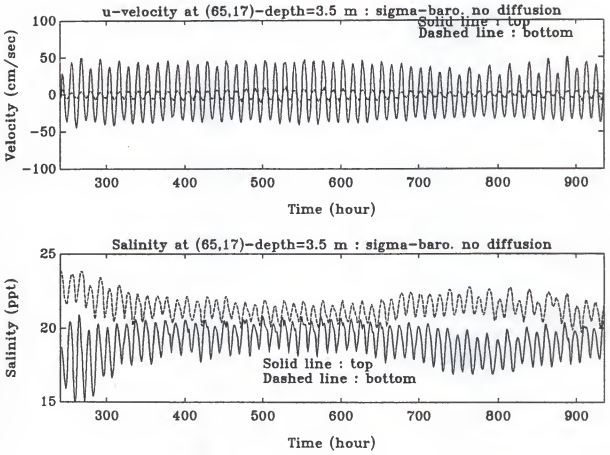

Figure 5.97: Time series of u-velocity and salinity in σ-baroclinic without diffusion at grid point (65,17).

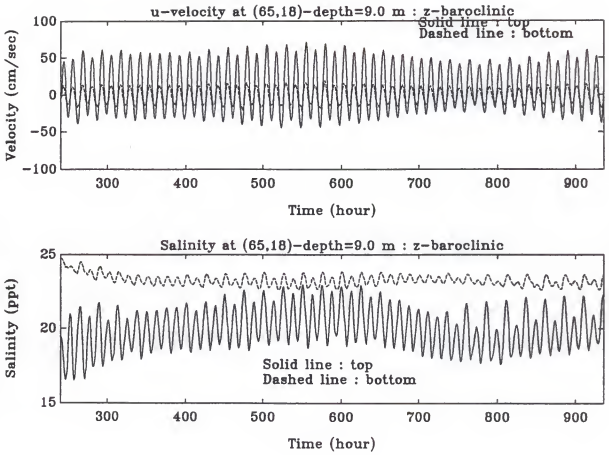

Figure 5.98: Time series of u-velocity and salinity in z-baroclinic with diffusion at grid point (65,18).

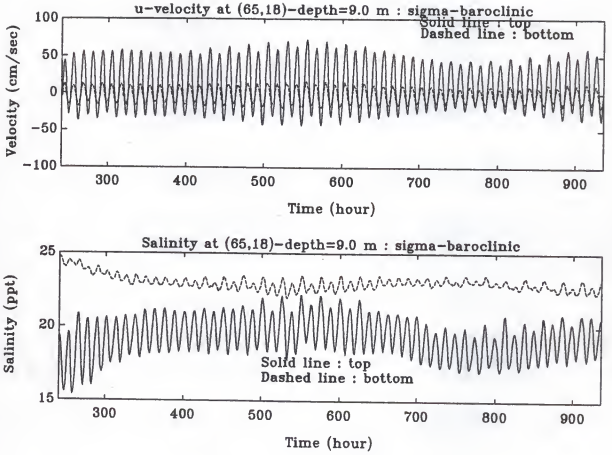

Figure 5.99: Time series of u-velocity and salinity in σ-baroclinic with diffusion at grid point (65,18).

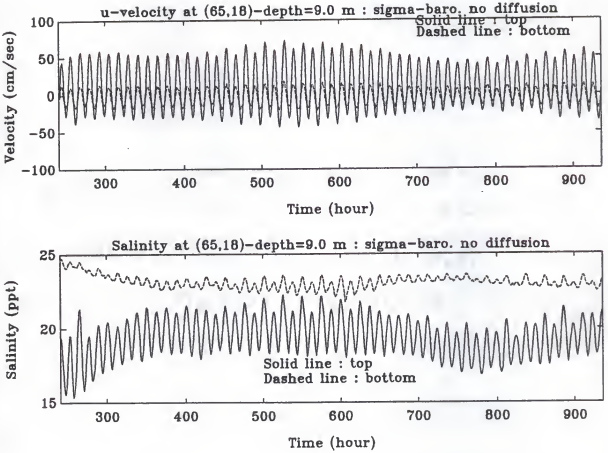

Figure 5.100: Time series of u-velocity and salinity in σ-baroclinic without diffusion at grid point (65,18).

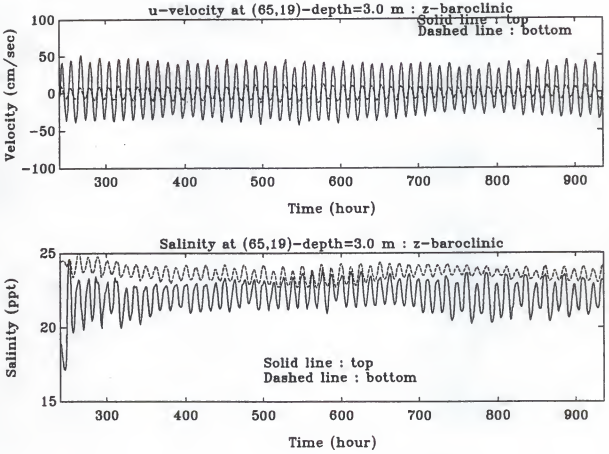

Figure 5.101: Time series of u-velocity and salinity in z-baroclinic with diffusion at grid point (65,19).

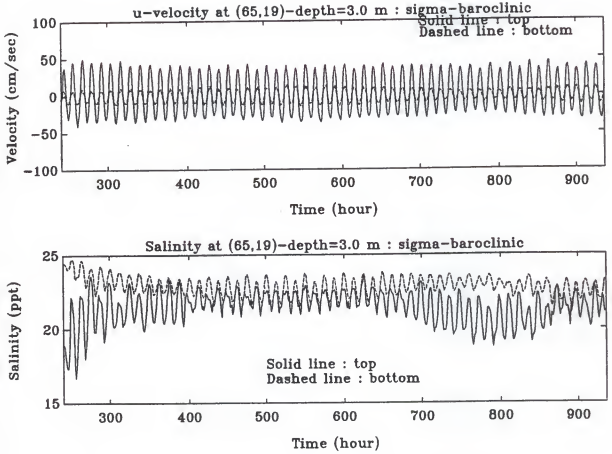

Figure 5.102: Time series of u-velocity and salinity in σ-baroclinic with diffusion at grid point (65,19).

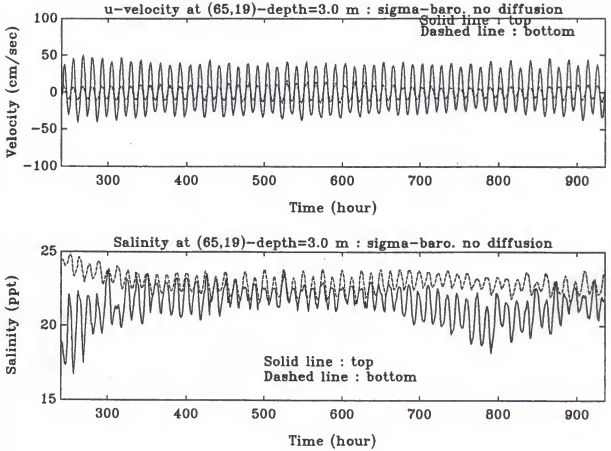

Figure 5.103: Time series of u-velocity and salinity in σ-baroclinic without diffusion at grid point (65,19).

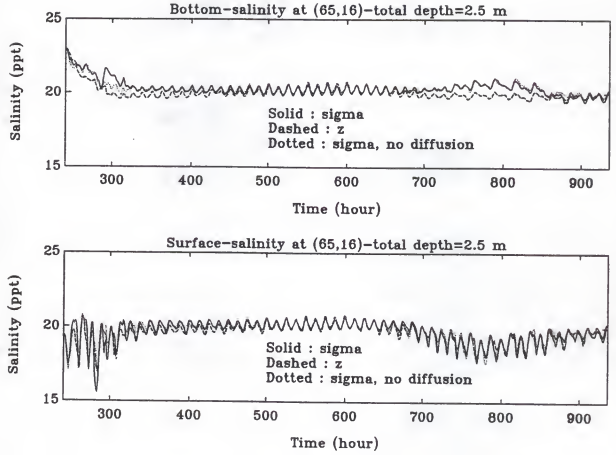

Figure 5.104: Time series of salinity in z-baroclinic with diffusion, σ-baroclinic with diffusion, and σ-baroclinic without diffusion at grid point (65,16).

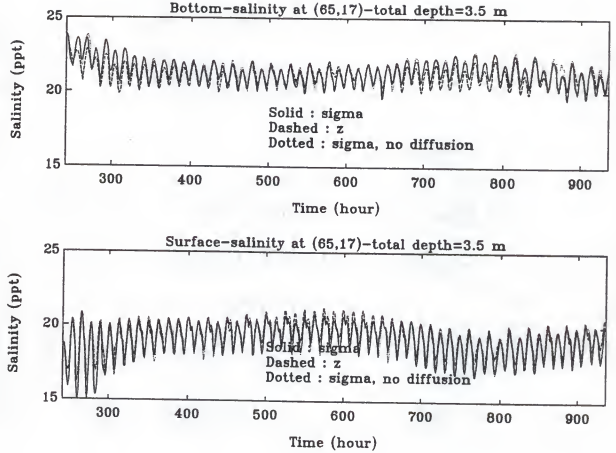

Figure 5.105: Time series of salinity in z-baroclinic with diffusion, σ-baroclinic with diffusion, and σ-baroclinic without diffusion at grid point (65,17).

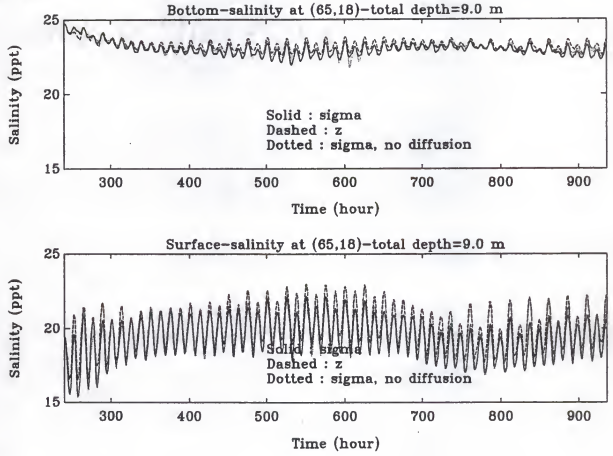

Figure 5.106: Time series of salinity in z-baroclinic with diffusion, σ-baroclinic with diffusion, and σ-baroclinic without diffusion at grid point (65,18).

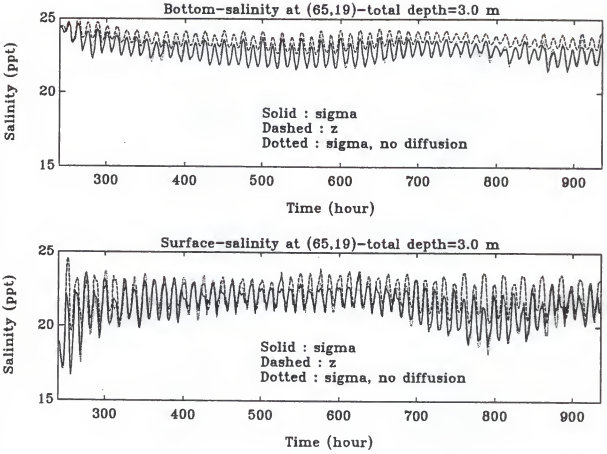

Figure 5.107: Time series of salinity in z-baroclinic with diffusion, σ-baroclinic with diffusion, and σ-baroclinic without diffusion at grid point (65,19).

CHAPTER 6
CONCLUSIONS

A three-dimensional curvilinear hydrodynamic model has been formulated, verified, and applied to the James River, a partially-mixed estuary. The focus of the circulation and salinity transport modeling study was on stratification-destratification phenomena associated with the spring-neap tidal cycle. Additionally, the development of a frontal system was found near Newport News Point. The model could simulate the frontal system.

The model is based on the time-variable, three-dimensional equations of continuity, momentum, and salt balance. The equations have been transformed using a curvilinear coordinate system in the horizontal and a σ-stretching technique in the vertical. The use of curvilinear coordinates allows the user to design the computational mesh effectively and resolve complex geometries.

A model of circulation and salinity transport for the partially-mixed estuary has been developed, and verified against analytical solutions, and applied to the James River. Also the sensitivity tests of various parameters have been performed.

The model is formulated on the basis of the three-dimensional, time-varying equations of continuity, momentum, and salt balance. The program code can handle the integration of the governing equations, using variable weighting factors from the fully-implicit scheme to the fully-explicit scheme. In doing so, the model can be more flexible to apply to a real situation. The time step of integration is more relaxed as the weighting factor of implicit scheme increases.

The model was formulated using weighting factor from implicit scheme ($\theta = 1$) to explicit scheme ($\theta = 0$). With this formulation, the model is more flexible when

applied to a special situation. In the present study, the implicit integration scheme for the momentum was used to relax CFL condition limiting the integration time step. The model solves the governing equations using a mode-splitting technique in which the external or vertically averaged mode and the internal or vertical structure are solved separately.

The vertical eddy coefficients for momentum and salinity were determined by the simplified second order equilibrium closure scheme. So an instantaneous velocity was considered for the eddy viscosity and diffusivity parameters. Compared to the equilibrium closure model, the kinetic energy closure model (Sheng and Villaret, 1989) contains an extra differential transport equation for q^2. However, no study has unequivocally demonstrated that the kinetic energy closure model always gives much better results than the equilibrium closure model in simulating estuarine circulation and transport. And the additional equations do not necessarily guarantee better model results.

A series of model test runs was performed against analytic solutions to check the accuracy of model prediction. Test of a forced constant surface slope showed that the surface slope balanced the bottom stress in the model. Model tests of seiche, tidal forcing, wind forcing, and density-induced forcing all showed good agreements with the analytic solutions.

Model calibration and validation was performed through the quantitative measures of deviation between model results and data. The use of quantitative measures of calibration and validation for hydrodynamic models will enhance model performance evaluation. A series of sensitivity tests were carried out to determine the sensitivity to the changes in some model parameters. Sensitivity to bottom friction between 0.002 to 0.004 showed that the differences were hardly noticeable. With time-varying bottom friction calculated from the law of the wall with Monin-Oboukhov length scale, the model result showed the best agreement with data. Roughness height was

another important parameter to affect the bottom stress. With a small roughness height, tidal elevation increased and phase lag decreased. The bathymetry was also an important factor to produce a good result, because it is directly related to the bottom friction. Space-time discretization can also result in an improper simulation because the discretization of the governing equations leads unavoidably to approximation errors. With small time step and fine grid, the convergence and stability can definitely be improved.

Besides numerical constraints, modeling of estuaries in three-dimensional structure has been hampered by lack of sufficient data for verification of long-term model simulations. Four series of surveys, however, were available for use of this study. Each case was conducted to make a vertical-longitudinal salinity profile along the axis of the river. Application of the model to the spring-neap stratification cycle was generally successful. The model simulation showed stratification-destratification in response to the change of tidal range. The stratification-destratification phenomenon was related to the instantaneous velocity, which was considered in the second order closure scheme.

The longitudinal motion of the salinity intrusion was simulated according to the river discharge. The head of salt intrusion moved up and down due to the change of river discharge. The intrusion moves downstream with inceasing river discharge. Also increasing river discharge caused an increase in relative stratification.

Frontal boundary was simulated in the model. The front near Newport News Point was revealed as a narrow zone of surface flow convergence and strong vertical transport.

It was found that with an estuarine system with a deep channel it is difficult to predict the correct stratification degree and the velocity field near the bottom. This problem comes from grid resolution of channel depth and σ transformation. Near steep topography the pressure gradient force is affected significantly with the

gradient of bottom topography in σ coordinate sytem. To reduce this problem, the use of z-baroclinic or z-grid model is highly recommended.

Again hydrodynamical numerical modeling in partially-mixed estuaries is a very complicated problem. In partially mixed estuaries, there are freshwater discharge, tidal forcing, and turbulent kinetic energy generated by a mean flow.

BIBLIOGRAPHY

Blumberg, A.F., A Numerical Investigation into the Dynamics of Estuarine Circulation. Chesapeake Bay Institute, The Johns Hopkins University,Technical Report 91, 1975.

Blumberg, A.F., A Two-Dimensional Numerical Model For the Simulation of Partially Mixed Estuary. Estuarine Processes (M. Wiley Ed.), Academic Press,New York, pp. 323-331, 1976.

Blumberg, A.F. and G.L. Mellor, Diagnostic and Prognostic Numerical Circulation Studies of the South Atlantic Bight. J. Geophysics Res., 88, pp. 4579-4592, 1983.

Boon, J.D. and K.P. Kiley, Harmonic Analysis and Tidal Prediction by the Method of Least Squares. Virginia Institute of Marine Science, Gloucester Pt., Va., Special Report 186, 1978.

Bowden, K.F., Circulation and Diffusion. Estuaries (G.H. Lauff Ed.), American Association for the Advancement of Science, Washington, D.C., pp. 15-36, 1967.

Bowden, K.F. and P. Hamilton, Some Experiments with a Numerical Model of Circulation and Mixing in a Tidal Estuary. Est. Coastal Mar. Sci. 3, p. 281, 1975.

Bursinger, J.A., J.C. Wyngaard, Y. Izumi, and E.F. Bradley, Flux-Profile Relationship in the Atmospheric Surface Layer. J. Atmos. Sci. 28, pp. 181-189, 1971.

Byrne, R.J., A.Y. Kuo, R.L. Mann, J.M. Brubaker, E.P. Ruzecki, P.V. Hyer, R.J. Diaz and J.H. Posenau, Newport Island: An Evaluation of Potential Impacts on Marine Resources of the Lower James River and Hampton Roads. Special Report in Applied Marine Science and Ocean Engineering, No. 283, VIMS, Virginia 23062, February 1987.

Cameron, W.M. and D.W. Pritchard, Estuaries. The Sea, (M.N. Hill Ed), Vol. 2. pp. 306-324, John Wiley and Sons, New York, 1963.

Caponi, E.A., The Simulation of Estuarine Circulation with a Fully Three-Dimensional Numerical Model. Estuarine Processes (M. Wiley Ed.), Academic Press, New York, pp. 332-346, 1976.

Cerco, C.F.," Two-Dimensional, Intratidal Model Study of Salinity Intrusion Structure and Motion in Partially-Mixed Estuaries", Ph.D. Dissertation, The College of William and Mary in Virginia, 283 pp., 1982.

Chao, S.-Y., Tidal Modulation of Estuarine Plumes. Journal of Physical Oceanography, 20 (7), pp. 1115-1123, 1990.

Doodson, A.T. and J. Proudman, Rep. Br. Assoc. Adv. Sci 1, 1923.

Eckart, C., Properties of Water, Part II. The Equations of State of Water and Sea Water at Low Temperatures and Pressures. Amer. J. Sci., 256, pp. 225-240, 1958.

Festa, J.F. and D.V. Hansen, A Two-Dimensional Numerical Model of Estuarine Circulation: The Effects of Altering Depth and River Discharge. Estuarine and Coastal Marine Science, 4, pp. 309-323, 1976.

Geyer, W.R. and D.M. Farmer, Tidal-Induced Variation of the Dynamics of a Salt Wedge Estuary. Journal of Physical Oceanography, 19, No. 4, pp. 1060-1072, 1989.

Haas, L.W., The Effect of the Spring-Neap Tidal Cycle on the Vertical Salinity Structure of the James, York, and Rappahannock Rivers, Virginia, U.S.A. Estuarine and Coastal Marine Science, 5, pp. 485-496, 1977.

Hamilton, P., On the Numerical Formulation of a Time Dependent Multi-Level Model of an Estuary, with Particular Reference to Boundary Conditions. Estuarine Processes (M. Wiley Ed.), Academic Press, New York, pp. 347-364, 1976.

Hamrick, J.M, A.Y. Kuo and G.M. Sisson, " Some Considerations in Model and Field Data Selection for Circulation Studies of the James River Estuary", Estuarine and Coastal Modeling (M.L. Spaulding Ed.), Proceedings of the Conference, ASCE, Newport, R.I., pp. 200-208, Nov. 15-17,1989.

Hansen, D.V. and M. Rattray, Jr., Gravitational Circulation in Straits and Estuaries. Journal of Marine Research, 23, pp.104-122, 1965.

Hansen, W., Theorie zur Errechnung des Wasserstandes und der Stromungen in Randmeeren nebst Anwendungen. Tellus, 8, pp. 287-300, 1956.

Haney, R.L., Notes and Correspondence: On the Pressure Gradient Force over Steep Topography in Sigma Coordinate Ocean Models. Journal of Physical Oceanography, 21, pp. 610-619, 1990.

Haven, D.S. and J.P. Whitcomb, The Origin and Extent of Oyster Reefs in the James River, Virginia. Jour. Shellfish Res. 3(2): pp. 141-151, 1983.

Heltzel, S.B. and M.A. Granat, Lower James River Circulation Study Virginia, Evaluation of Craney Island Enlargement Alternatives. Department of the Army, WES, Corps of Engineers, Technical Report HL-88-8, April 1988.

Hepworth, D and A.Y. Kuo, James River Seed Oyster Bed Project: Physical Data Report I. Data Report No.31, VIMS, June 1989.

Hess, K., Validation of a Tampa Bay Circulation Model. NOAA, National Ocean Service, Rockville, Md., 1991.

Ippen, A., Ed.. Estuary and Coastline Hydrodynamics. McGraw Hill, New York, 744 pp., 1966.

Johnson, B.H., VAHM-A Vertically Averaged Hydrodynamic Model Using Boundary-Fitted Coordinates. Hydraulic Laboratory, U.S. Army Engineer Waterways Experiment Station, September, 1980.

Johnson, B.H., K.W. Kim, Y.P. Sheng and R.E. Heath, Development of a Three-Dimensional Hydrodynamic Model of Chesapeake Bay. Estuarine and Coastal Modeling (M.L. Spaulding Ed.), Proceedings of the Conference, ASCE, Newport, R.I., pp. 162-171, Nov. 15-17,1989.

Kent, R.E. and D.W. Pritchard, A Test of Mixing Length Theories in a Coastal Plains Estuary. J. Mar. Res. 18, pp. 62-72, 1959.

Kinne, O., Physiology of estuarine organisms with special reference to salinity and temperature: general aspects, Estuaries (G.H. Lauff Ed.), American Association for the Advancement of Science, Washington, D.C., pp. 525-540, 1967.

Kjerfve, B., Hydrodynamics of Estuaries, Volume 1 Estuarine Physics, CRC Press,Inc., BocaRaton, Fla., 1988.

Laevastu, T., A Multilayer Hydrodynamical Numerical Model (W. Hansen Type). Environmental Protection Research Facility, U.S. Naval Postgraduate School, Monterey, California, Technical Note No. 2-74, 1974.

Lamb, H., Hydrodynamics. 6th edition. Dover Publications, New York, 1962.

Leendertse, J.J., Aspects of a Computational Model for Long Period Water Wave Propagation. Rand Corporation, Santa Monica, California, Rep. RM-5294-PR, 165 pp., 1967.

Leendertse, J.J. and S.-K. Liu, A Three-Dimensional Model for Estuaries and Coastal Seas. Vol. I: Principles of Computation. The Rand Corporation, Santa Monica, Report R-1417-OWRR, 57 pp., 1975.

Leonard, B.P., A Stable and Accurate Convective Modeling Procedure Based on Quadratic Upstream Interpolation. Computer Methods in Applied Mechanics and Engineering, 19, pp. 59-98, 1979.

Lynch, D.R., Progress in Hydrodynamic Modeling, Review of U.S. Contributions, 1979-1982. Reviews of Geophysics and Space Physics, 21 (3), pp. 741-754, 1983.

Lewellen, W.S., Use of Invariant Modeling.Handbook of Turbulence (W. Frost ed.), Vol. 1, Plenum Publishing Corp., New York, 1977.

Ludwick, J.C., Tidal Currents, Sediment Transport, and Sand Banks in Chesapeake Bay Entrance, Virginia. Estuarine Research (L.E. Cronin Ed.), Academic Press, New York, 365 pp., 1975.

Madala, R.V. and S.A. Piacsek. A Semi Implicit Numerical Model for Baroclinic Oceans, Journal of Computational Physics, 23, pp. 167-178, 1977.

Mellor, G.L. and T. Yamada. Development of a Turbulence Closure Model for Geophysical Fluid Problem. Review of Geophysics and Space Physics, 20 (4), pp. 851-875, 1982.

Munk, W.H. and E.R. Anderson, Notes on a Theory of the Thermocline. J. Mar. Res. 7, pp. 276-295, 1948.

O'Donnell, J., The Formation and Fate of a River Plume: A Numerical Model. Journal of Physical Oceanography, 20 (4), pp. 551-569, 1990.

Neumann, G and W.J. Pierson, Principles of Physical Oceanography., Prentice Hall, 545 pp., 1966.

Oey, L.-Y., G.L. Mellor and R.I. Hires, A Three-Dimensional Simulation of the Hudson-Raritan Estuary. Part I: Description of the Model and Model Simulations. J. Phys. Oceanogr., 15, pp. 1696-1692, 1985.

Peene, S.J. and Y.P. Sheng, Modeling Tidal and Wind Driven Circulation in Sarasota and Tampa Bay. Estuarine and Coastal Modeling, Proceedings of the 2nd International Conference, ASCE, Tampa, Fla., November 13-15, 1991.

Rattray, Jr. M. and D.V. Hansen. A Similarity Solution for Circulation in an Estuary. Journal of Marine Research, 20, pp. 121-133, 1962.

Roach, P.J., Computational Fluid Dynamics, Hermosa Publishers, 446 pp., 1976.

Rodi, W., Turbulence Models and Their Application in Hydaulics. International Association of Hydraulic Research, Delft, Netherlands, 1980.

Rodi, W., Examples of Calculation Methods for Flow and Mixing in Stratified Fluids. Journal of Geophysical Research, 92, (C5), pp. 5305-5328, 1987.

Sheng, Y.P., Hydraulic Applications of a Second-Order Closure Model of Turbulent Transport. Proceedings 1982 ASCE Hydraulic Division Specialty Conference on Applying Research to Hydraulic Practice (P. Smith Ed.), ASCE, Jackson, Miss., 1982.

Sheng, Y.P., Mathematical Modeling of Three-Dimensional Coastal Currents and Sediment Dispersion: Model Development and Application. Coastal Engineering Research Center, University of Florida, Fla., Technical Report CERC-TR-83-2 DACW39-80-C-0087, 297 pp., 1983.

Sheng, Y.P., A Turbulent Transport Model of Coastal Processes. Proceedings 19th International Conference on Coastal Engineering, ASCE, Houston, TX, pp. 2380-2396, 1984.

Sheng, Y.P., A New One-Dimensional Ocean Current Model. Aeronautical Research Associates of Princeton, Princeton, N.J., Technical Report No. 556, 1985.

Sheng, Y.P., Modeling Bottom Boundary Layers and Cohesive Sediment Dynamics. Estuarine Cohesive Sediment Dynamics (A.J. Mehta Ed.), Spring-Verlag, pp.360-400, 1986a.

Sheng, Y.P., Finite-Difference Models for Hydrodynamics of Lakes and Shallow Seas. Physics-Based Models of Lakes, Reservoirs, and Impoundments (W.G. Gray Ed.), ASCE, pp. 146-228, 1986b.

Sheng, Y.P., On Modeling Three-Dimensional Estuarine and Marine Hydrodynamics. Three-Dimensional Models of Marine and Estuarine Dynamics (J.C.J. Nihoul and B.M. Jamart Ed.), Elsevier, New York, pp. 35-88, 1987.

Sheng, Y.P., Evolution of a 3-D Curvilinear-Grid Hydrodynamic Model: CH3D, Estuarine and Coastal Modeling (M.L. Spauling Ed.), ASCE, Newport, R.I., pp. 40-49, 1989.

Sheng, Y.P. and H.L. Butler, Modeling Coastal Currents and Sediment Transport. Proc. 18th International Conference on Coastal Engineering, ASCE, pp. 1127-1148, 1982.

Sheng, Y.P. and S.S. Chiu, Tropical Cyclone Generated Currents. Proc. of the 20th International Conference on Coastal Engineering, ASCE, pp. 737-751, 1986.

Sheng Y.P. and J.-K. Choi. A Three-Dimensional Numerical Model of the James River and Hampton Roads Estuarine System. University of Florida, Gainesville, Florida, Report UFL/COEL-89/020, October 1989.

Sheng, Y.P., J.-K. Choi and A.Y. Kuo, Three-Dimensional Numerical Modeling of Tidal Circulation and Salinity Transport in James River Estuary. Estuarine and Coastal Modeling (M.L. Spaulding Ed.), Proceedings of the Conference, ASCE, Newport, R.I., pp. 209-218, Nov. 15-17,1989a.

Sheng Y.P., V. Cook, S. Peene, D. Eliason, P.F. Wang, and S. Schofield, A Field and Modeling Study of Fine Sediment Transport in Shallow Waters. Estuarine and Coastal Modeling (M.L. Spaulding Ed.), Proceedings of the Conference, ASCE, Newport, R.I., pp. 113-122, 1989b.

Sheng, Y.P., H.K. Lee and K.H. Wang, On Numerical Strategies of Estuarine and Coastal Modeling. Estuarine and Coastal Modeling (M.L. Spaulding Ed.), Proceedings of the Conference, ASCE, Newport, R.I., pp. 291-301, 1989c.

Sheng, Y.P. and C. Villaret, Modeling the Effect of Suspended Sediment Stratification on Bottom Exchange Processes. J. Geophys. Res., 94, pp. 1429-1444, 1989.

Simpson, J.H. and R.A. Nunes, The Tidal Intrusion Front: An Estuarine Convergence Zone. Estuarine, Coastal and Shelf Sci., 13, pp. 257-266, 1981.

Sokolnikoff, I.S., Tensor Analysis. John Wiley and Sons, Inc., New York, 1960.

Spaulding, M.L., Laterally Integrated Numerical Water Quality Model for an Estuary. Journal of Fluids Engineering, June, 1974.

Spaulding, M.L., A Vertically Averaged Circulation Model Using Boundary-Fitted Coordinates. Journal of Physical Oceanography, 14, pp. 973-982, 1984.

Swanson, C.J., A Three Dimensional Numerical Model System of Coastal Circulation and Water Quality. Ph.D. Dissertation, University of Rhode Island, Kingston, R.I., 147 pp., 1988.

Tennekes, H and J.L. Lumley, A First Course in Turbulence, MIT Press, Cambridge, Massachusetts, 1972.

Thames, F.C. Numerical Solution of the Incompressible Navier-Stokes About Arbitrary Two-Dimensional Bodies. Ph.D Dissertation, Mississippi State University, 1975.

Thames, F.C., J.F Thompson, C.W. Mastin and R.L. Waler, Numerical Solutions for Viscous and Potential Flow About Arbitrary Two-Dimensional Bodies Using Body-Fitted Coordinate System. J. Comput. Phys., 24., pp. 245-273, 1977.

Thomas, L.H., Computation of One-Dimensional Flows Including Shocks. Communications in Pure and Applied Mathematics, 7, pp. 76-87, 1954.

Thompson, J.F., Numerical Solution of Flow Problems Using Body-Fitted Coordinate Systems. Mississippi State University, State College, Miss., 1977.

Thompson, J.F., F.C. Thames and C.W. Mastin, Automatic Numerical Generation of Body-Fitted Curvilinear Coordinate Systems for Fields Containing Any Number of Arbitrary Two-Dimensional Bodies. J. Comput. Phys. 15, pp. 299-317, 1974.

Thompson, J.F., F.C. Thames and C.W. Mastin, TOMCAT-A Code for Numerical Generation of Boundary-Fitted Curvilinear Coordinate Systems on Fields Containing Any Number of Arbitrary Two-Dimensional Bodies. J. Comput. Phys. 24, pp. 274-302, 1977a.

Thompson, J.F., F.C. Thames and C.W. Mastin, Boundary- Fitted Curvilinear Coordinate System for Solution of Partial Differential Equations on Fields Containing Any Number of Arbitrary Two-Dimensional Bodies. NASA CR-2729, 1977b.

Wang, D.P. and A.J. Elliott, Non-Tidal Variability in the Chesapeake Bay and Potomac River: Evidence for Non-Local Forcing. Journal of Physical Oceanography, 8, pp. 225-232, 1978.

Wang, H.-P. and F.M. White, Multi-Leveled Finite Element Hydrodynamic Model of Block Island Sound. Department of Mechanical Engineering and Applied Mechanics, University of Rhode Island, Kingston, R.I., 152 pp., 1976.

Wang, J.D., Mathematical Modeling of Near Coastal Circulation. Ph.D. Dissertation, Massachusetts Institute of Technology, 1975.

Wang, J.D. and J.J. Connor, Mathematical Modeling of Near Coastal Circulation. Massachusetts Institute of Technology, Cambridge, Mass., Report No. MITSG 75-13, 1975.

Wilemse, J.B.T.M., G.S. Stelling and G.K. Verboom, Solving the Shallow Water Equations with an Orthogonal Coordinate Transformation. Delft Communica-

tion No. 356. Presented at International Symposium on Computational Fluid Dynamics, Tokyo, Japan, September 9-12, 1985.

Zalesak, S.T., Fully Multi-dimensional Flux-corrected Transport Algorithms for Fluids. J. Comp. Phys. 31, p. 375, 1979.

APPENDIX A
HIGHER-ORDER-TERMS (H.O.T.) IN σ-GRID SYSTEM

When second-order derivative terms in the momentum equation are transformed from (x, y, z, t) to (x', y', σ, t'), H.O.T.s are generated.

$$\begin{aligned}\frac{\partial}{\partial x}(A_H\frac{\partial u}{\partial x}) &= \frac{\partial}{\partial x'}(A_H\frac{\partial u}{\partial x'}) - \frac{1}{H}(\frac{\partial \zeta}{\partial x'} + \sigma\frac{\partial H}{\partial x'})[\frac{\partial}{\partial \sigma}(A_H\frac{\partial u}{\partial x'}) + \frac{\partial}{\partial x'}(A_H\frac{\partial u}{\partial \sigma})] \\ &- A_H\frac{\partial u}{\partial \sigma}[\frac{1}{H}(\frac{\partial^2 \zeta}{\partial x'^2} + \sigma\frac{\partial^2 H}{\partial x'^2}) - \frac{1}{H^2}(\frac{\partial \zeta}{\partial x'} + \sigma\frac{\partial H}{\partial x'})\frac{\partial H}{\partial x'}] \\ &+ \frac{1}{H^2}(\frac{\partial \zeta}{\partial x'} + \sigma\frac{\partial H}{\partial x'})^2\frac{\partial}{\partial \sigma}(A_H\frac{\partial u}{\partial \sigma})\end{aligned} \tag{A.1}$$

$$\begin{aligned}\frac{\partial}{\partial y}(A_H\frac{\partial u}{\partial y}) &= \frac{\partial}{\partial y'}(A_H\frac{\partial u}{\partial y'}) - \frac{1}{H}(\frac{\partial \zeta}{\partial y'} + \sigma\frac{\partial H}{\partial y'})[\frac{\partial}{\partial \sigma}(A_H\frac{\partial u}{\partial y'}) + \frac{\partial}{\partial y'}(A_H\frac{\partial u}{\partial \sigma})] \\ &- A_H\frac{\partial u}{\partial \sigma}[\frac{1}{H}(\frac{\partial^2 \zeta}{\partial y'^2} + \sigma\frac{\partial^2 H}{\partial y'^2}) - \frac{1}{H^2}(\frac{\partial \zeta}{\partial y'} + \sigma\frac{\partial H}{\partial y'})\frac{\partial H}{\partial y'}] \\ &+ \frac{1}{H^2}(\frac{\partial \zeta}{\partial y'} + \sigma\frac{\partial H}{\partial y'})^2\frac{\partial}{\partial \sigma}(A_H\frac{\partial u}{\partial \sigma})\end{aligned} \tag{A.2}$$

APPENDIX B
TRANSFORMATION OF GOVERNING EQUATIONS

B.1 Transformation Rules

As shown in Fig. 8 of Appendix A of Sheng (1986), the contravariant components (u^i) and physical components $u(i)$ of the velocity vector in the non-Cartesian system are locally parallel or orthogonal to the grid lines, while the covariant components (u_i) are generally not parallel or orthogonal to the local grid lines. The three components are identical in a Cartesian coordinate system. The following relationships are valid for the three components in a non-Cartesian system

$$u^i = (g_{ii})^{-1/2} u(i) \qquad \text{(no sum on i)} \tag{B.1}$$

$$u_i = (g_{ii})^{-1/2} g_{ij} u(j) \qquad \text{(no sum on i)} \tag{B.2}$$

$$u(i) \equiv \tilde{u}_i \tag{B.3}$$

where g is the diagonal element of the metric tensor g_{ij}

$$g_{ij} = \frac{\partial x^\ell}{\partial \xi^i} \frac{\partial x^n}{\partial \xi^j} \delta_{\ell n} \tag{B.4}$$

which for the two-dimensional case of interest is

$$g_{ij} = \begin{pmatrix} x_\xi^2 + y_\xi^2 & x_\xi x_\eta + y_\xi y_\eta \\ x_\eta x_\xi + y_\eta y_\xi & x_\eta^2 + y_\eta^2 \end{pmatrix} = \begin{pmatrix} g_{11} & g_{12} \\ g_{21} & g_{22} \end{pmatrix} \tag{B.5}$$

The three components follow different rules for transformation between the prototype and the transformed plane

$$\bar{u}^i = \frac{\partial \xi^i}{\partial x^j} u^j \tag{B.6}$$

$$\overline{u}_i = \frac{\partial \xi^j}{\partial x^i} u_j \tag{B.7}$$

$$\overline{u}(i) = (\overline{g}_{ii})^{1/2} \frac{\partial \xi^i}{\partial x^j} u(j) \tag{B.8}$$

where the unbarred quantities represent the components in the prototype system and the barred quantities represent the components in the transformed system.

B.2 Dimensionless Tensor Invariant Governing Equations

Before transforming the governing equations, it is essential to first write them in tensor-invariant form, i.e., equations which are independent of coordinate translation and rotation.

Based on extensive tests, we have concluded that using the contravariant components will yield the simplest form of the governing equations. For simplicity, we will use un-barred quantities to denote the variables in the transformed system unless otherwise indicated.

Following the rules described in the previous paragraph, we can obtain the following equations

$$\zeta_t + \frac{\beta}{\sqrt{g_o}} \frac{\partial}{\partial x^k} (\sqrt{g_o} H u^k) = 0 \tag{B.9}$$

$$\begin{aligned} \frac{1}{H} \frac{\partial H u^k}{\partial t} &= -\zeta !^k - g_{nj} \epsilon^{kj} u^n \\ &- \frac{Ro}{H} \left[(H u^\ell u^k)_{,\ell} + \frac{\partial h u^k \omega}{\partial \sigma} \right] \\ &+ \frac{E_v}{H^2} \frac{\partial}{\partial \sigma} \left(A_v \frac{\partial u^k}{\partial \sigma} \right) + E_H A_H u^k_{,m} !^m \\ &- \frac{Ro}{Fr_D^2} \left[H \int_\sigma^0 \rho !^k d\sigma + H !^k \left(\int_\sigma^\circ \rho d\sigma + \sigma \rho \right) \right] \end{aligned} \tag{B.10}$$

where $\partial / \partial x_k$ is the partial derivative, $g_{\ell n}$ is the metric tensor while $g_o \equiv J = x_\xi y_\eta - x_\eta y_\xi$ is the determinant of the metric tensor, u^k is the contravariant velocity, $(\ )_{,\ell}$ represents the covariant spatial derivative, $!^k$ represents the contravariant

spatial derivative, and ϵ^{kj} is the permutation tensor and

$$\begin{aligned} \epsilon^{12} &= -\frac{1}{\sqrt{g_o}} \\ \epsilon^{21} &= \frac{1}{\sqrt{g_o}} \\ \epsilon^{11} &= \epsilon^{22} = 0 \end{aligned} \tag{B.11}$$

The covariant and contravariant differentiations are defined by

$$u^i_{;j} = u^i_{:j} + D^i_{\alpha j} u^\alpha \tag{B.12}$$

$$S!^k = g^{km} S_{,m} \tag{B.13}$$

where :j represents partial differentiation and $D^i_{\alpha j}$ represents the Christoffel symbol of the second kind

$$D^i_{jk} = g^{in} D_{njk} \tag{B.14}$$

where g^{in} represents the inverse metric tensor, h_{in}, and D_{njk} is the Christoffel symbol of the first kind

$$D_{ijk} = \frac{1}{2}(g_{ij:k} + g_{ik:j} - g_{jk:i}) \tag{B.15}$$

B.3 Transformation of stress components

Using the chain rule of partial differentiation, the contravariant stress components are transformed from the Cartesian system (τ^1, τ^2) to the transformed system $(\overline{\tau}^1, \overline{\tau}^2)$, and vice versa. The unbarred quantities represent the components in the Cartesian system while the barred quantuties represent the components in the transformed system.

$$\overline{\tau}^1 = \frac{\partial \xi}{\partial x}\tau^1 + \frac{\partial \xi}{\partial y}\tau^2 \tag{B.16}$$

$$\overline{\tau}^2 = \frac{\partial \eta}{\partial x}\tau^1 + \frac{\partial \eta}{\partial y}\tau^2 \tag{B.17}$$

APPENDIX C
HORIZONTAL DIFFUSION TERMS IN BOUNDARY-FITTED GRIDS

The horizontal diffusion terms in u-velocity equation are

$$
\begin{aligned}
& u_{11}H_{11} + 2u_{12}H_{12} + u_{22}H_{22} \\
+\ & (D^1_{11}u)_1 H_{11} + (D^1_{11}u)_2 H_{12} + (D^1_{12}u)_1 H_{12} + (D^1_{12}u)_2 H_{22} \\
+\ & (D^1_{12}v)_1 H_{11} + (D^1_{12}v)_2 H_{12} + (D^1_{22}v)_1 H_{12} + (D^1_{22}v)_2 H_{22} \\
-\ & (D^1_{12}H_{12} + D^1_{22}H_{22})u_1 \\
+\ & (D^1_{11}H_{12} + D^1_{12}H_{22} - D^2_{11}H_{11} - 2D^2_{12}H_{12} - D^2_{22}H_{22})u_2 \\
+\ & (D^1_{12}H_{11} + D^1_{22}H_{12})v_1 + (D^1_{12}H_{12} + D^1_{22}H_{22})v_2 \\
+\ & [(D^1_{12}D^1_{12} + D^1_{22}D^2_{12} - D^1_{22}D^1_{11} - D^2_{22}D^1_{12})H_{22} + (D^1_{22}D^2_{11} - D^2_{12}D^1_{12})H_{12}]u \\
+\ & [(D^1_{12}D^2_{12} - D^2_{11}D^1_{22})H_{11} + (D^1_{11}D^1_{22} + D^1_{12}D^2_{22} - D^2_{12}D^1_{22} - D^1_{12}D^1_{12})H_{12}]v
\end{aligned}
\tag{C.1}
$$

The horizontal diffusion terms in v-velocity equation are

$$
\begin{aligned}
& v_{11}H_{11} + 2v_{12}H_{12} + v_{22}H_{22} \\
+\ & (D^2_{11}u)_1 H_{11} + (D^2_{11}u)_2 H_{12} + (D^2_{12}u)_1 H_{12} + (D^2_{12}u)_2 H_{22} \\
+\ & (D^2_{12}v)_1 H_{11} + (D^2_{12}v)_2 H_{12} + (D^2_{22}v)_1 H_{12} + (D^2_{22}v)_2 H_{22} \\
-\ & (D^2_{11}H_{11} + D^2_{12}H_{12})v_2 \\
+\ & (D^2_{12}H_{11} + D^2_{22}H_{12} - D^1_{11}H_{11} - 2D^1_{12}H_{12} - D^1_{22}H_{22})v_1 \\
+\ & (D^2_{11}H_{11} + D^2_{12}H_{12})u_1 + (D^2_{11}H_{12} + D^2_{12}H_{22})u_2 \\
+\ & [(D^2_{12}D^1_{12} - D^1_{22}D^2_{11})H_{22} + (D^1_{11}D^2_{12} + D^2_{11}D^2_{22} - D^1_{12}D^2_{11} - D^2_{12}D^2_{12})H_{12}]u \\
+\ & [(D^2_{11}D^1_{22} - D^1_{12}D^2_{12})H_{12} + (D^2_{12}D^2_{12} + D^2_{11}D^1_{12} - D^1_{11}D^2_{12} - D^2_{11}D^2_{22})H_{11}]v
\end{aligned}
\tag{C.2}
$$

where the H_{ij} are inverse metric tensor, the D^i_{jk} is the Christoffel symbol, and the other subscripts represent partial differentiation.

APPENDIX D
MORE COMPACT MOMENTUM EQUATIONS

The u-equation and v-equation are presented in the following

$$
\begin{aligned}
\frac{1}{H}\frac{\partial Hu}{\partial t} = & -\left(g^{11}\frac{\partial \zeta}{\partial \xi}+g^{12}\frac{\partial \zeta}{\partial \eta}\right)+\frac{g_{12}}{\sqrt{g_o}}u+\frac{g_{22}}{\sqrt{g_o}}v \\
& -\frac{Ro}{g_o H}\left\{x_\eta\left[\frac{\partial}{\partial \xi}\left(y_\xi\sqrt{g_o}Huu+y_\eta\sqrt{g_o}Huv\right)\right.\right. \\
& -\left.\frac{\partial}{\partial \eta}\left(y_\xi\sqrt{g_o}Huv+y_\eta\sqrt{g_o}Hvv\right)\right] \\
& -y_\eta\left[\frac{\partial}{\partial \xi}\left(x_\xi\sqrt{g_o}Huu+x_\eta\sqrt{g_o}Huv\right)\right. \\
& -\left.\left.\frac{\partial}{\partial \eta}\left(x_\xi\sqrt{g_o}Huv+x_\eta\sqrt{g_o}Hvv\right)\right]\right\}+g_o\frac{\partial Hu\omega}{\partial \sigma} \\
& +\frac{E_v}{H^2}\frac{\partial}{\partial \sigma}\left(A_v\frac{\partial u}{\partial \sigma}\right) \\
& -\frac{Ro}{Fr_a^2}\left[H\int_\sigma^0\left(g^{11}\frac{\partial \rho}{\partial \xi}+g^{12}\frac{\partial \rho}{\partial \eta}\right)d\sigma\right. \\
& +\left.\left(g^{11}\frac{\partial H}{\partial \xi}+g^{12}\frac{\partial H}{\partial \eta}\right)\left(\int_\sigma^0\rho d\sigma+\sigma\rho\right)\right] \\
& +E_H A_H\cdot(\text{Horizontal Diffusion of } u)
\end{aligned}
\tag{D.1}
$$

$$
\begin{aligned}
\frac{1}{H}\frac{\partial Hv}{\partial t} = & -\left(g^{21}\frac{\partial \zeta}{\partial \xi}+g^{22}\frac{\partial \zeta}{\partial \eta}\right)-\left(\frac{g_{11}}{\sqrt{g_o}}u+\frac{g_{21}}{\sqrt{g_o}}v\right) \\
& +\frac{Ro}{g_o H}\left\{y_\xi\left[\frac{\partial}{\partial \xi}\left(x_\xi\sqrt{g_o}Huu+x_\eta\sqrt{g_o}Huv\right)\right.\right. \\
& +\left.\frac{\partial}{\partial \eta}\left(x_\xi\sqrt{g_o}Huv+x_\eta\sqrt{g_o}Hvv\right)\right] \\
& -x_\xi\left[\frac{\partial}{\partial \xi}\left(y_\xi\sqrt{g_o}Huu+y_\eta\sqrt{g_o}Huv\right)\right. \\
& +\left.\left.\frac{\partial}{\partial \eta}\left(y_\xi\sqrt{g_o}Huv+y_\eta\sqrt{g_o}Hvv\right)\right]\right\}
\end{aligned}
\tag{D.2}
$$

$$+ \frac{E_v}{H^2}\frac{\partial}{\partial\sigma}\left(A_v\frac{\partial v}{\partial\sigma}\right)$$

$$- \frac{Ro}{F_r{}^2}\left[H\int_\sigma^\circ\left(g^{21}\frac{\partial\rho}{\partial\xi}+g^{22}\frac{\partial\rho}{\partial\eta}\right)d\sigma\right.$$

$$+ \left.\left(g^{21}\frac{\partial H}{\partial\xi}+g^{22}\frac{\partial H}{\partial\eta}\right)\left(\int_\sigma^\circ\rho d\sigma+\sigma\rho\right)\right]$$

$$+ E_H A_H \cdot (\text{Horizontal Diffusion})$$

APPENDIX E
FINITE DIFFERENCE EQUATIONS IN (ξ, η, σ) (THREE-TIME-LEVEL)

E.1 External Mode

The three-time-level scheme of vertically-integrated differential equations is written as follows

$$\zeta_t + \frac{\beta}{\sqrt{g_o}}\left[\frac{\partial}{\partial\xi}(\sqrt{g_o}U) + \frac{\partial}{\partial\eta}(\sqrt{g_o}V)\right] = 0 \tag{E.1}$$

$$U_t + Hg^{11}\zeta_\xi + Hg^{12}\zeta_\eta = \frac{g_{12}}{\sqrt{g_o}}U - C_{\tau\xi}U + D'_x \tag{E.2}$$

$$V_t + Hg^{12}\zeta_\xi + Hg^{22}\zeta_\eta = -\frac{g_{11}}{\sqrt{g_o}}U - \frac{g_{12}}{\sqrt{g_o}}V + D'_y \tag{E.3}$$

The above equations are written in finite difference forms as follows

$$\begin{aligned}\zeta^{n+1} - \zeta^{n-1} \;+\; & \frac{\beta\Delta T}{\Delta\xi\cdot\sqrt{g_o}}[T_1\delta_\xi(\sqrt{g_o}U)^{n+1} + (1-T_1)\delta_\xi(\sqrt{g_o}U^m)] \\ +\; & \frac{\beta\Delta T}{\Delta\eta\cdot\sqrt{g_o}}[T_1\delta_\eta(\sqrt{g_o}V^{n+1}) + (1-T_1)\delta_\eta(\sqrt{g_o}V^m)] = 0\end{aligned} \tag{E.4}$$

$$\begin{aligned}U^{n+1} - U^{n-1} \;+\; & \Delta T\left\{\frac{Hg^{11}}{\Delta\xi}\left[T_1\delta_\xi(\zeta^{n+1}) + (1-T_1)\delta_\xi(\zeta^m)\right]\right. \\ +\; & \left.\frac{Hg^{12}}{\Delta\eta}\left[T_1\delta_\eta(\zeta^{n+1}) + (1-T_1)\delta_\eta(\zeta^m)\right]\right\} \\ =\; - \;& \Delta T\left[T_2C_{\tau\xi}U^{n+1} + (1-T_2)C_{\tau\xi}U^m - T_3\frac{g_{12}}{\sqrt{g_o}}U^{n+1}\right.\end{aligned} \tag{E.5}$$

$$- \quad (1-T_3)\frac{g_{12}}{\sqrt{g_o}}U^m\Bigg] + D_x'^n$$

$$\begin{aligned} V^{n+1} - V^{n-1} &+ \Delta T\Bigg\{\frac{Hg^{12}}{\Delta\xi}\left[T_1\delta_\xi(\zeta^{n+1}) + (1-T_1)\delta_\xi(\zeta^m)\right] \\ &+ \frac{Hg^{22}}{\Delta_\eta}\left[T_1\delta_\eta(\zeta^{n+1}) + (1-T_1)\delta_\eta(\zeta^m)\right]\Bigg\} \\ = &- \Delta T\Bigg[T_2 C_{\tau\eta}V^{n+1} + (1-T_2)C_{\tau\eta}V^m + T_3\frac{g_{12}}{\sqrt{g_o}}V^{n+1} \\ &+ (1-T_3)\frac{g_{12}}{\sqrt{g_o}}V^m\Bigg] + D_y'^n \end{aligned} \tag{E.6}$$

The above equations can be written in ADI scheme as follows

X-sweep:

$$\begin{aligned} \zeta^* + T_1\alpha_x\delta_\xi(\sqrt{g_o}U^*) &= \zeta^{n-1} - \alpha_x(1-T_1)\delta_\xi(\sqrt{g_o}U^n) \\ &- \alpha_y\delta_\eta(\sqrt{g_o}V^n) + T_1\alpha_y\delta_\eta(\sqrt{g_o}V^n - \sqrt{g_o}V^{n-1}) \end{aligned} \tag{E.7}$$

$$\begin{aligned} &T_1\sqrt{g_o}\gamma^{11}\delta_\xi(\zeta^*) + \left[1 + \Delta t\left(T_2 C_{\tau\xi} - T_3\frac{g_{12}}{\sqrt{g_o}}\right)\right](\sqrt{g_o}U^*) \\ = &- T_1\sqrt{g_o}\gamma^{12}\delta_\eta(\zeta^{n-1}) + (\sqrt{g_o}U^{n-1}) \\ &- (1-T_1)\sqrt{g_o}\gamma^{11}\delta_\xi(\zeta^n) - (1-T_1)\sqrt{g_o}\gamma^{12}\delta_\eta(\zeta^n) \\ &- (\sqrt{g_o}U^n)\left[\Delta T(1-T_2)C_{\tau\xi} - \Delta t(1-T_3)\frac{g_{12}}{\sqrt{g_o}}\right] + D_x'^n \end{aligned} \tag{E.8}$$

Y-sweep:

$$\zeta^{n+1} + T_1\alpha_y\delta_\eta(\sqrt{g_o}V^{n+1}) = \zeta^* + T_1\alpha_y\delta_\eta(\sqrt{g_o}V^{n-1}) \tag{E.9}$$

$$\begin{aligned} &T_1\sqrt{g_o}\gamma^{22}\delta_\eta(\zeta^{n+1}) + \left[1 + \Delta t\left(T_2 C_{\tau\eta} + T_3\frac{g_{12}}{\sqrt{g_o}}\right)\right][\sqrt{g_o}V^{n+1}] \\ = &- T_1\sqrt{g_o}\gamma^{12}\delta_\xi(\zeta^*) - (1-T_1)\sqrt{g_o}\gamma^{12}\delta_\xi(\zeta^n) - (1-T_1)\sqrt{g_o}\gamma^{22}\delta_\eta(\zeta^n) \\ &+ (\sqrt{g_o}V^{n-1}) - (\sqrt{g_o}V^m)\left[\Delta t(1-T_2)C_{\tau\eta} + \Delta t(1-T_3)\frac{g_{12}}{\sqrt{g_o}}\right] + D_y'^n \end{aligned} \tag{E.10}$$

U^{n+1} is calculated again with ζ^{n+1}.

$$T_1\sqrt{g_o}\gamma^{12}\delta_\eta(\zeta^{n+1}) + (\sqrt{g_o}U^{n+1}) = (\sqrt{g_o}U^*) + T_1\sqrt{g_o}\gamma^{12}\delta_\eta(\zeta^{n-1}) \tag{E.11}$$

where T_1, T_2 and T_3 are all constants between 0 and 1. For example, the wave propagation terms are treated explicitly if $T_1 = 0$, but implicitly if $T_1 = 1$. m can be $n-1$ or n. Additional parameters appearing in the equations are

$$\begin{aligned}
\alpha_x &\equiv \frac{\beta\Delta t}{g_0\Delta\xi} \\
\alpha_y &\equiv \frac{\beta\Delta t}{g_0\Delta\eta} \\
\gamma^{11} &\equiv \frac{H\Delta t g^{11}}{\Delta\xi} \\
\gamma^{12} &\equiv \frac{H\Delta t g^{12}}{\Delta\xi} \\
\gamma^{22} &\equiv \frac{H\Delta t g^{22}}{\Delta\eta} \\
\gamma^{21} &\equiv \frac{H\Delta t g^{12}}{\Delta\eta}
\end{aligned} \tag{E.12}$$

The system of equations can be rewritten in the following matrix form

$$[A]F^{n+1} = AF^{n-1} + \bar{D} \tag{E.13}$$

$$[I + A_x]F^* = [B - A_y]F^{n-1} + \bar{D} \tag{E.14}$$

$$[I + A_y]F^{n+1} = F^* + A_y F^{n-1} \tag{E.15}$$

where

$$[A] = \begin{bmatrix} 1 & \alpha_x T_1\delta_\xi & \alpha_y T_1\delta_\eta \\ \sqrt{g_0}\gamma^{11}T_1\delta_\xi & 1 + \Delta T\left(C_{\tau\xi}T_2 - \frac{g_{12}}{\sqrt{g_0}}T_3\right) & 0 \\ \sqrt{g_0}\gamma^{22}T_1\delta_\eta & 0 & 1 + \Delta T\left(C_{\tau\eta}T_2 + \frac{g_{12}}{\sqrt{g_0}}T_3\right) \end{bmatrix} \tag{E.16}$$

$$[A_x] = \begin{bmatrix} 0 & \alpha_x T_1 \delta_\xi & 0 \\ \sqrt{g_0}\gamma^{11} T_1 \delta_\xi & \Delta T\left(C_{\tau\xi} T_2 - \frac{g_{12}}{\sqrt{g_0}} T_3\right) & 0 \\ 0 & 0 & 0 \end{bmatrix} \tag{E.17}$$

$$[A_y] = \begin{bmatrix} 0 & 0 & \alpha_y T_1 \delta_\eta \\ 0 & 0 & 0 \\ \sqrt{g_0}\gamma^{22} T_1 \delta_\eta & 0 & \Delta T\left(C_{\tau\eta} T_2 + \frac{g_{12}}{\sqrt{g_0}} T_3\right) \end{bmatrix} \tag{E.18}$$

$$[B] = \begin{bmatrix} 1 & 0 & 0 \\ 0 & 1 & 0 \\ 0 & 0 & 1 \end{bmatrix} \tag{E.19}$$

$$F = \begin{bmatrix} \zeta \\ \sqrt{g_0} U \\ \sqrt{g_0} V \end{bmatrix} \tag{E.20}$$

$$\bar{D} = \begin{bmatrix} -\alpha_x(1 - T_1\delta_\xi(\sqrt{g_0}U^m)) - \alpha_y(1 - T_1)\delta_\eta(\sqrt{g_0}V^m) \\ \sqrt{g_0}U^m \Delta T\left(-(1 - T_2)C_{\tau\xi} + (1 - T_3)\frac{g_{12}}{\sqrt{g_0}}\right) - \sqrt{g_0}\gamma^{11}(1 - T_1)\delta_\xi \zeta^m \\ -\sqrt{g_0}\gamma^{21}\delta_\eta \zeta^m + \Delta T D'_x \sqrt{g_0} \\ \sqrt{g_0}V^m \Delta T\left(-(1 - T_2)C_{\tau\eta} - (1 - T_3)\frac{g_{12}}{\sqrt{g_0}}\right) - \sqrt{g_0}\gamma^{12}\delta_\xi \zeta^m \\ -\sqrt{g_0}\gamma^{22}(1 - T_1)\delta_\eta \zeta^m + \Delta T D'_y \sqrt{g_0} \end{bmatrix} \tag{E.21}$$

E.2 Internal Mode

$$\begin{aligned} \frac{\partial}{\partial t} H\tilde{u} &= \frac{g^{12}}{\sqrt{g_o}} H\tilde{u} + \frac{g^{22}}{\sqrt{g_o}} H\tilde{v} + F_3 \\ &+ \frac{E_v}{H^2}\frac{\partial}{\partial\sigma}\left(A_v \frac{\partial H\tilde{u}}{\partial\sigma}\right) - (\tau_{s\xi} - \tau_{b\xi}) - F_2 \end{aligned} \tag{E.22}$$

$$\begin{aligned} \frac{\partial}{\partial t} H\tilde{v} &= -\frac{g^{11}}{\sqrt{g_o}} H\tilde{u} - \frac{g^{21}}{\sqrt{g_o}} H\tilde{v} + G_3 \\ &+ \frac{E_v}{H^2}\frac{\partial}{\partial\sigma}\left(A_v \frac{\partial H\tilde{v}}{\partial\sigma}\right) - (\tau_{s\eta} - \tau_{b\eta}) - G_2 \end{aligned} \tag{E.23}$$

and F_2 and G_2 indicate all the explicit terms in U and V equations, respectively, and F_3 and G_3 indicate all the explicit terms in the u and v equations, respectively. The subscript s indicates a ζ-point, subscript u indicates a u-point, and subscript v indicates v-point.

$$
\begin{aligned}
(H\tilde{u})^{n+1} &= (H\tilde{u})^{n-1} + 2\Delta t \frac{g^{12}}{\sqrt{g_o}} H^{n+1}\tilde{u}^{n+1} \\
&+ 2\Delta t \frac{g^{22}}{\sqrt{g_o}} H^n \tilde{u}^n + 2\Delta t (F_3 - F_2)^{n-1} \\
&+ 2\Delta t \frac{E_v}{(H^n)^2} \frac{\partial}{\partial \sigma} \left[A_v \frac{\partial}{\partial \sigma} (H^{n+1}\tilde{u}^{n+1}) \right] \\
&- (\tau_{s\xi} - \tau_{b\xi})^{n+1}
\end{aligned} \tag{E.24}
$$

$$
\begin{aligned}
(H\tilde{v})^{n+1} &= (H\tilde{v})^{n-1} - 2\Delta t \frac{g^{11}}{\sqrt{g_o}} H^n \tilde{v}^{n+1} \\
&- 2\Delta t \frac{g^{21}}{\sqrt{g_o}} H^{n+1}\tilde{v}^{n+1} + 2\Delta t (G_3 - G_2)^{n-1} \\
&+ 2\Delta t \frac{E_v}{(H^n)^2} \frac{\partial}{\partial \sigma} \left[A_v \frac{\partial}{\partial \sigma} (H^{n+1}\tilde{v}^{n+1}) \right] \\
&- (\tau_{s\eta} - \tau_{b\eta})^{n+1}
\end{aligned} \tag{E.25}
$$

BIOGRAPHICAL SKETCH

The author was born on April 2, 1954, in Busan, the largest harbor of Korea. He received the Bachelor of Science degree in oceanography at the Seoul National University in February, 1977. Right after that, he had served a military service for 26 months in the Korean Army, as a artillery officer (ROTC). After discharged from the service as a first lieutenant, he had worked as a research scientist at Korea Advanced Institute of Science and Technology (KAIST) until he came to the United States in 1985 to study a hydrodynamic modeling. During his working for KAIST, he earned a M.S. degree in physical oceanography. He had finished a master program in ocean engineering at the University of Rhode Island. The author joined the department of coastal and oceanographic engineering at the University of Florida in 1988 to continue his hydrodynamic modeling works.

He married a God-loving woman, Mija and has a nine-year-old son, Jungmin. His wife wants to have a daughter as her friend for the time when she gets old. Only God will make her wish come true.

This dissertation was submitted to the Graduate Faculty of the College of Engineering and to the Graduate School and was accepted as partial fulfillment of the requirements for the degree of Doctor of Philosophy.

December 1992

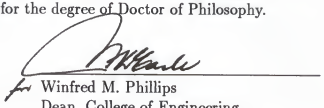

Winfred M. Phillips
Dean, College of Engineering

Madelyn M. Lockhart
Dean, Graduate School

I certify that I have read this study and that in my opinion it conforms to acceptable standards of scholarly presentation and is fully adequate, in scope and quality, as a dissertation for the degree of Doctor of Philosophy.

Y. Peter Sheng, Chairman
Professor of Coastal and Oceanographic Engineering

I certify that I have read this study and that in my opinion it conforms to acceptable standards of scholarly presentation and is fully adequate, in scope and quality, as a dissertation for the degree of Doctor of Philosophy.

Robert G. Dean
Graduate Research Professor of Coastal and Oceanographic Engineering

I certify that I have read this study and that in my opinion it conforms to acceptable standards of scholarly presentation and is fully adequate, in scope and quality, as a dissertation for the degree of Doctor of Philosophy.

D. Max Sheppard
Professor of Coastal and Oceanographic Engineering

I certify that I have read this study and that in my opinion it conforms to acceptable standards of scholarly presentation and is fully adequate, in scope and quality, as a dissertation for the degree of Doctor of Philosophy.

Louis H. Motz
Associate Professor of Civil Engineering